SECONDARY CIRCULATION IN A SINUOUS COASTAL PLAIN ESTUARY

A Dissertation
Presented to
The Academic Faculty

By

Susan Anne Elston

In Partial Fulfillment
of the Requirements for the Degree
Doctor of Philosophy in Earth and Atmospheric Sciences

Georgia Institute of Technology
May 2005

SECONDARY CIRCULATION IN A SINUOUS COASTAL PLAIN ESTUARY

Approved by:

Dr. Jackson O. Blanton, Advisor
Skidaway Institute of Oceanography
University System of Georgia

Dr. Judith A. Curry
School of Earth & Atmospheric Sciences
Georgia Institute of Technology

Dr. Derek M. Cunnold
School of Earth & Atmospheric Sciences
Georgia Institute of Technology

Dr. Harvey E. Seim
Department of Marine Sciences
University of North Carolina – Chapel Hill

Dr. Donald R. Webster
Civil and Environmental Engineering
Georgia Institute of Technology

Dr. Peter J. Webster
School of Earth & Atmospheric Sciences
Georgia Institute of Technology

Dr. Kuo C. Wong
College of Marine Studies
University of Delaware

Date Approved: February 18, 2005

All things by immortal power

Near or far, hiddenly

To each other linked are

That thou canst not stir a flower

Without troubling of a star

Francis Thompson, ‘The Mistress of Vision’

This work is dedicated to the memories of all those who have gone before,

wonderful teachers, inspiring mentors, dear family and friends,

that I have had the honor to know.

You give my achievements meaning and purpose.

ACKNOWLEDGMENTS

I would like to thank several people who made indispensable contributions to this dissertation. I am particularly indebted to my thesis advisor, Dr. Jackson Blanton, and to my committee members, Drs. Judy Curry, Harvey Seim, Derek Cunnold, Donald Webster, Peter Webster, and Kuo Wong, for their patience, guidance, support, and expert suggestions. I would like to thank Julie Amft, Guoqing Lin, Trent Moore, Cheryl Burden Ross, Mike Sharman, Joanna Garcia-Webb, and Kim Hunter for their camaraderie along with their valuable discussions and help in collecting, processing, and analyzing the data.

The able crew (Captain Jay Fripp, Raymond Sweate, Michael Richter, and Dana Ross) of the R/V BLUE FIN and R/V GANNET of the Skidaway Institute of Oceanography kept our research group well-fed and gave us dedicated enthusiasm and support in the carrying out of the numerous field experiments conducted for this research.

Special thanks go to Professors John Simpson and Francis Bretherton, Drs. Arnaldo Valle-Levinson, Robert Chant, Carol Janzen, M. Carla Curran, Tom Rippeth, and Henk Schuttelaars for giving me precious hours in discussion and encouragement. Editorial suggestions greatly improving this work go to my father and Lynette Love. Anna Boyette kindly assisted in preparing the graphical material.

I gratefully acknowledge the financial support of the Land Margin Ecosystems Research Program of the National Science Foundation (Grant No. DEB 9412089) to the University of Georgia, the State of Georgia through its Coastal Zone Management Program, a Presidential Fellowship from the Georgia Institute of Technology, a Rhodes Fellowship from the Department of Earth and Atmospheric Sciences at the

Georgia Institute of Technology, and the Skidaway Institute of Oceanography for supplementary funding and hosting me during my tenure as a graduate student.

Final thanks go to my dear friends and families: the Buchdas, the Elstons, the Grahams, the Petersons, the Sinnetts, and the Woods, and to my wonderful husband Patrick N. Graham for their unending patience, encouragement, assistance, support, and love as I pursue this endeavor.

TABLE OF CONTENTS

ACKNOWLEDGMENTS v

LIST OF TABLES x

LIST OF FIGURES xii

NOMENCLATURE xxi

SUMMARY xxv

1. INTRODUCTION 1

1.1 The Importance of Secondary Circulation to Estuarine Dynamics 1

1.2 Lateral Mixing 3

1.3 Dissertation Research Questions 5

2. SATILLA RIVER, GEORGIA 8

2.1 Discharge Conditions 11

2.2 Salinity Variations 15

2.2.1 Tidal Variations in Salinity 16

2.2.2 Fortnightly Variations in Salinity 17

2.2.3 Seasonal Variations in Salinity 18

3. SECONDARY CIRCULATION 22

3.1 Mechanisms that Generate Secondary Circulation 24

3.2 Mixing and Flow Scaling Parameters 27

3.3 Analytical Models of Secondary Circulation 29

3.3.1 Scale Estimates of Secondary Circulation 30

3.3.2 Coefficient Adjustments to Scaling Formulas for Secondary Circulation 35

3.3.3 Seim and Gregg Curvature-Induced Overturning Model 37

3.3.4 Lateral Momentum Balance in Natural Coordinates 39

3.3.5 Lateral Momentum Balance Model for the Satilla River, Georgia 40

4. MATERIALS AND METHODS 46

4.1 Instrumentation 46

4.1.1 Acoustic Doppler Current Profilers 46

4.1.2 Conductivity-Temperature-Depth Sensors 48

4.1.3 Surface Thermosalinograph 53

4.2 Methods of Deployment 54
4.2.1 Long Term Mooring Deployments 54
4.2.2 Bi-monthly Synoptic Surveys 55
4.2.3 Seasonal Mooring Deployments 55
4.2.4 Anchor Stations 57
4.2.5 Rapid Spatial Survey System 58
4.3 Methods of Data Processing 59
4.3.1 Acoustic Doppler Current Profilers 60
4.3.2 Conductivity-Temperature-Depth Sensors 61
4.3.3 Surface Thermosalinograph 62
5. FORTNIGHTLY SIGNAL OF SECONDARY CIRCULATION AT A BEND 64
5.1 Introduction 64
5.2 Materials and Methods 65
5.2.1 Experiment Site and Environmental Conditions 65
5.2.2 Seasonal Mooring Deployment – Spring 1997 68
5.3 Results and Discussion 72
5.3.1 Salinity and Velocity Distributions 72
5.3.2 Internal Froude Number Calculations 83
5.3.3 Seim and Gregg Curvature-Induced Overturning Model 85
5.4 Conclusions 93
6. COMPARISON OF SECONDARY CIRCULATION IN FOUR REACHES 96
6.1 Introduction 96
6.2 Materials and Methods 97
6.2.1 Experiment Site and Environmental Conditions 97
6.2.2 Seasonal Mooring Deployments – Spring 1997 and Fall 1999 103
6.3 Results and Discussion 112
6.3.1 Tidal and Subtidal Salinity Distributions 112
6.3.2 Tidal Velocity Distributions 114
6.3.3 Subtidal Velocity Distributions 125
6.3.4 The Effect of River Discharge on Secondary Circulation 128
6.3.5 Seim and Gregg Curvature-Induced Overturning Model 136
6.3.6 Scale Estimates of Secondary Circulation 138
6.3.7 Lateral Momentum Balance Model for the Satilla River, Georgia 141
6.3.8 Lateral Momentum Balance Model Sensitivity Analyses and Limitations 154
6.4 Conclusions 161
7. SECONDARY CIRCULATION SIGNATURE IN SPACE AT TWO BENDS 165
7.1 Introduction 165

7.2 Materials and Methods 169
7.2.1 Experiment Site and Environmental Conditions 169
7.2.2 Rapid Spatial Survey System – Spring 1999 173
7.2.3 Reduction of ADCP data to Mean Lower Low Water 184
7.2.4 Idealized Channel Cross-Sections and Principle Axis Determination 185
7.3 Results and Discussion 190
7.3.1 Spring and Neap Tide Salinity Distributions 190
7.3.1.1 Spring Tide – Maximum Ebb 193
7.3.1.2 Neap Tide – Maximum Ebb 194
7.3.2 Spring and Neap Tide Velocity Distributions 195
7.3.2.1 Spring Tide – Maximum Ebb 198
7.3.2.2 Neap Tide – Maximum Ebb 199
7.3.3. Secondary Circulation and the Axial Transfer of Momentum 202
7.3.4. Spatial Characteristics of Secondary Circulation 212
7.3.5 Lateral Momentum Balance Model for the Satilla River, Georgia 219
7.3.5.1 Spring Tide – Maximum Ebb 224
7.3.5.2 Spring Tide – Maximum Flood 225
7.3.5.3 Neap Tide – Maximum Ebb 226
7.3.5.4 Neap Tide – Maximum Flood 227
7.3.6 Lateral Momentum Balance Model Sensitivity Analyses and Limitations ... 232
7.4 Conclusions 244

8. FINAL SUMMARY AND CONCLUSIONS 247

9. RECOMMENDATIONS AND FUTURE RESEARCH 253

APPENDIX A: EQUATIONS 255

APPENDIX B: DEFINITIONS 262

REFERENCES 279

VITA 294

LIST OF TABLES

Table 3.1: Scale estimates for the Satilla River, Georgia. 34

Table 3.2: Recent estuarine experiments using the lateral momentum balance. An X is used to indicate which terms the authors used in their formation of a lateral momentum balance. Italics indicate the lateral momentum balances investigated in this study.....41

Table 5.1: LMER 4 mooring deployment locations. 69

Table 5.2: Broad Band ADCP setup specifications for the LMER 4 experiment. 70

Table 6.1: LMER 4 mooring deployment locations. 106

Table 6.2: Broad Band ADCP setup specifications for the LMER 4 experiment. 106

Table 6.3: SAT 2 mooring deployment locations. 109

Table 6.4: Work Horse ADCP setup specifications for the SAT 2 experiment. 110

Table 6.5: Summary table of river discharge contributions, minimum halting vertical density difference, and tidal straining (SIPS) conditions for the LMER 4 and SAT 2 experiments. 131

Table 6.6: Summary table for the overturning model results and the analytical scale formulas for LMER 4 and SAT 2 data.....132

Table 6.7: Summary of calculated values and 95% confidence intervals for the lateral momentum balance model applied to the LMER 4 and SAT 2 mooring data. The bold highlighted values indicate the balance of terms for a given choice of C_D. 150

Table 7.1: SAT 1 mooring deployment locations. 178

Table 7.2: SAT 1 Roving transect locations. 179

Table 7.3: Broad Band ADCP setup specifications for the SAT 1 experiment. 179

Table 7.4: The buoyancy frequency, the total axial transport per unit area, the total lateral transport per unit area, and the total axial momentum for the lateral cross-sections: Domain A 4/5 – Domain B 10/11. To assess acceleration and deceleration into and out of the channel bends, read down the table from A 4/5 – B 10/11 for flood tide and read up the table from B 10/11 – A 4/5 for ebb tide. 211

Table 7.5: The spatial and temporal characteristics of secondary circulation during spring and neap tides.....213

Table 7.6: Calculated values and 95% confidence intervals for the LMBM at the lateral sections: Domain A 4/5 – Domain B 10/11. 228

LIST OF FIGURES

Figure 2.1: An aerial photograph of the Satilla River in southeast Georgia. 9

Figure 2.2: A photograph of Sara's Creek in the upper Satilla River taken by S. Elston. 10

Figure 2.3: U.S. Geological Survey historical daily mean discharge data for the Satilla River at the Atkinson, Georgia, gauging station. 12

Figure 2.4: (a) The Satilla River discharge during the 1997 LMER 4 experiment. (b) The Satilla River discharge during the 1999 SAT 1 and SAT 2 experiments. Gray boxes denote the period of mooring deployments for each experiment. 13

Figure 2.5: (a) The Satilla River discharge during the SAT 1 and SAT 2 experiments. (b) The subtidal salinity measured at the moorings 3 – 7 (red, green, cyan, blue, and magenta lines, respectively) in the Satilla River during the 1999 SAT 1 and SAT 2 experiments. The black line represents the salinity field measured at the near ocean long-term mooring. Gray boxes denote the period of mooring deployments for each experiment. 15

Figure 2.6: (a) Synoptic survey of high water salinity in the Satilla River under moderate discharge conditions (February 1999). (b) Synoptic survey of high water salinity in the Satilla River under low discharge conditions (December 1999). 21

Figure 3.1: Photograph of a convergent axial foam front in the Satilla River, Georgia. This type of convergent front indicates the presence of a local secondary circulation. The photograph was taken by S. Elston at anchor during the 1997 LMER 4 experiment. 23

Figure 3.2: An illustration in the change of direction for the Coriolis force and the centrifugal force as a function of tidal direction (ebb or flow). 31

Figure 4.1: A photograph of the Skidaway Broad Band ADCP in tow off the starboard side of the R/V Gannet. 47

Figure 4.2: A photograph of a Skidaway Work Horse ADCP. A SeaCAT CTD is attached on the upper left leg of the mooring frame. 48

Figure 4.3: A photograph of a Skidaway MicroCAT CTD prior to deployment. 49

Figure 4.4: A photograph of the Skidaway SBE 19 profiling CTD on the starboard deck of the R/V Blue Fin. 50

Figure 4.5: A photograph of the Skidaway FSI CTD on the port deck of the R/V Gannet. 51

Figure 4.6: A photograph of a Skidaway MicroCAT CTD after a month-long late summer deployment. Rapid bio-fouling occurs when the ambient water temperature exceeds 25°C.....52

Figure 4.7: Map of Satilla River mooring deployment sites for the SAT 1 and SAT 2 experiments. The LMER 4 mooring was approximately 1 km on either side of SAT mooring number 3. 56

Figure 4.8: A schematic of the SAT 1 and SAT 2 mooring deployments. Note that the figure is not to scale. 57

Figure 4.9: A schematic of the rapid spatial survey system aboard the R/V Gannet. 59

Figure 5.1: Photograph of a local secondary circulation during late flood tide in the Satilla River. Water on the near side of the front (toward the outside of the channel bend) is about 1 PSU less than water on the far side of the front (toward the inside of the channel bend). The photograph was taken by S. Elston during the LMER 4 experiment. 65

Figure 5.2: Map of the Satilla River in southeast Georgia near the Florida border. Mooring locations for the March – April 1997 field survey are indicated in the first river bend by two diamonds and one circle. The diamond regions indicate locations of surface and bottom salinity measurements, and the circular region indicates the location of the acoustic current profiler and 25-hour anchor stations. 67

Figure 5.3: Salinity time series for the March – April 1997 LMER 4 field survey. The 40-hour low pass signature is plotted on top of the surface salinity data for each mooring location east and west of the anchor station location at river kilometer 13, respectively. River discharge ranged from 60 m^3 s^{-1} at the beginning of this field campaign to 7 m^3 s^{-1} at the end. Neap and spring tides are indicated by NP and SP, respectively. 74

Figure 5.4: (a) Density profiles taken during the neap LMER 4 anchor station. The maximum vertical density difference observed during the neap anchor station was $\Delta\rho$ = 5.1 kg m^{-3}. (b) Corresponding density profiles taken during the spring LMER anchor station. The maximum vertical density difference observed during the spring anchor station was $\Delta\rho$ = 1.4 kg m^{-3}. The different colors represent individual casts.....75

Figure 5.5: (a) Axial velocity profiles from the BB ADCP during the LMER 4 field experiment for (a) neap and (b) spring tides. Positive values indicate ebb flow and negative values indicate flood flow. 76

Figure 5.6: (a) BB ADCP velocity measurements taken during the LMER 4 field experiment in the along-channel (a) and cross-channel (b) directions. Positive values in the along-channel velocity (a) indicate ebb flow, and negative values indicate flood flow. Likewise, positive values in the cross-channel velocity (b) indicate flow to the outside of the channel bend (to the north), and negative values indicate the flow to the inside of the bend (to the south). NP and SP indicate neap and spring tides, respectively. 79

Figure 5.7: (a) Cross-channel BB ADCP velocity measurements taken during the LMER 4 field experiment. Positive values indicate flow to the outside of the channel bend and negative values indicate flow to the inside of the bend. Note: the section in the upper panel corresponds to a subset of the lower panel. (b) Results of a 40-hour low-pass filter applied to the lateral velocity at three levels (indicated by solid black lines in the upper panel). The three levels represent near bottom velocity (low bin ~ 3 mab), mid-depth velocity (mid bin ~ 5 mab), and near surface velocity (high bin ~ 7 mab). NP and SP indicate neap and spring tides, respectively. 80

Figure 5.8: Lateral velocity data at the first neap tidal cycle during the LMER 4 experiment. Positive values indicate flow to the outside of the channel bend, and negative values indicate flow to the inside of the channel bend. A secondary flow driven by channel curvature is directed toward the outside of the channel bend (red) in the near surface, and toward the inside of the bend (blue) in the near bottom. Note the presence of two stacked secondary cells from year days 91.4 to 91.6 and from year days 91.9 to 92.1. 81

Figure 5.9: (a) The Satilla River daily mean discharge during the LMER 4 experiment. (b) Subtidal cross-channel velocity (secondary flow) during the LMER 4 mooring deployment. Positive values (red) show flow to the outside of the bend, and negative values (blue) show flow to the inside of the bend. Note the difference in the strength and duration of the lowermost secondary cell at year days 92 and 105. 82

Figure 5.10: (a) Plot of the critical Fr_i limits and depth-average axial current during the LMER 4 neap anchor (a) and the LMER 4 spring anchor (b). Note that the region between the thick gray lines corresponds to $Fr_i^2 \leq 1$ and is derived from the measured density profiles and the axial current at neap (a) and at spring (b), respectively. 84

Figure 5.11: (a) A plot of alpha, a measure of the vertical shear in the axial current, during LMER 4 neap tide. (b) A plot of alpha during LMER 4 spring tide. The water level is indicated by a solid black line in both the upper and lower panels. 87

Figure 5.12: An illustration of the hypothesized secondary circulation mixing mechanism around a channel bend at neap (a) and at spring (b). The minimum axial current necessary to vertically mix the water column (Seim and Gregg 1997) and the maximum observed axial current are respectively given to the right of each illustration. 93

Figure 6.1: Map of the Satilla River in southeast Georgia near the Florida border. The mooring locations for the SAT 2 (September – October 1999) field survey are indicated by bold numbers 2 through 7. The LMER 4 mooring location (March – April 1997) corresponds with the SAT 2 Station 3. LT 1 refers to the long-term mooring (March 1999 – April 2000) near St. Andrews Sound. Darker colors indicate deeper depths. 99

Figure 6.2: (a) The Satilla River discharge during the 1997 LMER 4 experiment. (b) The Satilla River discharge during the 1999 SAT 2 experiment. NP and SP respectively refer to neap and spring tides. 102

Figure 6.3: High water axial surveys done in 1999 prior to instrument deployment, during peak observed river discharge, and prior to instrument retrieval during the SAT 1 and SAT 2 experiments. (a) River discharge was 17 m^3 s^{-1}. (b) River discharge was 97 m^3 s^{-1} just after a freshwater pulse event in late January. (c) River discharge was 21 m^3 s^{-1}. (d) River discharge was 4 m^3 s^{-1} after several months of little or no precipitation. (e) River discharge was 10 m^3 s^{-1} just after the pulse event associated with Hurricane Floyd. The white space indicates a one hour break in the axial survey. Numbers below each plot indicate Station locations. 103

Figure 6.4: A schematic of a SAT 2 mooring deployment. Note that the figure is not drawn to scale. 108

Figure 6.5: (a) Fortnightly salinity time series for the 1997 LMER 4 field survey. The 40-hour low pass signature is plotted on top of the surface salinity data for each mooring location. (b) Fortnightly salinity time series for the 1999 SAT 2 field survey. The 40-hour low pass signature is plotted on top of the surface salinity data for each mooring location. Neap and spring tides are indicated by NP and SP respectively. 119

Figure 6.6: Axial velocity profiles respectively for spring and neap tides at Station #3 (a & b), at Station #4 (c & d), at Station #5 (e & f), and at Station #6 (g & h). Positive values indicate ebb flow and negative values indicate flood flow. 120

Figure 6.7: (a) Lateral ADCP velocity measurements taken during spring tide at (a) LMER 4 Station #3; (b) SAT 2 Station #4; (c) SAT 2 Station #5; and at (d) SAT 2 Station #6. Positive values in all subpanels indicate flow to the outside of the bend, while respectively; negative values indicate flow to the inside of the bend. 121

Figure 6.8: (a) Lateral ADCP velocity measurements taken during neap tide at (a) LMER 4 Station #3; (b) SAT 2 Station #4; (c) SAT 2 Station #5; and at (d) SAT 2 Station #6. The repeated blue streak at ebb in subpanel c is an artifact generated by the tethering wire attaching the MicroCAT CTD to the ADCP mooring frame. Positive values as in Figure 6.6 indicate flow to the outside. 122

Figure 6.9: (a) Results of a Butterworth 40-hour low-pass filter applied to the cross-channel velocity, removing tidal variability, at four levels for (a) LMER 4 Station #3; (b) SAT 2 Station #4; (c) SAT 2 Station #5; and (d) SAT 2 Station #6. These levels represent near bottom velocity (low bin ~ 3.3 mab), low mid-depth velocity (low mid bin ~ 4.3 mab), high mid-depth velocity (mid high bin ~ 5.3 mab), and near surface velocity (high bin ~ 6.3 mab). NP and SP indicate neap and spring tides, respectively.....123

Figure 6.10: (a) Subtidal lateral velocity (secondary flow) at (a) Station #3 during LMER 4; (b) Station #4 during SAT 2; (c) Station #5 during SAT 2; and (d) Station #6 during SAT 2. Positive values (red) show flow to the outside of the bend, and negative values (blue) show flow to the inside of the bend. NP and SP indicate neap and spring tides, respectively.....124

Figure 6.11: Satilla River lateral momentum balance terms for LMER 4 Station #3. Freshwater discharge has been divided by 1 x 10^7 and plotted as a solid black line. Neap and spring tides are indicated by NP and SP, respectively.....146

Figure 6.12: Satilla River lateral momentum balance terms for SAT 2 Station #4. Freshwater discharge has been divided by 1 x 10^7 and plotted as a solid black line. Neap and spring tides are indicated by NP and SP, respectively.....147

Figure 6.13: Satilla River lateral momentum balance terms for SAT 2 Station #5. Freshwater discharge has been divided by 1 x 10^7 and plotted as a solid black line. Neap and spring tides are indicated by NP and SP, respectively.....148

Figure 6.14: Satilla River lateral momentum balance terms for SAT 2 Station #6. Freshwater discharge has been divided by 1 x 10^7 and plotted as a solid black line. Neap and spring tides are indicated by NP and SP, respectively.....149

Figure 6.15: Channel curvature and channel width defined with respect to the channel center-line (indicated by red) and with respect to the *thalweg* (indicated by black).....158

Figure 7.1: Map of the Satilla River in southeast Georgia near the Florida border. The mooring locations for the SAT 1 (January – March 1999) field survey are indicated by bold numbers 2 through 7. LT 1 refers to the long-term mooring (March 1999 – April 2000) near St. Andrews Sound. Darker colors indicate deeper depths. 171

Figure 7.2: Map of Domain A and Domain B in first bend of the Satilla River. Black lines indicate roving transect cross-sections. The depth variations (colorbar) in this figure are the same as shown in Figure 7.1. 172

Figure 7.3: The R/V Gannet boat tracks during the 13-hour Domain A and B rapid surveys. Circles indicate the location of the cross-sectional data as shown in Figure 7.2. 175

Figure 7.4: Tidal stage relative to MLLW during the (a) Domain A and (b) Domain B rapid surveys at spring tide. Circles indicate comparative maximum ebb tide conditions while squares indicate comparative maximum flood tide conditions. Numbers correspond to the beginning and end of the CTD casts taken during each Domain survey..... 176

Figure 7.5: Tidal stage relative to MLLW during the (a) Domain A and (b) Domain B rapid surveys at neap tide. Circles indicate comparative maximum ebb tide conditions while squares indicate comparative maximum flood tide conditions. Numbers correspond to the beginning and end of the CTD casts taken during each Domain survey..... 177

Figure 7.6: A schematic of the rapid spatial survey system aboard the R/V Gannet. 180

Figure 7.7: A photograph of the R/V Gannet active in a rapid spatial survey. 180

Figure 7.8: (a) Cross-section grid dimensions and orientation. (b) An idealized cross-section. 186

Figure 7.9: Principle axis determination based on the global mean of the depth-average lateral transport at cross-sections (a) B 10/11, (b) B 5/6, (c) A 9/10, and (d) A 4/5. The orientation and degrees of rotation are noted by orange lettering at each cross-section location. Likewise, after rotation to the new principle axis, the normalized average transport associated with the registered gridded idealized cross-sections for each location is shown in gray lettering. CCW and CW respectively indicate the counter-clockwise and clockwise directions. 189

Figure 7.10: (a) Plan view plot of SBE-21 surface track in Domain A 4/5 during maximum ebb at spring tide. (b) YZ plot of the SBE-21 surface track with FSI CTD casts in Domain A 4/5 during maximum ebb at spring tide. The leftmost cast corresponds to the north channel and the rightmost cast corresponds to the south channel. The salinity structure shown is stratified laterally ~ 2 PSU across the channel, stratified ~ 3 PSU vertically in the deep channel, and well-mixed vertically over the shoal. 193

Figure 7.11: (a) Plan view plot of SBE-21 surface track in Domain A 4/5 during maximum ebb at neap tide. (b) YZ plot of the SBE-21 surface track with FSI CTD casts in Domain A 4/5 during maximum ebb at spring tide. The leftmost cast corresponds to the north channel and the rightmost cast corresponds to the south channel. The salinity structure shown is stratified laterally ~ 2 PSU across the channel, stratified ~ 7 PSU vertically in the deep channel, and stratified vertically ~ 5 PSU over the shoal. 194

Figure 7.12: The (a) axial, (b) lateral, and (c) vertical velocity structure in Domain A 4/5 for maximum ebb conditions at spring tide. Red in subpanel (a) indicates ebb flow, red in subpanel (b) indicates flow to the outside of the channel bend, and red subpanel in (c) indicates upward flow. The bold solid line in the figure subpanels indicates the zero crossing and the approximate locations of the shallows, flank of the shoal (labeled as flank), and the *thalweg* are shown below each subpanel. 198

Figure 7.13: The (a) axial, (b) lateral, and (c) vertical velocity structure for maximum ebb at neap tide in Domain A 4/5. Red in subpanel (a) indicates ebb flow, red in subpanel (b) indicates flow to the outside of the channel bend, and red subpanel in (c) indicates upward flow. The bold solid line in the figure subpanels indicates the zero crossing and the approximate locations of the shallows, flank of the shoal (labeled as flank), and the *thalweg* are shown below each subpanel. 199

Figure 7.14: The tidally-averaged mean axial velocity in lateral cross-section Domain A 4/5 for (a) spring tide and for (b) neap tide. Seaward flow is indicated by positive values and landward flow is indicated by negative values. The bold solid line in the figure subpanels indicates the zero crossing. 200

Figure 7.15: The tidally-averaged mean lateral velocity in lateral cross-section Domain A 4/5 for (a) spring tide and for (b) neap tide. Flow toward the outside of the channel bend is indicated by positive values and flow toward the inside of the channel bend is indicated by negative values. The bold solid line in the figure subpanels indicates the zero crossing. 201

Figure 7.16: The spatial scales of secondary circulation and the transfer of axial momentum downriver (the core velocity in each subpanel multiplied by a constant density, $\rho_o = 1014$ kg m^{-3}) during maximum ebb at spring tide for sections (a) Domain B 10/11, (b) Domain B 5/6, (c) Domain A 9/10, and (d) Domain A 4/5.....205

Figure 7.17: The spatial scales of secondary circulation and respectively, the transfer of axial and lateral momentum in the downstream direction (the core velocity in each subpanel multiplied by a constant density, $\rho_o = 1014$ kg m^{-3}) during maximum ebb at spring tide for sections (a & b) Domain B 10/11, (c & d) Domain B 5/6, (e & f) Domain A 9/10, and (g & h) Domain A 4/5. 206

Figure 7.18: Axial velocity profiles at maximum ebb for spring tide conditions in the representative lateral cross-section Domain A 4/5. 207

Figure 7.19: The spatial scales of secondary circulation and the transfer of axial momentum downriver (the core velocity in each subpanel multiplied by a constant density, $\rho_o = 1014$ kg m^{-3}) during maximum ebb at neap tide for sections (a) Domain B 10/11, (b) Domain B 5/6, (c) Domain A 9/10, and (d) Domain A 4/5.....208

Figure 7.20: The spatial scales of secondary circulation and respectively, the transfer of axial and lateral momentum in the downstream direction (the core velocity in each subpanel multiplied by a constant density, $\rho_o = 1014$ kg m^{-3}) during maximum ebb at neap tide for sections (a & b) Domain B 10/11, (c & d) Domain B 5/6, (e & f) Domain A 9/10, and (g & h) Domain A 4/5. 209

Figure 7.21: Axial velocity profiles at maximum ebb for neap tide conditions in the representative lateral cross-section Domain A 4/5. 210

Figure 7.22: The axial velocity structure for cross-sections B 10/11 through A 4/5 during maximum ebb at spring tide. The darker red color indicates the location of the maximum axial velocity. Ovals indicate the location of the sinuous *thalweg*.....216

Figure 7.23: The lateral velocity structure for cross-sections B 10/11 through A 4/5 during maximum ebb at spring tide. The orange color indicates flow to the outside of the channel bend. Arrows indicate an orientation shift in the flow between lateral cross-sections. 217

Figure 7.24: The vertical velocity structure for cross-sections.....218
B 10/11 through A 4/5 during maximum ebb at spring tide. The red color indicates upward flow. Note the multiple appearances of vertical circulation cells.

Figure 7.25: Satilla River lateral momentum balance terms (blue curvature, red density, magenta bottom stress, and cyan Coriolis) during maximum ebb at spring tide for sections (a) Domain A 4/5, (b) Domain A 9/10, (c) Domain B 5/6, and (d) Domain B 10/11. The black dashed line in each subpanel represents the lateral cross-section bathymetry. The bottom stress term was calculated using the original drag coefficient, $C_D = 2.5 \times 10^{-3}$. 224

Figure 7.26: Satilla River lateral momentum balance terms (blue curvature, red density, magenta bottom stress, and cyan Coriolis) during maximum flood at spring tide for sections (a) Domain A 4/5, (b) Domain A 9/10, (c) Domain B 5/6, and (d) Domain B 10/11. The black dashed line in each subpanel represents the lateral cross-section bathymetry. The bottom stress term was calculated using the original drag coefficient, $C_D = 2.5 \times 10^{-3}$. 225

Figure 7.27: Satilla River lateral momentum balance terms (blue curvature, red density, magenta bottom stress, and cyan Coriolis) during maximum ebb at neap tide for sections (a) Domain A 4/5, (b) Domain A 9/10, (c) Domain B 5/6, and (d) Domain B 10/11. The black dashed line in each subpanel represents the lateral cross-section bathymetry. The bottom stress term was calculated using the low drag coefficient, $C_D = 3.1 \times 10^{-3}$. 226

Figure 7.28: Satilla River lateral momentum balance terms (blue curvature, red density, magenta bottom stress, and cyan Coriolis) during maximum flood at neap tide for sections (a) Domain A 4/5, (b) Domain A 9/10, (c) Domain B 5/6, and (d) Domain B 10/11. The black dashed line in each subpanel represents the lateral cross-section bathymetry. The bottom stress term was calculated using the original drag coefficient, $C_D = 2.5 \times 10^{-3}$. 227

Figure 7.29: Satilla River lateral momentum balance terms (blue curvature, red the sum of density, bottom stress, and Coriolis) illustrating the 'best fit' C_D choice for maximum flood at spring tide for sections (a) Domain A 4/5, (b) Domain A 9/10, (c) Domain B 5/6, and (d) Domain B 10/11. The black dashed line in each subpanel represents the lateral cross-section bathymetry. The bottom stress term was calculated using the original drag coefficient, $C_D = 2.5 \times 10^{-3}$. 236

Figure 7.30: Satilla River lateral momentum balance terms (blue curvature, red the sum of density, bottom stress, and Coriolis) illustrating the 'best fit' C_D choice for maximum flood at spring tide for sections (a) Domain A 4/5, (b) Domain A 9/10, (c) Domain B 5/6, and (d) Domain B 10/11. The black dashed line in each subpanel represents the lateral cross-section bathymetry. The bottom stress term was calculated using the low drag coefficient, $C_D = 3.1 \times 10^{-3}$. 240

Figure 7.31: The (a) curvature acceleration, the (b) Coriolis acceleration, and the (c) density acceleration terms for the LMBM at section Domain A 4/5 for maximum ebb at neap tide. The solid black line in the subpanels indicates the zero crossing. 241

Figure 7.32: The (a) curvature acceleration, the (b) Coriolis acceleration, and the (c) density acceleration terms for the LMBM at section Domain A 4/5 for maximum flood at spring tide. The solid black line in the subpanels indicates the zero crossing. 242

NOMENCLATURE

Units

cm	centimeter
°C	degree Centigrade
‰	parts per thousand
H	characteristic depth
h	hour
kg	kilogram
km	kilometer
kt	knot (nautical mile per second)
ℓ	liter
L	characteristic length
M	mass
m	meter
mab	meters above bottom
mb	millibar
mm	millimeter
Pa	Pascals (1 Pa ~ 10^2 mb)
ppt	parts per thousand (same as PSU)
PSU	practical salinity unit (1 PSU ~ 1 ‰)
s	second
T	characteristic time
U	characteristic velocity

Acronyms

ACE Basin	Ashepoo – Combahee – South Edisto River Basin
ADCP	Acoustic Current Doppler Profiler
BB ADCP	Broad Band Acoustic Current Doppler Profiler
CA	centrifugal acceleration
CF	Coriolis acceleration
CTD	Conductivity-Depth-Temperature
DGPS	Differential Global Positioning System
GA LMER	Georgia Land Margin Ecological Research Project
HW	High Water
HWS	High Water Slack
LBC	lateral baroclinic pressure gradient
LHS	left hand side
LMBM	Lateral Momentum Balance Model for the Satilla River
LMER4	Land Margin Ecological Research Experiment #4: March – April 1997
LW	Low Water
LWS	Low Water Slack
LT 1	Long term mooring #1 – near river kilometer 8
LT 2	Long term mooring #2 – near Woodbine, Georgia, near river kilometer 40
MHHW	Mean Higher High Water
MHW	Mean High Water
MLW	Mean Low Water
MLLW	Mean Lower Low Water
MSL	Mean Sea Level

NGDC	National Geophysical Data Center
NOAA	National Oceanic and Atmospheric Administration
NWS	National Weather Service
RDI	RD Instruments, Inc.
R/V	Research Vessel
RHS	right hand side
SAT 1	Satilla River, Experiment #1: January - March 1999
SAT 2	Satilla River, Experiment #2: September - October 1999
SBE	SeaBird Electronics, Inc.
SIPS	Strain Induced Periodic Stratification
TBT	Tri-butyl Tin antifoulant
USCG	United States Coast Guard
USGS	United States Geological Survey
VSS	vertical shear stress
WH ADCP	Work Horse Acoustic Current Doppler Profiler
WOC	White Oak Creek

Symbols

C_D	drag coefficient
$\Delta\rho$	differential density (between two layers)
ρ_o	ambient reference density
D_E	Ekman depth
Ek	vertical Ekman number
f	Coriolis parameter

Fr_d	densimetric Froude number
Fr_i	internal Froude number
g	gravitational acceleration
g′	reduced gravity
l_{M_2}	tidal excursion length
N_z	buoyancy or Brunt-Väisälä frequency
R	local radius of curvature
R_e	Reynolds number
Ri	gradient Richardson number
Ri_b	bulk Richardson number
R_o	Rossby number
$R_{o,def}$	Rossby deformation radius
S′	Burger number
$\tau_{n,b}$	lateral bottom shear stress
$\tau_{s,b}$	axial bottom shear stress
T_{adv}	advective time scale
T_{bc}	baroclinic time scale
T_f	frictional relaxation time scale
U	total flow in the horizontal direction
$\overline{U}$	mean flow in the horizontal direction
U_{rms}	root-mean-square (rms) flow in the horizontal direction
U_n	lateral, transverse, or cross-channel velocity (in natural coordinates)
U_s	streamwise or along-channel velocity (in natural coordinates)

SUMMARY

Transport and mixing of momentum and salt in an estuary varies in time and space due to river discharge, changes in tidal amplitude and phase, wind stress, and lateral mixing processes. Lateral mixing commonly refers to poorly resolved, rarely quantified interaction(s) between flows induced by secondary circulation, river discharge, wind stress, and tidal forces. Modern instrumentation and better computational techniques have generated a resurgent interest in better comprehending such interactions. The intent of this dissertation is to observe, describe, parameterize, and quantifying secondary circulation using acoustic current meters in a sinuous coastal plain estuary. This endeavor is made to improve our general understanding of secondary circulation, to identify its primary driving forces, and to better parameterize key physical processes necessary for further study in current numerical models.

Secondary circulation is a broad and often confusing term used to describe several mechanisms whose result is to vertically overturn the water column along the transverse axis of a channel. Most commonly, secondary circulation is generated by one or more of the following mechanisms: channel curvature, unusual bottom topography or channel geometry, planetary rotation, and/or the differential advection of density. Secondary circulation may be composed of one or more cells that can act to reduce or enhance local velocity and density gradients. A physical manifestation of secondary flow is often observed as foam or slick lines down the longitudinal axis of an estuary.

Field data for this dissertation was collected in the naturally sinuous Satilla River in southeast Georgia during the spring of 1997 and during the spring and fall of 1999. A

shallow coastal plain estuary, the Satilla is a typical partially-mixed estuary characterized by 2 - 2.5 meter range semidiurnal tides. It has a strong neap-to-spring axial current inequality ranging from 0.5 m s^{-1} to 2.0 m s^{-1} and, likewise, has strong neap-to-spring vertical salinity variations in the *thalweg* from 7 PSU to 2 PSU. The density structure of the Satilla River is most sensitive to variations in salinity.

In the Satilla River, secondary circulation driven by channel curvature dominates the lateral momentum balance on time scales longer than the fortnightly tidal cycle. The signal of secondary circulation is modulated on the neap-to-spring cycle due to changes in the interaction of the vertical density gradient and the speed of the axial current. At neap, the vertical stratification can limit or halt the local transverse circulation. A first order inviscid balance between the lateral baroclinic gradient and centrifugal acceleration is sufficient to explain the observed modulation. Changes in freshwater discharge do not directly affect the strength and modulation of the transverse circulation, but rather, affect the location of the maximum axial and vertical salinity gradients.

The balance of mechanisms responsible for the strength and location of secondary flows in the Satilla River varies with channel geometry, discharge conditions, fortnightly tidal cycle, ebb and flood tidal phase, and lateral cross-channel position. A steady-state momentum balance between the Coriolis acceleration, centrifugal acceleration, the lateral baroclinic gradient, and bottom stress is sufficient to explain the observed changes in secondary circulation on the tidal and fortnightly time scales in the Satilla River under widely different discharge conditions and in several differently curved channel reaches. The primary momentum balance at spring tide is between centrifugal acceleration and bottom stress. At neap tide, depending on local stratification and form drag, the primary

momentum balance shifts from a two-way balance between centrifugal acceleration and the lateral baroclinic gradient at low drag states to a three-way balance between centrifugal acceleration, the lateral baroclinic gradient, and bottom stress at high drag states. The change in the balance of forces that drive secondary circulation in a channel cross-section varies with lateral position. In the *thalweg*, the dynamic balance is between the centrifugal acceleration and the lateral baroclinic pressure gradient. In the shallows and on the shoal flanks, the dynamic balance is between the centrifugal acceleration, the lateral baroclinic pressure gradient, and bottom stress. Bottom stress drives secondary circulation in the very shallow intertidal areas of the Satilla River where bathymetry changes rapidly, acting independently of tidal phase (ebb or flood).

It is important to be able to understand what processes generate and limit the strength of secondary circulation in estuaries in order to predict the length of the salt intrusion, the locus of momentum transfer, and to determine the dispersion and distribution of various properties (e.g., larvae, sediment, and pollutants) in the estuarine environment.

1. INTRODUCTION

1.1 The Importance of Secondary Circulation to Estuarine Dynamics

Estuaries have always been important in the development and growth of human societies. These unique transitional environments between riverine systems and the coastal ocean are among the most biologically productive areas in the world, and are a major source of drinking and industrial water for many coastal communities. This is especially true in today's society where over 23% of the world's population lives within 100 miles of a coastline (Nicholls and Smalls 2002), and in a nation whose urban centers are ever expanding coastward.

Understanding the balances of momentum and salt in an estuary are fundamental to the study of estuarine dynamics. In addition, this knowledge is important for understanding the dispersion of pollutants and the distribution of biological and chemical properties in the marine and nearshore environment. Public health concerns regarding a higher standard of water quality and increased mariculture development in estuarine environments make comprehending and quantifying these balances particularly timely subjects.

Examples of local concerns in Savannah, Georgia, range from the fate and transport of heavy metal effluent historically discharged by the U.S. Department of Energy Savannah River Site into the Savannah River estuary (Mulholland and Olsen 1992) to the debate on the withdrawal, treatment, use, and potential underground storage of river water as a freshwater drinking source for coastal Georgia and South Carolina (*'New' water getting bad reviews',* Dewig 1999; '*Florida water officials pitch aquifer*

storage', Williams 1999; *'State to close water deal'*, Farrington 2003). Regional crabbers are concerned about the fate of the Georgia blue crab, which appears to be less disease resistant with increasingly warmer, salty waters (*'Disease killing area blue crab'*, Krueger 1999). Additional local concerns focus on ever increasing areas of marsh die-off and on increased development in the coastal zone environment (*'Environment challenged'*, Landers 2003; *'Alabama, Florida seek to block new water allotments for Georgia'*, Reeves 2004).

Further, a better understanding estuarine dynamics could significantly aid in the placement and maintenance of freshwater drinking facilities (Dunne and Leopold 1978; Prandle 1985) as well as the potential to reduce crop loss in marginally productive areas, e.g., rice paddies and crawfish farms (Clarke and Gibson 1987; Uehara 1984; Walter Stevens, personal communication). This is especially important for the United States, a nation whose major urban centers (for example: New York, Washington, D.C., Miami, Seattle, San Francisco, and San Diego) are expanding coastward, and whose major source of drinking water is from rivers and groundwater in the estuarine environment (World Resources Institute 1994).

The distribution of salt and momentum in an estuary vary in both time and space due to river discharge, changes in tidal amplitude and phase, wind stress, lateral mixing processes, and frictional processes at both the bottom and lateral boundaries (Savenije 1993). Classical estuarine studies (Pritchard 1952; Pritchard 1956; Bowden 1963; Hansen and Rattray 1965) have often focused on the along-channel aspects of the salt and momentum balance. This is largely because the dominant scale of motion in an estuary is directed longitudinally, and older technology limited measurements to this direction. By

assuming that estuarine transport occurs principally in the longitudinal direction, complex mathematical formulations become more tractable, yielding reasonable analytical solutions that explain a variety of observed phenomena. Although this classical picture explains much about the estuarine circulation, it obscures the additional contributions to the local and estuarine-wide salt and momentum balances made by lateral transport processes, of which secondary circulation is one of the primary mechanisms.

To improve our understanding of the salt and momentum balances in an estuary, detailed three-dimensional observations and enhanced conceptual models that include lateral variability are needed. The evolution of instrumentation necessary to obtain detailed field measurements along with the recent advances in numerical modeling techniques, access to high-speed computing facilities, and the development of new acoustic profiling instruments have brought renewed interest in understanding the effect of secondary circulation on estuarine dynamics. This dissertation will address how recently acquired three-dimensional observations, containing detailed measurements of lateral variability in both time and space, provide a unique opportunity to improve our understanding of how secondary circulation operates and its relationship to changes in the lateral momentum balance.

1.2 Lateral Mixing

Lateral mixing and exchange are little understood and poorly defined processes in estuarine dynamics (Geyer and Signell 1992; Garrett 2002). Lateral mixing commonly refers to poorly resolved, rarely quantified non-linear interactions between river discharge, wind stress, and secondary processes such as transverse or secondary circulation. The redistribution of salt and momentum by lateral mixing is often

mentioned in the literature as a significant contributing factor in altering the local salt flux and changes in larvae, momentum, and sediment distributions in an estuary. Scaling arguments are commonly used (Gill 1982; Dutton 1987; Pond and Pickard 1989; Holton 1992) as a way to neglect these smaller scale lateral processes. Consequently, advances on this subject, particularly in partially mixed estuaries, have been limited (Trowbridge et al. 1999).

While the ability to collect and analyze detailed observational data has greatly improved our knowledge of the three-dimensional flux of estuarine properties, few investigations appear to have been done which are able to quantify the contributions of secondary flows to changes in the lateral momentum balance. It is often difficult and expensive to collect the detailed comprehensive field data required for a proper examination of this problem. This is particularly true in the case of lateral studies, which need to collect simultaneously both longitudinal and lateral data (Kjerfve and Proehl 1979). Because of cost and time constraints, most recent field studies (Nunes and Simpson 1985; Huzzey and Brubaker 1988; Garvine et al. 1992; Wong 1994; Swift et al. 1996; Turrell et al. 1996; Valle-Levinson et al. 2000; Valle-Levinson, Wong, and Lwiza 2000) have focused on lateral mixing processes on very short time scales (on the order of a few tidal cycles) assuming nearly well-mixed conditions. To reduce complexity and better identify key processes, these studies have been generally conducted in straight reaches and under constant discharge conditions. While research by the previously mentioned authors has increased our understanding of lateral mixing processes, several questions still remain. For example: How does the strength and signature of secondary circulation differ between a channel bend and a straight reach? How does the signal of

secondary circulation change between well-mixed and stratified conditions? What is the impact of changes in seasonal discharge on the signature of secondary circulation? What is the impact of drought and severe storms on secondary circulation? Does secondary circulation lead to enhanced lateral mixing? And if so, does this lead to an increase or decrease in the local salt flux?

The goal of this research is to understand the role of secondary circulation in estuarine mixing. Specifically, this research will examine the signal of secondary circulation on the tidal and fortnightly time scales (12.42 hours and 14 days, respectively) and quantify the contribution of secondary circulation to the lateral momentum balance in both time and space under different environmental conditions. The changes in the lateral momentum balance between spring and neap in both curved and straight channel reaches under different discharge and stratification conditions will receive special attention.

1.3 Dissertation Research Questions

While the aforementioned studies have increased our understanding of lateral mixing processes and specifically secondary circulation, several questions linger on its role and impact in estuarine dynamics. What exactly is secondary circulation? How is it identified in acoustic data? Does it have a characteristic signal? Are there particular length and/or time scales critical to understanding secondary circulation? How is it modified under different environmental conditions? What are the broader influences and implications of secondary circulation? The structure of this dissertation will be guided by three main questions as they relate to secondary circulation and focus on the tidal and fortnightly time scales. Questions regarding secondary circulation on time scales longer than these variations are limited by the length and type of available data sets.

- *What are the characteristics of secondary circulation in estuaries?*
- *What are the principal mechanisms that generate secondary circulation?*
- *How does the balance of mechanisms that generate secondary circulation change with time (over the tidal and fortnightly cycles) and with space (laterally in a channel bend)?*

These questions will be addressed by focusing on the development of the following specific objectives and tools:

- Identify and describe the signature of secondary flow in acoustic current data.
- Identify and parameterize mechanisms that drive secondary circulation.
- Quantify and compare a steady-state lateral momentum balance at four seasonal moorings during spring and neap tide.
- Develop methodology to grid, interpolate, and register three-dimensional irregularly spaced data to a prescribed mean lower low water datum (MLLW).
- Quantify and compare a steady-state lateral momentum balance in four lateral cross-sections at spring and neap during maximum ebb and maximum flood tides.

The remainder of this dissertation is divided into eight sections as described herein. Chapter 2 provides a detailed description of the study site, the Satilla River in southeast Georgia. Chapter 3 details background information on secondary circulation and important flow scaling parameters, including a discussion of the lateral momentum balance as a framework for analyzing the detailed three-dimensional Satilla River data sets. Chapter 4 gives a detailed description of the materials and methods used in this

study, including sections on instrumentation, methods of deployment, and general data processing techniques.

The main chapters of this dissertation are Chapters 5 through 7. Each of these chapters is written in manuscript format, featuring a brief introduction, a site description and methods section, results, discussion, and conclusions. Written independently, Chapters 5, 6, and 7 will be submitted at the first available opportunity for publication. Due to the format nature of these chapters, redundancy in some of the material is unavoidable. The focus of Chapter 5 is the fortnightly signal of secondary circulation. Chapter 5 is a look at the characteristics of secondary circulation at one location in space during one seasonal mooring deployment. The temporal characteristics of secondary flow in four consecutive channel reaches and the effect of seasonal changes in freshwater input are examined in Chapter 6. Chapter 6 investigates the changes in secondary circulation at many locations during two seasonal mooring deployments. Chapter 7 examines the details of the spatial character of secondary flow in opposing channel bends by developing methodology to adjust, rotate, and grid irregularly spaced data to the mean lower low water (MLLW) datum. Chapter 7 also focuses on changes in the strength and character of secondary circulation in several lateral cross-sections during a series of seasonal surveys. Chapter 8 summarizes and provides additional discussion on the conclusions of Chapters 5 through 7. The final chapter of this dissertation, Chapter 9, provides recommendations and ideas for future research.

2. SATILLA RIVER, GEORGIA

The Satilla River, in south Georgia, offers a unique site for better understanding of secondary circulation. Little studied, nor heavily impacted by human activities, this pristine river has one main sinuous channel and is joined near its freshwater limit by a large tidal creek. Easily accessible and subject to a wide variety of environmental conditions, it has been selected as the study site for this dissertation research.

The Satilla is a small mesotidal 'blackwater' river whose headwaters originate in the sandy coastal plain of Georgia (Figure 2.1). On average, it has 2.5 meter range semidiurnal tides with pronounced fortnightly variability and is little affected by clay materials from the Piedmont of Georgia. The predominant dark tea color of the water is due to tannic acid derived from humic materials found in the extensive flood plain swamps bordering the river. Anthropogenic influences such as development and pollution from industrial processes, residential sources, and agricultural runoff are low along the Satilla. This little-studied river, confined to within a 120 mile segment of the coast, offers a unique look at understanding the link between differing landscape characteristics, geologic setting, and flow rate. Because of its beneficial geographic location, the Satilla shares similar temperature extremes, rainfall patterns, and tidal regimes with other shallow [more in-depth studied] estuaries along Georgia's coast (Howard and Frey 1975; Davis 1985; Sexton and Hayes 1996).

Figure 2.1: An aerial photograph of the Satilla River in southeast Georgia.

The Satilla has a drainage basin of 9143 km^2 and a length of about 362 km from its headwaters to the Atlantic Ocean near Brunswick, Georgia (Dame et al. 2000) and has an average flow of 78 m^3 s^{-1} (United States Geological Survey National Water Information System (USGS 2004)). The main channel is marked by nine channel bends and two short straight reaches between its mouth at St. Andrews Sound between Jekyll and Cumberland Islands and Woodbine, Georgia, at river kilometer 38. (River kilometer markings are shown in Figure 2.6). The majority of these bends are broadly concave (curve to the north, radius of curvature ~ 1200 m) each followed by more sharp convex

bends (bend to the south, radius of curvature ~ 800 m). The bends are roughly three to four kilometers apart and start at six kilometers from the ocean (0 km) up to river kilometer 33. The river's average channel width varies between 200 – 500 m and has an average depth in the *thalweg* (deep channel) of about 10 m. A triple junction near river kilometer 26 divides the flow of the Satilla River between its main branch to the south and White Oak Creek (WOC), a tidal creek to the north. Northeast of WOC, communication from the upper watershed into the Satilla marsh system is minimal. Dike-constructed local roadways and semi-permanent sediment fences due to continuous construction on nearby Interstate 95 likely contribute to the reduced upland exchange.

Figure 2.2: Extensive salt marshes at Sara's Creek in the upper Satilla River. The stand of trees in the background is located at Crows Harbor Reach (Courtesy S. Elston, 1999).

The river bottom is mostly made of fine to coarse sand, except in swampy areas where there is an additional overlay of organic muck (Howard and Frey 1975). *Spartina alternaflora* and *Juncus roemerianus* salt marshes border the Satilla up to just past the triple junction between the Satilla and WOC (Figure 2.2). Beyond the triple junction, flood plain swamps of black gum and cypress border the nearly fresh river (Sexton and Hayes 1996; Moran et al. 1999; Dame et al. 2000).

Morphologically, the Satilla, like many Georgia and South Carolina estuaries, is classified as an ebb-tidal system (Sexton and Hayes 1996). The Satilla exhibits several features of an ebb-tidal delta including a sinuous deep ebb channel, a weaker marginal flood channel, several swash bars (near river kilometer 2 around Horseshoe Shoal), and a terminal lobe, which defines the extent of the delta, that extends 2 kilometers out past the mouth of the river into St. Andrews Sound.

2.1 Discharge Conditions

Discharge conditions recorded at the Atkinson, Georgia, U.S. Geological Survey (USGS) gauging station, on the upper Satilla River vary widely on a seasonal, annual, and historical basis. Historically, over the past 70 years, annual freshwater input ranges from between 150 $m^3 s^{-1}$ and 400 $m^3 s^{-1}$. These discharge conditions are punctuated by freshet events with discharges of between 600 and 800 $m^3 s^{-1}$. A record low freshwater discharge measuring 0.42 $m^3 s^{-1}$ was recorded on September 26, 1990, while a record high freshwater discharge measuring 1902.9 $m^3 s^{-1}$ was recorded on April 6, 1948. A histogram of historical discharge conditions suggests that the river discharge in the Satilla is weakly periodic in nature on a 25-year cycle. Annual discharge conditions in the

Satilla River are generally higher during fall and winter months due to the influence of hurricanes and nor'easters (Figure 2.3).

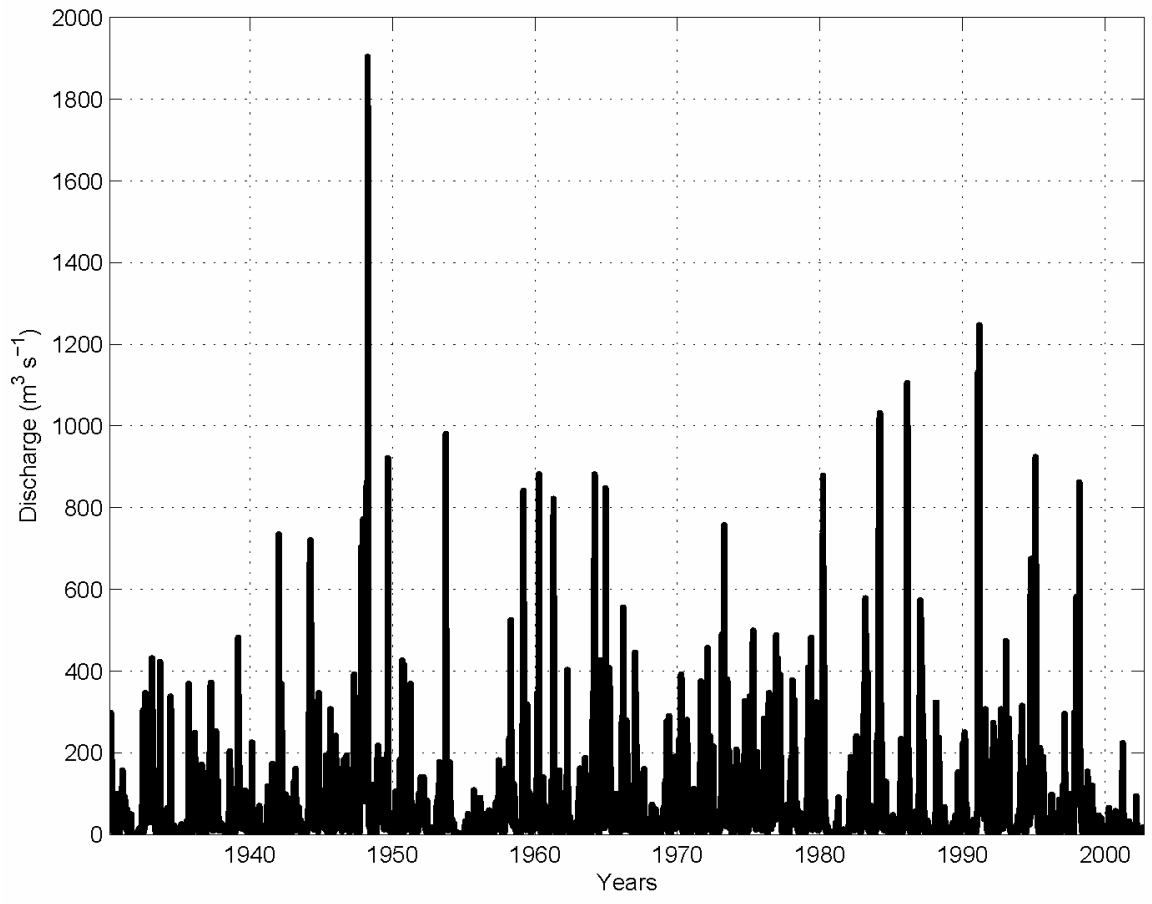

Figure 2.3: U.S. Geological Survey historical daily mean discharge data for the Satilla River at the Atkinson, Georgia, gauging station.

The 1997 Land Margin Ecological Research Project experiment (LMER 4) and the 1999 Satilla SAT1 and SAT 2 experiments occurred, respectively, shortly before and during a period of extended drought for coastal Georgia. Average discharge conditions ranged from near normal at 80 m^3 s^{-1} during the LMER 4 experiment to significantly below normal at 15 m^3 s^{-1} during the SAT 1 and 2 experiments. Freshwater discharge

varied substantially (almost 300 m^3 s^{-1}) shortly before and during the LMER 4 experiment from 295 m^3 s^{-1} in late February to slightly over 7 m^3 s^{-1} near the end of April. Freshwater input during the SAT 1 and SAT 2 experiments ranged from 118 m^3 s^{-1} in early February 1999 to just below 1 m^3 s^{-1} in early June of 1999 (Blanton et al. 2001). Individual freshet events punctuated the abnormally low discharge seen in the Satilla starting the summer of 1999 and into early 2000. Short-lived severe weather outbreaks and hurricanes were responsible for a majority of the observed freshwater discharge events (Figure 2.4).

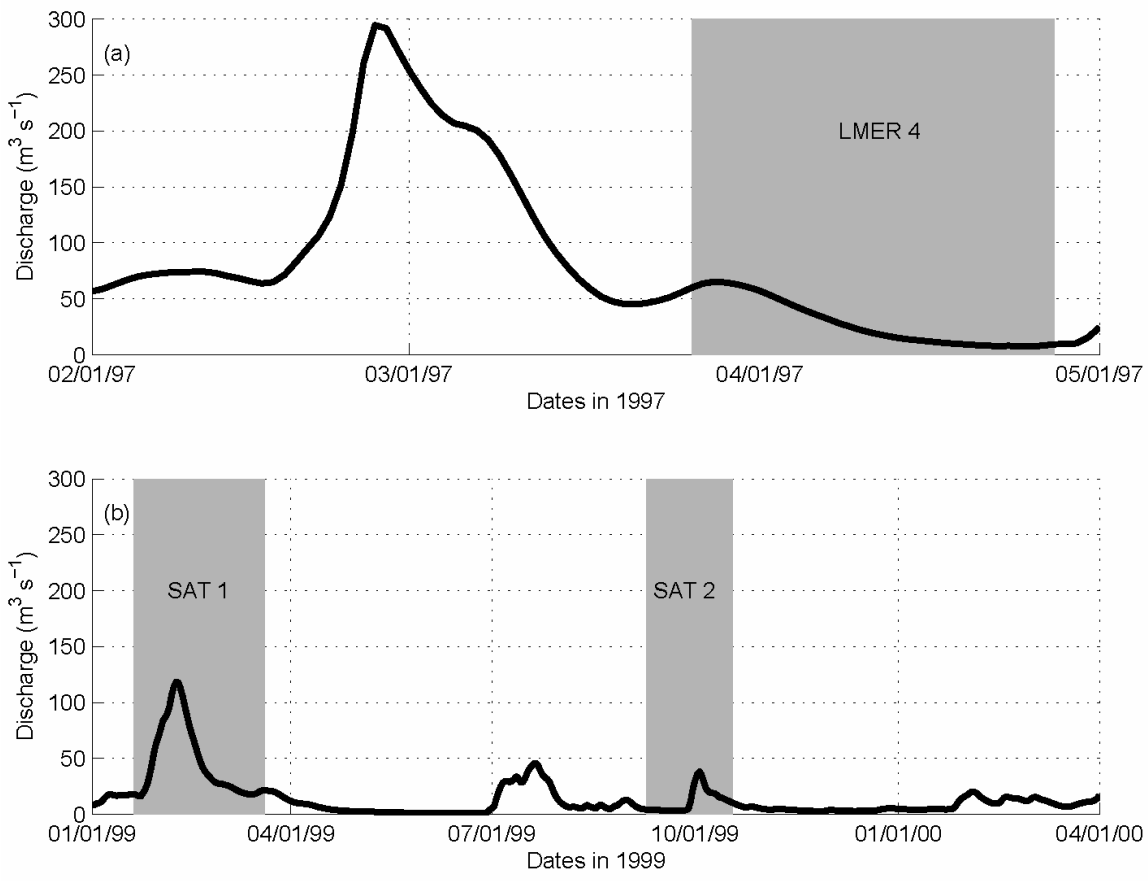

Figure 2.4: (a) The Satilla River discharge during the 1997 LMER 4 experiment. (b) The Satilla River discharge during the 1999 SAT 1 and SAT 2 experiments. Gray boxes denote the period of mooring deployments for each experiment.

The discharge data for the SAT 1 and SAT 2 experiments provides a unique opportunity to diagnose the response and recovery time of the estuary to individual weather events. The 1999 study period was marked by four extreme weather events: a record severe weather outbreak on January 21-22, 1999, Hurricane Dennis (August 30, 1999), Hurricane Floyd (September 15, 1999), and Hurricane Irene (October 15, 1999). The January severe weather outbreak and Hurricanes Floyd and Irene had the largest impact on the salinity and pressure fields as indicated by the long-term moorings near river kilometers 8 and 40. The January severe weather outbreak and Hurricane Floyd had the largest influence on changes in the freshwater discharge for the Satilla River. In both cases, the response time (or lag time) to a precipitation event exceeding 22 millimeter is about 20 days, resulting in a rapid increase in freshwater discharge and a rapid drop in the subtidal salinity field by approximately 15 PSU throughout the estuary (Figure 2.5). The response of the subtidal salinity field to Hurricane Dennis was less dramatic due to its fast-moving nature and to the predominant up-welling winds associated with this storm. The recovery period, the length of time to return to pre-freshet conditions, appears to be approximately 70 days, as indicated by the salinity data from the near ocean long-term mooring. These results are in agreement with those of Blanton et al. (2001) and support their hypothesis that in estuaries similar to the Satilla, that there would likely be a rapid response in the salinity field to a freshwater discharge event and a delayed response in the recovery period to pre-freshet conditions.

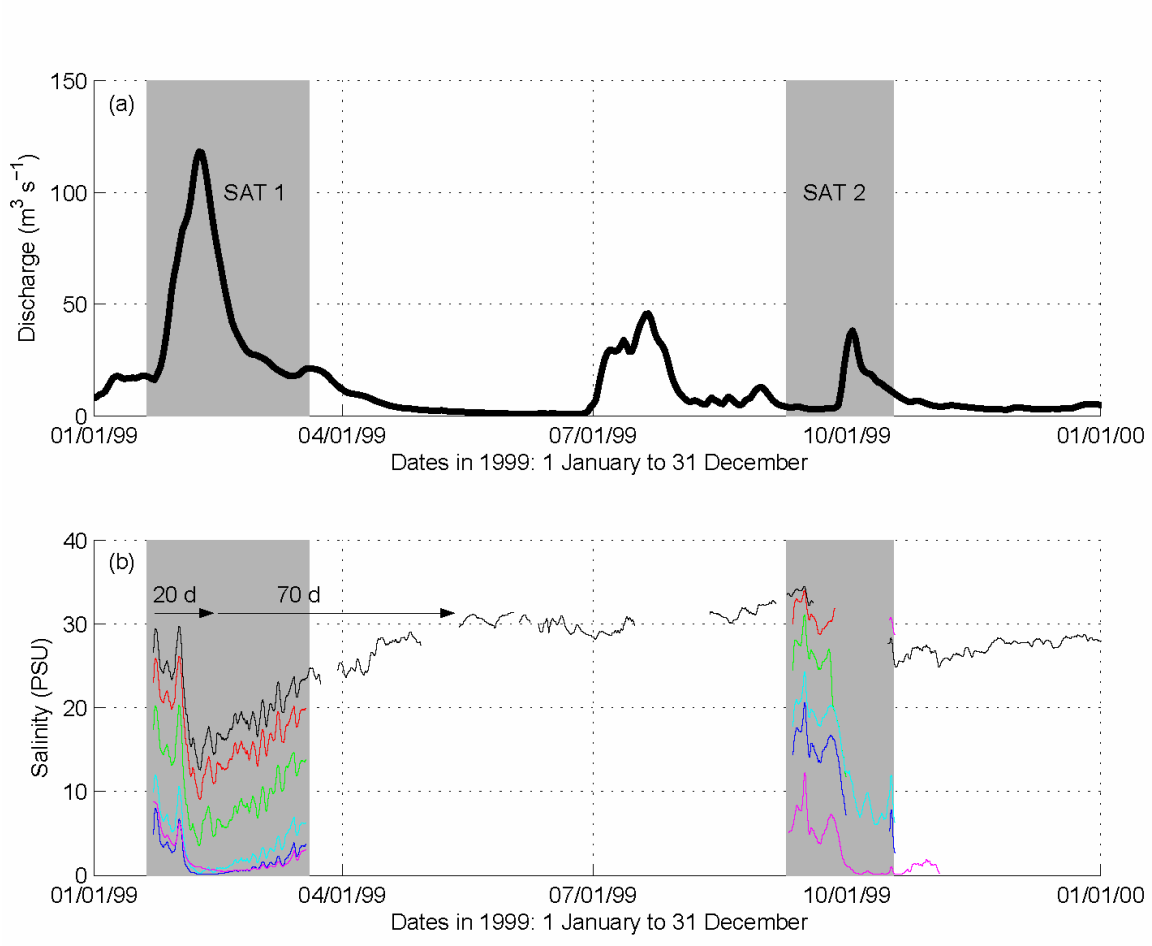

Figure 2.5: (a) The Satilla River discharge during the SAT 1 and SAT 2 experiments. (b) The subtidal salinity measured at the moorings 3 – 7 (red, green, cyan, blue, and magenta lines, respectively) in the Satilla River during the 1999 SAT 1 and SAT 2 experiments. The black line represents the salinity field measured at the near ocean long-term mooring. Gray boxes denote the period of mooring deployments for each experiment.

2.2 Salinity Variations

The salinity structure in the Satilla River varies widely on the tidal, fortnightly, and seasonal cycles. This variation is due to a combination of factors including synoptic weather patterns, severe storms (hurricanes and nor'easters), tides, and freshwater discharge. From previous studies, it has been found that the largest contributors to changes in the salinity structure of the Satilla River are severe storms which produce

down-welling or up-welling winds (trapping water or flushing water out of the estuary), tides, and freshwater discharge (Elston 1998, unpublished data; Dame et al. 2000; Blanton et al. 2001).

2.2.1 Tidal Variations in Salinity

In the Satilla, over a 25-hour tidal cycle, the salinity at a fixed location varies by about 6 PSU at neap tides to about 15 PSU during spring tides. Correspondingly, the vertical structure of tidal salinity varies between stratified conditions at neap tides to nearly well-mixed conditions at spring tides. The actual rate of change in tidal salinity between low water and high water depends largely on the strength of tidal mixing, which is modulated by fortnightly changes in tidal amplitude. Tidal straining, due to the interaction of the sheared axial currents with the longitudinal salinity gradient, can also modulate tidal salinity by amplifying vertical stratification on ebbs and reducing vertical stratification on floods (Simpson et al. 1990).

Determining the tidal excursion, the distance over which a water parcel travels during one phase of the tidal cycle (ebb or flood), is a good way to estimate the effect of tidal advection on the axial salinity field. The tidal excursion is given by the expression

$$l_{M_2} = \frac{2U_{s,rms}}{\omega_{M_2}} \quad \textbf{(2.1)}$$

where $U_{s,rms}$ is the root-mean-square (rms) streamwise velocity (m s^{-1}) and ω_{M_2} is the frequency (s^{-1}) of the dominant tidal constituent (here, M_2). In the Satilla River, the average value of l_{M_2} is 12 kilometers. The tidal excursion also has a fortnightly modulation of approximately 7 kilometers, from 8 kilometers during neap tides when the rms axial velocity is around 0.5 m s^{-1} to 15 kilometers during spring tides when the rms

axial velocity is around 1.0 m s^{-1}. The tidal excursion estimates agree well with the observed changes for the Satilla River in the axial salinity difference observed at a fixed location between low and high water.

2.2.2 Fortnightly Variations in Salinity

As with variations in tidal salinity, the fortnightly variations in salinity for the Satilla River are largely affected by changes in tidal amplitude and river discharge. In addition, observed changes in the lateral and vertical salinity structure between spring and neap tides are likely related to the geomorphology of the Satilla River. Similar to ebb dominant estuaries of coastal South Carolina, the Satilla features a sinuous *thalweg* (deep channel) that is separated from a secondary shallow channel by a series of shoals (Sexton and Hayes 1996). At spring tides, communication is limited between the two channels to times of high water and is virtually non-existent during times of low water.

Based on observations, conditions at neap tide show a vertically stratified system with $(\Delta s)_z$ = 7 PSU (13 to 21 PSU) in the deep channel and $(\Delta s)_z$ = 2 PSU difference over the shoal region (15 to 17 PSU) with a nearly well-mixed lateral structure of about $(\Delta s)_h$ = 2 PSU (ranging from 13 to 15 PSU) across the channel. Not surprisingly, due to the slower axial currents associated with neap tides and the sinuous nature of the Satilla, the vertical density gradient is significantly greater than the horizontal density gradient. This suggests that the currents at neap do not provide enough mixing energy to overcome strong vertical stratification. The well-mixed shoal area is shallow and requires less energy input locally to mix the water column. The salinity in the shoal area is approximately equal to the mean value of the salinity in the deep channel, indicating that there is communication between the two channels during neap tides.

At spring tides, the salinity structure reflects a laterally stratified system with $(\Delta s)_h$ = 5 PSU (13 to 18 PSU) from bank-to-bank and a nearly well-mixed vertical structure ranging from $(\Delta s)_z$ = 2 PSU (13 to 15 PSU) in the deep channel to $(\Delta s)_z$ = 0 PSU (vertically well-mixed at 17 PSU) over the shoal region. As anticipated, the mixing power associated with the high velocity spring tide current easily overturns the vertical density gradient and homogenizes the water column. However, the same current increases the horizontal shear and the lateral density gradients as the water flows around the numerous channel bends in the river. Consequently, less dense water is often found in the deep channel. The lighter water is separated from the heavier water which is forced into the shoal region near the channel center. Surface fronts are often observed upriver of the shoal region during an incoming tide where waters of different salinities collide and partially re-mix before entering the next channel bend. In combination with curvature effects, the resultant fortnightly salinity structure of the Satilla River appears to shift from a vertically stratified two layer system at neap tides to a laterally stratified two channel system at spring tides. These observations are discussed further and shown in Chapter 7.

2.2.3 Seasonal Variations in Salinity

Seasonal variations in salinity are largely affected by changes in freshwater discharge (Blanton et al. 2001). The seasonal differences in the Satilla River axial salinity distribution can be observed in Figure 2.6. The upper panel shows a synoptic high water survey done in February 1999 under moderate discharge conditions (80 m^3 s^{-1}). Similarly, a synoptic high water survey done in December 1999 under low discharge conditions (10 m^3 s^{-1}) is shown in the lower panel. For reference, river

kilometer 15 is just east of Bailey Cut and river kilometer 20 is just west of Bailey Cut. The end of Crows Harbor Reach is at about river kilometer 26. Ceylon is located near Satilla River kilometer 32 (*cf.* Figure 2.6 for river kilometer locations).

In February 1999, the mixing zone, defined here as in Blanton et al. (2001) by a median salinity of 15 PSU, was observed between the mouth of St. Andrews Sound at the ocean (0 kilometer) and Crows Harbor Reach. In December 1999, the mixing zone shifted upriver by approximately 15 kilometers and was located between the west end of Bailey Cut and at a site past Ceylon. Due to logistics, the freshwater boundary was not detected during the December 1999 survey; however, the salinity was found to exceed 10 PSU near Woodbine, Georgia, located near river kilometer 40. Typical salinity values recorded at Woodbine, Georgia, are around 2 PSU as determined from several bi-monthly synoptic surveys and a four month monitoring station.

A series of synoptic field observations suggest that the longitudinal salinity gradient varies from 2 PSU km^{-1} during high discharge conditions to 0.75 PSU km^{-1} during low discharge conditions. Between February 1999 and December 1999, it appears that the decrease in freshwater discharge not only reduced the axial salinity gradient, but also shifted the mixing zone upriver by a considerable distance. These results are similar to those found by Blanton et al. (2001) in the Satilla River and by Alexander et al. (2003) in the Ashepoo – Combahee – South Edisto (ACE) River Basin. Both groups found a similar relationship to changes in freshwater discharge, freshwater volume, and the axial salinity gradient. During high flow conditions, these two studies found that the trend in the axial salinity gradient was exponential in nature, wherein the salinity decreased rapidly upriver from the ocean in an asymptotic fashion. Likewise, during low flow

conditions, these two studies found that the trend in the axial salinity gradient was quadratic in nature, wherein the salinity decreased slowly near the ocean and then decreased more rapidly closer to the freshwater limit at 0 PSU (Blanton et al. 2001; Alexander et al. 2003).

Seasonally, the axial salinity distribution in the Satilla River appears to be governed by the classical estuarine (or gravitational) circulation, in which there is a net flow of water seaward in the surface and a net flow of water landward at depth. As discharge decreases, the freshwater volume decreases, and the barotropic pressure head necessary to flush out the estuary also decreases. This allows for more effective 'salt creep' in the estuary, a condition that reduces the axial salinity gradient, shifts the mixing zone upriver, and increases the length of salt water intrusion.

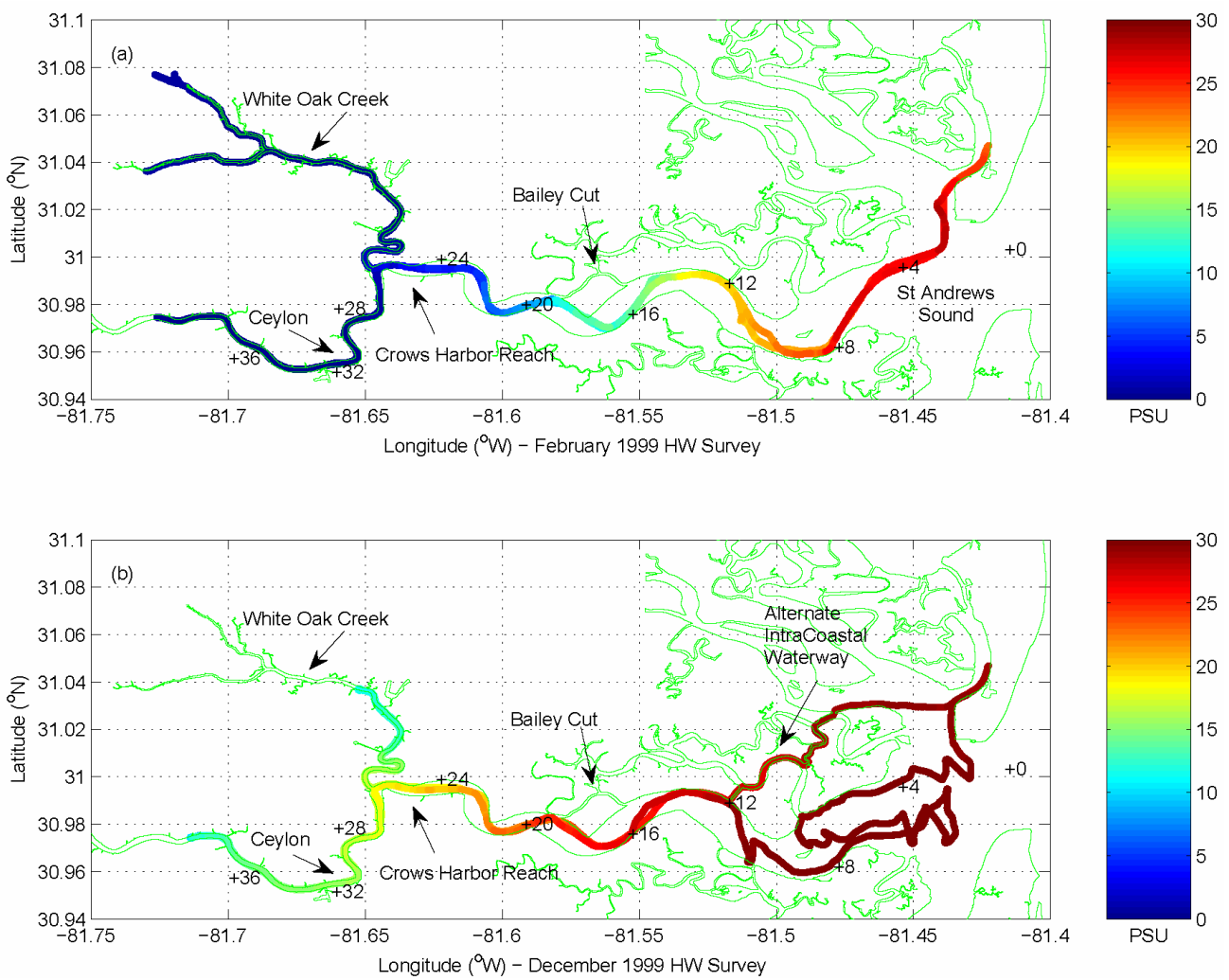

Figure 2.6: (a) Synoptic survey of high water salinity in the Satilla River under moderate discharge conditions (February 1999). (b) Synoptic survey of high water salinity in the Satilla River under low discharge conditions (December 1999).

3. SECONDARY CIRCULATION

Secondary circulation is a well known, little-studied physically driven and/or dynamically driven process that significantly affects the lateral and vertical mixing processes in both air and water. A secondary circulation (also known as a transverse circulation, a secondary current, or a secondary flow) is a field of fluid motion considered to be superimposed on the primary field of motion generally through the action of friction or centrifugal acceleration and exists in the vicinity of solid boundaries (Huschke 1989). Secondary circulation is a broad and often confusing term used to describe several mechanisms whose result is to vertically overturn the water column along the secondary (transverse) axis of the channel. As such, secondary circulation may be composed of one or more lateral cells that can potentially reduce or enhance local gradients. In the field, a physical manifestation of secondary flow is often observed as one or more convergent foam or divergent slick lines along the longitudinal axis of the estuary at the interaction site between two adjacent secondary cells (Figure 3.1).

In combination with other lateral mixing mechanisms, such as river discharge or wind stress, secondary circulation is often mentioned in the literature as a contributing factor to altering the distribution of salt and momentum in an estuary (Trowbridge et al. 1999; Geyer et al. 2000; Garrett 2002; Lerczak and Geyer 2004). However, despite the noted importance of lateral mixing and secondary flows to estuarine dynamics, scaling arguments are often used as a method to neglect such lateral exchange processes, which are commonly an order-of-magnitude smaller than tidal currents in the axial flow field.

Figure 3.1: Photograph of a convergent axial foam front in the Satilla River, Georgia. This type of convergent front indicates the presence of a local secondary circulation. This photograph was taken by S. Elston at anchor during the 1997 LMER 4 experiment.

Despite the difficulties in measuring secondary flows, several recent studies have found that the budgets of momentum and salt can be significantly affected by their presence (Murray and Siripong 1978; Fischer et al. 1979; Kalkwijk and Booij 1986; Garvine et al. 1992; Wong 1994; Dronkers 1996; Lerczak and Geyer 2004). Likewise, recent work by Peters (1997), Chant (2002), and Lerczak and Geyer (2004) has determined that local estuarine characteristics (channel depth and width) and the transition between spring and neap, due to the associated changes in stratification, tidal mixing power, and river volume flux, are important in modifying both the strength and form of secondary flows. Changes in these features ultimately affect the distribution of momentum and the dispersion of salt.

3.1 Mechanisms that Generate Secondary Circulation

Several mechanisms can generate a secondary flow or circulation. A widely studied mechanism is the differential advection of density (Nunes and Simpson 1985; Turrell and Simpson 1988; Turrell et al. 1996; Swift et al. 1996; Lerczak and Geyer 2004), whereby the axial density gradient interacts with the lateral shear of the axial current generated by boundary friction to produce transverse density gradients. A diagnostic model (Nunes and Simpson 1985) for this type of secondary circulation assumes that the transverse circulation is in equilibrium with the lateral density gradients, and that the laterally directed baroclinic forces are balanced by friction. When the current velocities are slow and the lateral salinity gradients are maximized, as is often characteristic of late flood to early ebb, the lateral density gradients induce a gentle density driven 'secondary' vertical and horizontal circulation, the presence of which is marked by axial fronts or slicks at the water's surface. The actual appearance and particular timing of axial fronts and slicks most likely depends on the local estuarine characteristics that maximize the lateral salinity and velocity gradients.

Secondary circulation is also caused by irregular channel bathymetry or geometry (Kantha and Rosati 1990; Ridd et al. 1998). The physical morphology of an estuary leads to secondary circulation due to the frictional effects of lateral and bottom boundaries and/or by channel curvature (Britter and Simpson 1978; Falcón 1984; Mertz and Gratton 1995; Seim and Gregg 1997). Secondary circulation due to channel curvature exists in the same orientation regardless of the flow direction (flood versus ebb). However, its strength may be altered depending on whether the flow is cyclonic (counterclockwise) or anticyclonic (clockwise) in the channel bend and depending on its interaction with other

mechanisms that drive secondary flow (Dyer 1997). In open channels and natural river meanders, the flow around a bend produces a transverse circulation, which results from a local imbalance between the vertically varying centrifugal acceleration and the cross-channel pressure gradient (Bathurst et al. 1977; Callander 1978; Geyer 1993; Seim and Gregg 1997). Bottom currents, slowed by friction, are weaker than the depth-averaged axial flow, and this imbalance leads to a near bottom flow towards the inside of the bend. Likewise, the unconstrained near surface currents are stronger than the axial depth-averaged flow, which leads to an outwardly directed near surface flow. A compensating downward flow on the outside of the bend and an opposite upward flow on the inside of the bend complete the circulation pattern (Geyer 1993; Dyer 1997). A common feature associated with curvature-induced secondary flow is that the cross-sectional bathymetric structure has a scour hole near the outside of the bend and a shallow area near the inside of the bend (Dronkers 1996; Dyer 1997).

In a stratified fluid, the outcome of this force imbalance leads to a cross-channel structure in which the lightest water is near the surface at the outside of the bend, and the densest water is near the bottom at the inside of the bend (Seim and Gregg 1997). Given sufficient strength in both axial flow and channel curvature, the strength of the resultant secondary circulation can be enough to rapidly mix the water column by turbulent exchange. At times, however, when the axial flow decreases sufficiently, a balance can be achieved between the barotropic water slope and the opposing depth-varying baroclinic component of the density field induced by the tides. When this occurs, secondary circulation in the deep channel can be reduced or halted, allowing part of the

lateral density structure to be maintained around the channel bend (Chant and Wilson 1997; Seim and Gregg 1997).

Secondary circulation generated by frictional interaction with lateral and/or bottom boundaries is complex and often difficult to separate. This separation becomes even more difficult when the other mechanisms that drive secondary flows are present. Most often, frictional effects are parameterized and modeled by an eddy viscosity that may have several forms and values (Falcón 1984; Nunes and Simpson 1985; Mertz and Gratton 1995; Swift et al. 1996; Turrell et al. 1996). While estimates of secondary flow due to frictional effects are useful, great caution must be used in their interpretation.

In large estuaries, such as the Chesapeake Bay, secondary flow can be induced by the Coriolis force as a result of the earth's rotation (Callander 1978; Kasai et al. 2000; Lerczak and Geyer 2004). The importance of planetary rotation can be estimated by calculating the Rossby number (R_o), the ratio of centrifugal acceleration to the Coriolis force in a rotating fluid (Apel 1990) and is given by the expression:

$$R_o = \frac{U_s^2 / R}{fU} = \frac{U_s}{fR} \quad \textbf{(3.1)}$$

where U_s is the characteristic axial velocity, R is the radius of curvature, and

$$f = 2\Omega \sin\phi \quad \textbf{(3.2)}$$

is the Coriolis parameter. This is similar to the R_o form used by Geyer (1993b) in a weakly curved domain to determine the importance of planetary rotation to channel curvature effects. Small R_o numbers indicate that the primary dynamic balance can be considered geostrophic and that curvature effects may be neglected (Holton 1992).

3.2 Mixing and Flow Scaling Parameters

It is often difficult to measure precisely the different mechanisms that drive secondary circulation. As a result, it is instructive to use common parameters to determine 'mixing potential' and to apply scaling techniques to estimate the importance of different mechanisms that drive secondary flow. The gradient Richardson number (Ri), the ratio of buoyancy to shear and an indicator on the condition of potential for turbulent mixing (Ferziger et a. 2002), is often used to express hydrodynamic 'mixing potential.' In a curved reach, however, the flow responds to centrifugal acceleration as the primary mixing mechanism, not shear instability, making Ri a poor mixing indicator (Seim and Gregg 1997; Ferziger et al. 2002). This is particularly true in the case of transverse flow, since it tends to occur in locations with strong cross-channel gradients.

In a stratified fluid, an alternative scaling to measure 'mixing potential' is the internal Froude number (Fr_i), an indicator on the condition of state of turbulent mixing (Ferziger et al. 2002) and an inverse form of the bulk Richardson number, which indicates the relative strength of axial shear to the strength of vertical stratification (Dunne and Leopold 1978; Huschke 1989; Seim and Gregg 1997). In general, Fr_i is the ratio of inertial forces to the buoyancy force and is given by

$$Fr_i^2 = \frac{\overline{U_s^2}}{g'h} \quad \textbf{(3.3)}$$

and where

$$g' = g\Delta\rho_z / \rho_o \quad \textbf{(3.4)}$$

is reduced gravity, $\overline{U_s}$ is the characteristic depth-average (streamwise) axial velocity, h is the total water depth, and g is the acceleration due to gravity. Fr_i^2 can be interpreted as

the ratio of the axial current speed to the velocity of the shallow-water wave at a density interface (Apel 1990; Dyer 1997). When $Fr_i^2 < 1$, the flow is subcritical, indicating that the stabilizing effect of the vertical stratification dominates the destabilizing effect of the vertical shear. In this state, the adjustment time of the density field is shorter than the displacement time (advection) of the density field downstream. Wave energy can accumulate locally as an oscillating lateral seiche continuously adjusts the density field (Fischer et a. 1979). In contrast, supercritical flow ($Fr_i^2 > 1$) indicates that the necessary destabilizing forces are of the same order or greater than the stabilizing forces, and that the fluid will have sufficient momentum to overcome the buoyancy force which results in a water column that may be locally well-mixed (Fischer et al. 1979; Tritton 1988). There are other forms of the Froude number such as the densimetric Froude number (Fr_d) used by Huzzey (1982). Fr_d is often used to describe flows of more than one layer, while Fr_i is used for bulk estimates in stratified flow.

The Burger number (S′) indicates the importance of stratification to rotation effects. It is a modified ratio of R_o to Fr given by the expression:

$$S' = \frac{HR_o}{LFr} = \frac{N_z h}{2fR} \quad \textbf{(3.5)}$$

where H and L are the characteristic depth and length, R_o and Fr are the general Rossby and Froude numbers, h is the depth, f is the Coriolis parameter, R is the radius of curvature, and

$$N_z = \sqrt{g'/H} \quad \textbf{(3.6)}$$

is the vertical buoyancy or the Brunt-Väisälä frequency. Subcritical S′, (S′ < 1), indicates that the flow field is rotational but modified by stratification effects.

A supercritical S′, however, indicates that the flow field is stratified but modified by rotation. The Rossby radius of deformation,

$$R_{o,def} = \frac{N_z h}{2f} \quad (\mathbf{3.7}),$$

is included in this form of S′, which gives the minimum length scale (horizontal or vertical) on which rotation effects are significant.

The Ekman number indicates the relative importance of viscous forces to the Coriolis force (Gill 1982). It is given by the expression

$$Ek = \frac{N_z}{fh^2} \quad (\mathbf{3.8})$$

where h is the depth of the *thalweg* (Kasai et al. 2000). Small Ek indicates that viscous forces are weaker than the Coriolis force and the dynamic balance becomes nearly geostrophic. The influence of the Ekman boundary layer can likewise be estimated from the Ekman depth, D_E, given by the expression:

$$D_E = \sqrt{2EkH} \quad (\mathbf{3.9})$$

where Ek is the Ekman number and H is the depth of the deep channel (Gill 1982; Kasai et al. 2000). Estimates of these flow parameters and their dimensions for the Satilla River are found in Table 3.1 at the end of Subsection 3.3.1.

3.3 Analytical Models of Secondary Circulation

Recent advancements in computer techniques, acoustic instruments, and rapid survey strategies have generated a renewed interest in understanding the role of secondary circulation in estuarine dynamics. This section provides a review of the most currently used analytical models for diagnosing and detailing secondary flow. This review will discuss scale estimates of secondary circulation, the Seim and Gregg (1997)

curvature-induced overturning model, and the lateral momentum balance in natural coordinates. The final subsection of this chapter will develop the lateral momentum balance model as applied to the Satilla River estuary.

3.3.1 Scale Estimates of Secondary Circulation

Scale estimates are useful first-order approximations in evaluating the strength of secondary circulation as well as for estimating the relative importance of mechanisms that drive such flows. Following Geyer (1993b), Seim and Gregg (1997), and earlier analytical work by Kalkwijk and Booij (1986) in unstratified flow, it is possible to estimate the theoretical limits on the strength of transverse circulation driven by centrifugal acceleration (channel curvature) and the Coriolis force. Assuming that the baroclinic pressure gradient is sufficiently small, the along-channel velocity obeys a logarithmic profile, and the eddy viscosity is parabolic in form, the maximum secondary circulation velocity (U_n) due to channel curvature effects is given by

$$U_{n,curve} \approx \frac{6\left|\bar{U}_s\right|h}{R} \quad \textbf{(3.10)}$$

where $\bar{U}_s$ is the depth-averaged streamwise velocity, h refers to the total water depth, and R is the radius of curvature (*cf.* Geyer 1993; Seim and Gregg 1997). Similarly, the maximum secondary circulation velocity due to the Coriolis effect is given by

$$U_{n,Coriolis} \approx 3fh \quad \textbf{(3.11)}$$

(*cf.* Geyer 1993) where f is the Coriolis parameter and h is the water depth. Note that the maximum velocity for secondary flows induced by Coriolis acceleration has no dependence on velocity. It is strictly dependent on the water depth and the latitude, and is oriented to the right of the axial current in the Northern Hemisphere. Therefore, the

Coriolis force will enhance secondary flows in bends to the north (concave), east, and west when the flow is cyclonic (counterclockwise) and limit secondary flows in bends to the south (convex), east, and west when the flow is anticyclonic (clockwise). Since the direction of flow reverses between flood and ebb, secondary flows due to channel curvature and the Coriolis force are additive in concave bends on flood and in convex bends on ebb. Likewise, secondary flows are reduced at flood in convex bends and at ebb in concave bends because the centrifugal force opposes the Coriolis force.

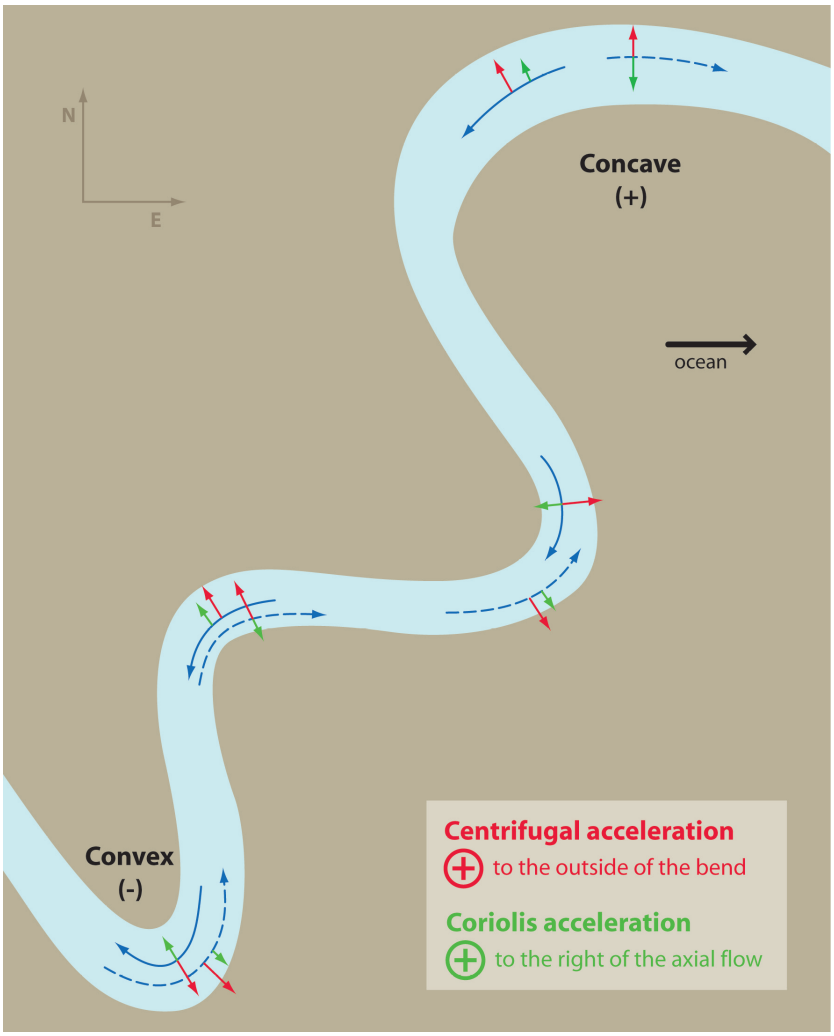

Figure 3.2: An illustration in the change of direction for the Coriolis force and the centrifugal force as a function of tidal direction (ebb or flow).

Mertz and Gratton (1995) derive a scale estimate for frictionally-driven secondary flow by assuming a balance between the Coriolis force and vertical stress divergence. Using a Reynolds stress formulation for the vertical shear stress, a transverse flow driven by 'frictional steering' can be scaled as

$$U_{n,friction} \approx \frac{\tau_{n,b}}{f \rho_o h} \quad \textbf{(3.12)}$$

where f is the Coriolis parameter, $\tau_{n,b}$ is the bottom shear stress in the lateral direction, ρ_o is an ambient reference density, and *h* is the depth of the main channel. Assuming that the cross-channel velocities are no more than 30% of the axial velocities, and assuming that shear is largely determined by maximum current speeds, shear stress can be assumed to be completely determined by the axial flow (Kalkwijk and Booij 1986; Geyer 1998; Geyer et al. 2000; Ott et al. 2002; Seim et al. 2002). As a result, bottom stress can be expressed in terms of the streamwise velocity in the following expression:

$$\tau_{n,b} = \rho_o C_D \left| u_{n,1mab} \right| u_{n,1mab} = \frac{1}{16} \rho_o C_D \left| u_{s,1mab} \right| u_{s,1mab} \quad \textbf{(3.13)}$$

where C_D is the drag coefficient, ρ_o is an ambient reference density, and $u_{n,1mab}$ and $u_{s,1mab}$ are the normal and streamwise velocities, respectively, at one meter above the bottom (mab). The second expression in Equation 3.13 is scaled by $1/16$ to account for the maximum observed cross-channel velocities which can be as high as one-quarter of the observed axial velocity $\left(u_n^2 = \left(0.25 \cdot u_s \right)^2 = 0.0625 \cdot u_s^2 \right)$. In a similar manner, it is possible to derive an expression to scale density driven secondary flows (Nunes and Simpson 1985). Assuming a balance between the baroclinic component of the lateral

pressure gradient (the variable density component) and vertical stress divergence, secondary circulation driven by the differential advection of density can be expressed as

$$U_{n,density} \approx \frac{1}{4}\left(\sqrt{\frac{g'h}{C_D B}}\right) \quad \textbf{(3.14)}$$

where g′ is reduced gravity, h is the *thalweg* depth, B is the channel width, and C_D is as above. As with the scale estimate for frictionally-driven secondary flow, the velocity characteristics of density driven secondary flow are derived from u_s. Therefore, a coefficient of one-fourth accounts for and relates the speed of the calculated lateral velocity to the axial velocity characteristics of the maximum internal wave speed (Gill 1982; Ott 2000). In this form, the scale estimate for density driven secondary flow can be interpreted as the phase speed of an internal wave affected by form drag in a channel cross-section. Note, unlike Coriolis and curvature driven secondary flows, scale estimates for friction and density driven secondary flows are sensitive to the choice of C_D.

The strength of secondary circulation is sensitive to changes in the speed and direction of the axial flow, bottom stress, and baroclinic pressure gradients. Mathematically, the strength of the secondary flow may also be different because of the assumed parabolic form of the eddy viscosity (Geyer 1993). Despite this however, scale analysis and parameter evaluation are useful tools for a first-order understanding of secondary circulation. A summary of length scales, flow parameters, and scale estimates of secondary flow for the Satilla River is presented in Table 3.1. Based on the characteristic values for the Satilla, it is likely that the driving mechanisms for secondary circulation in this river will be centrifugal acceleration, friction, and density.

Table 3.1: Length scales, flow parameters, and scale estimates of secondary circulation for the Satilla River, Georgia.

PARAMETER	EQUATION AND SCALE
Axial Length Scale	$L_x = 1500$ m
Transverse Length Scale	$L_y = 150$ m
Depth Scale	$H = h = 10$ m
Effective Channel Width	$B = 200$ - 500 m
Local Radius of Curvature	$R = 800 – 2500$ m
Depth Averaged Axial Velocity	$U_s = 1.5$ m s^{-1}
Depth Averaged Transverse Velocity	$U_n = 0.25$ m s^{-1}
Depth Averaged Vertical Velocity	$w \approx 2.3 \times 10^{-4}$ m s^{-1}
Ambient Reference Density	$\rho_{o,w} = 1013.8$ kg m^{-3}
Axial Time Scale	$L_x/U_s \approx 1000$ s
Transverse Time Scale	$L_y/U_n \approx 600$ s
Vertical Time Scale	$H/w \approx 4.35 \times 10^4$ s
Vertical Buoyancy Frequency	$N_z = \sqrt{g'/H} = 0.035$ - 0.070 s^{-1}
Reduced Gravity	$g' = g\Delta\rho_z/\rho_o = 0.012$ - 0.049
Coriolis parameter	$f = 2\Omega \sin\phi = 7.5114 \times 10^{-5}$ s^{-1}
Rossby number	$R_o = \frac{U_s}{fR} = 7.99$
Ekman number	$Ek = \frac{N_z}{fh^2} = 4.66 – 9.32$
Burger number	$S' = \frac{HR_o}{LFr} = \frac{N_z h}{2fR} = 0.93$ - 1.86
Vertical Rossby Deformation Radius	$R_{o,def} = \frac{N_z h}{2f} = 2.3$ - 4.7 km
Internal Froude number	$Fr_i^2 = \frac{\overline{U_s^2}}{g'h} = 0.80$ - 7.73
Coriolis driven secondary flow	$U_{n,Coriolis} \approx 3fh = 0.002$ m s^{-1}
Curvature driven secondary flow	$U_{n,curve} \approx \frac{6\lvert\bar{U}_s\rvert h}{R} = 0.11$ m s^{-1}
Density driven secondary flow	$U_{n,density} \approx \frac{1}{4}\left(\sqrt{\frac{g'h}{C_D B}}\right) = 0.06$ m s^{-1}
Friction driven secondary flow	$U_{n,friction} \approx \frac{\tau_{n,b}}{f\rho_o h} = 0.08$ m s^{-1}

3.3.2 Coefficient Adjustments to Scaling Formulas for Secondary Circulation

As developed in the previous section, the analytical scale estimation formulas for secondary circulation are useful tools to quickly evaluate the strength and the physical importance of secondary flows driven by channel curvature, the Coriolis effect, friction, and the differential advection of density. These formulas can be easily applied to a number of different channel reaches or to a number of different estuaries for direct comparison in a consistent straightforward manner. Discussed in Section 3.3.1, scale estimates for secondary flow were developed based on analytical models and laboratory studies. However, recent research and observations by several authors (Huzzey and Brubaker 1988; Ridd et al. 1998; MacCready 1999; Valle-Levinson and Atkinson 1999; Kasai et al. 2000; Valle-Levinson et al. 2000a; and Seim et al. 2002) suggest that such theoretically derived secondary flow scale estimates must be adjusted with the appropriate coefficients to match locally observed secondary flows and to insure proper scaling for estuaries with variably curved channel reaches.

In the Satilla, as in other estuaries (Huzzey and Brubaker 1988; Valle-Levinson and Atkinson 1999; and Valle-Levinson et al. 2000a), the core of axial velocity is asymmetrical relative to the channel center-line, occurring near the outside bank and concentrated in the *thalweg*, where the strongest secondary flows principally occur. Confined to the *thalweg,* the importance of secondary flows driven by centrifugal and Coriolis acceleration are often underestimated (Valle-Levinson and Atkinson 1999; Kasai et al. 2000; Valle-Levinson et al. 2000a) by approximately one-half relative to the original scale factors as developed from the 1986 flume study by Kalkwijk and Booij. In contrast, secondary circulation driven by the differential advection of density is often

overestimated, as this type of secondary flow is composed of a pair of counter-rotating secondary circulation cells (Ridd et al. 1998), generally confined to the *thalweg*, subject to the constraints of the internal density field and strongest at times of slack water (Turrell et al. 1996; Ridd et al. 1998). Each cell in the density-driven pair is approximately one-half of the *thalweg* width, and can overturn the water column no faster than that maximum internal wave speed (Gill 1982; MacCready 1999; Ott 2000), such that the correct multiplication coefficient of one-sixteenth is necessary to match field observations to the earlier derived scale parameter for density-driven transverse flows. The scale parameter for frictionally-driven secondary flow relates the square of the transverse velocity to the axial velocity, with a scaling coefficient of one-sixteenth, by assuming that the transverse shear stress is determined by the axial flow field (Kalkwijk and Booij 1986; Geyer 1998; Geyer et al. 2000; Ott et al. 2002; Seim et al. 2002) and that the transverse velocity is no more than 25% of the axial velocity (Nunes and Simpson 1985; Valle-Levinson and Atkinson 1999; Seim et al. 2002). As a result, no coefficient adjustment is necessary to match field observations in the Satilla to the scale formula for frictionally-driven secondary circulations. However, if the link between the transverse flow field and the axial flow field were substantially different than 25%, an adjustment would be necessary to scale the field data to the strength estimation formula for frictionally-driven secondary flow. Consequently, the revised scale parameter formulas for determining the strength of secondary flow by Coriolis and centrifugal accelerations, the differential advection of density, and frictional steering are given respectively as follows:

$$U_{n,Coriolis} \approx 6fh \quad \textbf{(3.15)}$$

$$U_{n,curve} \approx \frac{12\left|\bar{U}_s\right|h}{R} \quad \textbf{(3.16)}$$

$$U_{n,density} \approx \frac{1}{16}\left(\sqrt{\frac{g'h}{C_D B}}\right) \quad \textbf{(3.17)}$$

$$U_{n,friction} \approx \frac{1}{16}\frac{1}{fh}C_D u_{s,1mab}^2 \quad \textbf{(3.18)}$$

where f is the Coriolis parameter and h is the depth of the *thalweg*, $\bar{U}_s$ is the depth-averaged streamwise velocity, R is the local radius of curvature, g′ is reduced gravity, C_D is the drag coefficient, B is the effective channel width (the lesser of bank to bank or bank to shoal distance), and $u_{s,1mab}$ is the axial velocity at one meter above the bottom (mab).

3.3.3 Seim and Gregg Curvature-Induced Overturning Model

While a first-order lateral momentum balance between the pressure gradient force and vertical shear stress divergence is suitable for a weakly curved domain (R ~ 10 km), it is not sufficient to describe the observed dynamics of a highly curved partially mixed estuary like the Satilla River. Rather, we assume a first-order lateral momentum balance that follows the overturning model derived by Seim and Gregg (1997) for the Tacoma Narrows of Puget Sound. Written in natural coordinates and based on an inviscid cross-channel momentum balance between centrifugal acceleration and the lateral baroclinic pressure gradient, the Seim and Gregg (1997) curvature-induced overturning model can be expressed mathematically by the equation:

$$-\frac{\left(u_s^2-\overline{u_s^2}\right)}{R}=-\frac{g}{\rho_o}\int_z^\eta\frac{\partial\rho}{\partial n}dz+\frac{g}{\rho_o}\frac{\partial\overline{\rho}}{\partial n}h \quad \textbf{(3.19)}$$

where the first term is the secondary flow driven by the imbalance between the depth-dependent (u_s) and the depth-average streamwise velocity ($\overline{u}_s$) over a radius of curvature R, the second term is the depth-dependent baroclinic pressure gradient, and the third term is the depth-average baroclinic pressure gradient. Seim and Gregg (1997), in an effort to evaluate the third term, assume that the cross-channel density gradient can be represented by its depth-average value. Using alpha, given by the expression

$$\alpha=\left(u_s^2-\overline{u_s^2}\right)\Big/\overline{u_s^2} \quad \textbf{(3.20)}$$

as a measure of vertical shear and scaling the right hand side of Equation 3.19 as $\frac{g}{\rho_o}\frac{\Delta\overline{\rho}}{B}h$ where g is gravity, $\Delta\overline{\rho}$ is the depth-average density difference, ρ_o is an ambient reference density, and B is the effective channel width (the smaller of bank-to-bank or bank-to-shoal distance) reduces Equation 3.19 to the following:

$$-\frac{\left(u_s^2-\overline{u_s^2}\right)}{R}=\frac{g}{\rho_o}\frac{\Delta\overline{\rho}}{B}h \quad \textbf{(3.21)}.$$

Rewriting Equation 3.21 in terms of a minimum $\overline{u}_s$ to overcome the local effects of buoyancy gives the following expression

$$\overline{u_s^2}\geq\frac{1}{\alpha}\frac{R}{B}\frac{gh}{\rho_o}\Delta\overline{\rho}=\frac{1}{\alpha}\frac{R}{B}g'h \quad \textbf{(3.22)}$$

where R is the radius of curvature and g′ is reduced gravity. This model is most easily interpreted as the minimum depth-average axial speed necessary to overcome the vertical density difference and overturn the water column (Seim and Gregg 1997).

For simplicity, Equation 3.22 can also be expressed in terms of Fr_i^2 where

$$\alpha Fr_i^2 \frac{B}{R} \geq 1 \quad \textbf{(3.23)}$$

and where

$$Fr_i^2 = \frac{\overline{u_s^2}}{g'h} \quad \textbf{(3.3)},$$

as given in Section 3.2 is a necessary condition for the centrifugal acceleration to overcome the buoyancy force and mix the density field. Despite its sensitivity to α, a robust feature of the Seim and Gregg (1997) overturning model is the scaling by R/B, which makes the final results less sensitive to the initial choice of R or B. A full derivation of the Seim and Gregg (1997) overturning model is provided in Appendix A.

3.3.4 Lateral Momentum Balance in Natural Coordinates

Following the work of several recent authors (Table 3.2), the lateral momentum balance in natural coordinates is used as a framework for understanding cross-channel estuarine dynamics. Within this framework, depending on physical location and available data sets, different force balances can be explored to understand and capture essential system dynamics. Formulated in natural coordinates, a coordinate system whose primary orientation follows the instantaneous axial flow field, it allows key physical forces in the lateral momentum balance to be directly expressed in a simplified mathematical form.

The lateral momentum balance in natural coordinates for stratified flow in a curving channel can be written as the following expression:

$$\frac{\partial u_n}{\partial t} + u_s \frac{\partial u_n}{\partial s} + f u_s - \frac{u_s^2}{R} + g \frac{\partial \eta}{\partial n} = -\frac{g}{\rho_o} \int_z^\eta \frac{\partial \rho}{\partial n} dz + \frac{\partial}{\partial z}\left(A_z \frac{\partial u_n}{\partial z} \right) \quad \textbf{(3.24)}$$

where the first term in Equation 3.24 is local time rate of change in the transverse velocity, the second term is the advective acceleration of transverse velocity by the axial velocity, the third and fourth terms are the Coriolis and centrifugal accelerations, respectively, the fifth term is the barotropic pressure gradient, the sixth term is the lateral baroclinic pressure gradient, and the seventh term is the vertical shear stress divergence where A_z is the vertical eddy viscosity. In natural coordinates, the subscript *s* denotes the streamwise or axial direction, the subscript *n* denotes normal or lateral direction, and u_s and u_n respectively, are the associated axial and lateral velocities. A full development of the lateral momentum balance in natural coordinates is detailed in Appendix A.

3.3.5 Lateral Momentum Balance Model for the Satilla River, Georgia

While the Seim and Gregg (1997) overturning model is a good first-order approximation to explain the lateral dynamics in the highly curved reaches of the Satilla River, it is unlikely this model will apply equally well to all sections of the river or at all places in a cross-section. For this reason and based on scale estimates for secondary flow in the Satilla River (*cf.* Table 3.1), a balance between the centrifugal acceleration (CA), the lateral pressure gradient force (LBC), and vertical shear stress divergence (VSS) is explored. The effect of the Coriolis acceleration (CF) is added to this balance, despite its weak nature in the Satilla, for model portability. It is expected that there will be a shift in the balance of terms (from CA ≈ LBC at neap tides to CA ≈ VSS at spring tides) in the lateral momentum balance model for the Satilla, because of the river's sinuous nature, its variable density structure, and its bathymetric features. Formulated in this manner, the results of this investigation can be directly compared with other estuarine studies that use the lateral momentum balance as their framework (Table 3.2).

Table 3.2: Recent estuarine experiments using the lateral momentum balance. An X is used to indicate which terms the authors used in their formation of a lateral momentum balance. Italics indicate the lateral momentum balances investigated in this study.

$$\frac{\partial u_n}{\partial t} + u_s \frac{\partial u_n}{\partial s} + f u_s - \frac{u_s^2}{R} + g \frac{\partial \eta}{\partial n} = -\frac{g}{\rho_o} \int_z^\eta \frac{\partial \rho}{\partial n} dz + \frac{\partial}{\partial z}\left(A_z \frac{\partial u_n}{\partial z} \right)$$

(A) (B) (C) (D) (E) (F) (G)

A local accel	B advective accel	C Coriolis accel	D centrifugal accel	E barotropic gradient	F baroclinic gradient	G shear stress	Authors
				X	X	X	Nunes and Simpson 1985
		X				X	Kalkwijk and Booij 1986
			X			X	Kalkwijk and Booij 1986
			X			X	Geyer 1993
		X		X	X		Mertz and Gratton 1995
		X				X	Mertz and Gratton 1995
			X		X	X	Dronkers 1996
				X	X	X	Swift, Fredriksson, and Celikkol 1996
X	X	X	X		X		Chant and Wilson 1997
			X		X		Seim and Gregg 1997
		X		X	X	X	Kasai, Hill, Fujiwara, and Simpson 2000
	X	X		X	X	X	Valle-Levinson, Wong, and Lwiza 2000
			X		X		Lacy and Monismith 2001
X	X				X	X	Lacy and Monismith 2001
			X		X		*Elston 2005 (this study)*
		X	X		X	X	*Elston 2005 (this study)*

This dissertation extends the work of Geyer (1993b), Dronkers (1996), and Seim and Gregg (1997) by combining the effects of the lateral density gradient, bottom stress, and planetary rotation to enhancing or limiting secondary circulation. This model formulation was chosen because it combines the effects of the deep channel (where most of the momentum is captured in the *thalweg* and subject to the strongest lateral baroclinic gradient) and the effects away from the deep channel in the region of the shoals and shallows. An attractive feature about this model formulation is that it accounts for the effects of secondary flow regardless of instrument position in a channel cross-section: either in the deep channel or in the shoal region.

The depth-dependent lateral momentum balance in natural coordinates for stratified flow in a curving channel is given by Equation 3.25 as

$$\frac{\partial u_n}{\partial t} + u_s \frac{\partial u_n}{\partial s} + f u_s - \frac{u_s^2}{R} + g \frac{\partial \eta}{\partial n} = -\frac{g}{\rho_o} \int_z^\eta \frac{\partial \rho}{\partial n} dz + \frac{\partial}{\partial z}\left(A_z \frac{\partial u_n}{\partial z} \right) \quad \textbf{(3.25)}$$

Depth-averaging (indicated by the overbar) Equation 3.25 yields Equation 3.26.

$$\frac{\partial \overline{u}_n}{\partial t} + \overline{u_s \frac{\partial u_n}{\partial s}} + f\overline{u}_s - \frac{\overline{u_s^2}}{R} + g \frac{\partial \eta}{\partial n} = -\frac{g}{\rho_o} \frac{\partial \overline{\rho}}{\partial n} h - \frac{\tau_{n,b}}{\rho_o h} \quad \textbf{(3.26)}$$

Subtracting Equation 3.26 from Equation 3.25 and substituting

$$\frac{\tau_n}{\rho_o} = \left[A_z \frac{\partial u_n}{\partial z} \right]_{z=-h} \quad \textbf{(3.27)}$$

yields Equation 3.28, which eliminates the contribution of the barotropic water slope, a difficult parameter to measure or estimate accurately.

$$\frac{\partial\left(u_n-\overline{u}_n\right)}{\partial t}+u_s\frac{\partial u_n}{\partial s}-\overline{u_s\frac{\partial u_n}{\partial s}}+f\left(u_s-\overline{u}_s\right)-\frac{\left(u_s-\overline{u_s^2}\right)}{R}=$$

$$=-\frac{g}{\rho_o}\int_z^\eta\frac{\partial\rho}{\partial n}dz+\frac{g}{\rho_o}\frac{\partial\overline{\rho}}{\partial n}h+\frac{\partial}{\partial z}\left(\frac{\tau_n}{\rho_o}\right)+\frac{\tau_{n,b}}{\rho_o h} \quad \textbf{(3.28)}$$

The potential for steady-state conditions is determined by T_{bc}, the baroclinic adjustment time, the time scale associated with an inviscid balance between centrifugal acceleration and the lateral baroclinic gradient. T_{bc} can be evaluated using the expression

$$T_{bc}=\frac{B}{\sqrt{g'h}} \quad \textbf{(3.29)},$$

where B is the channel width, *g'* is reduced gravity, and h is the depth of the *thalweg* (Chant and Wilson 1997; Lacy and Monismith 2001).

Likewise, the potential to neglect advective acceleration is determined by comparing the frictional relaxation time scale,

$$T_f=\frac{L_s}{\overline{u}_s} \quad \textbf{(3.30)},$$

the time associated with the generation or destruction of a secondary circulation (Kalkwijk and Booij 1986; Geyer 1993), to the advective time scale,

$$T_{adv}=\frac{L_s}{\overline{u}_s\Delta u_n} \quad \textbf{(3.31)},$$

the time associated with the advection of the secondary circulation downstream. In Equations 3.30 and 3.31, L_s is the length scale of the axial flow field, $\overline{u}_s$ is the depth-average streamwise velocity, and Δu_n is the change in the normal (lateral) velocity over the distance L_s (Geyer 1993).

For the Satilla River, T_{bc} ranges between 10 minutes at spring tides and 19 minutes at neap tides, indicating that a steady-state assumption is possible and that the secondary circulation is quasi-stationary with respect to semidiurnal forcing. Similarly, $T_f \approx 24$ minutes and $T_{adv} \approx$ 96 minutes, indicating that secondary circulations are generated more quickly than they are advected downstream ($T_f > T_{adv}$), and in this model formulation, advective accelerations can be neglected.

Assuming steady-state calculations and neglecting advective acceleration simplifies Equation 3.28 to the following lateral momentum balance model (LMBM):

$$f\left(u_s - \overline{u}_s\right) - \frac{\left(u_s^2 - \overline{u_s^2}\right)}{R} = -\frac{g}{\rho_o}\int_z^\eta \frac{\partial \rho}{\partial n} dz + \frac{g}{\rho_o}\frac{\partial \overline{\rho}}{\partial n} h + \frac{\partial}{\partial z}\left(\frac{\tau_n}{\rho_o}\right) + \frac{\tau_{n,b}}{\rho_o h} \quad \textbf{(3.32)}$$

where the first and second terms in Equation 3.32 are secondary flow driven by the imbalance between the depth-dependent and the depth-average Coriolis and centrifugal acceleration, respectively, the third term is the lateral baroclinic pressure gradient, the fourth term is the depth-average lateral baroclinic pressure gradient, the fifth term is a Reynolds parameterization of vertical shear stress divergence, and the sixth term is bottom shear stress. In Equation 3.32, bottom shear stress is expressed as

$$\tau_{n,b} = \rho_o C_D \left|u_{n,1mab}\right| u_{n,1mab} = \frac{1}{16}\rho_o C_D \left|u_{s,1mab}\right| u_{s,1mab} \quad \textbf{(3.33)}$$

to account for the contributions of the lateral velocity (which can be approximated by scaling the axial velocity) to the observed shear stress. A full development of the lateral momentum balance model for the Satilla River is detailed in Appendix A.

Equation 3.32 will be used in Chapter 6 to evaluate the lateral momentum balance at a series of seasonal moorings during spring and neap tides. Likewise, Equation 3.32 will be used in Chapter 7 to examine a series of channel cross-sections during spring and neap tides under maximum ebb and maximum flood conditions, when acceleration is at a minimum. The depth-average lateral baroclinic gradient and bottom shear stress are assumed to represent the importance of the depth-dependent lateral baroclinic gradient and vertical shear stress, respectively. Thus, Equation 3.32 will used to evaluate the directly calculated balance between the centrifugal acceleration (term 2) and the sum of the Coriolis acceleration (term 1), the depth-average lateral baroclinic gradient (term 4), and the bottom shear stress (term 6) from the Satilla River data sets.

4. MATERIALS AND METHODS

4.1 Instrumentation

Several different instruments were used to assess environmental conditions during the LMER 4, SAT 1, and SAT 2 experiments. Chapter 4 details the different instrument types, instrument error, modes of deployment, and general data processing techniques. This chapter also illustrates by photograph or schematic figure common instrument types used in physical oceanography, which may not be familiar to all readers.

4.1.1 Acoustic Doppler Current Profilers

An Acoustic Doppler Current Profiler (ADCP) is a high frequency current meter that uses coded acoustic pulses to measure three-dimensional water column velocities over a range of depths. Assuming there are sufficient scatters in the water column, the three-dimensional velocity field is derived from these 'bin' measurements by determining the Doppler shift in the return signal. An ADCP is often used in either a moored or vessel-mounted application.

The ADCPs used by Skidaway Institute of Oceanography (SkIO) during the LMER 4, SAT 1, and SAT 2 Satilla River experiments were made by RD Instruments, Inc. and were in one of two general configurations: Broad Band ADCP (BB ADCP) and Work Horse ADCP (WH ADCP). The BB ADCP (Figure 4.1) is a 600 kHz profiler with the capability of bottom tracking. It was configured as an upward-looking, bottom mounted mooring during LMER 4 in 1997 sampling every 15 minutes in 0.5 meter bins. The BB ADCP was configured as a downward looking, vessel-mounted fast ping ADCP during the SAT 1 and SAT 2 experiments in 1999 sampling every 12 minutes in 0.5

meter bins. Navigational input and bottom tracking failed for the BB ADCP on March 10, 1999. Correct navigational data derived from a redundant fathometer and the thermosalinograph surface water mapper on the Research Vessel (R/V) Gannet was appended to the BB ADCP spatial survey data.

Figure 4.1: A photograph of the Skidaway Broad Band ADCP in tow off the starboard side of the R/V Gannet.

WH ADCPs are designed for use in fixed application (Figure 4.2). The WH ADCPs used by SkIO during the 1999 SAT 1 and SAT 2 experiments operated at either 300 kHz or 600 kHz and were configured as upward-looking, bottom mounted moorings sampling every 12 minutes in 0.5 meter bins. Each WH ADCP mooring was fitted with a SeaCAT CTD to accurately measure near bottom temperature, salinity, and depth.

SeaCAT CTD data was used to correct water depths in post-retrieval WH ADCP data when insufficient scatters were present for a clear return of the surface water level signal (Emery and Thompson 1998; Ott 2000). Bio-fouling was nearly eliminated on the WH ADCPs by applying a thin mixture of cayenne pepper and marine grade silicon grease to each of the transducer faces before deployment.

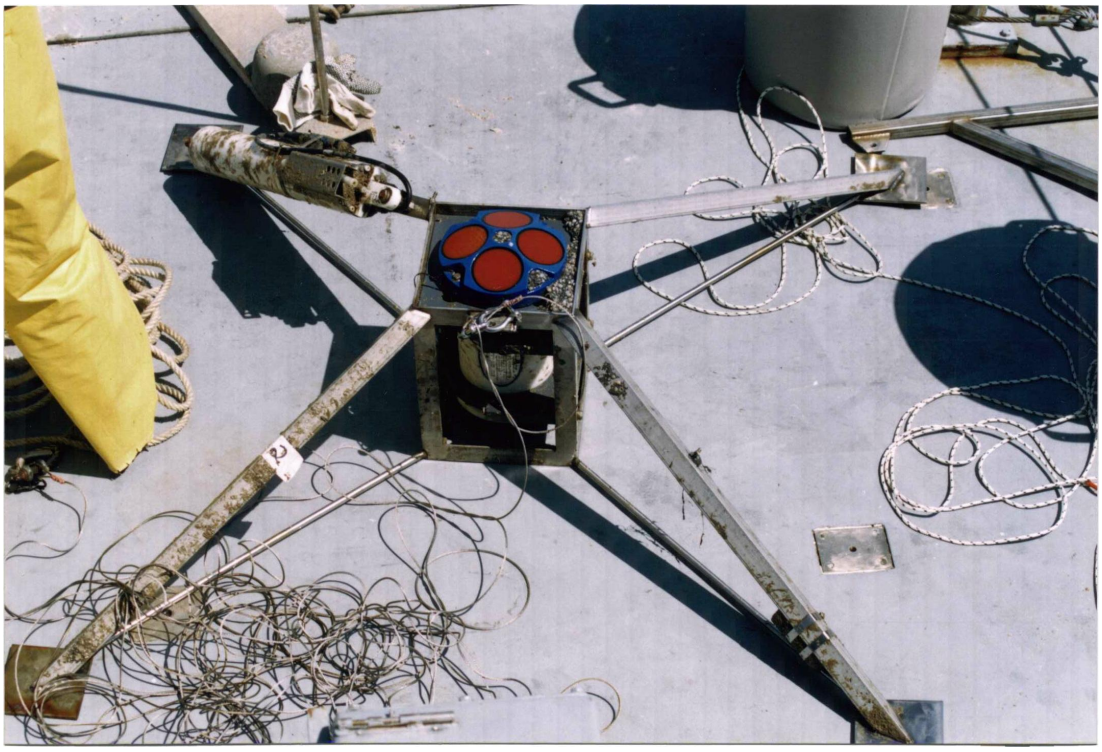

Figure 4.2: A photograph of a Skidaway Work Horse ADCP. A SeaCAT CTD is attached on the upper left leg of the mooring frame.

4.1.2 Conductivity-Temperature-Depth Sensors

A Conductivity-Depth-Temperature (CTD) sensor is an electronic instrument designed to measure nearly continuous temporal profiles of conductivity, temperature, and pressure (depth) in the water column. The salinity is derived from the temperature

and conductivity measurements using internationally adopted UNESCO protocol (1985). A CTD is often used in a moored or a profiling application. Modern CTDs have the functional capability to internally record the data stream and provide real-time measurements through means of a marine-grade conducting cable.

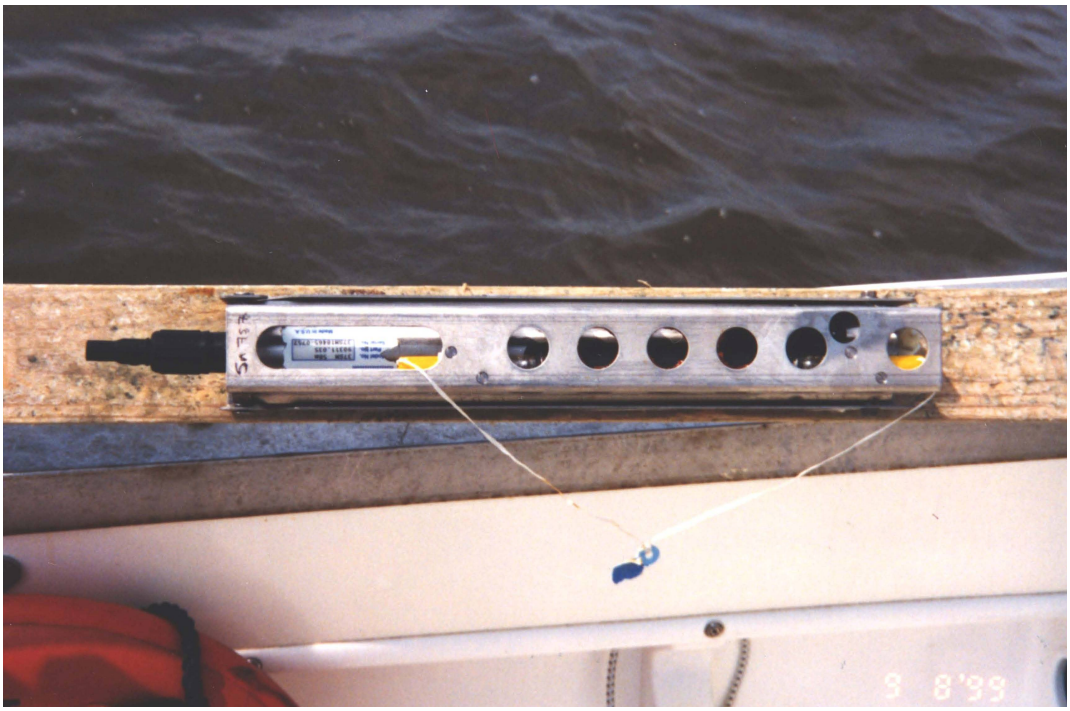

Figure 4.3: A photograph of a Skidaway MicroCAT CTD prior to deployment.

The CTDs used by SkIO during the LMER 4, SAT 1, and SAT 2 Satilla River experiments were made by Sea-Bird Electronics, Inc. (MicroCAT 37-SM, SeaCAT 16, and SeaCAT 19) and Falmouth Scientific Instruments (FSI CTD). The MicroCATs were used in a fixed application during SAT 1 and SAT 2 as either tethered surface moorings or as long-term bottom mounted moorings (Figure 4.3). The SeaCAT 16 CTDs were used in a fixed application as bottom mounted moorings in conjunction with an ADCP

(BB ADCP during LMER 4 and WH ADCPs during SAT 1 and SAT 2) or as tethered surface moorings during SAT 1 and SAT 2. The SeaCAT 19 CTD was used in LMER 4, SAT 1, and SAT 2 for vertical profiling during high and low water surveys, anchor stations, mooring deployments, and mooring retrievals (Figure 4.4). The FSI CTD was used in a profiling application aboard the R/V Gannet (a 5.5 meter catamaran) during rapid spatial surveys (Figure 4.5).

Figure 4.4: A photograph of the Skidaway SBE 19 profiling CTD on the starboard deck of the R/V Blue Fin.

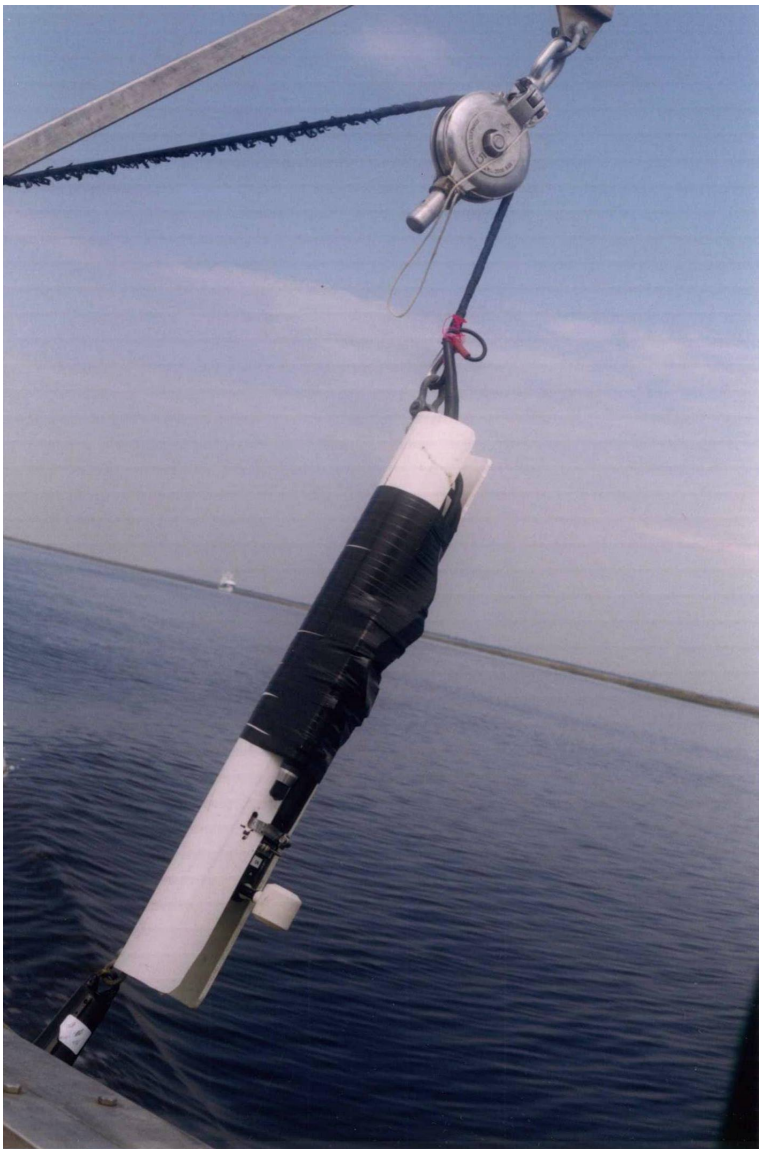

Figure 4.5: A photograph of the Skidaway FSI CTD on the port deck of the R/V Gannet.

The moored MicroCAT and SeaCAT 16 CTDs sampled every 6 minutes and coincided with the ADCP measurements. The profiling SeaCAT 19 CTD internally recorded data at 4 Hz and broadcast real-time data at 1 Hz on the R/V Blue Fin (the 24 meter primary research vessel). The FSI CTD sampled at approximately 2.8 Hz with a data transmission rate of 9600 baud during SAT 1, but due to a large hysteresis in the

data between up and down casts, the FSI CTD sample rate was improved to approximately 3.9 Hz by adjusting the data transmission rate to 19200 baud for SAT 2. While the higher baud rate for the FSI CTD during SAT 2 reduced the hysteresis problem, the instrument neither sampled at a steady frequency nor at higher than 3.9 Hz for either experiment. As a result, cross-calibration casts were performed between the FSI CTD and SeaCAT 19 CTD and were used to correct the FSI CTD downcasts to the UNESCO standard for salinity, density, temperature, and depth.

Figure 4.6: A photograph of a Skidaway MicroCAT CTD after a month-long late summer deployment. Rapid bio-fouling occurs when the ambient water temperature exceeds 25°C.

SeaCAT 16 and SeaCAT 19 CTD temperature, salinity, and depth data are of excellent quality. Small tubes filled with Tri-butyl Tin (TBT) attached to either ends of

the conductivity cell on the SeaCAT 16 CTDs significantly reduced bio-fouling during mooring deployments. However, bio-fouling reduced the quality of bottom mounted MicroCAT CTD salinity to discrete month-long intervals (Figure 4.6). The quality of bottom mounted MicroCAT CTD salinity was significantly improved by the addition of SeaCAT TBT tubes on either end of the conductivity cell and the application of marine grade silicon grease on the housing around the conductivity cell prior to deployment. Temperature and pressure data for the SeaCAT CTDs and MicroCAT CTDs were of excellent quality and were not affected by bio-fouling.

4.1.3 Surface Thermosalinograph

A surface thermosalinograph is an externally powered conductivity-temperature sensor that is integrated with a global positioning unit and designed for shipboard use and water surface sampling while underway. The surface thermosalinograph used by SkIO during the SAT 1 and SAT 2 experiments was manufactured by Sea-Bird Electronics, Inc., (SBE-21) and installed on the R/V Gannet where it was interfaced with a Differential Global Positioning System (DGPS). The SBE-21 unit sampled every 5 seconds and measured approximately 1 liter of water per sample. During long surveys, significant timing errors were diagnosed in the spatial position of the SBE-21 data file. This error was determined to be due to a combination of a time interval calculation and a delayed response in the SBE-21 unit when writing data to a log file. A redundant fathometer which recorded depth, spatial position, and time at 2 second intervals linked to the same DGPS unit as the SBE-21 was used to correct the data delay of 0.21 seconds per sample.

4.2 Methods of Deployment

Data for the LMER 4, SAT 1, and SAT 2 experiments were collected in one or more of five operational modes. Time series data was obtained from long term CTD deployments and from an array of moored surface and bottom instruments. Seasonal spatial data was derived from bi-monthly synoptic surveys aboard the R/V Gannet. Vertical profiles of the water column were obtained during high and low water surveys, anchor stations aboard the R/V Blue Fin, and during instrument deployment and retrieval. Lastly, short term spatial and temporal data was collected during 'rapid spatial surveys' aboard the R/V Gannet.

4.2.1 Long Term Mooring Deployments

Two long term moorings were deployed in the Satilla River to measure seasonal and annual changes in temperature, salinity, and pressure, and to provide near ocean and upriver real-time boundary conditions applicable in a numerical model. The first long term mooring (LT 1) was attached to a U.S. Coast Guard channel marker (USCG A14) near river kilometer 8. Temperature, salinity, and pressure data were collected at LT 1 (LT 1 in Figure 4.7) for a one year period from early March 1999 through early April 2000 at a 6 minute interval. Pressure data collected at this location was used to reduce rapid spatial survey ADCP data on a prescribed grid to mean lower low water (MLLW). The second long term mooring (LT 2) was attached to an old railroad bridge upriver near Woodbine, Georgia, at river kilometer 40. Temperature, salinity, and pressure data were collected at LT 2 (LT2 in Figure 4.7) for three months from early September 1999 through December 1999 also at a 6 minute interval.

4.2.2 Bi-monthly Synoptic Surveys

Longitudinal synoptic surveys were conducted from December 1998 through April 2000 on a bi-monthly schedule at low and high water to spatially map the seasonal changes in surface temperature and salinity (*cf.* Figure 2.7) and water depth under changing discharge conditions. These bi-monthly synoptic surveys were done using the R/V Gannet SBE-21 system and coincided with an instrument swap at LT 1. Recorded water depths were reduced to MLLW using data from LT 1. The adjusted survey depths were then used to update the bathymetry of the Satilla River from the last National Oceanic and Atmospheric Administration (NOAA) bathymetric survey done in 1929.

4.2.3 Seasonal Mooring Deployments

Seasonal moorings were deployed at the same pre-determined locations to collect a thirty to sixty day time series of temperature, salinity, pressure, and optical backscatterance, at two heights, near surface and near bottom. The companion three-dimensional velocity data was measured at selected moorings using an upward-looking bottom mounted ADCP. The LMER 4 seasonal mooring field was deployed from 26 March 1997 to 25 April 1997 during high to moderate discharge conditions. The SAT 1 and SAT 2 seasonal mooring fields were deployed, respectively, from 20 January 1999 to 19 March 1999 during moderate to low discharge conditions and from 9 September 1999 to 18 October 1999 during low discharge conditions punctuated by hurricanes. Figure 4.7 shows the location of the SAT 1 and SAT 2 mooring field and Figure 4.8 shows a schematic of the mooring configuration used during the SAT 1 and SAT 2 experiments. For reference, the LMER 4 mooring field was deployed approximately 1 kilometer on either side of the SAT mooring location 3 in Figure 4.7.

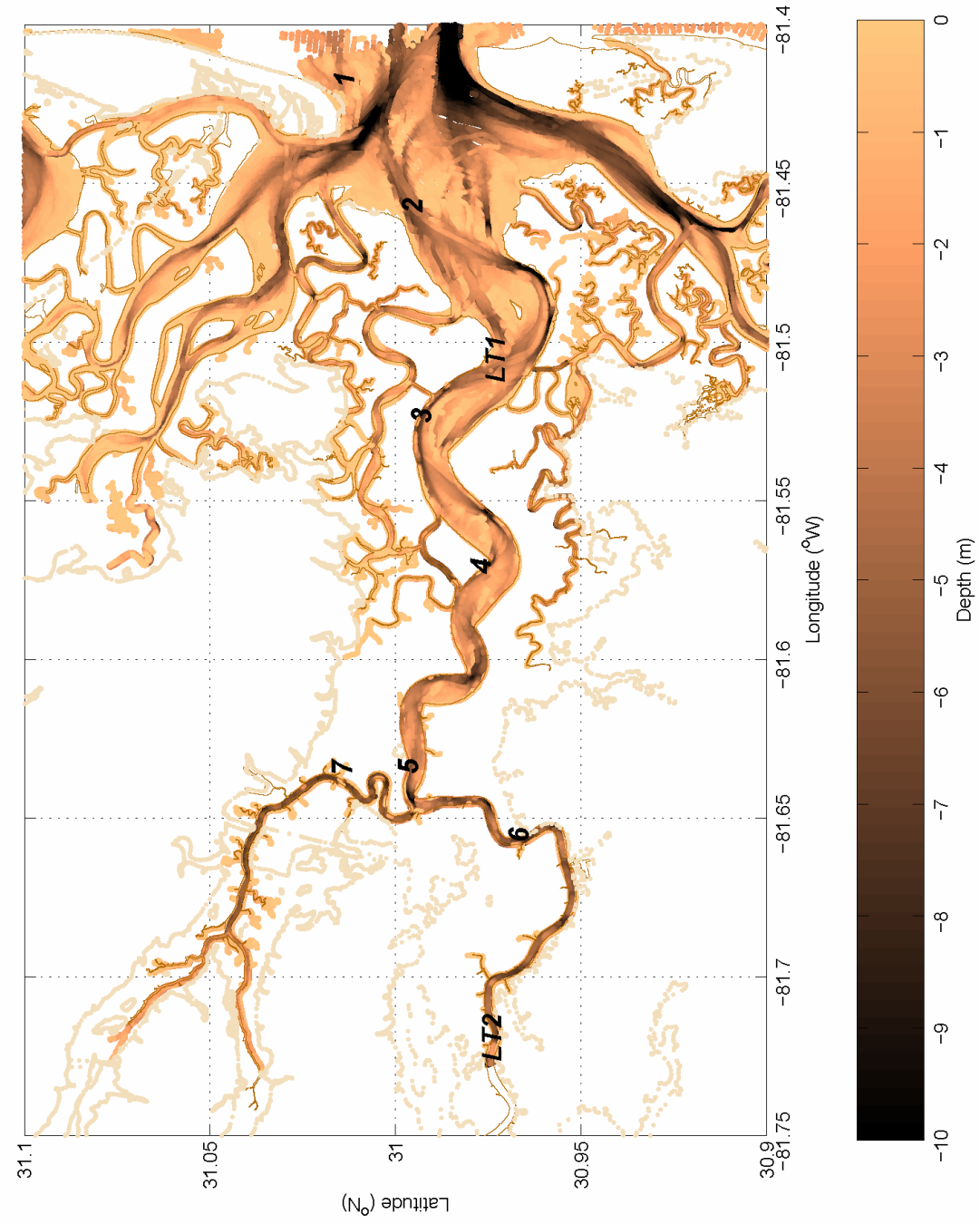

Figure 4.7: Map of Satilla River mooring deployment sites for the SAT 1 and SAT 2 experiments.

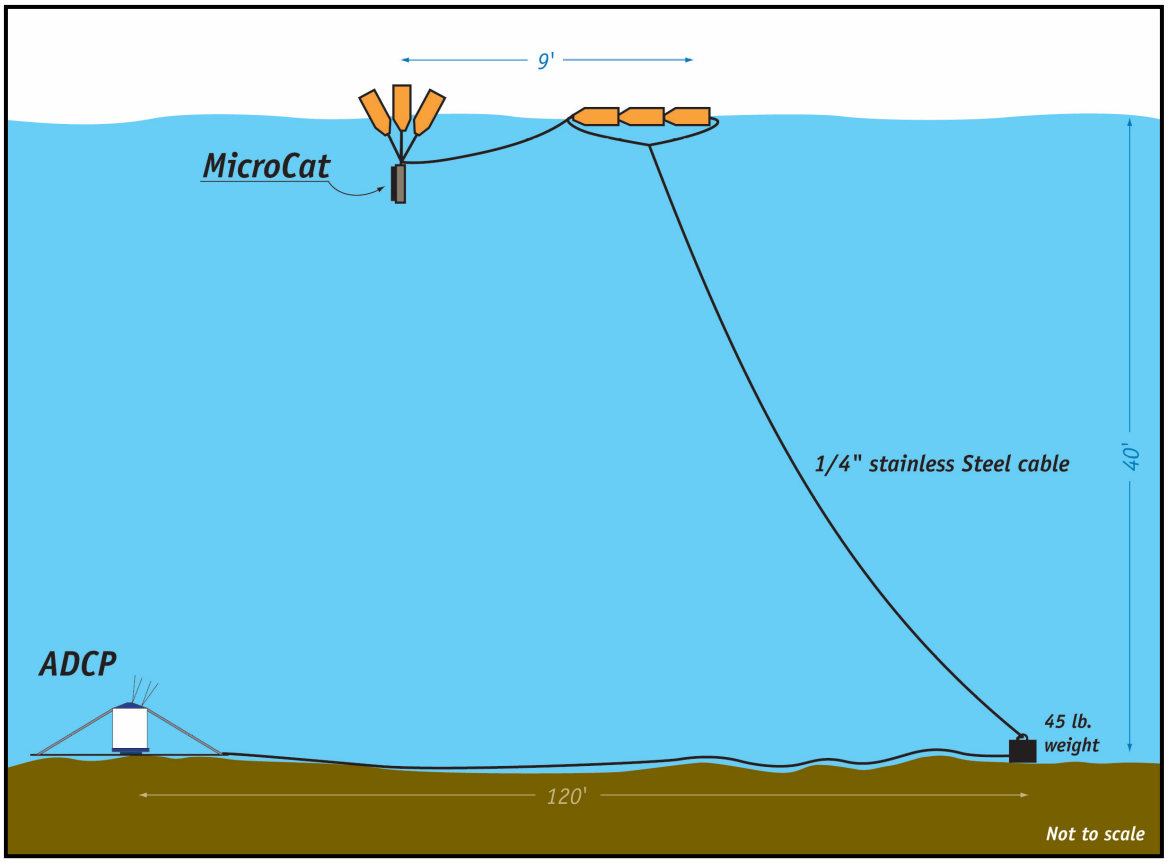

Figure 4.8: A schematic of the SAT 1 and SAT 2 mooring deployments. Note that the figure is not to scale.

4.2.4 Anchor Stations

Anchor stations were conducted at neap and at spring, shortly after the seasonal moorings were deployed, during the LMER 4, SAT 1, and SAT 2 experiments. Anchor station data consisted of hourly CTD profiles that included temperature, salinity, pressure, optical backscatterance, and fluorescence taken aboard the R/V Blue Fin. CTD profiles were taken hourly for a 25-hour tidal cycle and more frequently, every half-hour for a two hour period, around low water slack (LWS) and high water slack (HWS) to better determine the timing and the change in conditions between the ebb and flood tides. Depths were determined by in-situ fathometry while latitude and longitude positions were

obtained with a shipboard DGPS on the R/V Blue Fin. The LMER 4 anchor station operated for a continuous 25 hour period while the SAT 1 and SAT 2 anchor stations each operated for a continuous 13 hour period in conjunction with the R/V Gannet rapid spatial surveys.

4.2.5 Rapid Spatial Survey System

'Rapid spatial surveys' were conducted during SAT 1 and SAT 2 in the spring and fall of 1999. Rapid spatial surveys and anchor stations were conducted simultaneously, at neap and at spring, in one of four pre-determined 4 km reaches of the Satilla River. The rapid spatial surveys and the anchor stations each operated for a continuous 13 hour period in order to resolve the time varying three-dimensional structure of the river on the tidal time scale. Performed aboard the R/V Gannet, the rapid spatial surveys were designed to collect high resolution temperature, salinity, optical backscatterance, velocity, depth, and position at an interval of 15 seconds or less. These data were acquired using the surface pumped temperature-salinity system (SBE-21) installed on the R/V Gannet (linked to DGPS and fathometry), stop and drop FSI CTD casts at predetermined locations and over the mooring field, and a towed 600 kHz BB ADCP to resolve three-dimensional currents in the axial, lateral, and vertical directions. Exact locations and depths were determined by a shipboard DGPS unit and fathometry on the R/V Gannet. The tidally resolving 'rapid survey' data was collected while the mooring field was in place in an effort to ground truth the data and to relate the changes between the tidal and 'seasonal' time scales. Figure 4.9 shows a schematic of the rapid spatial survey system.

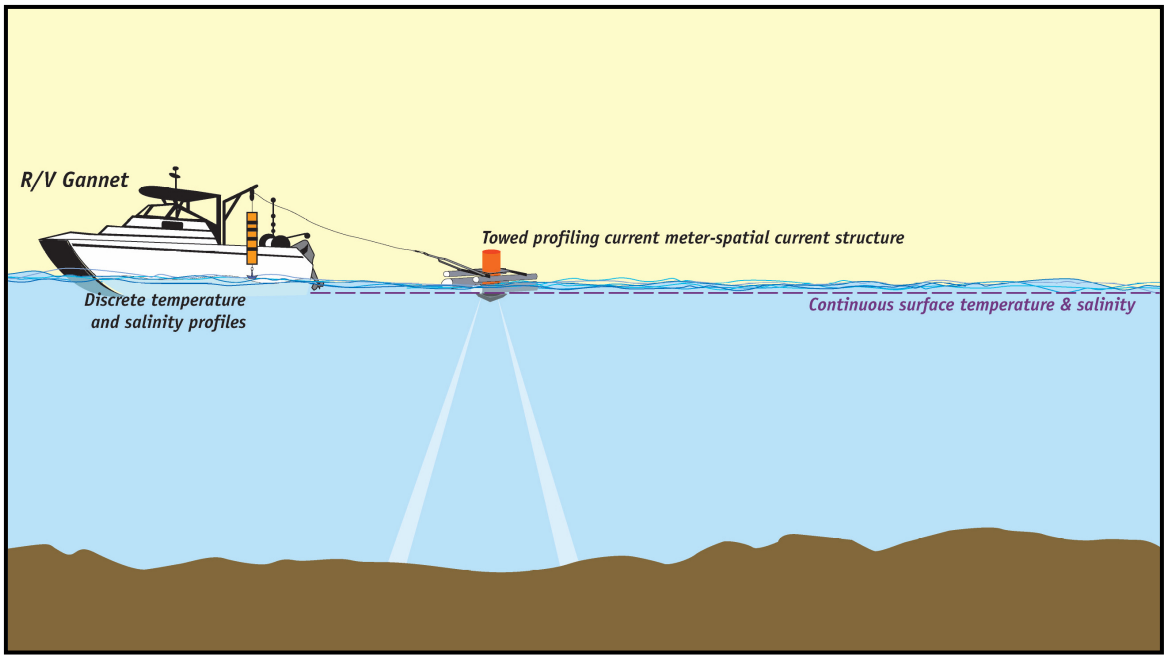

Figure 4.9: A schematic of the rapid spatial survey system aboard the R/V Gannet.

4.3 Methods of Data Processing

This section describes general data processing techniques for the ADCPs, CTDs, and the SBE-21 Thermosalinograph used during the LMER 4, SAT 1, and SAT 2 experiments. In general, the type of data processing required for each instrument type depends on the structure of the original data, the instrument type, and the instrument manufacturer. Processing software provided by the manufacturer with each instrument type was tested for accuracy and precision to the internationally accepted UNESCO standard (1985) for temperature, salinity, and density. In some cases, processing software provided by the manufacturer was not used to generate the final output data files, as it was determined significant errors were introduced using the manufacturer's software rather than by using original MATLAB code derived to the UNESCO standard (1985) for seawater.

4.3.1 Acoustic Doppler Current Profilers

The data recorded by the WH ADCPs and the BB ADCP is in one of two formats, depending on its use in a moored or towed application. The original data recorded by the WH ADCPs and the moored BB ADCP was in raw single ping format while the original data recorded by the roving BB ADCP was in both raw single ping format (noted by an *R extension) and ensemble averaged format (noted by a *P extension). The ensemble averaged data is the raw single ping data averaged internally in the BB ADCP over a predetermined time period. Navigational data was not included in the raw single ping format, but could be extracted from DGPS data and appended to the processed ADCP data when necessary.

The RDI DOS-based software Transect™ version 2.8 was used to acquire the BB ADCP data and the RDI Windows-based WinADCP™ was used to acquire the WH ADCP data. Due to several conversion errors previously discovered in the manufacturer's software (Dr. Harvey E. Seim, personal communication), the software provided with the RDI WH ADCPs and the BB ADCP for post-processing the data was not used. Instead, the WH ADCP and BB ADCP data was processed using a developed combination of C-programs, UNIX awk scripts, and modified MATLAB scripts (Klymak 1998; Seim 1999). The WH ADCP and moored BB ADCP data is processed by first using a C-program to convert the data from a binary format to a MATLAB readable format, and then by using a MATLAB script to concatenate the data files for each survey day. Although the post-processing of the towed BB ADCP data follows a similar scheme to that of the WH ADCPs, it is more complicated because it is necessary to consider the contribution of errors from both the motion of the roving BB ADCP and of the

ship that is towing it. The roving BB ADCP data is processed by first using a C-program to convert the data from a binary format to a MATLAB readable format, next by appending the appropriate navigational data (derived from either the BB ADCP navigational data file or from an external source of DGPS data), and then by correcting the data for compass errors by determining the misalignment angle between the ship's DGPS position and the BB ADCP bottom track displacements. Lastly, the individually processed roving BB ADCP data files are concatenated for each survey day. The resultant output data files for both the WH ADCPs and the BB ADCP are in a MATLAB readable format that contains the detailed three-dimensional velocity measurements, the survey specific instrument setup parameters, and the post-processing correction coefficients.

4.3.2 Conductivity-Temperature-Depth Sensors

The raw data recorded by the SBE CTD 16 and SBE CTD 19 were in hexadecimal format. The SBE DOS-based software SeaTerm 1621™ version 4.236 was used to initiate logging of the SBE CTD 16 and 19 units while the SBE Seasave for DOS version 4.236 was used to acquire and store the data collected respectively by the CTDs. A companion SBE DOS-based software package, Seasoft™ version 4.236 was used to derive the salinity and density from the hexadecimal temperature and conductivity data to the UNESCO protocol (1985). The hexadecimal data was then converted to ASCII format using a module in Seasoft™ version 4.236 that resulted in two ASCII output files, a descriptive header file and a processed data file containing the scan number, temperature, conductivity, depth, salinity, density, fluorescence, and optical backscatterance variables.

The raw data recorded by the SBE MicroCAT CTDs was in ASCII format. Due to random missing data errors in the upload process using the SBE SeaTerm for Windows™ and conversion errors in the SBE DOS-based CNV37™ module, the SBE software provided with the SBE SM-37 MicroCATs was not used for data processing. Instead, a series of original UNIX-based awk and sed scripts were used in conjunction with original MATLAB scripts to process the MicroCAT data following the accepted UNESCO protocol (1985). The UNIX awk and sed scripts and the MATLAB scripts used to process the SM-37 MicroCAT data are available on request.

The raw data recorded by the FSI CTD was in ASCII format. Due to inconsistencies in the sampling frequency (varying between 2.8 Hz and 3.9 Hz for each cast) of the fast thermistor on the FSI CTD and a large hystersis in the temperature, conductivity, and salinity data between upcasts and downcasts, the manufacturer's software provided with the FSI CTD was not used for data processing. Instead, the FSI CTD data was calibrated to the SBE CTD 19 data to correct for the sampling frequency errors, after which an original UNIX-based awk script was used in conjunction with an original MATLAB script to process the FSI CTD data following the accepted UNESCO protocol (1985). The UNIX awk script and the MATLAB script used to process the FSI CTD data are available on request.

4.3.3 Surface Thermosalinograph

The raw data stream recorded by the SBE-21 Thermosalinograph was in hexadecimal format. The SBE DOS-based software SeaTerm 1621™ version 4.236 was used to initiate logging of the SBE-21 unit while the SBE Seasave for Windows™ version 2.7 was used to acquire and store the data collected by the SBE-21 unit while in

transit. A companion SBE DOS-based software package, Seasoft™ version 4.236 was used to derive the salinity and density from the hexadecimal temperature and conductivity data to the UNESCO protocol (1985). The hexadecimal data was then converted to ASCII format using a module in Seasoft™ version 4.236 that resulted in two ASCII output files, a descriptive header file and a processed data file containing the scan number, temperature, conductivity, depth, salinity, density, latitude, and longitude, and time variables.

5. FORTNIGHTLY SIGNAL OF SECONDARY CIRCULATION AT A BEND

5.1 Introduction

There are abundant observations indicating the presence and importance of secondary circulation in the Satilla River. Surface fronts, consisting of foam lines and slicks, are frequently observed along the channel axis throughout the river. During a 1997 survey, a foam line front associated with late flood (Figure 5.1) had enough lateral strength to move an anchored research vessel back and forth on its pivot point toward the convergent foam line. Concurrent with the presence of this foam line, a small boat sampled the temperature and salinity characteristics across the front. Water on the north side of front (toward the outside of the channel bend) was a clear dark tea color and about 1 PSU less than the water on the south side of the front. Water on the south side (toward the inside of the channel bend) had a muddy chalky-like appearance, similar to unstirred hot chocolate. Subsequently, a slick line, which was observed during early ebb, formed in approximately the same location, while current velocities were relatively low.

This chapter investigates the modulation in the strength and character of secondary circulation due to channel curvature and density stratification on the fortnightly time scale. In the Satilla, it appears that over a time period longer than the 14-day spring-to-neap tidal cycle, observed secondary circulation in a channel bend is consistent with a transverse circulation driven by centrifugal acceleration. However, on a shorter time scale, it appears that the strength of the local density stratification may limit or halt the naturally occurring transverse circulation.

Figure 5.1: Photograph of a local secondary circulation during late flood in the Satilla River. Water in the foreground (dark colored and turbulent) is about 1 PSU less than the water on the far side (light-colored and less turbulent) of the front. The photograph was taken by S. Elston during the 1997 LMER 4 experiment.

5.2 Materials and Methods

5.2.1 Experiment Site and Environmental Conditions

Field data for this experiment, LMER 4, was collected between 26 March – 25 April 1997 over two complete neap and spring tidal cycles as part of the Georgia Land Margin Ecosystems Research Program (GA LMER) in the pristine and naturally sinuous Satilla River of southeast Georgia. A shallow coastal plain river near the Georgia/Florida border, the Satilla is a partially mixed estuary which experiences 1 to 2.5 meter range semidiurnal tides. It has a drainage basin of 9143 km^2 and a length of about 362 kilometers from its headwaters to the Atlantic Ocean (Dame et al. 2000; Blanton et al. 2001). The Satilla has an average discharge of less than 80 m^3 s^{-1} but can vary from 0 to

150 m^3 s^{-1} over an annual cycle. Its 'black' water is a dark tea color that originates from tannic acids which are derived from humic substances found in the extensive flood plain swamps that border the river. The Satilla has a strong neap-to-spring axial current inequality ranging from 0.5 m s^{-1} to 1.5 m s^{-1} and its density structure is largely controlled by variations in salinity.

The main channel of the Satilla is marked by nine channel bends and two short straight reaches that extend from its mouth between Jekyll and Cumberland Islands to 38 kilometers upriver (Figure 5.2). The majority of these bends are broadly concave (bends to the north, radius of curvature ~ 1200 m) each followed by more sharp convex bends (to the south, radius of curvature ~ 800 m). The bends are roughly three to four kilometers apart, starting six kilometers from the ocean (0 km) and extending 33 kilometers upriver.

Meteorological data from Kings Bay, Georgia (KNBQ) between 26 March – 25 April 1997 show that the atmospheric conditions in the latter half of March 1997 were unusually warm and dry and were followed by an extended cold wet period throughout most of April 1997. There were 14 days (of the total 31-day period) during which haze and fog conditions were reported as significant (unusual) weather. Three major precipitation events occurred in March – April 1997, the largest event occurring shortly after instrument retrieval at the end of April. The first event occurred on April 7, 1997, shortly before the spring anchor station and the second event occurred on April 23, 1997, a week after the neap anchor station. Estimated system response time for a precipitation event in the Satilla River is on the order of 20 days; and as a result, the effects of the first precipitation event were not observed during this study period.

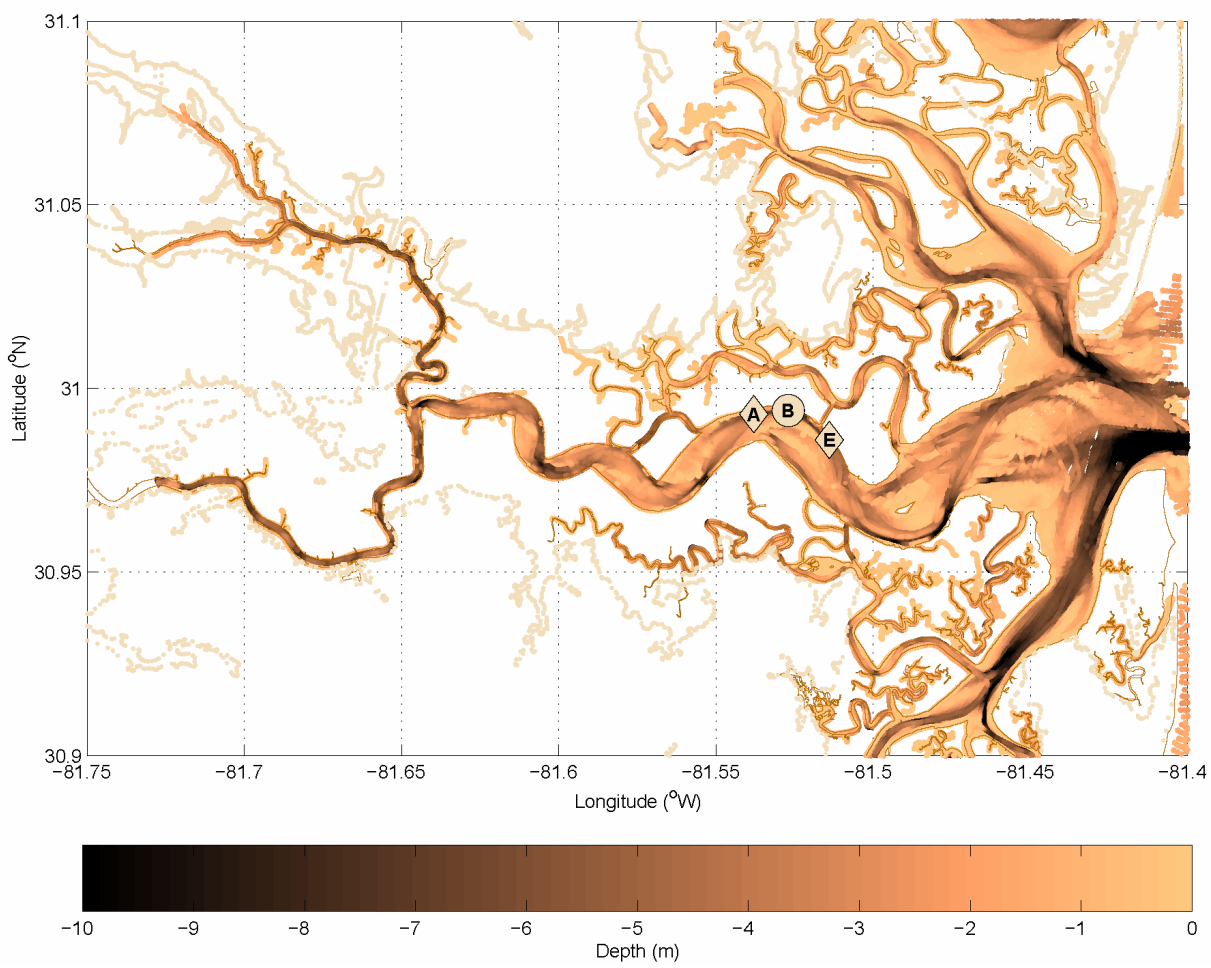

Figure 5.2: Map of the Satilla River in southeast Georgia near the Florida border. Mooring locations for the March – April 1997 field survey are indicated in the first river bend by two diamonds and one circle. The diamond regions indicate locations of surface and bottom salinity measurements, and the circular region indicates the location of the acoustic current profiler and 25-hour anchor stations.

Freshwater discharge varied substantially (almost 300 $m^3 s^{-1}$) shortly before and during LMER 4 experiment from 295 $m^3 s^{-1}$ in late February to slightly over 7 $m^3 s^{-1}$ near the end of April (*cf.* Figure 2.4a). Discharge at the beginning of the LMER 4 mooring deployment (26 March) was approximately 63 $m^3 s^{-1}$ and progressively dropped to a low value of 7 $m^3 s^{-1}$ by the end of the 31-day sampling period (25 April). Freshwater discharge during the two neap-spring cycles of the LMER 4 experiment decreased by nearly 50 $m^3 s^{-1}$ between the first neap-spring pair (60 $m^3 s^{-1}$ and 50 $m^3 s^{-1}$, respectively) and the second neap-spring pair (13 $m^3 s^{-1}$ and 7 $m^3 s^{-1}$, respectively).

5.2.2 Seasonal Mooring Deployment – Spring 1997

The primary data collected for the LMER 4 experiment was from an array of moored instruments and two anchor stations (one at neap and one at spring) on the Research Vessel (R/V) Blue Fin in the first major bend (R ~ 1200 m) of the Satilla River, between 12 and 16 kilometers from the ocean's mouth (Figure 5.2, the bend where circle B is located). In this chapter, this section of the Satilla River, the study site, will be referred to as Domain A. Two mooring frames, approximately 2 kilometers apart, were each outfitted at 0.66 meters above bottom (mab) and 2.50 mab with a Sea-Bird Electronics, Inc., (SBE) SeaCAT Conductivity-Temperature-Depth sensor (CTD) and at 1.00 mab with an InterOcean S4 current meter. Temperature, salinity, depth, optical backscatterance (OBS), and velocity measurements were made every 6 minutes for a 31-day period at these two locations which are indicated by diamonds A and E in Figure 5.2. Between these two mornings, a 600 kHz RD Instruments, Inc., (RDI) Broad Band Acoustic Doppler Current Profiler (BB ADCP), indicated by the circle B in Figure 5.2, was used to obtain detailed three-dimensional current measurements in the axial,

transverse, and vertical directions. The BB ADCP was mounted in an upward-looking position at 0.4 mab in a stainless steel frame. The BB ADCP sampled every 15 minutes during the same 31-day period in 0.5 m bin increments, beginning at 1.24 mab to 0.5 m below the water surface. A Benthic Acoustic Stress Sensor (BASS) was deployed just west of the BB ADCP. The BASS tripod (Williams et al. 1987) measured three-dimensional turbulent velocities at four levels: 0.28, 0.66, 0.98, and 1.28 mab and collected data every 10 minutes in 4.5-minute long bursts at a frequency of 2 Hz. Mooring locations and the BB ADCP setup conditions for the LMER 4 experiment are respectively summarized in Tables 5.1 and 5.2.

Table 5.1: LMER 4 mooring deployment locations.

Station	Sensor Depth (mab)	Water Depth (m)	Instrument (serial #)	Parameters Measured	Latitude (°N)	Longitude (°W)
♦ A	2.50	10.0	SC 1835	C, Obs, P, T	30° 59.58′	81° 32.28′
♦ A	1.00	10.0	S4 908	C, T, V	30° 59.58′	81° 32.28′
♦ A	0.66	10.0	SC 848	C, Obs, P, T	30° 59.58′	81° 32.28′
● B	0.3 - 1.3	9.6	BASS	V+	30° 59.57′	81° 31.49′
● B	0.4+	9.5	ADCP	V+	30° 59.64′	81° 31.62′
♦ E	2.50	10.3	SC 1836	C, Obs, P, T	30° 59.16′	81° 30.84′
♦ E	1.00	10.3	S4 909	C, T, V	30° 59.16′	81° 30.84′
♦ E	0.66	10.3	SC 849	C, Obs, P, T	30° 59.16′	81° 30.84′
Anchor	Profiling	10.0	Gafanhoto	C, Obs, P, T, V+, seds	Near 30° 59.64′	Near 81° 31.62′

* mab = meters above bottom; C = conductivity; Obs = optical backscatterance; P = pressure; T = temperature; V = current velocity; V+ = current velocity profile

Table 5.2: Broad Band ADCP setup specifications for the LMER 4 experiment.

LMER Satilla River, Georgia	Experiment 4 26 March to 25 April 1997
Acoustic Frequency	600 kHz (Broad Band ADCP)
Beam Angle	20 degrees
Transducer Depth	1 m
Bin Length	0.5 m
Sampling Interval	15 minutes
Pulse Length	0.72 m
Blanking Interval	0.5 m
Center of First Bin	1.24 m
Profiling Mode	4
Pings per Ensemble	150
Pings per Ensemble Average	fixed instrument, internally recording
Single Ping Velocity Error	0.65 m s^{-1}
Dynamic Velocity Error	3.38 x 10^{-3} m s^{-1}
Bottom Track	Not Applicable
Data Acquisition	RD Instruments Software (Transect)
Navigation	Global Positioning (DGPS)
Ship Speed	moored instrument, upward-looking

A suspended sediment profiler ('Gafanhoto', courtesy of G. Kineke) equipped with an OBS sensor, a Marsh McBirney electromagnetic current meter, and an Ocean Sensors CTD was used during anchor stations on hourly basis to obtain a time series of water properties, flow conditions, and suspended sediment concentrations throughout the water column. 'Gafanhoto' (grasshopper in Portuguese) is an open frame tripod with a trapezoidal shape which stands 0.91 m high and has a vane to keep it oriented into the principal axis flow direction (Sternberg et al. 1991). The tripod was additionally equipped with a KVH Industries Model ROV103 fluxgate digital compass and a set of four pumps that operate on an electronic timer to activate the water/suspended sediment sampling unit. The current meter, OBS sensor, and pump nozzle were mounted at 0.2 m above the bed, and the CTD was mounted at 0.31 m above the bed. The integrated pump

sampling system provided an in-situ calibration for the onboard OBS sensor. Water/sediment samples were obtained at three levels during each CTD cast (near bottom, mid-depth, and near surface) providing a range of suspended sediment concentrations and particle sizes.

Water column depths were determined in-situ on the R/V Blue Fin with a subsurface fathometer. Latitude and longitude positions during instrument deployment, retrieval, and at anchor stations were determined in-situ from a Differential Global Positioning System (DGPS) installed on the R/V Blue Fin. Latitude and longitude positions during the small boat lateral survey of the secondary circulation front were determined using a hand-held Garmin 12 DGPS unit.

In general, salinity and velocity data from the moored CTDs and the BB ADCP were of excellent quality. Bottom salinity measured at Station E had spurious noise and an intermittent signal suggesting that the conductivity cell was blocked by debris. The moored BB ADCP signal returns sporadically failed to detect the water surface level, which was likely due to an insufficient quantity of scattering particles or to a glass-smooth water surface as occasionally observed in the Satilla (Emery and Thompson 1998; Ott 2000). Bottom SeaCAT CTD pressure data at Station E (0.66 mab) was used to uniformly correct the BB ADCP data for missing surface returns, remove the near surface side lobe energy returns, and adjust the depth of the velocity observations to a standard datum. Contaminating side lobe energy generated by transducer beam interference near the 'reflecting surface' (for an upward-looking ADCP, the water surface) was removed using the data range expression

$$R_{valid} = H_r \cos\varphi \quad \textbf{(5.1)}$$

where H_r is the range depth (the total observed water depth minus the instrument depth), and φ is the beam angle (generally 20°) of the transducer faces with the horizontal plane (Emery and Thompson 1998). Removing side lobe energy from the BB ADCP data reduced the vertical data range near the reflecting surface by approximately 6% (60 centimeters for H_r = 10 m). Because the LMER 4 BB ADCP bins were 0.5 m in size, it was necessary to remove the first two bins (totaling 1 meter) near the water surface to account for and eliminate side lobe energy from the observed data. The BB ADCP data was rotated through an angle of -14º (clockwise) to align the U and V components of velocity with the streamwise and normal flow directions. BASS and 'Gafanhoto' measurements will not be discussed further as they are described in detail, respectively, by Seim et al. (2002) and Blanton et al. (2003).

5.3 Results and Discussion

5.3.1 Salinity and Velocity Distributions

Figure 5.3 shows the tidal and subtidal salinity time series for the near surface SeaCAT CTDs moored 1 kilometer on either side of the BB ADCP (*cf.* Stations A and E in Figure 5.2). Subtidal salinity at the station closest to the ocean (SC 1836, identified as Salinity East) was around 16 PSU in late March and increased to around 24 PSU in late April. Likewise, the subtidal salinity at the station west of the BB ADCP mooring (SC 1835, identified as Salinity West) was around 12 PSU in late March and increased to around 23 PSU in late April. The longitudinal salinity gradient decreased from 2 PSU km^{-1} to 1 PSU km^{-1} as a river discharge dropped from 63 m^3 s^{-1} at the beginning of the LMER 4 mooring deployment to just over 7 m^3 s^{-1} at the end of April 1997. This decrease in the axial salinity gradient was associated with a decrease in freshwater

discharge (Seim et al. 2002; Blanton et al. 2003). Upper and lower salinity data at Station A suggest that a decrease in the axial salinity gradient corresponds to a decrease in the vertical salinity gradient; however, the extent of the decrease is difficult to determine because the sensors at Station A are only 2 meters apart and the corroborating salinity data at Station E is suspect.

Neap and spring 25-hour anchor station CTD density profiles are shown in Figure 5.4. Density values over the tidal cycle varied over a range of 7 kg m^{-3} (~ 9 PSU) during the neap anchor station and over a range of 15 kg m^{-3} (~ 18 PSU) during the spring anchor station. Figure 5.4 demonstrates that the dynamic range in density at a fixed location during neap tides is approximately half that observed during spring tides. The vertical density gradient at neap (upper panel in Figure 5.4) shifts from stratified conditions for most of the tidal cycle to nearly well-mixed conditions for a short duration only during late flood and early ebb. The maximum vertical density difference observed at the neap anchor station was $\Delta\rho$ = 5.1 kg m^{-3} (a vertical salinity difference of ~ 6.6 PSU). The lower panel Figure 5.4 shows the vertical density profile comparatively during the spring anchor station. During spring, the vertical density gradient is nearly well-mixed at all times except for early ebb where it is weakly stratified. The maximum vertical density difference observed at the spring anchor station was $\Delta\rho$ = 1.4 kg m^{-3} (a vertical salinity difference of ~ 1.8 PSU). A distinguishing and important difference between neap and spring density profiles is the shift between the stratified conditions at neap to the nearly well-mixed conditions at spring. As discussed in Chapter 3, the strength of the vertical density gradient is an important factor in determining the effectiveness of overturning by secondary circulation.

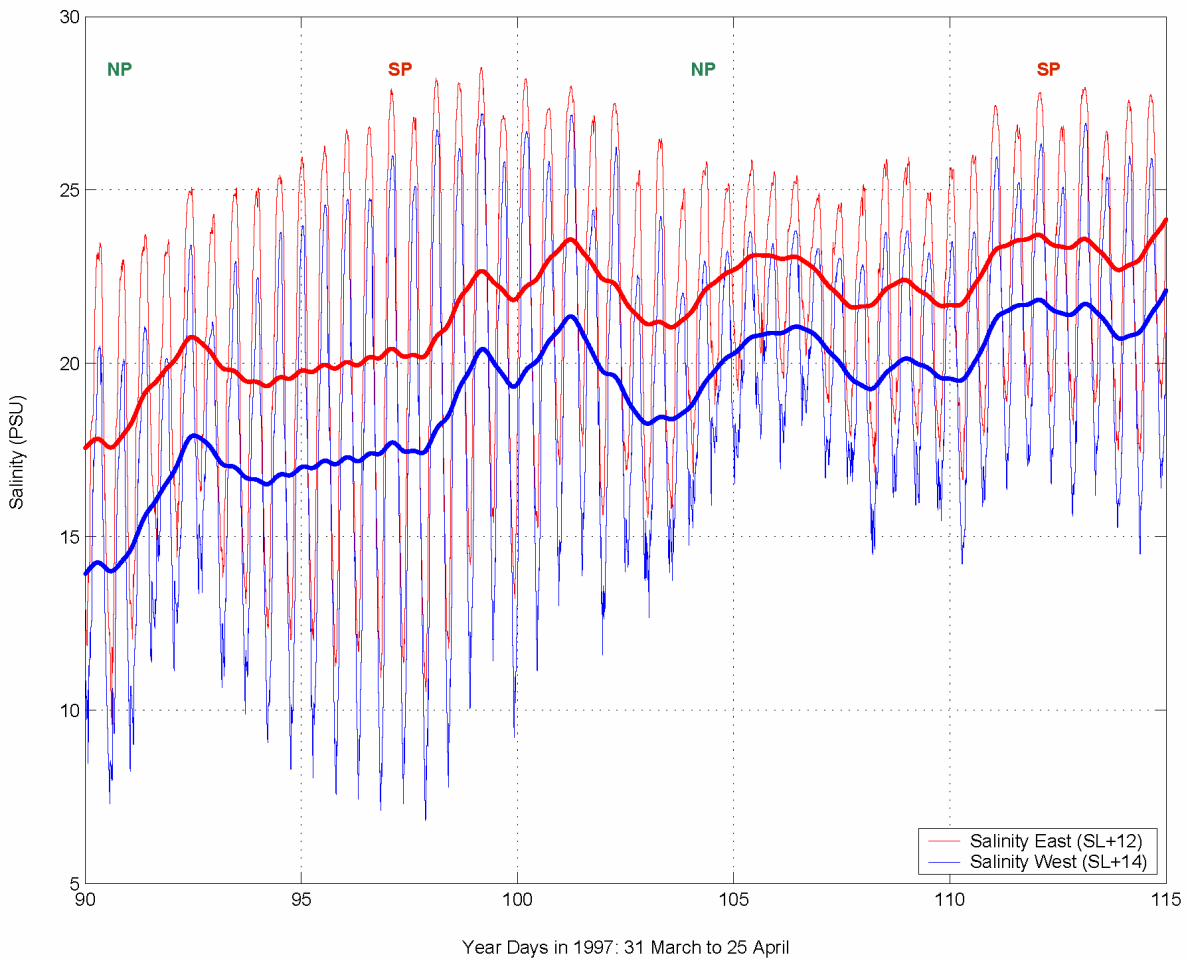

Figure 5.3: Salinity time series for the March – April 1997 LMER 4 field survey. The 40-hour low pass signature is plotted on top of the surface salinity data for each mooring location east and west of the anchor station location at river kilometer 13, respectively. River discharge ranged from 63 m^3 s^{-1} at the beginning of this field campaign to 7 m^3 s^{-1} at the end. Neap and spring tides are indicated by NP and SP, respectively.

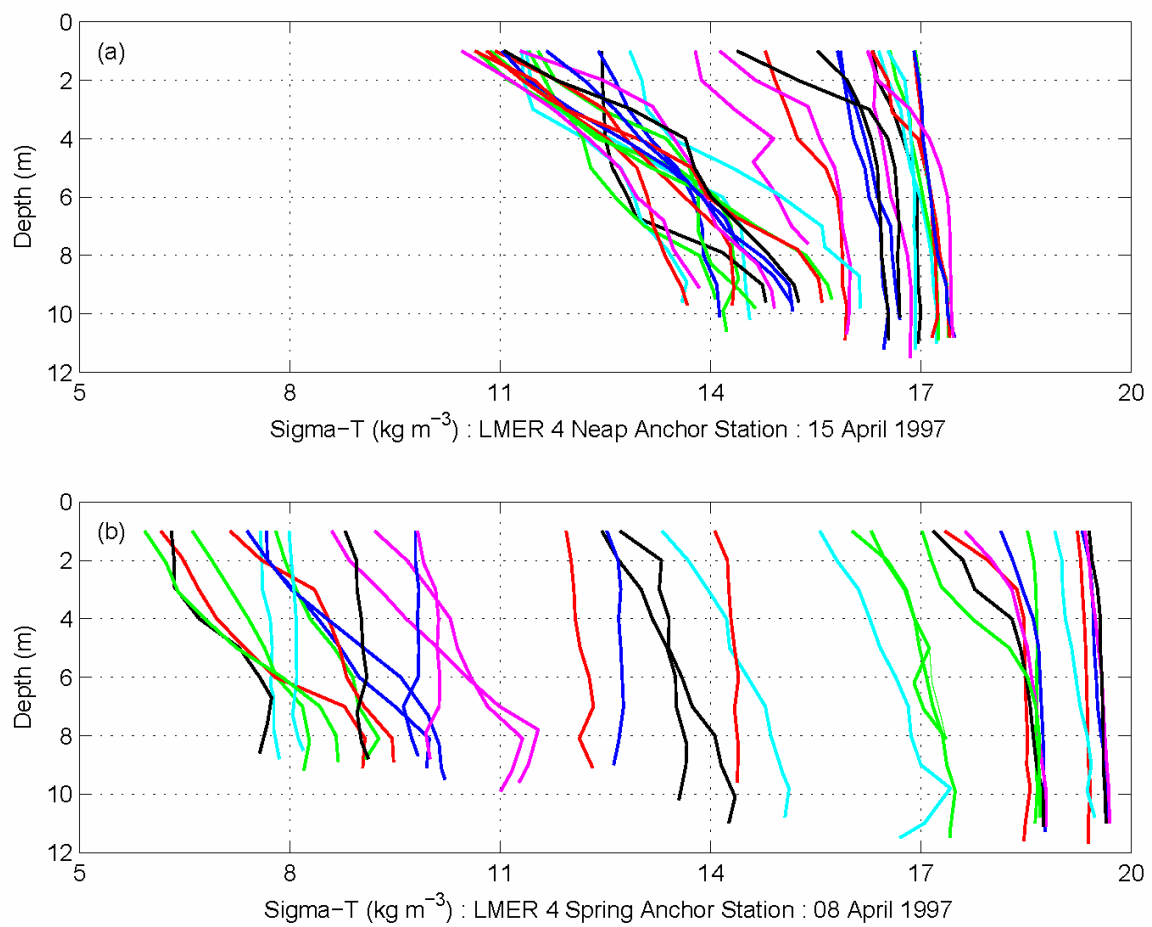

Figure 5.4: (a) Density profiles taken during the neap LMER 4 anchor station. The maximum vertical density difference observed during the neap anchor station was $\Delta\rho$ = 5.1 kg m^{-3}. (b) Corresponding density profiles taken during the spring LMER anchor station. The maximum vertical density difference observed during the spring anchor station was $\Delta\rho$ = 1.4 kg m^{-3}. The different colors represent individual casts.

Axial velocity profiles for the first neap and spring tide of the LMER 4 experiment are shown in Figure 5.5. Velocity shear during ebb tides (red in Figure 5.5) was fairly uniform over the depth for both neap and spring tides, while the velocity shear during flood tides (blue in Figure 5.5) was more variable in character. The highest velocity shear during flood tide was concentrated below approximately 4.5 meters for neap tide and was concentrated below approximately 4 meters for spring tide.

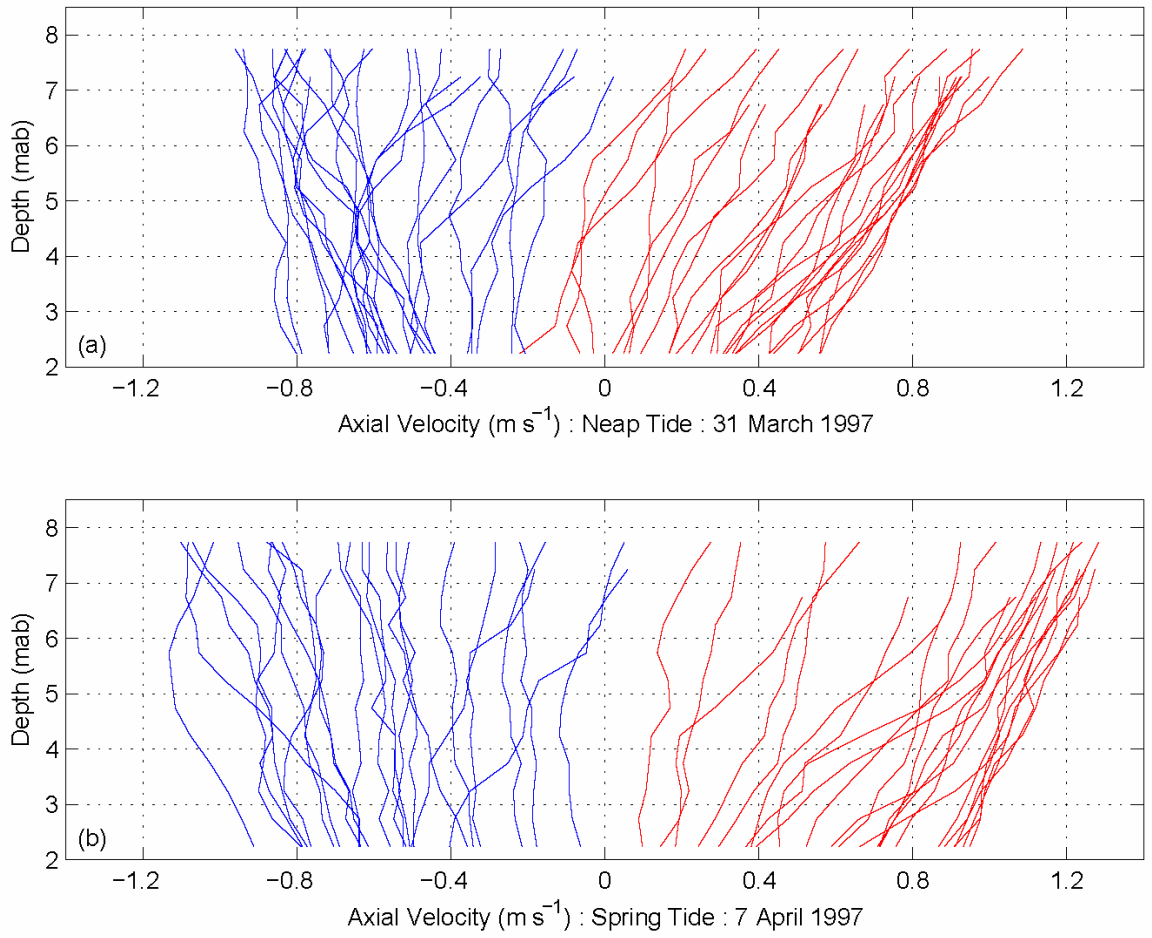

Figure 5.5: (a) Axial velocity profiles from the BB ADCP during the LMER 4 field experiment for (a) neap and (b) spring tides. Positive values indicate ebb flow and negative values indicate flood flow.

For clarity, a subset of along-channel and cross-channel velocity BB ADCP measurements taken during the March – April 1997 LMER 4 experiment are shown respectively in the upper and lower panels of Figure 5.6. A right-handed reference frame is used, where north and east are positive, to describe the BB ADCP data. In the upper panel, positive values indicated by red signify ebb flow (negative values signify flood flow) and in the lower panel, positive values similarly indicated by red signify flow to the outside of the channel bend (negative values indicated by blue signify flow to the inside

of the channel bend). The timing of neap and spring tides are indicated by NP and SP, respectively, below each panel. Note that the scale of the axial velocity is ±1.00 m s^{-1} and the scale of the lateral velocity is ±0.25 m s^{-1}. At times, the lateral velocity is 25% of the axial velocity, larger than the 10% of the axial flow field that is commonly assumed (Geyer 1993; Chant 2002; Lerczak and Geyer 2004). From scale estimates in Chapter 3, channel curvature was determined to be the primary mechanism for driving secondary flow in the Satilla River. The effect of centrifugal acceleration on acoustic current data is illustrated by the lateral velocity in the lower panel of Figure 5.6. Flow is directed to the outside of the channel bend in the near surface and is directed toward the inside of the channel bend at depth. The signature of secondary circulation is the strongest and most apparent during ebb tides (red in the near surface and blue in the near bottom) when both the axial velocity and the vertical shear of the axial current are at a maximum (Ott 2000; Blanton et al. 2002; Ott 2002). This pattern is consistent with tidal straining (Simpson et al. 1990), which acts to enhance vertical shear and stratification on ebbs and reduce vertical shear and stratification on floods.

The strength (speed) and character (direction and form) of secondary flow in Domain A during the LMER 4 experiment and changes in the signature of secondary circulation on the fortnightly time scale are illustrated in Figure 5.7. An initial observation of the transverse velocity profile (secondary flow) reveals a unique repetitive pattern (circled in Figure 5.7a between year days 91 and 93) that occurs near neap tides but does not occur near spring tides. In order to understand the nature of this signal, a Butterworth 40-hour low pass filter, to remove tidal variability, was applied to the transverse velocity profile at three levels: 3 mab, 5 mab, and 7 mab (shown as black lines

in Figure 5.7a). The subtidal results, from filtering out the tide, are shown in Figure 5.7b, where the green line indicates near surface flow, the blue line indicates flow at mid-depth, and the red line indicates near bottom flow for the LMER 4 experiment. Over the 31-day mooring deployment (Figure 5.7b), subtidal cross-channel flow near the surface was directed toward the outside of the bend (~ 0.030 m s^{-1}), as was the flow at mid-depth (~ 0.005 m s^{-1}), while the flow at depth was weak and oriented toward the inside of the bend (~ -0.005 m s^{-1}). This pattern is consistent with secondary circulation driven by channel curvature (centrifugal acceleration) and suggests the presence of a single secondary circulation cell that can locally mix throughout the depth of the water column. Over a fortnight, the subtidal signature of secondary flow at spring tide is similar to that induced by channel curvature and is approximately 50% larger than the 31-day average. At neap tide, the subtidal signature of secondary circulation is more complicated (Figure 5.7b). The subtidal signature of secondary flow at neap indicates that the near surface flow is weak, though still directed toward the outside of the bend, flow at mid-depth is toward the inside of the bend, and flow near the bottom is directed toward the outside of the bend. This pattern suggests the presence of two vertical circulation cells, each about one-half the depth of the water column. The uppermost cell (from 5 to 8 mab) has a circulation pattern consistent with flow around a channel bend, while the lowermost cell (from 2 to 5 mab) has a weak and occasionally opposing circulation pattern. Note it is not possible to explicitly state the circulation pattern below 2 m, because the BB ADCP cannot profile the entire water column. It is clear from Figure 5.7b (*cf.* mid-bin reversal around year days 92 and 104) that the signature (strength, direction, and form) of the secondary flow changes dramatically between neap and spring.

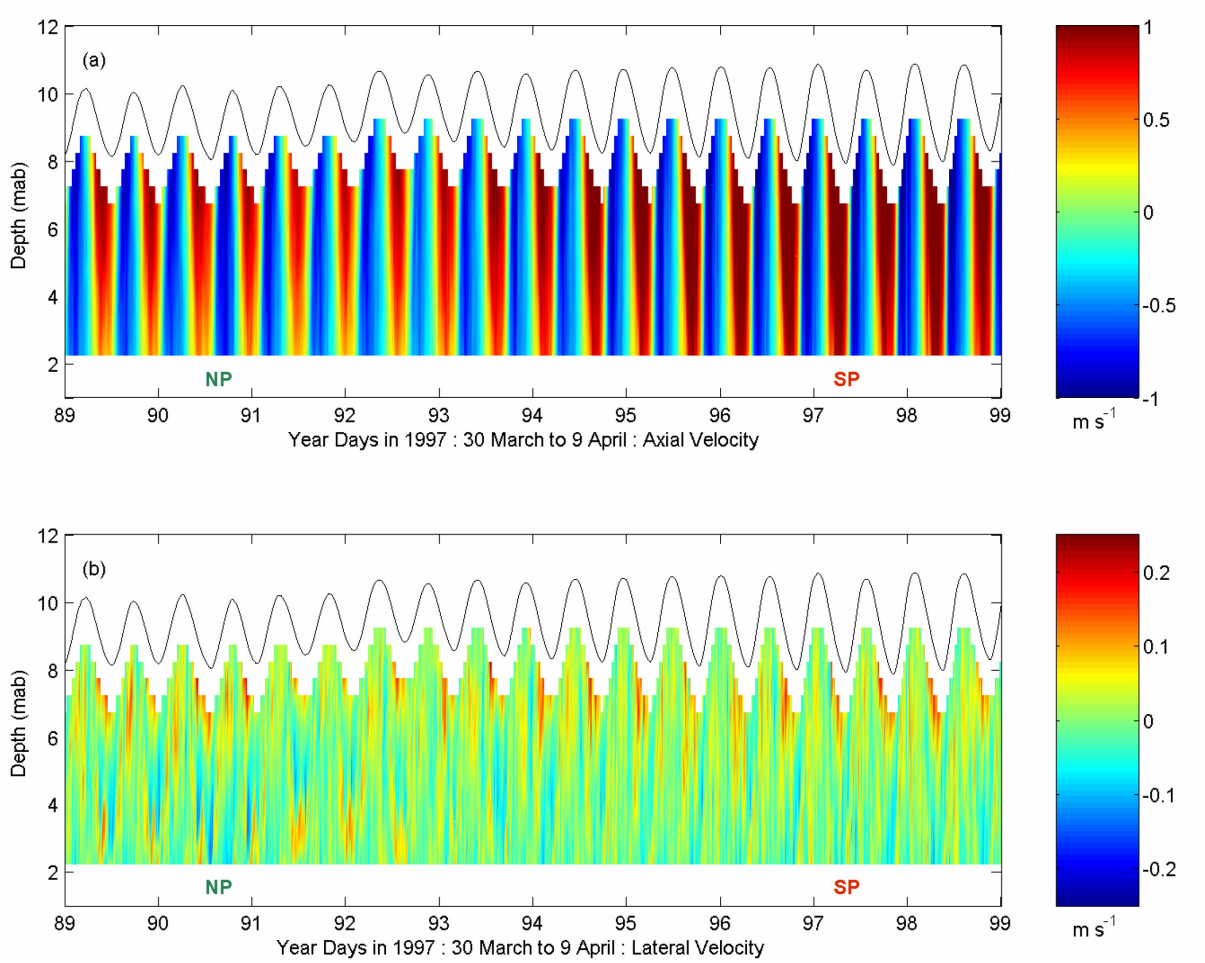

Figure 5.6: BB ADCP velocity measurements taken during the LMER 4 field experiment in the along-channel (a) and cross-channel (b) directions. Positive values in the along-channel velocity (a) indicate ebb flow, and negative values indicate flood flow. Likewise, positive values in the cross-channel velocity (b) indicate flow to the outside of the channel bend (to the north), and negative values indicate the flow to the inside of the bend (to the south). NP and SP indicate neap and spring tides, respectively.

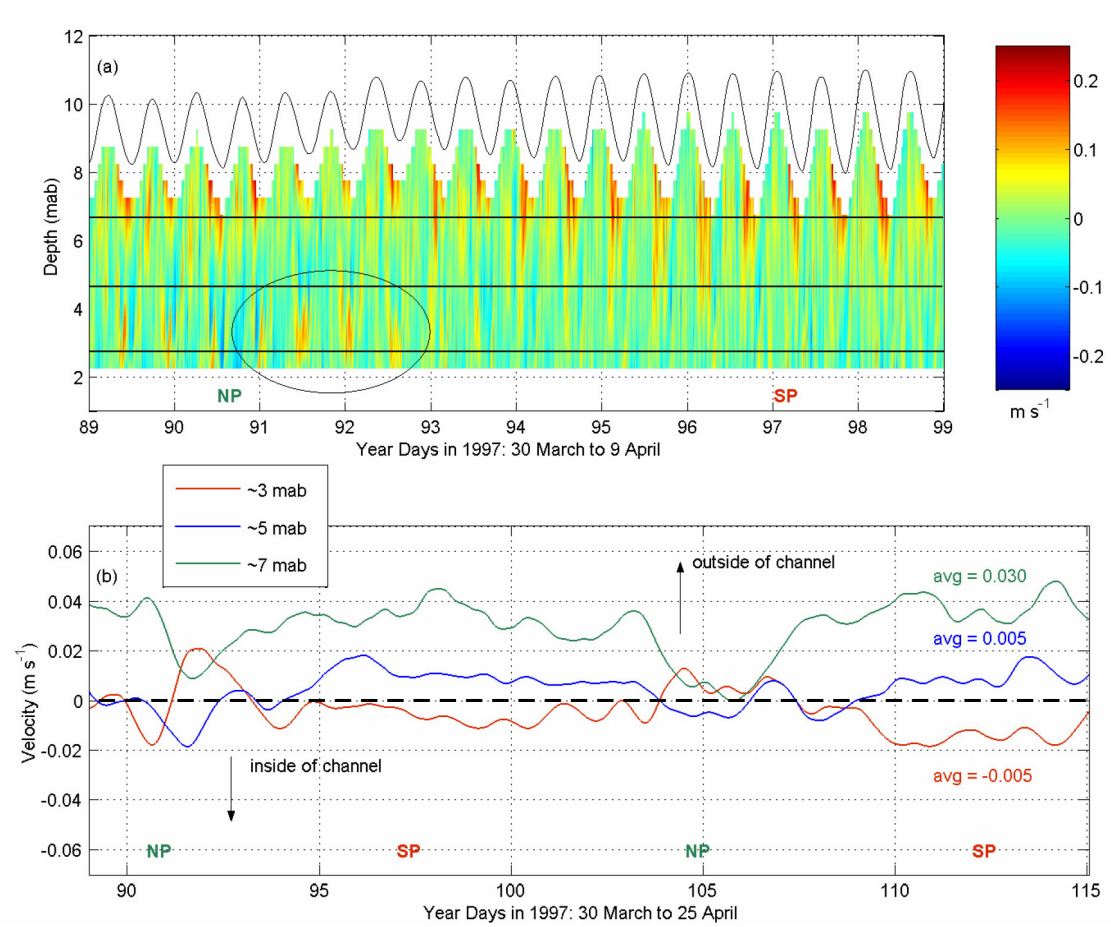

Figure 5.7: (a) Cross-channel velocity from BB ADCP measurements taken during the LMER 4 field experiment. Positive values indicate flow to the outside of the channel bend and negative values indicate flow to the inside of the bend. Note the section in the upper panel corresponds to a subset of the lower panel. (b) Results of a 40-hour low-pass filter applied to the lateral velocity at three levels (indicated by solid black lines in the upper panel). The three levels represent near bottom velocity (low bin ~ 3 mab), mid-depth velocity (mid bin ~ 5 mab), and near surface velocity (high bin ~ 7 mab). NP and SP indicate neap and spring tides, respectively.

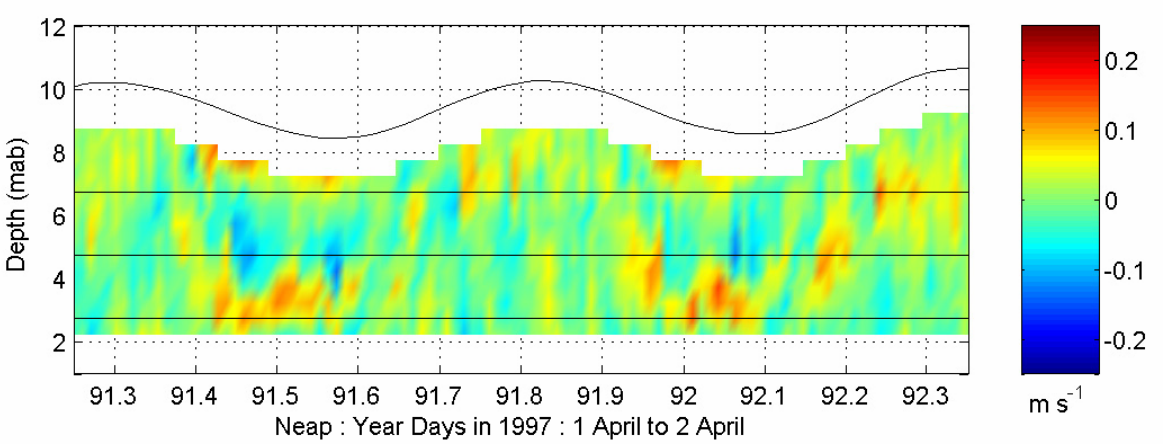

Figure 5.8: Lateral velocity data at the first neap tidal cycle during the LMER 4 experiment. Positive values indicate flow to the outside of the channel bend, and negative values indicate flow to the inside of the channel bend. A secondary flow driven by channel curvature is directed toward the outside of the channel bend (red) in the near surface, and toward the inside of the bend (blue) in the near bottom. Note the presence of two stacked secondary cells from year days 91.4 to 91.6 and from year days 91.9 to 92.1.

The results of additional analysis on the tidal and subtidal lateral velocity data over a series of shorter time periods (individual neap and spring cycles, ebb and floods, and maximum ebb and maximum flood conditions) suggest that the lower 'second cell' is generated during the ebb phase of the neap tide when tidal straining amplifies the vertical density gradient (Simpson et al. 1990). The appearance of the lower cell in the tidal lateral velocity data is illustrated by Figure 5.8. During the ebb phase of the neap tide, the lowermost cell of the two-cell configuration appears to grow vertically, which in turn reduces the mixing depth of the uppermost curvature driven cell. The stacked cell configuration may still be present through the early flood phase of the neap tide until the interface between the two cells is eroded. The strength and duration of the lowermost cell in the neap tide two-cell circulation pattern, as noted by the magnitude and duration of the positive low bin velocity in Figure 5.9b (1.4 days compared to 0.6 days) and by the

closed contours between 2 and 4 mab in Figure 5.9b (1.8 days compared to 1.2 days), appear to decrease with an observed decrease in river discharge. As shown in Figure 5.9a, the river discharge during the LMER 4 experiment decreased from approximately 60 m^3 s^{-1} during the first neap tide (year day 91, 1 April 1997) to approximately 13 m^3 s^{-1} during the second neap tide (year day 105, 15 April 1997).

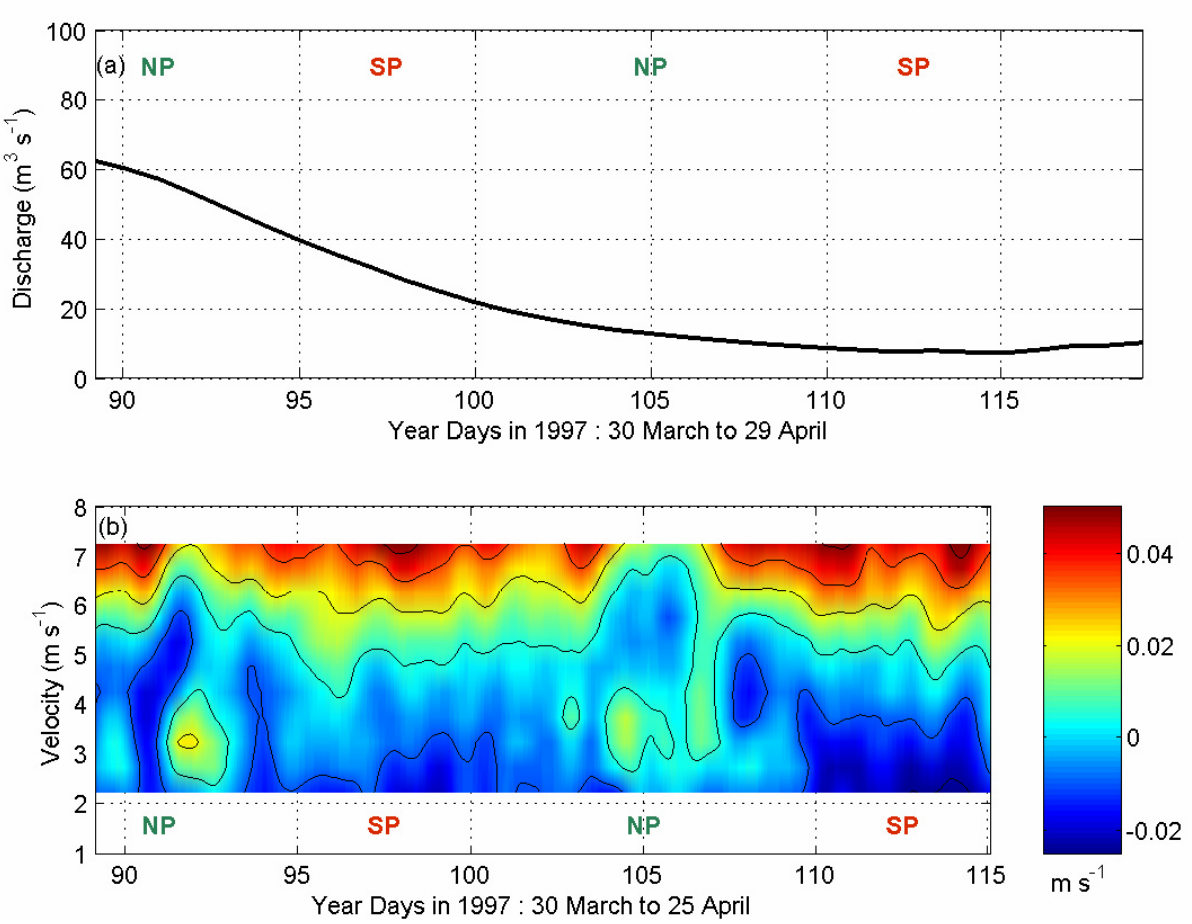

Figure 5.9: (a) The Satilla River daily mean discharge during the LMER 4 experiment. (b) Subtidal cross-channel velocity (secondary flow) during the LMER 4 mooring deployment. Positive values (red) show flow to the outside of the bend, and negative values (blue) show flow to the inside of the bend. Note the difference in the strength and duration (1.8 days compared to 1.2 days) of the lowermost secondary cell at year days 92 and 105.

5.3.2 Internal Froude Number Calculations

A first-order indicator on the importance of stratification to the observed neap-to-spring changes in the BB ADCP data is determined from internal Froude number calculations, Fr_i^2, where

$$Fr_i^2 = \frac{\overline{U_s^2}}{g'h} \quad \textbf{(5.2)}$$

in which $\overline{U_s}$ is the streamwise depth-average velocity, g′ is reduced gravity, and h is the water depth. The maximum vertical density differences observed during the neap ($\Delta\rho_z$ = 5.1 kg m^3) and spring ($\Delta\rho_z$ = 1.4 kg m^3) anchor stations (Figure 5.4) and an ambient reference density of ρ_o = 1014 kg m^3 were used to calculate reduced gravity values, g′, respectively, at neap (g′ = 0.049 m s^{-2}) and spring (g′ = 0.014 m s^{-2}) tides. Likewise, the value of $\overline{U_s}$ was calculated for both neap and spring tides using the moored BB ADCP at Station B (*cf.* Figure 5.2). From the g′ calculations and using h = 10 m, a calculated $\overline{U_s}$ = 0.64 m s^{-1} for neap tides, and $\overline{U_s}$ = 1.04 m s^{-1} for spring tides, respectively give a Fr_i^2 estimate of 0.84 at neap and a Fr_i^2 estimate of 7.73 at spring. This suggests that the stabilizing effects of vertical stratification are dominant at neap tides and the destabilizing effects of shear are dominant at spring tides.

Because Fr_i^2 varies over a tidal cycle, an alternative way to understand these results is to determine the bounds on the depth-average axial velocity that give a critical internal Froude number, Fr_i^2 = 1. The bounds on $\overline{U_s}$ can be calculated from a rewritten form of Equation 5.2 as follows:

$$\sqrt{\left(Fr_i^2\right)g'h} = \overline{U_s} \quad \textbf{(5.3)}.$$

Using Equation 5.3, setting $Fr_i^2 = 1$, and using the values of g′ and h as given above, yields $\overline{U_s} = \pm 0.7$ m s^{-1} for neap tides and $\overline{U_s} = \pm 0.37$ m s^{-1} for spring tides which are shown as thick gray lines, respectively, in the upper and lower panels of Figure 5.10. The depth-average axial currents for the neap (15 April 1997) and spring (8 April 1997) anchor stations are super-imposed as thick blue lines in the upper and lower panels of Figure 5.10.

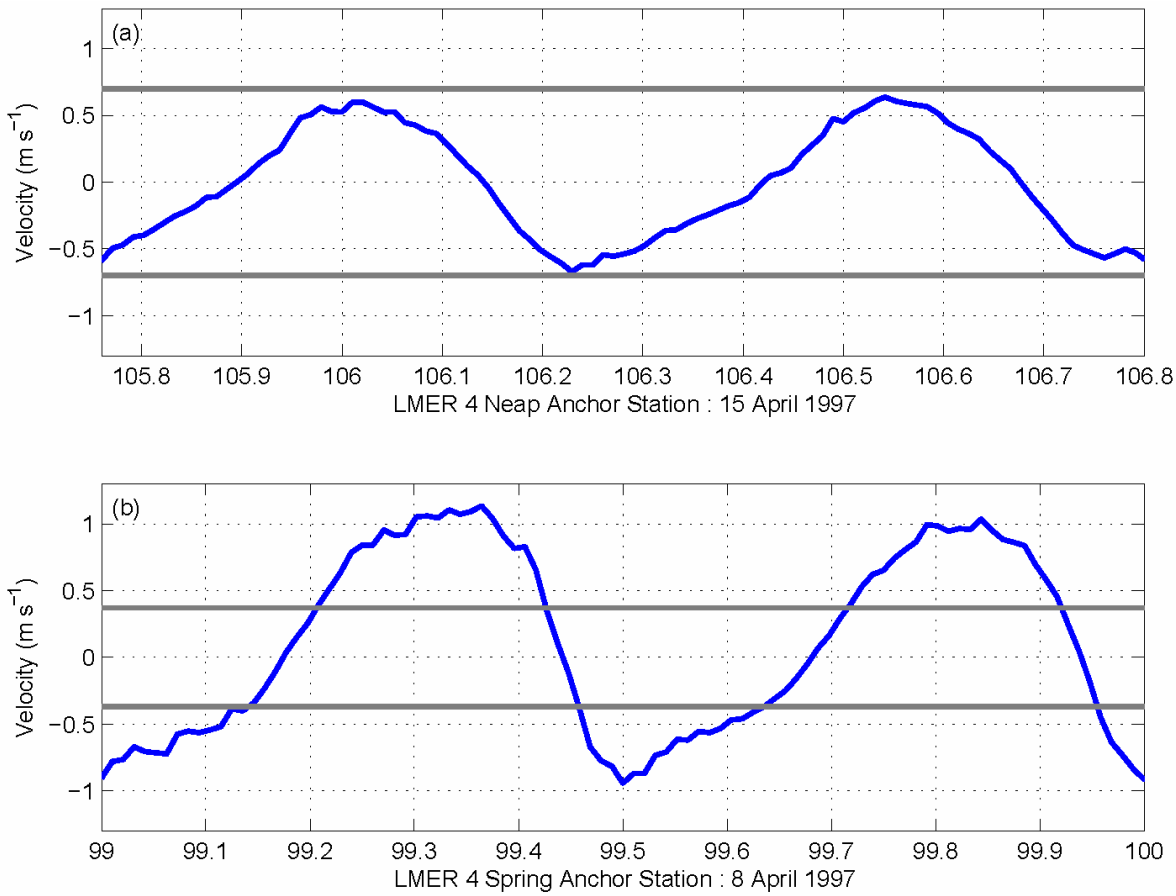

Figure 5.10: Plot of the critical Fr_i limits and depth-average axial current during the LMER 4 neap anchor (a) and the LMER 4 spring anchor (b). Note that the region between the thick gray lines corresponds to $Fr_i^2 \leq 1$ and is derived from the measured density profiles and the axial current at neap (a) and spring (b), respectively.

If the depth-average axial velocity is within the subcritical Fr_i^2 range ($Fr_i^2 \leq 1$), the stabilizing effect of vertical stratification dominates the destabilizing effect of vertical shear, suggesting that the local vertical salinity gradient could halt the secondary circulation due to shear effects. Results plotted in Figure 5.9 show that the neap depth-average axial velocity was within the required bounds, in contrast to the spring velocity, which transitioned too quickly through the subcritical range for local stratification effects to modify the secondary circulation. While the Fr_i^2 is a useful estimate on the potential impact of changes in fortnightly stratification on secondary flow, it can only determine favorable, not sufficient, conditions for such interactions.

5.3.3 Seim and Gregg Curvature-Induced Overturning Model

The Seim and Gregg (1997) curvature-induced overturning model provides a rigorous approach to evaluating the interaction between the depth-varying lateral baroclinic gradient and the barotropic curvature-induced secondary flow. As discussed in Chapter 3, this model is based on a steady-state balance between centrifugal acceleration and the tidally-generated lateral baroclinic density gradient in a channel bend. In a curved reach, this model determines the minimum axial velocity necessary to overcome the lateral baroclinic density gradient and mix the water column by turbulent exchange. It is expressed by

$$\overline{u_s^2} \geq \frac{1}{\alpha}\frac{R}{B}g'h \quad \textbf{(5.4)}$$

where $\overline{u}_s$ is the depth-average streamwise velocity, R is the local radius of curvature, B is the channel width, g′ is reduced gravity, h is the depth of the *thalweg*, and

$$\alpha = \left(u_s^2 - \overline{u_s^2}\right) / \overline{u_s^2} \quad \textbf{(5.5)}$$

is a measure of the vertical shear, which is based on the deviation between the maximum and depth-average axial current.

Plots of α (alpha) calculated from Equation 5.5 for neap and spring tide are shown in Figure 5.11. Peaks in α are seen starting near maximum ebb and lasting until just after low water during both neap and spring tides. At neap, the peaks in α (upper panel in Figure 5.11) vary between ~ 0.3 and ~ 0.8 and have an average peak value of ~ 0.55. At spring, the peaks in α (lower panel in Figure 5.11) appear to have a larger range between ~ 0.35 to nearly 1.5. Excluding the peak value of 1.5 between year days 97.75 and 98, the average peak value of α at spring is ~ 0.48, which is slightly lower than the observed α at neap.

Using the α values from Figure 5.11 (α = 0.55 for neap and α = 0.48 for spring), $g' = 0.049$ m s^{-2} and $g' = 0.014$ m s^{-2}, for neap and spring tides respectively, and the average values of R, B, and h for the Satilla River (R = 1250 m, B = 400 m, and h = 10 m), the *minimum axial overturning velocity,* $\overline{u}_{s,over}$ *,* was calculated from Equation 5.4 to be 1.67 m s^{-1} at neap and 0.95 m s^{-1} at spring. The *maximum observed axial velocity*, u_s, at neap was 0.6 m s^{-1} (*cf.* Figure 5.10a) which suggests that the combination of a strong vertical density gradient and weak axial current can halt part or all of the curvature-induced secondary circulation. Likewise, the *maximum observed axial velocity,* u_s, at spring was 1.1 m s^{-1} (*cf.* Figure 5.10b) which suggests that the axial current was sufficient to overcome the weaker vertical density gradient and mix the water column from top to bottom.

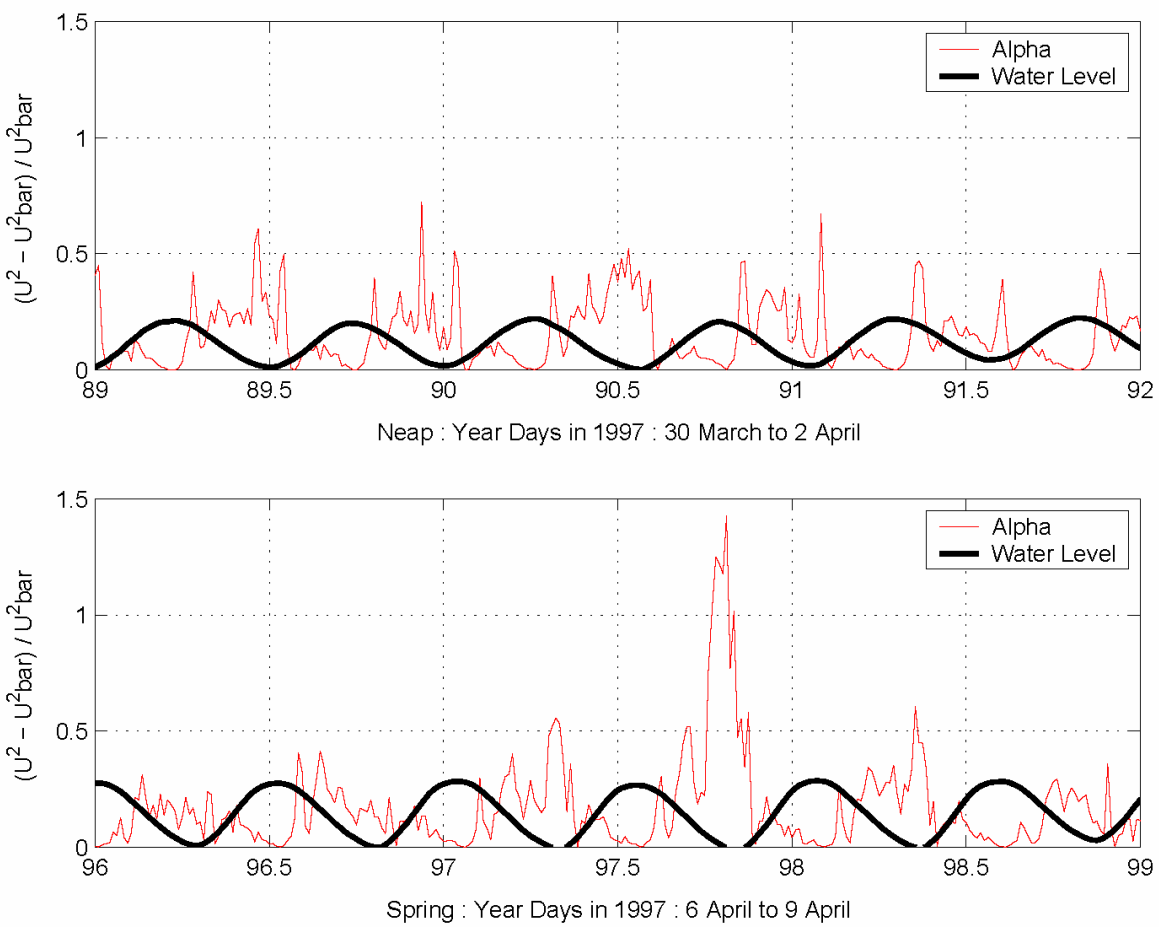

Figure 5.11: (a) A plot of alpha, a measure of the vertical shear in the axial current, during LMER 4 neap tide. (b) A plot of alpha during LMER 4 spring tide. The water level is indicated by a solid black line in both the upper and lower panels.

As previously mentioned, in Chapter 3, the strength of the secondary circulation is sensitive to several factors, one of which is the depth-varying lateral baroclinic pressure gradient. If there is sufficient vertical stratification, it is possible for the lateral baroclinic pressure gradient to temporarily shut down part or all of the barotropic curvature driven transverse circulation. This mechanism would explain the presence and variable size of the uppermost circulation cell as observed in the BB ADCP data (Figure 5.9b). The presence of the lowermost cell may be due to internal adjustments of the density field

(Chant 2002; Seim et al. 2002) or to the downstream advection of an eroding upstream secondary circulation pattern (Hey 1984; Kalkwijk and Booij 1986; Nelson and Smith 1989). The necessary vertical stratification to halt secondary circulation driven by centrifugal acceleration can be determined from an alternate expression of Equation 5.4. Rearranging Equation 5.4 and expressing reduced gravity in its full form as

$$g' = g\Delta\rho_z / \rho_o \quad \textbf{(5.6)}$$

in order to solve for $\Delta\rho_z$ or the minimum vertical density difference to balance centrifugal acceleration gives

$$\Delta\rho_z \geq \overline{u_s^2}\,\alpha \frac{\rho_o}{gh}\frac{B}{R} \quad \textbf{(5.7)}.$$

At neap tide, assuming $\overline{u}_s$ = 0.64 m s^{-1}, α = 0.55, ρ_o = 1014 kg m^{-3}, B = 400 m, g = 9.81 m s^{-2}, h = 10 m, and R = 1250 m; the minimum $\Delta\rho_z$ sufficient to shut down curvature driven secondary flow is calculated to be 0.75 kg m^{-3} (~ 0.96 PSU). Similarly, at spring tide, assuming $\overline{u}_s$ = 1.04 m s^{-1}, α = 0.48, g′ = 0.014 m s^{-2}, and h, R, and B are as given above; the minimum $\Delta\rho_z$ necessary to shut down secondary flow by channel curvature is calculated to be 1.97 kg m^{-3} (~ 2.54 PSU).

It is clear, in comparison with the observed vertical density profiles (*cf.* Figure 5.4) and the calculated results of Equation 5.7 that the lateral baroclinic pressure gradient is sufficient to halt curvature-induced secondary flow at neap (calculated $\Delta\rho_z$ = 0.75 kg m^{-3} and observed $\Delta\rho_z$ = 5.1 kg m^{-3}), but seldom at spring (calculated $\Delta\rho_z$ = 1.97 kg m^{-3} and observed $\Delta\rho_z$ = 1.4 kg m^{-3}). This result implies that during neap tides, mixing in the lower half of the *thalweg* can be reduced, if not halted, by the interaction of

the baroclinic vertical density gradient and the barotropic centrifugal acceleration, thereby maintaining a coherent density structure in the deep channel throughout the channel bend and for potentially longer than a tidal cycle. The coherent density structure could be maintained until it encounters changes in flow speed or direction (due to variations in the speed or direction of the axial current, rapidly changing bathymetry, increased bottom friction, or flow modifications at an inflection point between channel reaches) as it approaches the next channel bend.

The structure of the curvature driven secondary flow in the study area fluctuates fortnightly between a classical single cell configuration at spring to a more complicated stacked double-cell configuration at neap. Daily discharge data and BB ADCP observations of other neap-spring pairs during the LMER 4 experiment suggest that the lower cell in the double-cell configuration weakens as the vertical salinity gradient approaches the minimum vertical density difference to halt curvature driven secondary flow or when there is a decrease in freshwater input to below 20 $m^3 s^{-1}$ (Figure 5.9). The observed correspondence between a decrease in river discharge and a weakened vertical salinity gradient is supported by other recent estuarine studies (Dyer 1997; Ott 2002). As freshwater input decreases, the axial salinity gradient decreases, this in turn, reduces the lateral and vertical salinity gradients, leading to unrestricted mixing by curvature driven secondary circulation.

At neap, the uppermost circulation cell is driven by channel curvature while the lowermost cell may be due to either internal adjustments of the density field by lateral seiching (Chant 2002; Seim et al. 2002) or the downstream advection of an eroding secondary circulation cell (Hey 1984; Kalkwijk and Booij 1986; Nelson and Smith 1989).

In an effort to determine the likelihood that lateral seiching or downstream advection generates the observed lower cell, a comparison is made between the advective time scale, T_{adv} (Geyer 1993) and the lateral seiche time scale, T_{seiche} (Chant 2002). As discussed in Chapter 3, the advective time scale is given by the expression

$$T_{adv} = \frac{L_s}{\overline{u}_s \Delta u_n} \quad \textbf{(5.8)}$$

where L_s is the length scale of the axial flow field, $\overline{u}_s$ is the depth-average streamwise velocity, and Δu_n is the change in the normal (lateral) velocity over the distance L_s (Geyer 1993). The lateral seiche time scale is given by the expression

$$T_{seiche} = \frac{2B}{\sqrt{g'h}} \quad \textbf{(5.9)},$$

and not surprisingly, it is twice T_{bc}, the baroclinic adjustment time. In Equation 5.9, the variable B is the channel width, g′ is reduced gravity, and h is the *thalweg* depth. Calculating T_{adv} and T_{seiche} from observational data, assuming L_s = 1500 m, Δu_n = 0.25 m s^{-1}, B = 400 m, h = 10 m, and g′ = 0.049 m s^{-2} and $\overline{u}_s$ = 0.64 m s^{-1} for neap and g′ = 0.014 m s^{-2} and $\overline{u}_s$ = 1.04 m s^{-1} for spring tides respectively, yields $T_{adv} \approx 96$ minutes and $T_{seiche} \approx 19 - 36$ minutes for respective neap and spring tide conditions. From these estimates, it is likely that the lower cell at neap is generated by lateral seiching in response to the relaxation of the lateral density gradient during a shift from ebb to flood tides. BB ADCP observations (*cf.* Figures 5.7a and Figure 5.8) demonstrate that the lower cell persists from ebb to early flood, and that the lower cell is generally oriented in the same direction as the upper cell and not ‘backwards’ (as would be an eroding upstream cell) supporting the lateral seiche conclusion. Furthermore, observations by

Seim et al. (2002) of wave-like features in the bottom salinity measurements at this location just after low water reinforce the idea that the lower cell is due to lateral seiching in response to the relaxation of the pycnocline between ebb and flood.

Observed changes in the strength and duration of the local lower secondary cell are likely due to changes in the lateral seiche time scale, T_{seiche}, which increases in response to reduced vertical stratification (*cf.* Equation 5.9). Seim et al. (2002) determined a water parcel would travel ~ 3 kilometers before completing one helical secondary circulation circuit. This length is twice the calculated streamwise length of the oscillating seiche,

$$L_{seiche} = \overline{u}_s T_{seiche} \quad \textbf{(5.10)},$$

at the study site during neap tide. Bends in the Satilla are roughly three to four kilometers apart, suggesting that the lower cell observed at neap tides during periods of strong vertical stratification is a local feature and could only be detected in nearby downstream bends within close proximity (1500 m). In addition, the weakening of the lower cell at neap from a decreased vertical salinity gradient or during decreased freshwater discharge, is likely the result of the difference in the time between tide reversals (~ 30 minutes from ebb to flood) and an increased seiche time (~ 50 minutes for weak stratification – 1 PSU difference in the vertical). The implication is that during spring tides or neap tides with weak vertical stratification, the tide reversal occurs more quickly than the lateral seiching, which reduces the longevity of the seiche and its communication of the lateral density gradient through the channel bend.

The difference in the secondary circulation structure between neap and spring tides is illustrated in Figure 5.12. Schematically, during neap (Figure 5.12a), the flow

entering a bend is stratified with the lightest water at the outside of the bend. Secondary circulation attempts to overturn the water column and is partially successful. Because the baroclinic pressure gradient increases with depth and the curvature driven secondary circulation is only effective in the upper water column, some of the vertical density gradient is retained as the water continues to flow around the bend. If no further mixing mechanisms are encountered (e.g., flow around an opposing bend, changes in bathymetry, changes in axial current speed) the flow will return as much as possible to its previous vertically stratified condition. Lateral seiching occurs in response to the adjustment process of the flow field trying to return to its previous stratified state. Correspondingly, during spring (Figure 5.12b), the flow entering a bend may or may not be partly mixed. In either case, the flow exceeds the minimum along-channel overturning velocity, mixes throughout the water column, and continues to flow around the bend in a nearly well-mixed state. It is important to note that the generation of lower cell at neap is a local feature and is independent of stratification conditions prior to the channel bend.

If secondary flow is the primary vertical mixing mechanism and it becomes limited or halted, the amount of momentum and salt flux may be locally higher in the channel cross-section than would be otherwise predicted. In this way, secondary circulation can significantly affect the local flux of salt and momentum by increasing the amount of each that is retained or 'trapped' (i.e., not mixed) at channel bends. Understandably, the effect of secondary circulation cannot be neglected when trying to understand the distribution and dispersion of salt and momentum in an estuary.

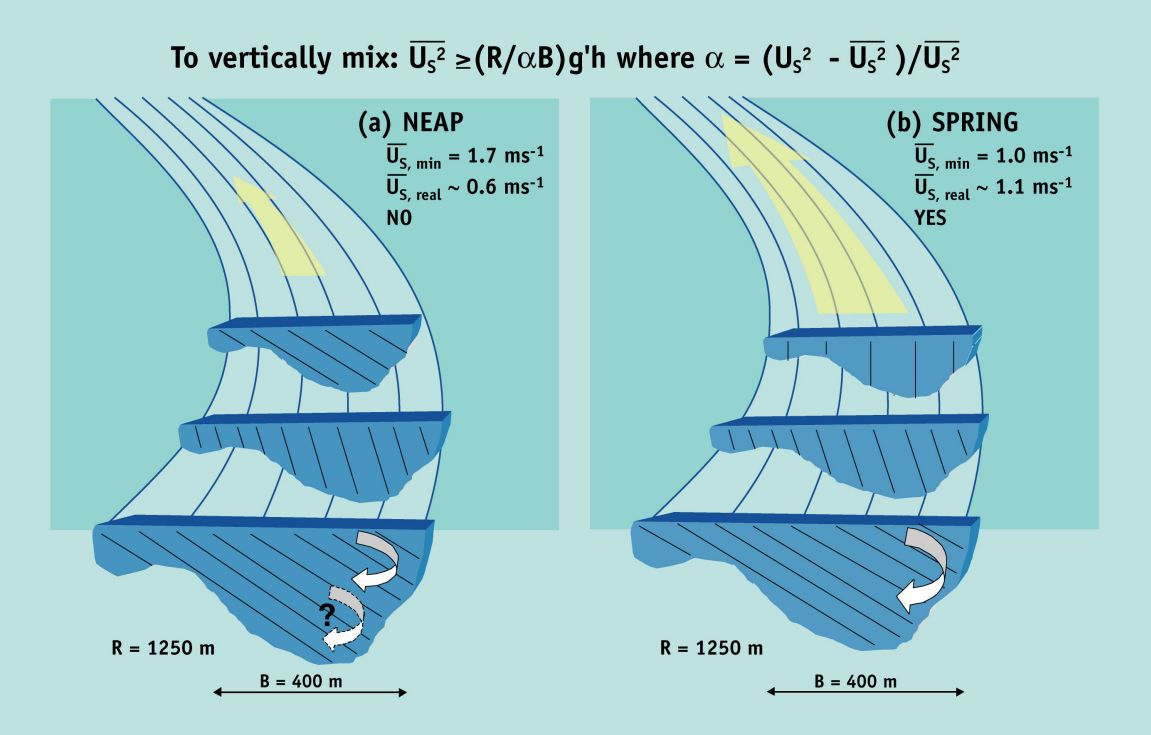

Figure 5.12: An illustration of the hypothesized secondary circulation mixing mechanism around a channel bend at neap (a) and at spring (b). The minimum axial current necessary to vertically mix the water column (Seim and Gregg 1997) and the maximum observed axial current are respectively given to the right of each illustration.

5.4 Conclusions

This chapter demonstrates that the strength of the mechanisms that drive secondary flow in a stratified channel bend can be modulated on the fortnightly cycle in response to changes in the axial current speed, the lateral baroclinic gradient, neap-to-spring variations in salinity, and freshwater discharge. Acoustic current meter data can be used to directly observe and quantify the strength and the direction of curvature-induced secondary circulation. Secondary circulation in the first major bend of the Satilla River is consistent with flow due to channel curvature except possibly at neap tides when

the shear of the along-channel flow is too small to overcome the cross-channel baroclinic pressure gradient force.

Seim and Gregg (1997) provide a simple method for estimating the critical along-channel flow velocity necessary below which secondary flow due to channel curvature can be halted, by quantifying the contribution of the axial current to the strength of the centrifugal acceleration. The Seim and Gregg (1997) curvature-induced overturning model was used to demonstrate that conditions necessary to limit or halt curvature-induced secondary flow at the study site in the Satilla River, Georgia, can be met near neap tide for up to two days but do not occur at spring tide (Figures 5.9b and 5.10). The implications of these model results suggest that the density structure characteristics at neap tide could be maintained around a channel bend, potentially longer than a tidal cycle, until either the mixing properties (e.g., river discharge, bottom topography, flow separation) change or another bend is encountered, leading to an unexpected local increase in salt and/or momentum. Secondary circulation can act as a 'trapping' mechanism (i.e., it can effectively limit vertical mixing to the upper half of the water column) during neap tide when the vertical salinity difference is sufficient ($\geq$ 1 PSU) and axial current is weak (≤ 0.65 m s^{-1}).

The character of the secondary circulation pattern at the channel bend study site alters between a single circulation cell at spring to a stacked two-cell configuration at neap. The single cell configuration is due to curvature-induced secondary flow. Likewise, the uppermost cell of the two-cell configuration is due to curvature-induced secondary flow while the lowermost cell is generated by a relaxation of the pycnocline between ebb and flood tides (Figure 5.8). The strength and duration of the lowermost

cell in the two-cell configuration decreases in response to a decrease in the vertical salinity gradient or to a decrease in freshwater discharge (Figure 5.9). Furthermore, the observed correspondence between a decrease in river discharge and a weakened vertical salinity gradient is supported by other recent estuarine studies (Dyer 1997; Ott 2002). As freshwater input decreases, the axial salinity gradient decreases, this in turn, reduces the lateral and vertical salinity gradients, which can enhance mixing by secondary circulation.

Clearly, the mixing effect of secondary circulation cannot be neglected when trying to understand the balance of salt or momentum in an estuary. Further research must be done on detailed longitudinal and lateral data under different discharge conditions and in channel reaches of differing curvature to better understand the importance of secondary circulation in regulating vertical mixing. Furthermore, it is important to understand the mechanisms that regulate the strength, duration, and location of secondary circulation in order to clarify its role in local mixing. Knowledge of this role will better able us to predict important parameters such as the length of the salt intrusion and to determine the dispersion and distribution of various waterborne properties (e.g., larvae, sediment, and pollutants) in the estuarine environment.

6. COMPARISON OF SECONDARY CIRCULATION IN FOUR REACHES

6.1 Introduction

Transport and mixing of momentum and salt in an estuary varies in time and space due to river discharge, changes in tidal amplitude and phase, wind stress, and lateral mixing processes. Lateral mixing, a complex and poorly understood phenomenon, includes secondary processes such as transverse (or secondary) circulation. Secondary circulation or flow is a broad and often confusing term which is used to describe several mechanisms whose result is to vertically overturn the water column along the secondary (transverse) axis of a channel. Most commonly, an observed secondary flow can be attributed to channel curvature, domain size (the Coriolis effect), frictional effects of irregular channel bathymetry or geometry, and/or the interaction between the lateral shear of the axial current with the axial salinity gradient (the differential advection of density) associated with the tides.

A secondary circulation may be composed of one or more cells that can reduce or enhance local gradients. In the field, a physical manifestation of secondary flow is often observed as one or more foam lines down the longitudinal axis of an estuary. Depending on the strength of the secondary flow, the balance of momentum and salt can be significantly affected (Murray and Siripong 1978; Fischer et al. 1979; Kalkwijk and Booij 1986; Garvine et al. 1992; Wong 1994). Recent research has demonstrated that changes in axial velocity and fortnightly density structure can alter the strength and character of a secondary flow (Peters 1997; Chant 2002; Lerczak and Geyer 2004).

The results of Chapter 5 suggest that the balance of forces that regulate the strength and duration of secondary flow changes on the fortnightly tidal cycle. The objective of this chapter is to explore the transition in the balance of mechanisms responsible for generating observed transverse circulations in four physically different estuarine reaches. Specifically, the focus of Chapter 6 is to examine and quantify the observed secondary circulation in three opposing channel bends (concave – a bend to the north, convex – a bend to the south, and a narrow bend to the west) in combination with a straight reach during spring and neap tides under different discharge conditions. Time series in these four reaches, over two complete neap-spring cycles, are examined in order to identify the impact of changes in freshwater discharge and the impact of variations in channel curvature and bend orientation on the characteristics of secondary flow. These four cases are further divided into two groups based on the fortnightly tide condition (spring or neap) where the strength of secondary flow is evaluated relative to the ambient discharge conditions (moderate/normal and low).

6.2 Materials and Methods

6.2.1 Experiment Site and Environmental Conditions

The Satilla is a pristine and naturally sinuous shallow river whose headwaters originate in the sandy coastal plain of Georgia. Located near the Georgia/Florida border, the Satilla is a partially mixed estuary which experiences 1 to 2.5 meter range semidiurnal tides. Confined to a 120 mile segment of the coast, the Satilla offers a unique look at understanding the link between differing landscape characteristics, geologic setting, and flow rate. Axial currents at spring tide are on the order of 1 m s^{-1} to 1.5 m s^{-1} while axial currents at neap tide are weaker and vary between 0.3 m s^{-1} and

0.65 m s^{-1}. The Satilla has an average discharge of 78 m^3 s^{-1} (USGS 2004) but can vary from 0 to 150 m^3 s^{-1} over an annual cycle. A histogram of historical daily discharge data from 1931 to 2004 suggests that the extremes in river discharge for the Satilla are weakly periodic on a 25-year cycle. Fortnightly variations in the observed density structure in the Satilla River are primarily the result of changes in salinity.

Hydrodynamically, the Satilla is classified as an ebb-dominant estuary (Frey and Basan 1985). Here, an ebb-dominant estuary is defined as one in which the ebb phase of the tidal cycle is marked by higher current velocities and a shorter duration than the flood phase of the tidal cycle. Fortnightly and seasonal variations in currents and sediment flux also demonstrate the influence of an ebb-dominant hydrology (Nichols and Biggs 1985).

Bordered by extensive salt marshes, the Satilla is known as a 'blackwater' river due to the large amounts of decaying humic substances which produce tannic acids. A triple junction near river kilometer 26 divides the flow of the Satilla River between its main branch to the south and White Oak Creek (WOC), a tidal creek to the north. Upriver, beyond the triple junction at river kilometer 26, the Satilla is a nearly fresh river where mariculture (crawfish farms) and old rice plantations still thrive.

The main channel of the Satilla is marked by nine channel bends and two short straight reaches that extend from its mouth between Jekyll and Cumberland Islands to 38 kilometers upriver. The majority of these bends are broadly concave (bends to the north, radius of curvature ~ 1200 m) each followed by more sharp convex bends (to the south, radius of curvature ~ 800 m). The bends have a channel width between 200 – 500 meters and are roughly three to four kilometers apart, starting six kilometers from the ocean (0 km) and extending 33 kilometers upriver (Figure 6.1).

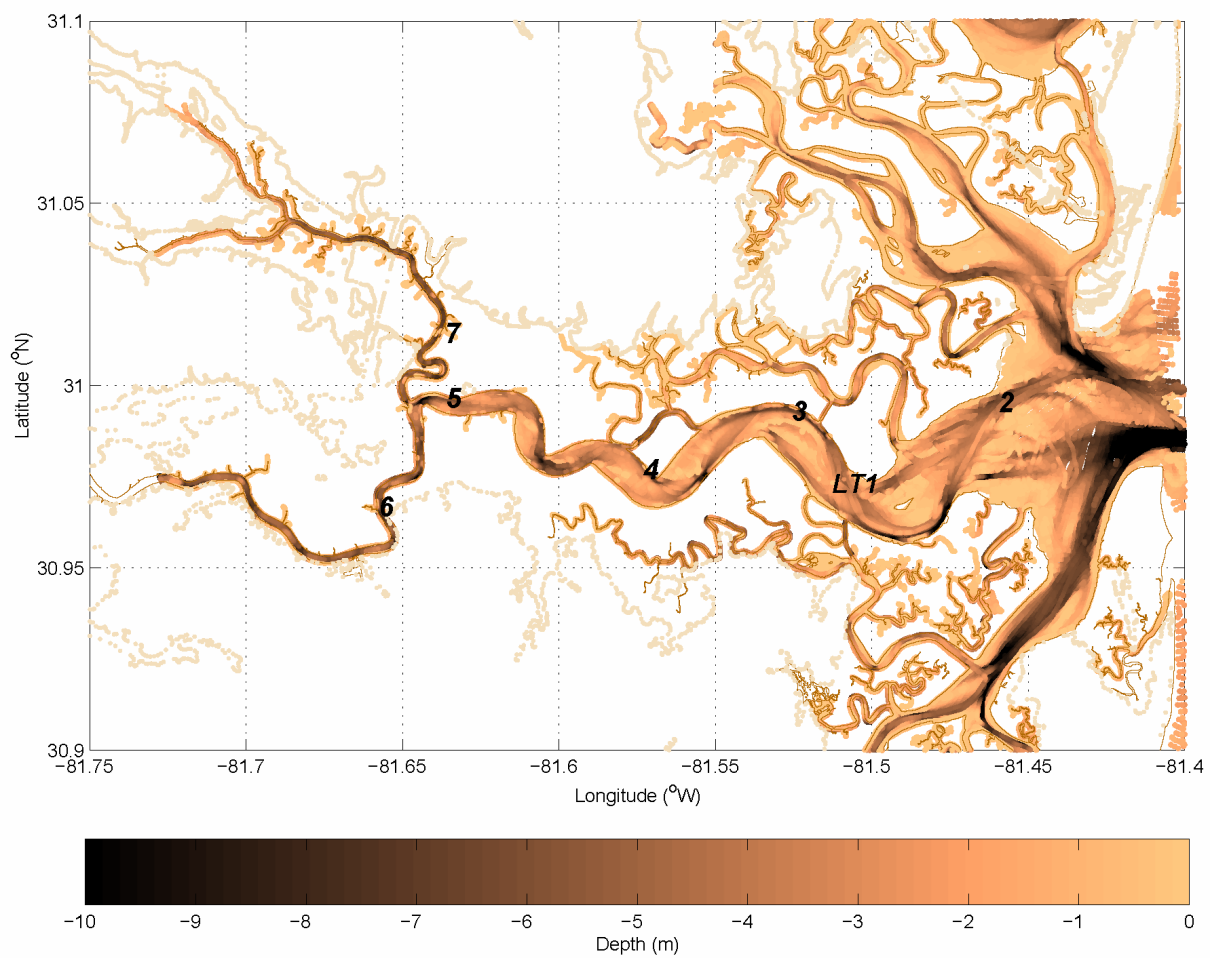

Figure 6.1: Map of the Satilla River in southeast Georgia near the Florida border. The mooring locations for the SAT 2 (September – October 1999) field survey are indicated by bold numbers 2 through 7. The LMER 4 mooring location (March – April 1997) corresponds with the SAT 2 Station 3. LT 1 refers to the long-term mooring (March 1999 – April 2000) near St. Andrews Sound. Darker colors indicate deeper depths.

This experiment focuses on the seasonal moorings, comparing high discharge conditions in the spring with low discharge conditions in the fall, in four particular reaches of the Satilla River with different curvature radii (R) and channel widths (B). The first reach, centered on Station 3, is a bend to the north (R ~ 1333 m, B ~ 292 m) located just past the Alternate IntraCoastal Waterway between 12 and 16 kilometers upriver from the estuary mouth at St. Andrews Sound. The second reach, centered on Station 4, is a bend to the south (R ~ 1375 m, B ~ 250 m) located upriver between river kilometers 16 and 20 and is adjacent to the Station 3 reach. Crows Harbor Reach, the reach centered on Station 5, is a relatively straight section (R ~ 2583 m, B ~ 271 m) of the Satilla and is located between 23 and 26 kilometers upriver of St. Andrews Sound. The last reach, centered on Station 6, is a bend to the west (R ~ 1250 m, B ~ 167 m) located adjacent to the Station 5 reach between river kilometers 28 and 32. This reach is situated on the main trunk of the Satilla River past the triple junction with WOC near Ceylon (*cf.* Figure 2.6).

Meteorological data from Kings Bay, Georgia (KNBQ) for the LMER 4 experiment period (26 March – 25 April 1997) show that the atmospheric conditions in the latter half of March 1997 were unusually warm and dry and were followed by an extended cold wet period throughout most of April 1997. There were 14 days (of the total 31-day period) during which haze and fog conditions were reported as significant (unusual) weather. Three major precipitation events occurred in March – April 1997: the first event occurred on April 7, 1997, the second occurred on April 23, 1997, and the third occurred near the end of April 1997. In the Satilla, the lag time for a precipitation

event to be recorded at the Fort Atkinson tidal gauge is about 20 days; and as a result, the effects of the first precipitation event were not observed during this study period.

Meteorological data from Brunswick, Georgia (091340) show that the atmospheric conditions during the SAT 2 experiment (8 September – 20 October 1999) were unusually warm and dry. Southern Georgia was under severe drought conditions in 1999 during which average daily temperatures were 6°C to 8°C above normal and average daily precipitation was less than a trace. The daily high temperature exceeded 32°C from 10 April 1999 through 27 October 1999, approximately two months longer than average conditions. Record-setting temperatures were reported starting in early June 1999 and lasted through late July 1999. Three major hurricanes, each associated with precipitation exceeding 22 millimeters, Dennis (August 30), Floyd (September 15), and Irene (October 15) affected coastal Georgia shortly before and during the SAT 2 experiment. The largest precipitation event (cumulative precipitation of 81 mm) associated with Hurricane Floyd was observed as a discharge event of 38 m^3 s^{-1} twenty days later on October 4, 1999, at the Fort Atkinson USGS gauging station and in the SAT 2 subtidal salinity and pressure fields of the mooring data. The SAT 2 experiment was ended early shortly after Hurricane Irene.

The 1997 LMER 4 and the 1999 Satilla SAT 2 experiments occurred, respectively, shortly before and during a period of extended drought for coastal Georgia. Average discharge conditions ranged from near normal at 80 m^3 s^{-1} during the LMER 4 experiment to significantly below normal at 15 m^3 s^{-1} during the SAT 2 experiment. Freshwater discharge varied substantially (almost 300 m^3 s^{-1}) shortly before and during the LMER 4 experiment. Discharge at the beginning of the LMER 4 mooring

deployment was approximately 63 m^3 s^{-1} and dropped to a low value of 7 m^3 s^{-1} by the end of 31-day sampling period (Figure 6.2a). The discharge at the beginning of the SAT 2 mooring deployment was around 3 m^3 s^{-1}, rose to nearly 40 m^3 s^{-1} in response to Hurricane Floyd in early October, and then dropped to 19 m^3 s^{-1} shortly before the end of the 42-day sampling period (Figure 6.2b).

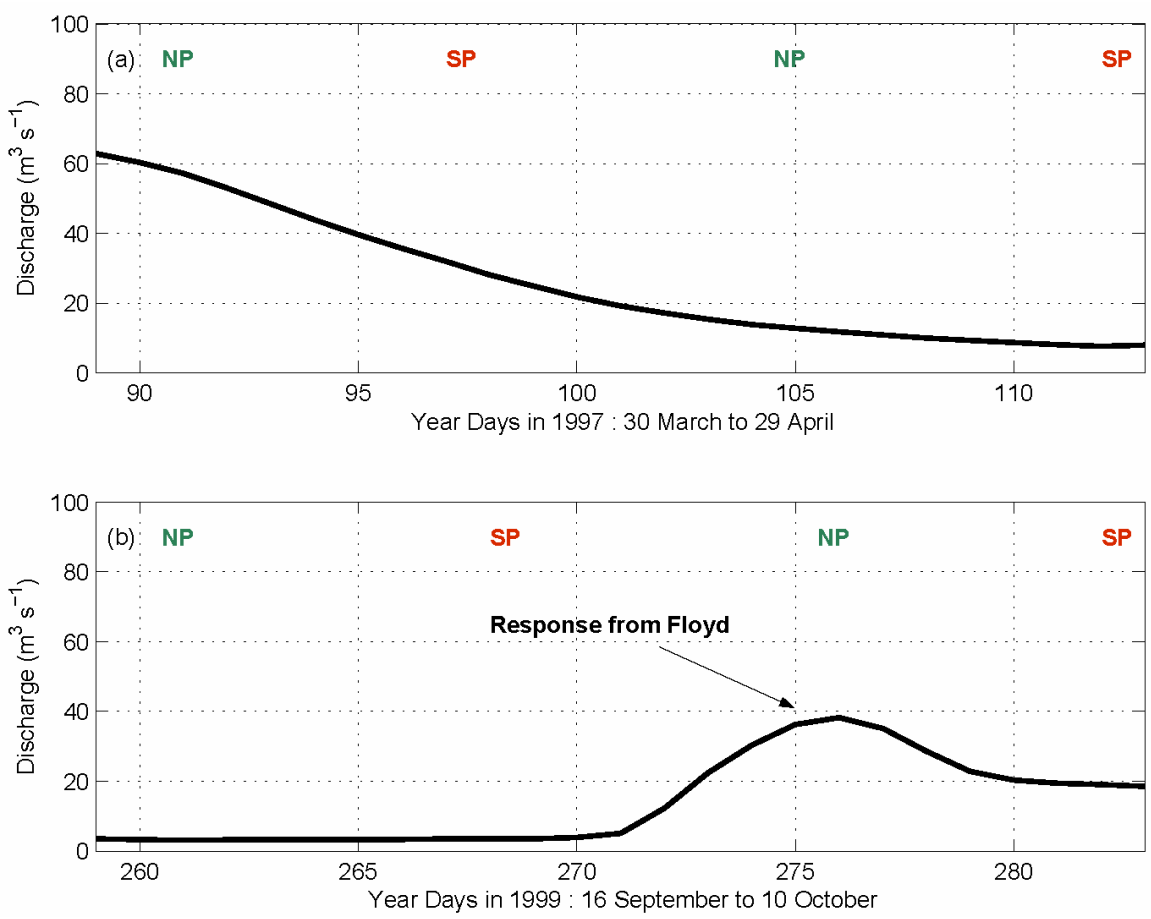

Figure 6.2: (a) The Satilla River discharge during the 1997 LMER 4 experiment. (b) The Satilla River discharge during the 1999 SAT 2 experiment. NP and SP respectively refer to neap and spring tides.

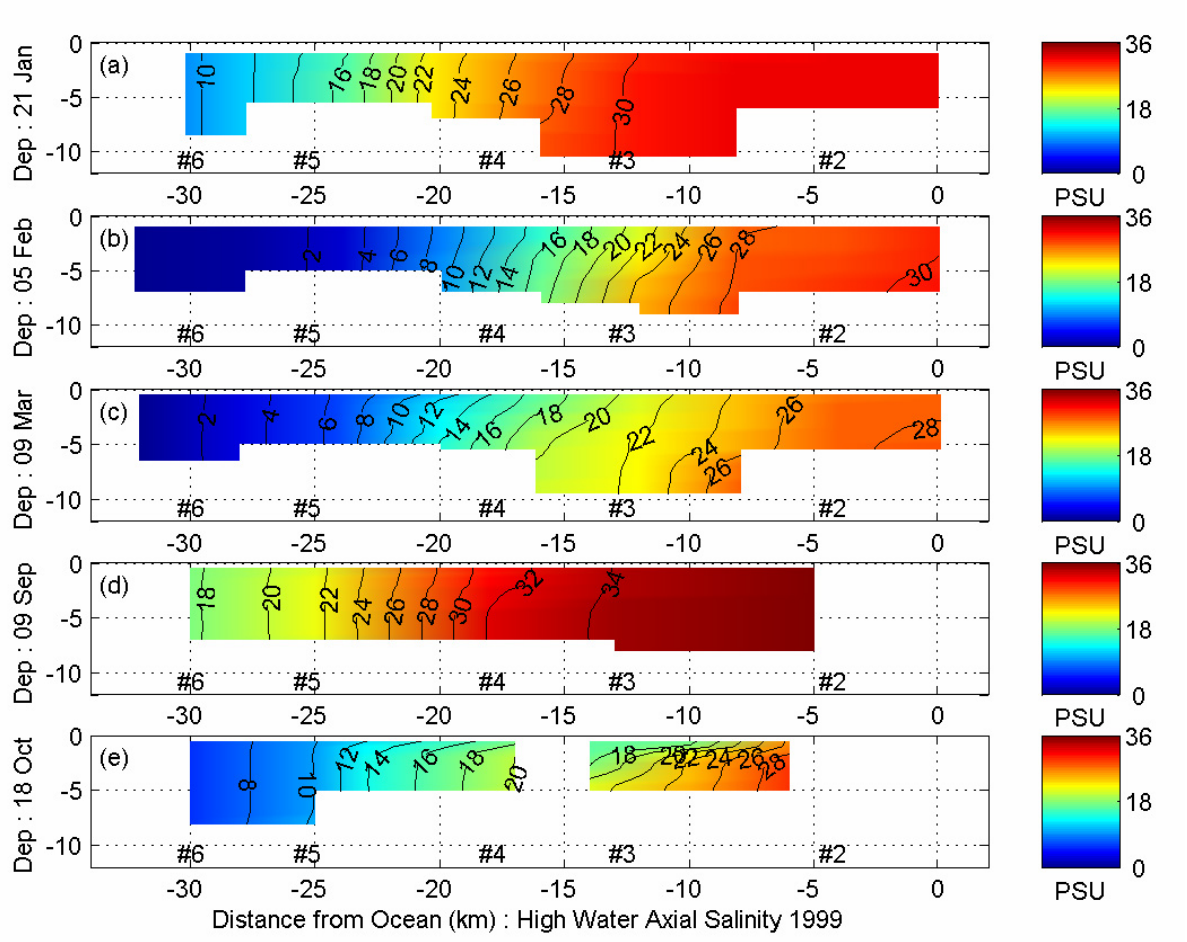

Figure 6.3: High water axial surveys done in 1999 prior to instrument deployment, during peak observed river discharge conditions, and prior to instrument retrieval during the SAT 1 and SAT 2 experiments. (a) River discharge was 17 m^3 s^{-1}. (b) River discharge was 97 m^3 s^{-1} just after a freshwater pulse event in late January. (c) River discharge was 21 m^3 s^{-1}. (d) River discharge was 4 m^3 s^{-1} after several months of little or no precipitation. (e) River discharge was 10 m^3 s^{-1} just after the pulse event associated with Hurricane Floyd. The white space indicates a one hour break in the axial survey. Numbers below each plot indicate Station locations.

6.2.2 Seasonal Mooring Deployments – Spring 1997 and Fall 1999

The primary data sources for this study are derived from the 1997 LMER 4 (25 March – 27 April 1997) and the SAT 2 (8 September – 20 October 1999) seasonal mooring deployments. Additional supplementary data on ambient water level, temperature, and salinity is derived from five axial surveys conducted along the deep

channel of the estuary under different discharge conditions (Figure 6.3) and from the near ocean long-term mooring at USGC Marker A14 (*cf.* LT 1 in Figure 6.1). The LMER 4 and SAT 2 experiments occurred, respectively, during characteristic periods of moderate (~ normal) and low river discharge.

Data collected for the LMER 4 experiment in 1997 was from an array of moored instruments and two anchor stations (one at neap and one at spring) on the Research Vessel (R/V) Blue Fin in the first major bend (R ~ 1200 m) of the Satilla River (Station 3 in Figure 6.1). Two mooring frames, one each at river kilometers 12 and 14, were equally outfitted at 0.66 meters above bottom (mab) and 2.50 mab with a Sea-Bird Electronics, Inc., SeaCAT Conductivity-Temperature-Depth sensor (CTD) and at 1.00 mab with an InterOcean S4 current meter. Temperature, salinity, depth, optical backscatterance (OBS), and velocity measurements were made every 6 minutes for a 31-day period at these two locations. Between these two mornings, at river kilometer 13, a 600 kHz RD Instruments, Inc., Broad Band Acoustic Doppler Current Profiler (BB ADCP), indicated by Station 3 in Figure 6.1, was used to obtain detailed three-dimensional current measurements in the axial, transverse, and vertical directions. The BB ADCP was mounted in an upward-looking position at 0.4 mab in a stainless steel frame. The BB ADCP sampled every 15 minutes during the same 31-day period in 0.5 m bin increments, beginning at 1.24 mab to 0.5 m below the water surface. Mooring locations and the BB ADCP setup conditions for the LMER 4 experiment are respectively summarized in Tables 6.1 and 6.2. River bathymetry was determined in-situ by a subsurface fathometer, while latitude and longitude positions were determined using a Differential Global Positioning System (DGPS) installed on the R/V Blue Fin.

In general, salinity and velocity data from the LMER 4 moored CTDs and the BB ADCP were of excellent quality. Bottom salinity measured at the eastern CTD mooring site (river kilometer 12) had spurious noise and an intermittent signal suggesting that the conductivity cell was blocked by debris. Likewise, the moored BB ADCP signal returns sporadically failed to detect the water surface level, which was likely due to an insufficient quantity of scattering particles (Emery and Thompson 1998; Ott 2000). Pressure data from the lower sensor (0.66 mab) at the eastern CTD mooring site was used to uniformly correct the BB ADCP data for missing surface returns, to remove the near surface side lobe energy returns, and to adjust the depth of the velocity observations to a standard datum. Contaminating side lobe energy generated by transducer beam interference near the 'reflecting surface' (for an upward-looking ADCP, the water surface) was removed using the data range expression

$$R_{valid} = H_r \cos\varphi \quad \textbf{(6.1)}$$

where H_r is the range depth (the total observed water depth minus the instrument depth), and φ is the beam angle (generally 20°) of the transducer faces with the horizontal plane (Emery and Thompson 1998). Removing side lobe energy from the BB ADCP data reduced the vertical data range near the reflecting surface by approximately 6% (60 centimeters for H_r = 10 m). Because the LMER 4 BB ADCP bins were 0.5 m in size, it was necessary to remove the first two bins (totaling 1 meter) near the water surface to account for and eliminate side lobe energy from the observed data. The BB ADCP data was rotated through an angle of -14º (clockwise) to align the U and V components of velocity with the streamwise and normal flow directions.

Table 6.1: LMER 4 mooring deployment locations.

Station	Sensor Depth (mab)	Water Depth (m)	Instrument (serial #)	Parameters Measured	Latitude (°N)	Longitude (°W)
A	2.50	10.0	SC 1835	C, Obs, P, T	30° 59.58′	81° 32.28′
A	1.00	10.0	S4 908	C, T, V	30° 59.58′	81° 32.28′
A	0.66	10.0	SC 848	C, Obs, P, T	30° 59.58′	81° 32.28′
3 B	0.4+	9.5	ADCP	V+	30° 59.64′	81° 31.62′
E	2.50	10.3	SC 1836	C, Obs, P, T	30° 59.16′	81° 30.84′
E	1.00	10.3	S4 909	C, T, V	30° 59.16′	81° 30.84′
E	0.66	10.3	SC 849	C, Obs, P, T	30° 59.16′	81° 30.84′
Anchor	Profiling	10.0	Gafanhoto	C, Obs, P, T, V+, seds	Near 30° 59.64′	Near 81° 31.62′

* mab = meters above bottom; C = conductivity; Obs = optical backscatterance; P = pressure; T = temperature; V = current velocity; V+ = current velocity profile

Table 6.2: Broad Band ADCP setup specifications for the LMER 4 experiment.

LMER Satilla River, Georgia	Experiment 4 26 March to 25 April 1997
Acoustic Frequency	600 kHz (BB ADCP)
Beam Angle	20 degrees
Transducer Depth	1 m
Bin Length	0.5 m
Sampling Interval	15 minutes
Pulse Length	0.72 m
Blanking Interval	0.5 m
Center of First Bin	1.24 m
Profiling Mode	4
Pings per Ensemble	150
Pings per Ensemble Average	fixed instrument, internally recording
Single Ping Velocity Error	0.65 m s^{-1}
Dynamic Velocity Error	3.38 x 10^{-3} m s^{-1}
Bottom Track	Not Applicable
Data Acquisition	RD Instruments Software (Transect)
Navigation	Global Positioning (DGPS)
Ship Speed	moored instrument, upward looking

Data collected for the SAT 2 experiment in 1999 consisted of spatially-detailed 'rapid surveys' aboard a small maneuverable research vessel (R/V Gannet), an array of moored surface and bottom instruments, 13-hour anchor stations from a larger research vessel (R/V Blue Fin), synoptic surveys throughout the estuary, and a long-term monitoring site. Anchor station data consisted of hourly CTD profiles, which included temperature, salinity, pressure, OBS, and fluorescence. Depths were determined in-situ from a subsurface recording fathometer while latitude and longitude positions were obtained with a shipboard DGPS on the R/V Blue Fin and R/V Gannet. Synoptic surveys were conducted periodically at low and high water in an effort to define the seasonal longitudinal salinity (density) structure throughout the Satilla.

Moored data for SAT 2 experiment was collected between 8 September 1999 and 20 October 1999 at predetermined locations that coincided with the 1997 LMER 4 and 1999 SAT 1 experiments (bold numbers in Figure 6.1). A pyramid shaped stainless steel frame was placed at each mooring location on which a subsurface (~ 0.5 mab) Sea-Bird Electronics, Inc., SeaCAT CTD and an upward-looking RD Instruments, Inc., Workhorse ADCP (WH ADCP) were mounted. A Sea-Bird Electronics, Inc., MicroCAT CTD was tethered with forty feet of stainless steel cable to each pyramid to measure surface temperature and salinity (Figure 6.4). Temperature, salinity, pressure, and OBS were recorded at 6 minute intervals by the SeaCAT and MicroCAT CTDs while the WH ADCPs measured depth, velocity, and acoustic backscatter at 12 minute intervals starting at 1.24 mab to 0.5 m below the water surface. InterOcean S4 current meters were used alternately with the WH ADCPs at a two mooring locations. Mooring locations and the WH ADCP setup conditions for the SAT 2 experiment are respectively summarized

in Tables 6.3 and 6.4. Shipboard DGPS and in-situ fathometry, on both the small (R/V Gannet) and large (R/V Blue Fin) research vessels, were used to determine the exact locations and depths of the mooring placements.

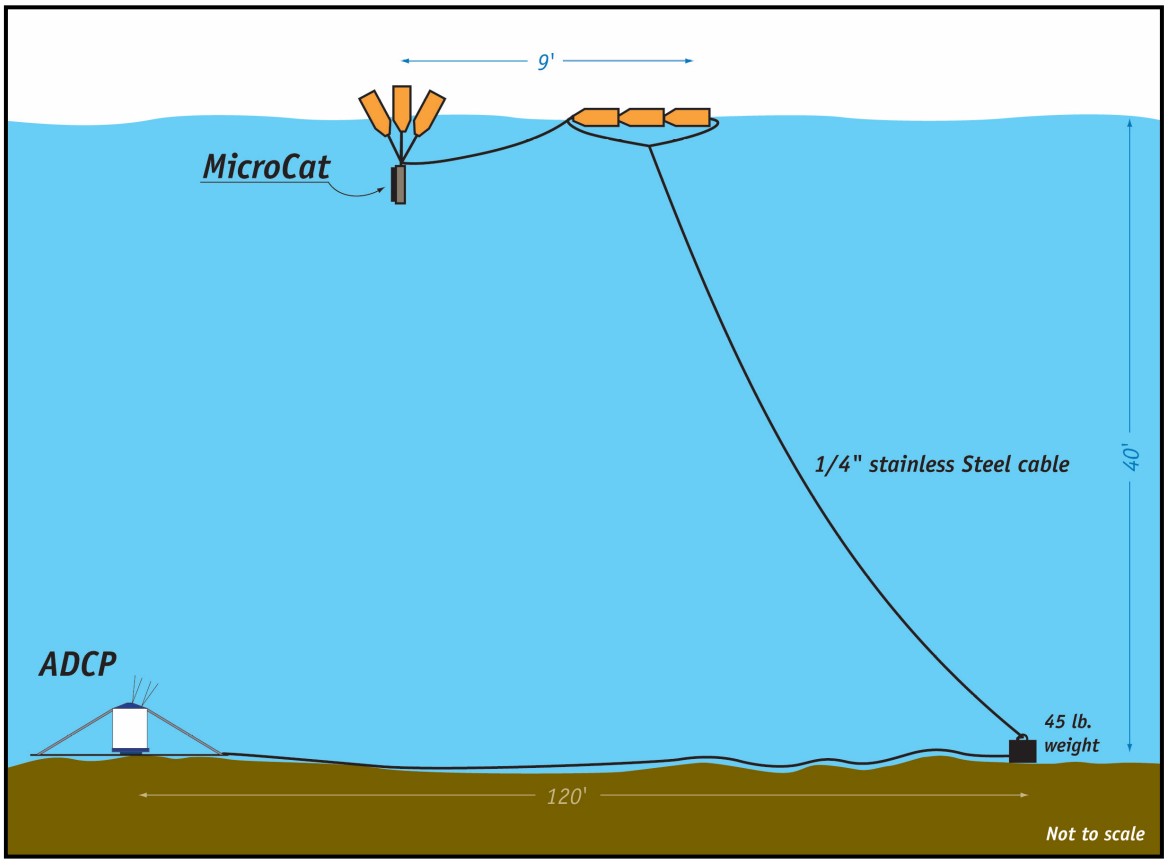

Figure 6.4: A schematic of the SAT 2 mooring deployment. Note that the figure is not drawn to scale.

Data at the long-term monitoring (LT) site consisted of a 13-month time series (9 March 1999 to 4 April 2000) at a 6 minute interval of temperature, salinity, and pressure. This site was located downriver of Domain A near river kilometer 8 (*cf.* LT 1 in Figure 6.1). Data collected at LT 1 was used to monitor and relate changes in temperature, salinity, and pressure over the annual cycle to changes in freshwater

discharge. The LT 1 data pressure data was used to adjust the depth component of the moored CTDs and moored WH ADCPs to the prescribed datum of mean lower low water (MLLW), hereafter a technique referred to as the water level reduction process.

Table 6.3: SAT 2 mooring deployment locations**.**

Station	Sensor Depth (mab)	Water Depth (m)	Instrument (serial #)	Parameters Measured	Latitude (°N)	Longitude (°W)
2	Floating	8.9	MC 703	C, T	30° 59.74′	81° 27.58′
2	1.00	8.9	S4 908	C, T, V	30° 59.74′	81° 27.58′
2	0.74	8.9	SC 848	C, Obs, P, T	30° 59.74′	81° 27.58′
3	Floating	9.3	MC 703	C, T	30° 59.59′	81° 31.55′
3	1.00	9.3	S4 909	C, T, V	30° 59.59′	81° 31.55′
3	0.89	9.3	SG 20	P, T	30° 59.59′	81° 31.55′
4	Floating	7.9	MC 704	C, T	30° 58.63′	81° 34.40′
4	0.40	7.9	WH 721	V+	30° 58.63′	81° 34.40′
4	0.66	7.9	SC 849	C, Obs, P, T	30° 58.63′	81° 34.40′
5	Floating	9.6	MC 705	C, T	30° 59.80′	81° 38.18′
5	0.40	9.6	WH 722	V+	30° 59.80′	81° 38.18′
5	0.71	9.6	SC 2722	C, Obs, P, T	30° 59.80′	81° 38.18′
6	Floating	8.5	MC 672	C, T	30° 58.02′	81° 39.47′
6	0.40	8.5	WH 690	V+	30° 58.02′	81° 39.47′
6	0.66	8.5	SC 1836	C, Obs, P, T	30° 58.02′	81° 39.47′
7	1.00	10.2	S4 2098	D, V	31° 00.87′	81° 38.32′
7	0.64	10.2	SC 1834	C, Obs, P, T	31° 00.87′	81° 38.32′
LT 1	Piling	1.1	MC 757	C, P, T	30° 58.40′	81° 30.78′

* mab = meters above bottom; C = conductivity; Obs = optical backscatterance; P = pressure; T = temperature; V = current velocity; V+ = current velocity profile

Table 6.4: Work Horse ADCP setup specifications for the SAT 2 experiment.

SAT Satilla River, Georgia	Experiment 2 09 September to 18 October 1999
Acoustic Frequency	600 kHz & 300 kHz (WH ADCPs)
Beam Angle	20 degrees
Transducer Depth	1 m
Bin Length	0.5 m
Sampling Interval	12 minutes
Pulse Length	0.72 m
Blanking Interval	0.25 m
Center of First Bin	0.87 m (600 kHz) & 1.24 m (300 kHz)
Profiling Mode	4
Pings per Ensemble	300
Pings per Ensemble Average	Fixed instrument, internally recording
Single Ping Velocity Error	0.46 m s^{-1}
Dynamic Velocity Error	3.06 x 10^{-4} to 2.12 x 10^{-3} m s^{-1}
Bottom Track	Not Applicable
Data Acquisition	RD Instruments Software (WinADCP)
Navigation	Global Positioning (DGPS)
Ship Speed	moored instrument, upward looking

Salinity data from the SAT 2 moored SeaCAT CTDs were of excellent quality. Small tubes filled with the antifoulant Tri-butyl Tin (TBT) attached to either ends of the conductivity cell on the SeaCATs CTDs significantly reduced bio-fouling during mooring deployments. Optical backscatter sensors on the moored SeaCAT CTDs, however, were blocked by thick marine sediments and mud within a few weeks of deployment. Salinity data from moored MicroCAT CTD (at the long-term monitoring site) were of good quality. Bio-fouling initially reduced the quality of bottom mounted MicroCAT CTD salinity data to discrete month-long intervals when the ambient water temperature was over 25ºC. The quality of bottom mounted MicroCAT CTD salinity was significantly improved for the remaining seven months of deployment by the addition of SeaCAT CTD TBT tubes on either end of the conductivity cell and the

application of marine grade silicon grease on the housing around the conductivity cell prior to deployment. Tethered MicroCAT CTD data was of good quality. Due to rough weather and a highly corrosive environment, several of the tethered MicroCAT CTDs broke free approximately twenty days after the initial deployment on September 9, 1999. All but one tethered CTD was retrieved, and in most cases, each instrument was re-deployed to its original location within a few days. The tethered MicroCAT CTD at Station 5 remained in place during the entire SAT 2 mooring deployment. As a result, the vertical salinity gradient information for this chapter is calculated using the surface and bottom salinity data at this site. The vertical salinity gradient calculated using data at Mooring 5 is of a similar nature to the shorter length vertical salinity gradients calculated respectively at Moorings 4 and 6 due to the temporary loss of the tethered MicroCAT CTDs. Therefore, it is assumed that the vertical salinity gradient at Station 5 is representative of the vertical salinity gradient for Stations 4 and 6 during the SAT 2 experiment. Temperature and pressure data for the SeaCAT CTDs and the MicroCAT CTDs were of excellent quality and were unaffected by bio-fouling.

Velocity data from the WH ADCPs was of excellent quality. Bio-fouling was nearly eliminated on the WH ADCPs by applying a thin mixture of cayenne pepper and marine grade silicon grease to each of the transducer faces before deployment. The WH ADCPs, as with the BB ADCP during the LMER 4 experiment, likely due to a glass-like water surface, sporadically failed to detect the water surface level (Emery and Thompson 1998; Ott 2000). Pressure data from the lower CTD at each WH ADCP station (0.66 mab, 0.71 mab, and 0.66 mab, respectively for Stations 4, 5, and 6) was used to uniformly correct the WH ADCP data for missing surface returns, to remove the near

surface side lobe energy returns, and to adjust the depth of the velocity observations to a standard datum. Contaminating side lobe energy, as with the LMER 4 BB ADCP data, was removed from the WH ADCP data using the data range expression given by Equation 6.1. Removing side lobe energy from the WH ADCP data reduced the vertical data range near the reflecting surface by approximately 6% (60 centimeters for H_r = 10 m). Because the SAT 2 WH ADCP bins were also 0.5 m in size, it was necessary to remove the first two bins (totaling 1 meter) near the water surface to account for and eliminate side lobe energy from the observed data. The WH ADCP data at Station 4, Station 5, and Station 6 were each rotated respectively through an angle of -52º (clockwise), -16º (clockwise), and -86º (clockwise) to align the U and V components of velocity with the streamwise and normal flow directions.

6.3 Results and Discussion

6.3.1 Tidal and Subtidal Salinity Distributions

Figure 6.5 compares a neap-to-spring time series of the surface tidal and subtidal salinities for the LMER 4 (upper panel) and the SAT 2 (lower panel) mooring deployments. The 9-day period depicted in each panel corresponds to an interval during which tidal conditions were similar for the two experiments and during which the tethered CTDs were functioning properly at their original deployment location. The upper most panel in Figure 6.5 shows the tidal and subtidal salinity time series for the LMER 4 SeaCAT CTDs that were moored to 1 kilometer on either side of the BB ADCP at Station 3 (*cf.* Figure 6.1). Subtidal salinity at the station closest to the ocean (Salinity East in Figure 6.5a) was around 16 PSU in late March of 1997 and increased to around 20 PSU in early April of 1997. Likewise, the subtidal salinity at the upriver station, west of

the BB ADCP mooring (Salinity West in Figure 6.5a) was around 12 PSU in late March and increased to around 18 PSU in early April. The longitudinal salinity gradient decreased from 2 PSU km^{-1} to 1 PSU km^{-1} as a river discharge dropped from 63 m^3 s^{-1} at the beginning of the LMER 4 mooring deployment to approximately 35 m^3 s^{-1} at the end of the first week in April 1997 (*cf.* Figure 6.2). This observed decrease in the axial salinity gradient was associated with a decrease in freshwater discharge (Seim et al. 2002; Blanton et al. 2003). Upper and lower salinity data at the western LMER 4 CTD site (river kilometer 14) suggest that a decrease in the axial salinity gradient corresponds to a decrease in the vertical salinity gradient; however, the extent of the decrease is difficult to determine because the sensors at the western CTD site are separated vertically by only 2 meters and the corroborating salinity data at the eastern CTD site is suspect.

Comparatively, the lower panel in Figure 6.5 shows the surface tidal and subtidal salinity time series for the SAT 2 MicroCAT CTDs that were moored respectively at Station 3 (river kilometer 13), Station 4 (river kilometer 18), Station 5 (river kilometer 26), and Station 6 (river kilometer 32) as marked in bold on Figure 6.1. Subtidal salinity at Station 3 (red line in Figure 6.5b) was around 34 PSU in mid-September of 1999 and slowly decreased to around 30 PSU by late September 1999. Likewise, the subtidal salinity at Station 4, (blue line in Figure 6.5b) was around 30 PSU in mid-September and, in a similar manner, decreased to approximately 26 PSU by late September. The subtidal salinity at Stations 5 and 6 (magenta and cyan lines respectively in Figure 6.5b) correspondingly decreased from 24 PSU in mid-September to 20 PSU near the end of September at Station 5 and decreased from 20 PSU in mid-September 1999 to 16 PSU in late September 1999 at Station 6. Though the subtidal salinity at Stations 3, 4, 5, and 6

showed a decrease between year days 259 and 268, the longitudinal salinity gradient remained steady at around 0.75 PSU km^{-1} over the 10 day period. Comparatively, the river discharge also remained steady during this 10 day period near a historically low value of 3 m^3 s^{-1} (Figure 6.2). Note that the impact of long-term drought conditions (beginning in May of 1997 and lasting until May 2001) on the axial salinity distribution can be observed by comparing the salinity in the upper panel of Figure 6.5 interpolated to river kilometer 13 (SL+13) to the salinity in the lower panel of Figure 6.5 at Station 3 (SL+13). The salinity at river kilometer 13 increased from around 20 PSU during the LMER 4 survey to a near ocean value of 34 PSU during the SAT 2 survey. A salinity range along the channel axis comparable to that during the LMER 4 experiment was found to have shifted upriver by nearly 20 kilometers to just past Station 6 (SL+32) during the SAT 2 experiment. Ocean-like salinities well into the estuary (Figure 6.3d) combined with a weak axial salinity gradient (0.75 PSU km^{-1}) were associated with a reduced vertical salinity gradient during the SAT 2 experiment. As a result, it is expected that during the SAT 2 experiment, the vertical density structure had a limited impact on reducing curvature-induced secondary flow.

6.3.2 Tidal Velocity Distributions

Axial velocity profiles for the neap and spring tides occurring near or during the anchor station surveys dates are shown in Figure 6.6. As seen in Chapter 5, the velocity shear during ebb tides (red in Figure 6.6) was fairly uniform over the depth for both neap and spring tides, while the velocity shear during flood tides (blue in Figure 6.6) had a more variable nature. At Station 3, the highest velocity shear during flood tide was concentrated below approximately 4.5 meters at neap tide and was concentrated below

approximately 4 meters at spring tide. In contrast, for flood tide at the other mooring locations (Station 4, Station 5, and Station 6), the velocity shear tended to remain concentrated below 4 meters for both spring and neap tide.

A spring and a neap subset of cross-channel Acoustic Doppler Current Profiler (ADCP) velocity measurements taken during the LMER 4 experiment at Station 3 and during the SAT 2 experiment at Stations 4, 5, and 6 are shown respectively in Figures 6.7 and 6.8. A right-handed reference frame is used, where north, east, and up are positive, to describe the ADCP data. Positive values indicated by red signify flow toward the outside of the channel bend while negative values indicated by blue signify flow toward the inside of the channel bend. Note that the scale of the lateral velocity is ± 0.25 m s^{-1}. The cross-channel velocity in the Satilla River can be as much as 25% of the along-channel velocity, which is similar to that observed in other estuaries (Nunes and Simpson 1985; Seim and Gregg 1997), and it is larger than 10% of the axial flow field that is commonly assumed to scale away the non-linear effects of secondary flow (Geyer 1993; Chant 2002; Lerczak and Geyer 2004).

Based on scale estimates as described in Chapter 3, the dominant mechanisms for driving secondary flow in the Satilla River are channel curvature, friction, and the differential advection of density. The signature of secondary flow driven by channel curvature (centrifugal acceleration) is most clearly illustrated by the cross-channel velocities at Stations 3, 4, and 6 during spring tide in plot subpanels a, b, and d of Figure 6.7. Flow is directed to the outside of the channel bend in the near surface and is directed toward the inside of the channel bend at depth. The signature of secondary circulation is the strongest and most apparent during ebb tides (red/yellow in the near surface and

blue/green in the near bottom) when both the axial velocity and the vertical shear of the axial current are at a maximum (Ott 2000; Blanton et al. 2002; Ott 2002). The curvature driven secondary flow at Station 6 (Figure 6.7d) is weaker, as the flow is confined to a narrow channel and the ratio of channel curvature to channel width, R/B, is greater (7.5) than that at Stations 3 and 4 (respectively, 4.6 and 5.5).

The signature of secondary flow driven by the differential advection of density during spring tide is illustrated by the cross-channel velocity at Station 5 in Figure 6.7c. Here, the direction of the secondary circulation cell reverses between near surface flow to the north (flow to the south at depth) during ebb tides and near surface flow to the south (flow to the north at depth) during flood tides. The differential advection of density, due to the interaction of the axial density gradient with the lateral shear of the axial current, produces transverse gradients during ebb and flood. Two laterally adjacent density driven secondary circulation cells develop as mass conserving adjustment flows act to redistribute the density field and reduce the lateral density gradients. The orientation of the density driven secondary circulation cells alternate with a change in the direction of tidal flow and are commonly observed on the surface as slick lines during ebb and foam fronts during flood. During ebb, the differential advection of density leads to an increase in density along the channel banks and a decrease in density near the channel center, generating an inward-directed lateral density gradient at depth. This results in the formation of two laterally adjacent divergent secondary circulation cells, of which the northernmost cell has near surface flow directed toward the north and flow at depth directed toward the south. The southernmost cell has an equal and opposite circulation pattern. The two lateral cell circulation pattern is reversed during flood tides, as the

differential advection of density increases density near the channel center and reduces density near the channel banks, generating an outward-directed lateral density gradient at depth. This case results in the formation of two laterally adjacent convergent secondary circulation cells. Here, the northernmost adjusting secondary circulation cell has near surface flow directed toward the south and flow at depth directed toward the north. Likewise, the southernmost cell has an equal and opposite circulation pattern. As the mooring at Station 5 is located in the *thalweg* near the north bank of the channel, the ADCP measurements capture the divergent cell characteristics of the northernmost secondary cell during ebb tides and its convergent cell characteristics during flood tides.

Figure 6.8 illustrates the strength and character of secondary flow at neap tide during the LMER 4 and SAT 2 experiments at Stations 3, 4, 5, and 6. Curvature driven secondary flow at Station 4 is approximately half the strength during neap tide (Figure 6.8b) as during spring tide (Figure 6.7b), while the strength of curvature driven flow at Station 6 remains relatively unchanged between neap (Figure 6.8d) and spring tide (Figure 6.7d) conditions. Station 6 is confined to a narrow curved channel beyond the junction between the Satilla River and White Oak Creek near river kilometer 30 (*cf.* Figure 2.6) where the vertical density gradient is generally weak (*cf.* Figure 6.3). Shear effects dominate the flow field at Station 6, suggesting that it is likely the cause of the minor observed differences at this location between neap and spring tides.

At Station 3 (Figure 6.8a), curvature driven secondary flow departs from an 'expected' channel curvature signature of one vertical circulation cell by the appearance of a lower secondary circulation cell (from 2 to 5 mab) that occurs during ebb tides between year days 89.25 and 91.75. The presence of the lowermost secondary circulation

cell reduces the mixing depth of the upper curvature driven secondary circulation cell by approximately half, from 6 meters at spring tide to 3 meters at neap tide. Results from Chapter 5 suggest that the strength and duration of the lowermost secondary circulation cell at Station 3 during neap tide decreases with a decrease in vertical stratification or with a decrease in freshwater discharge. Chapter 5 results also suggest that the lower cell in the stacked cell configuration at Station 3 during neap tide is generated by a lateral seiche as the pycnocline relaxes between ebb and flood tides, which is diagnosed by the observance of wave-like features in the lower salinity measurements as the tides reverse from ebb to flood (Seim et al. 2002) and by comparing the advection time scale, T_{adv}, to the lateral seiche time scale, T_{seiche}.

Density driven secondary flow, also weaker during neap tide, regulates the flow at Station 5 in Figure 6.8c. The direction of the secondary circulation switches between a pair of divergent secondary circulation cells at ebb to a pair of convergent secondary circulation cells at flood.

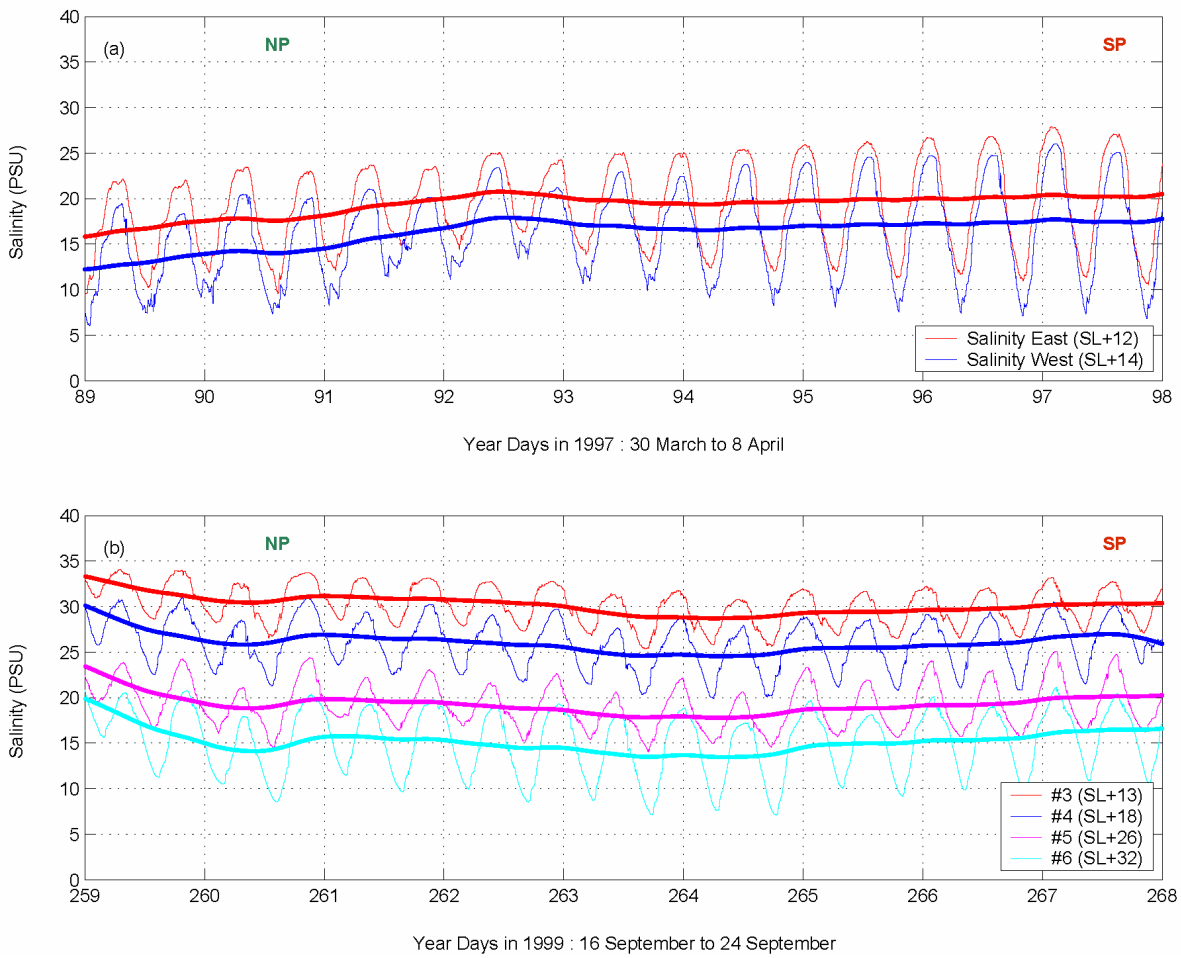

Figure 6.5: (a) Fortnightly salinity time series for the 1997 LMER 4 field survey. The 40-hour low pass signature is plotted on top of the surface salinity data for each mooring location. (b) Fortnightly salinity time series for the 1999 SAT 2 field survey. The 40-hour low pass signature is plotted on top of the surface salinity data for each mooring location. Neap and spring tides are indicated by NP and SP respectively.

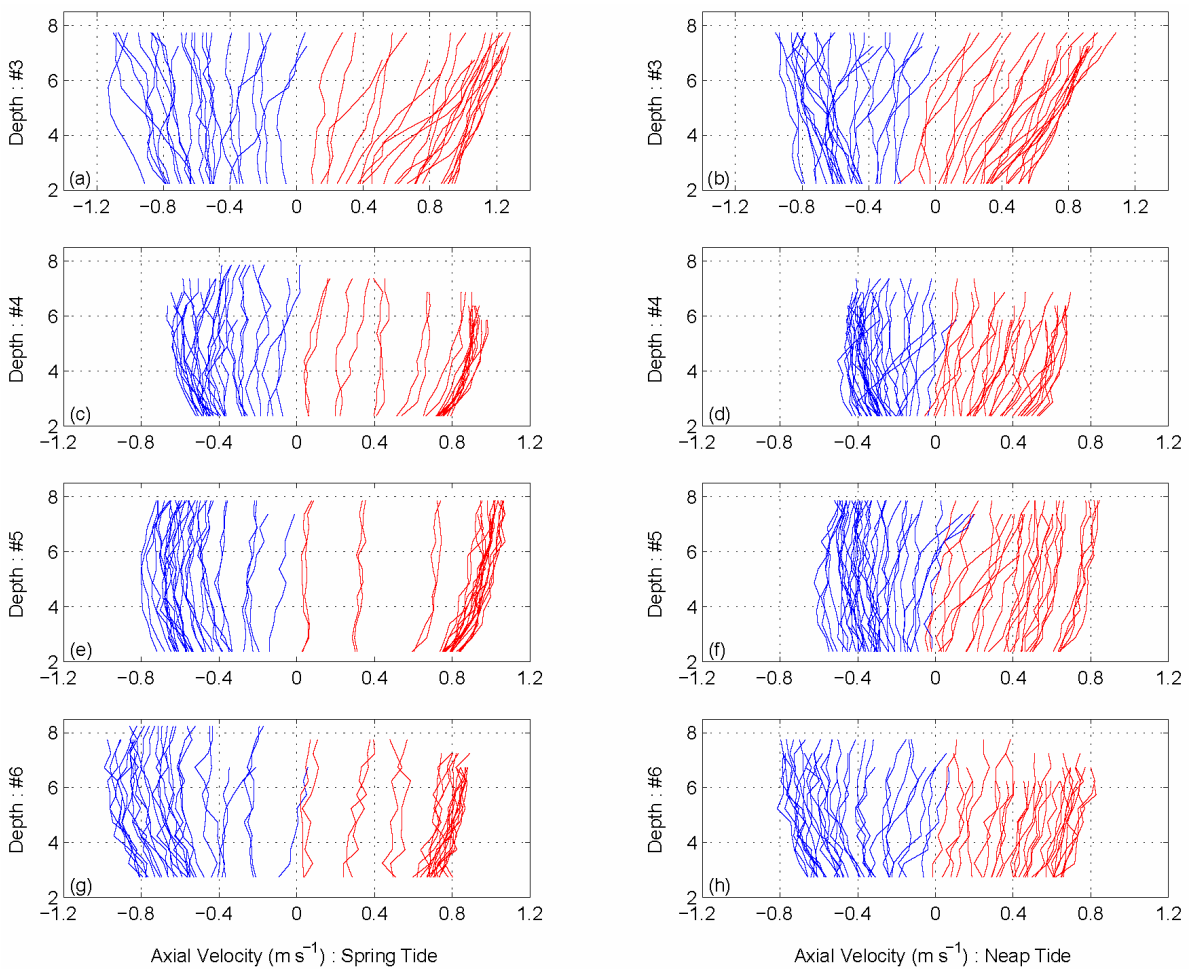

Figure 6.6: Axial velocity profiles respectively for spring and neap tides at Station #3 (a & b), at Station #4 (c & d), at Station #5 (e & f), and at Station #6 (g & h). Positive values indicate ebb flow and negative values indicate flood flow.

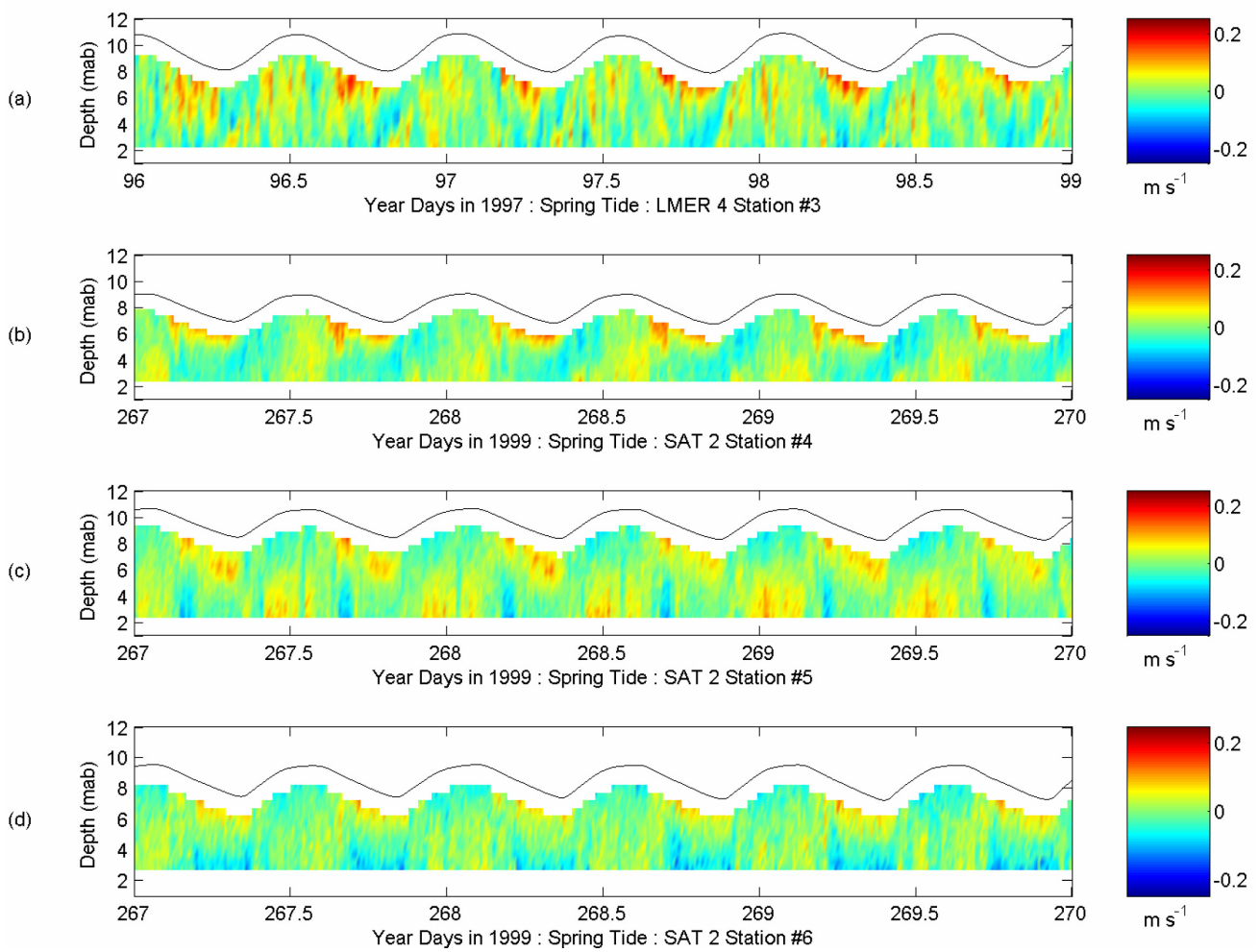

Figure 6.7: Lateral ADCP velocity measurements taken during spring tide at (a) LMER 4 Station #3; (b) SAT 2 Station #4; (c) SAT 2 Station #5; and at (d) SAT 2 Station #6. Positive values in all subpanels indicate flow to the outside of the bend, while respectively; negative values indicate flow to the inside of the bend.

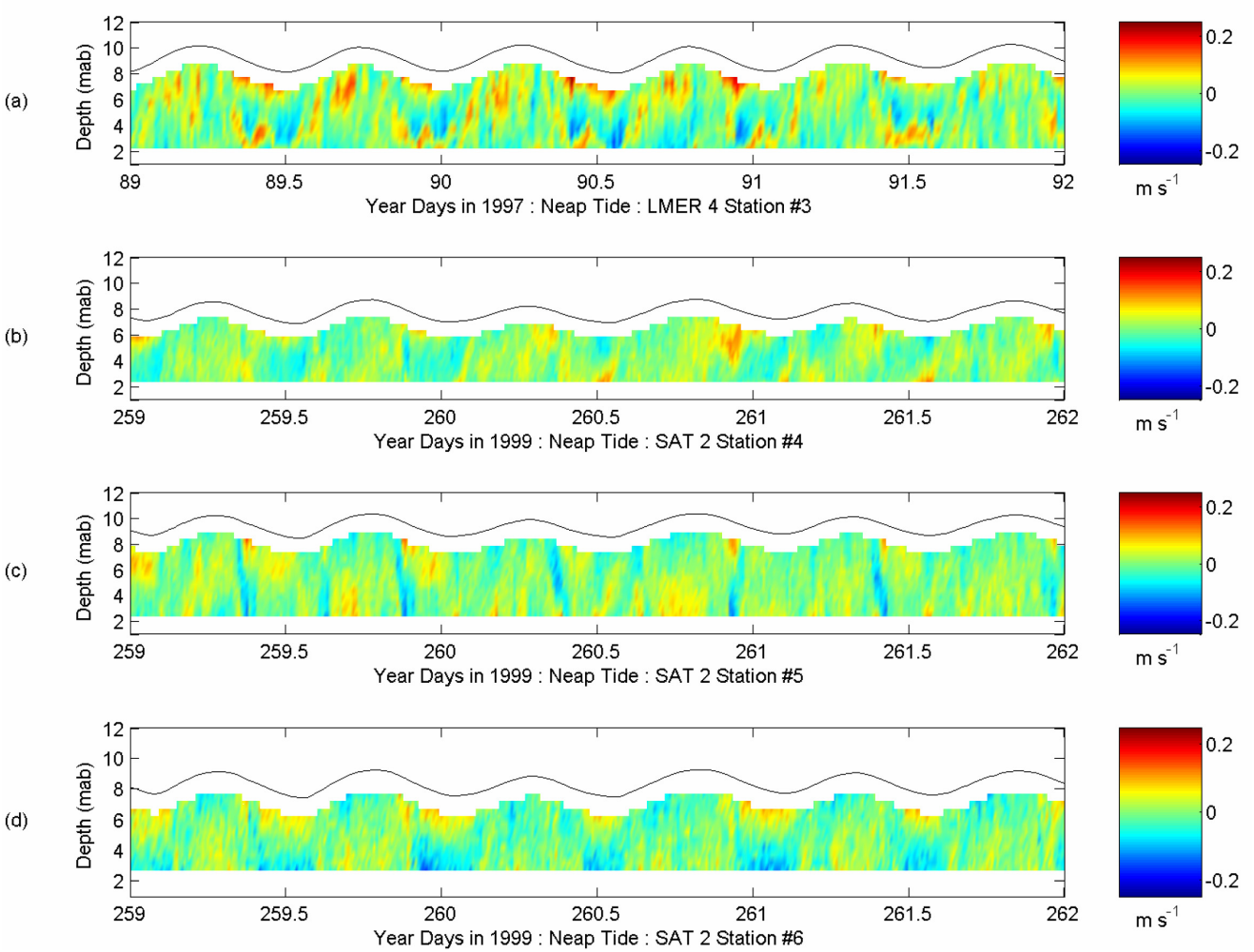

Figure 6.8: (a) Lateral ADCP velocity measurements taken during neap tide at (a) LMER 4 Station #3; (b) SAT 2 Station #4; (c) SAT 2 Station #5; and at (d) SAT 2 Station #6. The repeated blue streak at ebb in subpanel c is an artifact generated by the tethering wire attaching the MicroCAT CTD to the ADCP mooring frame. Positive values as in Figure 6.6 indicate flow to the outside.

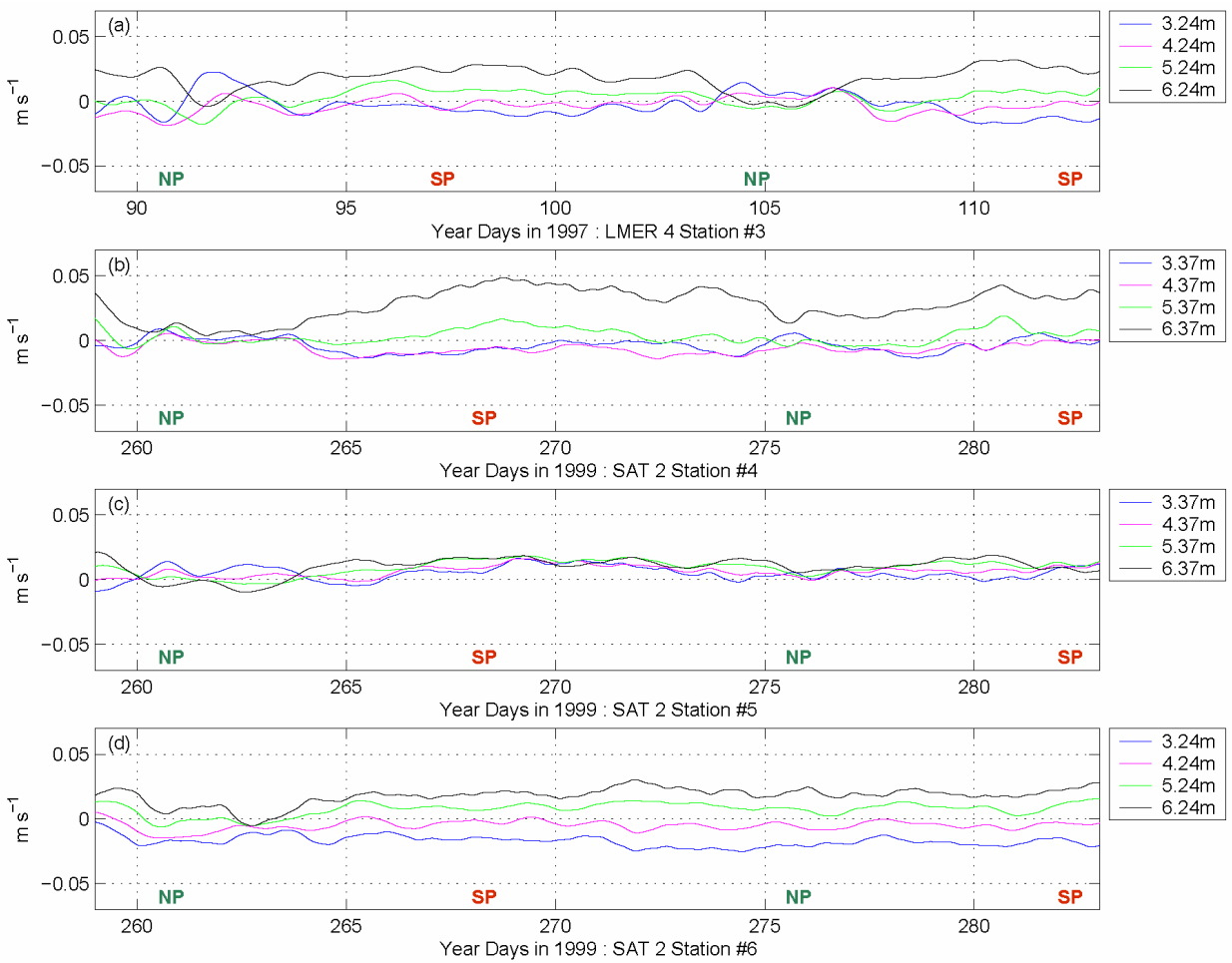

Figure 6.9: (a) Results of a Butterworth 40-hour low-pass filter applied to the cross-channel velocity, removing tidal variability, at four levels for (a) LMER 4 Station #3; (b) SAT 2 Station #4; (c) SAT 2 Station #5; and (d) SAT 2 Station #6. These levels represent near bottom velocity (low bin ~ 3.3 mab), low mid-depth velocity (low mid bin ~ 4.3 mab), high mid-depth velocity (mid high bin ~ 5.3 mab), and near surface velocity (high bin ~ 6.3 mab). NP and SP indicate neap and spring tides, respectively.

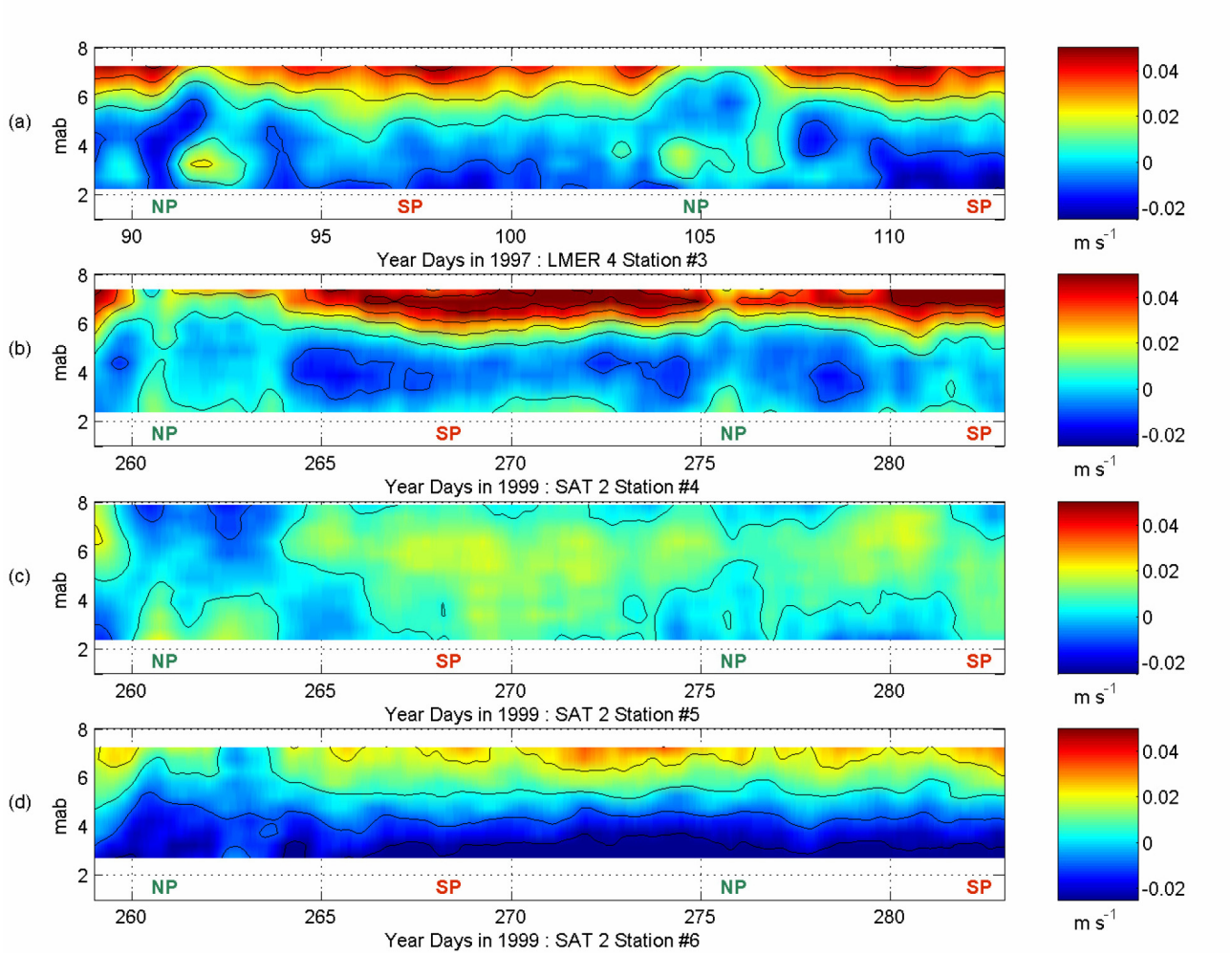

Figure 6.10: (a) Subtidal lateral velocity (secondary flow) at (a) Station #3 during LMER 4; (b) Station #4 during SAT 2; (c) Station #5 during SAT 2; and (d) Station #6 during SAT 2. Positive values (red) show flow to the outside of the bend, and negative values (blue) show flow to the inside of the bend. NP and SP indicate neap and spring tides, respectively.

6.3.3 Subtidal Velocity Distributions

The subtidal strength and character of secondary flow over two fortnightly cycles during the LMER 4 and SAT 2 experiments are shown in Figure 6.9. At Station 3 (Figure 6.9a), the average subtidal cross-channel flow in the near surface was directed toward the outside of the bend (~ 0.020 m s^{-1}), as was the flow at high mid-depth (~ 0.004 m s^{-1}), while the flows at low mid-depth and the near bottom were weak and oriented toward the inside of the bend (respectively, ~ -0.003 m s^{-1} and ~ -0.005 m s^{-1}). Likewise, at Station 4 (Figure 6.9b), the average subtidal cross-channel flow in the near surface was directed toward the outside of the bend (~ 0.026 m s^{-1}), as was the flow at high mid-depth (~ 0.005 m s^{-1}), while the flows at low mid-depth and the near bottom were also weak and oriented toward the inside of the bend (approximately -0.004 m s^{-1} and -0.002 m s^{-1}, respectively). Similarly, at Station 6 (Figure 6.9d), the average subtidal cross-channel flow in the near surface was directed toward the outside of the bend (~ 0.017 m s^{-1}), as was the flow at high mid-depth (~ 0.008 m s^{-1}), while the flows at low mid-depth and the near bottom were oriented toward the inside of the bend (approximately -0.005 m s^{-1} and -0.016 m s^{-1}, respectively). These patterns are consistent with secondary circulation driven by channel curvature (centrifugal acceleration) and suggest the presence of a single secondary circulation cell that can locally mix throughout the depth of the water column. The pattern at Station 5 (Figure 6.9c), located in a straight reach of the Satilla River, suggests the presence of a density driven secondary circulation cell. As the Station 5 mooring was located in the *thalweg* or main ebb channel of the river, this result is not unexpected. Average subtidal cross-channel flow at Station 5 (Figure 6.9c) in the near surface was weaker than curvature driven secondary flow in the near surface and was

directed toward the outside of the bend (~ 0.009 m s^{-1}), as was the flow at high mid-depth (~ 0.008 m s^{-1}), low mid-depth (~ 0.005 m s^{-1}), and the near bottom (~ 0.005 m s^{-1}).

The subtidal signature of secondary flow for individual spring tides at Stations 3 and 4 (SP in Figures 6.9a and 6.9b), and for individual spring and neap tides at Station 6 (SP and NP in Figure 6.9d) are similar to that induced by channel curvature and are approximately 50% larger than their averages over the 25-day comparison period. The subtidal signature of secondary flow for individual spring and neap tides at Station 5 (SP and NP in Figure 6.9c) is similar to that induced by an ebb dominant density driven secondary circulation, and unlike Stations 3, 4, and 6, has approximately the same strength as its 25-day average. At neap tides, the subtidal signature of secondary flow at Stations 3 and 4 (NP in Figures 6.9a and 6.9b) is more complicated. While more pronounced at Station 3 (year days 90.5 to 94 and 104 to 106.5) than at Station 4, (year days 259.5 to 264 and 274.5 to 276.5) the subtidal signature of secondary flow at neap indicates that the near surface flow is weak, though still directed toward the outside of the bend, flow at high mid-depth is toward the inside of the bend, flow at low mid-depth is either weak toward the outside of the bend or near zero, and flow near the bottom is directed toward the outside of the bend. This pattern suggests the presence of two vertical circulation cells. At Station 3, each cell is about one-half the depth of the water column (*cf.* Figure 6.8a) corresponding to a vertical depth of about 3 meters, while at Station 4 (*cf.* Figure 6.8b), the lower cell is barely perceptible and has a vertical depth of between 1 to 2 meters (the difference in depth between the low mid-depth bin and bottom bin in Figure 6.9b). It is not possible to explicitly state the circulation pattern below 2 m, because the ADCPs cannot profile the entire water column. The dominant uppermost cell

has a circulation pattern consistent with flow around a channel bend, while the lowermost cell has a weak and a similar flow orientation as the upper cell. The appearance of the lower cell at Station 4 coincides with a series of precipitation events with cumulative totals between 33 and 81 mm. Though river discharge conditions were extremely low during the SAT 2 experiment, it appears that presence of the lower secondary circulation cell responds to steady discharge conditions and to pulse precipitation events in a similar manner.

Results from Chapter 5 suggest that the lower 'second cell' is generated during the ebb phase of the neap tide when tidal straining amplifies the vertical density gradient (Simpson et al. 1990). During the ebb phase of the neap tide, the lowermost cell of the two-cell configuration appears to grow vertically, which in turn reduces the mixing depth of the uppermost curvature driven cell. The stacked cell configurations have been observed to last through the early flood phase of the neap tide until the vertical salinity gradient diminishes and the interface between the two cells erodes. The strength, duration, and vertical depth of the lowermost cell in the neap tide two-cell circulation pattern, as noted by the magnitude and duration of the positive low bin velocity in Figures 6.10a and 6.10b and by the closed contours between 2 and 4 mab in Figure 6.10a, all appear to decrease with an observed decrease in the vertical salinity gradient (*cf.* Figures 6.3d and 6.3e) and/or a decrease in river discharge (*cf.* Figure 6.2).

As seen in Chapter 5, the structure of the curvature driven secondary flow in the study area fluctuates fortnightly between a classical single cell configuration at spring to a more complicated stacked double-cell configuration at neap. At neap, the uppermost circulation cell is driven by channel curvature while the lowermost cell is the result of

lateral seiching in response to internal adjustments of the density field between ebb and flood tides (Chant 2002; Seim et al. 2002). Lateral seiching was found to be a local feature and is likely only to be detected in nearby downstream bends within close proximity (1500 m).

6.3.4 The Effect of River Discharge on Secondary Circulation

Changes in the vertical salinity gradient due to changes in freshwater input are demonstrated in the axial salinity surveys shown in Figure 6.3. At each Station (whose locations are indicated below each subpanel plot), the density of contour lines in Figure 6.3 indicates the strength of the vertical salinity gradient. Figures 6.3a through 6.3c show the axial salinity distribution for late January through early March 1999, when the river discharge ranged from a normal 20 m^3 s^{-1} in late January to a freshwater pulse of nearly 120 m^3 s^{-1} in early February and a return to near normal discharge conditions (20 m^3 s^{-1}) in early March 1999. Likewise, Figures 6.3d and 6.3e show the axial salinity distribution under drought conditions (4 m^3 s^{-1}) and shortly after a freshwater pulse due to Hurricane Floyd and during the initial approach of Hurricane Irene (indicated by the shallow freshwater layer between river kilometers 8 and 14).

Based on Figure 6.3, it is likely that vertical variations in salinity will be important in determining the strength of the curvature driven secondary flow at Stations 3 and 4. However, vertical variations in salinity are not likely to be important in determining curvature driven flow characteristics at Station 6 due to either a very weak vertical salinity gradient or to little or no change in the vertical salinity gradient with a change in discharge conditions. The subtidal cross-channel velocity (used here as a proxy for estimating conditions when overturning by secondary circulation can be

reduced by the vertical density gradient) for Stations 3, 4, and 6 as shown in Figures 6.10a, 6.10b, and 6.10d suggest that changes in the vertical density gradient is a probable cause for the observed differences in the signature of curvature driven secondary circulation at neap tides between Stations 3 and 4 and in comparison to Station 6.

Changes in freshwater discharge for the Satilla River can alter both the strength and location of the maximum vertical density gradient along the axis of the estuary (*cf.* Figure 6.3). The remainder of this section explores the relationship between changes in freshwater discharge (as either a steady input or freshwater pulse) and changes in the structure and strength of observed secondary flows. As suggested in Chapter 5, the strength of observed secondary circulations in the Satilla River decreases with a decrease in freshwater input. This response to changes in discharge is similar for both spring and neap tides, with the exception that at neap, the decrease in freshwater input additionally reduces not only the strength of the lower secondary circulation cell, but its presence as well. This is not surprising, as the lower cell is due to a balance between centrifugal acceleration and the lateral baroclinic gradient, which is shifted upriver and/or weakened locally during low discharge conditions. Likewise, because of the low discharge and drought conditions throughout much of the SAT 2 experiment, a lower secondary cell is not likely to develop except at Station 4, which despite changes in river discharge, is the location of the maximum vertical salinity gradient during most of the SAT 2 deployment (*cf.* Figure 6.3).

By convention, the influence of river discharge can be related to changes in the axial velocity by the following expression:

$$\overline{u}_Q = \frac{Q_f}{Bh} \quad \textbf{(6.2)}$$

where $\overline{u}_Q$ is the average axial velocity due to freshwater discharge, Q_f is the freshwater discharge in $m^3\ s^{-1}$, B is the channel width, and h is the average cross-sectional depth. Assuming that changes in freshwater discharge only modify the barotropic water slope, the effect of changes in freshwater discharge to the average axial velocity (expressed by $\overline{u}_Q$) can be added by superposition to the depth-average axial velocity ($\overline{u}_s$, assumed to be 0.64 m s^{-1} at neap and 1.04 m s^{-1} at spring) to form the adjusted streamwise velocity ($\overline{u}_{adj} = \overline{u}_s + \overline{u}_Q$). Using a range of observed discharge values during the LMER 4 and SAT 2 experiments (150 $m^3\ s^{-1}$, 50 $m^3\ s^{-1}$, and 10 $m^3\ s^{-1}$) and a peak value of 300 $m^3\ s^{-1}$ as observed by Chant (2002) in Kill van Kull, and a channel depth of 10 m, the estimated contribution to the average axial velocity due to changes in freshwater discharge are shown in row 8 of Table 6.5. Discharge contributions ($\overline{u}_Q$) to the adjusted streamwise velocity vary from approximately 0.003 m s^{-1} at Station 3 for a freshwater input of 10 $m^3\ s^{-1}$ to as high as 0.18 m s^{-1} (Q_f = 300 $m^3\ s^{-1}$, B = 167 m, and h = 10 m) for a freshwater input of 300 $m^3\ s^{-1}$ at Station 6. As seen in Table 6.5 rows 10 and 11, river discharge equal or greater than above 50 $m^3\ s^{-1}$ plays a fractionally more important role in modifying the adjusted streamwise velocity ($\overline{u}_{adj}$), while river discharge below approximately 35 $m^3\ s^{-1}$ (calculated using Equation 6.2, assuming an average B = 250 m and h = 10 m) appears to have little or no impact on the strength of the adjusted streamwise velocity.

Table 6.5: Summary of river discharge velocity contributions, minimum halting vertical density difference, and tidal straining (SIPS) conditions for the LMER 4 and SAT 2 experiments.

PARAMETER	LMER 4 Station #3	SAT 2 Station #4	SAT 2 Station #5	SAT 2 Station #6
Radius of Curvature (R)	1333 m	1375 m	2583 m	1250 m
Channel Width (B)	292 m	250 m	271 m	167 m
Reduced gravity (g')				
Neap	0.048 m s^{-2}	0.037 m s^{-2}	0.019 m s^{-2}	0.021 m s^{-2}
Spring	0.014 m s^{-2}	0.012 m s^{-2}	0.013 m s^{-2}	0.006 m s^{-2}
River discharge characteristics				
Q_f *– High, Medium, Low* (m^3 s^{-1})	150, 50, 10	150, 50, 10	150, 50, 10	150, 50, 10
$\overline{u}_Q$ *– High, Medium, Low* (m s^{-1})	0.05, 0.02, 0.003	0.06, 0.02, 0.004	0.06, 0.02, 0.004	0.09, 0.03, 0.006
Adjusted streamwise velocity ($\overline{u}_s + \overline{u}_Q$)				
Neap (m s^{-1}) *– High, Medium, Low*	0.69, 0.66, 0.64	0.70, 0.66, 0.64	0.70, 0.66, 0.64	0.73, 0.67, 0.65
Spring (m s^{-1}) *– High, Medium, Low*	1.09, 1.06, 1.04	1.10, 1.06, 1.04	1.10, 1.06, 1.04	1.13, 1.07, 1.05
Minimum vertical density difference ($\Delta\rho_z$)				
Neap – High Q ($150\ m^3\ s^{-1}$)	0.60 kg m^{-3}	0.50 kg m^{-3}	0.31 kg m^{-3}	0.39 kg m^{-3}
Neap – Medium Q ($50\ m^3\ s^{-1}$)	0.54 kg m^{-3}	0.45 kg m^{-3}	0.27 kg m^{-3}	0.33 kg m^{-3}
Neap – Low Q ($10\ m^3\ s^{-1}$)	0.51 kg m^{-3}	0.42 kg m^{-3}	0.26 kg m^{-3}	0.31 kg m^{-3}
Spring – High Q ($150\ m^3\ s^{-1}$)	1.49 kg m^{-3}	1.24 kg m^{-3}	0.76 kg m^{-3}	0.94 kg m^{-3}
Spring – Medium Q ($50\ m^3\ s^{-1}$)	1.41 kg m^{-3}	1.15 kg m^{-3}	0.70 kg m^{-3}	0.85 kg m^{-3}
Spring – Low Q ($10\ m^3\ s^{-1}$)	1.35 kg m^{-3}	1.11 kg m^{-3}	0.68 kg m^{-3}	0.82 kg m^{-3}
SIPS variation with Q (strain/mix ratio)				
Neap – High Q – 2 PSU km^{-1}	14.57	14.17	14.17	13.08
Neap – Medium Q – 1.5 PSU km^{-1}	11.90	11.90	11.90	11.54
Neap – Low Q – 1 PSU km^{-1}	8.53	8.53	8.53	8.27
Spring – High Q – 2 PSU km^{-1}	5.86	5.75	5.75	5.44
Spring – Medium Q – 1.5 PSU km^{-1}	4.62	4.62	4.62	4.52
Spring – Low Q – 1 PSU km^{-1}	3.23	3.23	3.23	3.16

Table 6.6: Summary table for the overturning model results and the analytical scale formulas for LMER 4 and SAT 2 data.

PARAMETER	LMER 4 Station #3	SAT 2 Station #4	SAT 2 Station #5	SAT 2 Station #6
Radius of Curvature (R)	1333 m	1375 m	2583 m	1250 m
Channel Width (B)	292 m	250 m	271 m	167 m
Vertical density departure ($\Delta\rho_z$)				
Neap	4.55 kg m^{-3}	3.87 kg m^{-3}	2.01 kg m^{-3}	2.16 kg m^{-3}
Spring	1.62 kg m^{-3}	1.54 kg m^{-3}	1.30 kg m^{-3}	0.87 kg m^{-3}
Reduced gravity (g')				
Neap	0.048 m s^{-2}	0.037 m s^{-2}	0.019 m s^{-2}	0.021 m s^{-2}
Spring	0.014 m s^{-2}	0.012 m s^{-2}	0.013 m s^{-2}	0.006 m s^{-2}
Internal Froude number (Fr_i^2)				
Neap	0.85	1.11	2.16	1.95
Spring	7.73	9.01	8.32	18.03
Overturning Velocity ($\alpha = 0.55$)				
Neap	2.00 m s^{-1}	1.92 m s^{-1}	1.81 m s^{-1}	1.69 m s^{-1}
Spring	1.07 m s^{-1}	1.10 m s^{-1}	1.50 m s^{-1}	0.82 m s^{-1}
Observed Axial Velocity				
Neap	0.59 m s^{-1}	0.48 m s^{-1}	0.54 m s^{-1}	0.52 m s^{-1}
Spring	1.31 m s^{-1}	1.23 m s^{-1}	1.16 m s^{-1}	1.25 m s^{-1}
Coriolis driven secondary flow	0.45 cm s^{-1}	0.45 cm s^{-1}	0.45 cm s^{-1}	0.45 cm s^{-1}
Curvature driven secondary flow				
Neap	5.83 cm s^{-1}	5.49 cm s^{-1}	6.53 cm s^{-1}	6.25 cm s^{-1}
Spring	11.65 cm s^{-1}	10.97 cm s^{-1}	13.06 cm s^{-1}	12.50 cm s^{-1}
Density driven secondary flow				
Neap	4.86 cm s^{-1}	4.84 cm s^{-1}	3.35 cm s^{-1}	4.42 cm s^{-1}
Spring	2.90 cm s^{-1}	3.05 cm s^{-1}	2.69 cm s^{-1}	2.81 cm s^{-1}
Friction driven secondary flow				
Neap	5.84 cm s^{-1}	3.66 cm s^{-1}	5.73 cm s^{-1}	7.56 cm s^{-1}
Spring	11.24 cm s^{-1}	7.37 cm s^{-1}	10.61 cm s^{-1}	10.87 cm s^{-1}

Increases or decreases in the adjusted streamwise velocity ($\overline{u}_{adj} = \overline{u}_s \pm \overline{u}_Q$) due to changes in freshwater input can be related to changes in the vertical density gradient by using an alternate form of the Seim and Gregg (1997) model, given by the expression:

$$\Delta\rho_z \geq \left(\overline{u}_s \pm \overline{u}_Q\right)^2 \alpha \frac{\rho_o}{gh}\frac{B}{R} \quad \textbf{(6.3)}$$

where $\overline{u}_s$ is the depth-average axial velocity, $\overline{u}_Q$ is the average axial velocity due to freshwater discharge, $\alpha = \left(u_s^2 - \overline{u_s^2}\right)/\overline{u_s^2}$ is a measure of the vertical shear, which is based on the deviation between the maximum and depth-average axial current, ρ_o is an ambient reference density, B is the effective channel width (the lesser of bank to bank or bank to shoal), g is the acceleration due to gravity, h is the depth of the *thalweg*, and R is the local radius of curvature. In this form, the Seim and Gregg (1997) model gives the minimum vertical density difference necessary to shut down curvature-induced secondary circulation on ebb when $\overline{u}_s + \overline{u}_Q$ are additive and on flood when $\overline{u}_s - \overline{u}_Q$ are subtractive. As in the Satilla, centrifugal acceleration is the primary mechanism for driving secondary flows in Kill van Kull, the site where Chant (2002) observed weakened secondary flows as freshwater discharge increased. Therefore, it is possible using Equation 6.3 to estimate the minimum vertical density difference necessary to shut down curvature-induced secondary flow at ebb under different discharge conditions in both the Satilla and Kill van Kull, and to identify the states when a lower secondary circulation cell may develop.

Using a representative value of α ($\alpha \approx 0.55$) for estuaries where the maximum difference between the instantaneous and depth-average axial velocity is approximately 0.25 (Seim and Gregg 1997), the average values of ρ_o, h, and the average axial velocity

during neap and spring tides for the Satilla River (ρ_o = 1014 kg m^3, h = 10 m, $\overline{u}_s$ = 1.04 m s^{-1} at spring and $\overline{u}_s$ = 0.64 m s^{-1} at neap tides), the minimum density difference calculations for Stations 3, 4, 5, and 6 are shown in rows 13 to 18 of Table 6.5 during three discharge conditions: high (150 m^3 s^{-1}), medium (50 m^3 s^{-1}), and low (10 m^3 s^{-1}). It is apparent that as the river discharge increases, for both neap and spring tides, the minimum vertical density difference needed to shut down secondary circulation also increases, and in particular, increases more rapidly in channel reaches with a higher B/R ratio. In the case of Chant's (2002) peak river discharge observation of 300 m^3 s^{-1}, using Equation 6.3 and assuming B = 250 m, h = 10 m, and the average axial velocity ($\overline{u}_s$) as given as above, a vertical density difference of $\Delta\rho_z$ = 0.84 kg m^{-3} would be necessary to halt curvature-induced secondary flow during neap tide while a vertical density difference of $\Delta\rho_z$ = 2.09 kg m^{-3} would be necessary to halt curvature-induced secondary flow during spring tide. Density profiles collected during the LMER 4 experiment (*cf.* Figure 5.4) show that the maximum vertical density gradient observed during neap tides is approximately $\Delta\rho_z$ = 5.1 kg m^{-3} and that during spring tides is on the order of $\Delta\rho_z$ = 1.14 kg m^{-3}, suggesting that the addition of freshwater discharge alone could be sufficient to weaken or halt secondary flow driven by centrifugal acceleration. As a result, during high discharge conditions, the strength of curvature-driven secondary flow is more likely to be weaker, while during low discharge conditions, curvature-driven secondary flow is more likely to be halted, and a lower secondary circulation cell may develop. The impact of changes in river flow on curvature-driven secondary circulation during intermediate river discharge conditions is unclear. However, it is possible that during times of intermediate freshwater input,

secondary flow at spring tide would have features that resemble those during high discharge conditions, while secondary flow at neap tide would resemble those during low discharge conditions. As seen in Table 6.5, the impact of changes in freshwater discharge, alone, can generate a sufficient vertical density gradient to modify the strength and the character of secondary flows.

In addition to changes in river discharge, the form and strength of curvature-driven secondary flow can be modified during ebb tide by tidal straining or SIPS, strain-induced periodic stratification (Simpson et al. 1990). Tidal straining, due to the interaction of the sheared axial currents with the longitudinal salinity gradient modulates the tidal salinity by amplifying the vertical stratification on ebb and reducing the vertical stratification on flood. As a result, secondary flow driven by centrifugal acceleration, in addition to being sensitive to changes in river discharge, is likely to be modified by SIPS during the ebb phase of the tidal cycle. The importance and strength of tidal straining is determined by comparing the effect of tidal mixing to tidal straining, given by the following expression:

$$\frac{1}{\rho_o}\frac{\partial \rho}{\partial x} > 2.2x10^{-5}\left(\frac{\overline{u}_{adj}}{h}\right)^2 \quad \textbf{(6.4)}$$

where $\frac{1}{\rho_o}\frac{\partial \rho}{\partial x}$ represents the axial density gradient (an indicator of tidal straining) and $\left(\frac{\overline{u}_{adj}}{h}\right)^2$ represents the strength of tidal mixing relative to the axial velocity and channel depth (Simpson et al. 1990). The ratio of SIPS to tidal mixing (the strain/mix ratio in Table 6.5) for the three discharge conditions and the associated axial salinity gradient

($\frac{\partial s}{\partial x}$ = 2 PSU km^{-1} for Q_f = 150 m^3 s^{-1}, $\frac{\partial s}{\partial x}$ = 1.5 PSU km^{-1} for Q_f = 50 m^3 s^{-1}, and $\frac{\partial s}{\partial x}$ = 1 PSU km^{-1} for Q_f = 10 m^3 s^{-1}) relative to changes in river discharge observed during the LMER 4 and SAT 2 experiments (*cf.* Section 6.3.1) are shown in rows 20-25 of Table 6.5. These calculations were done using Equation 6.4 and assuming $\rho_o = 1014$ kg m^{-3}, h = 10 m, and $\overline{u}_{adj} = \overline{u}_s + \overline{u}_Q$ from Table 6.5 rows 10 and 11 is the adjusted streamwise velocity for neap and spring tides due to changes in river discharge. Table 6.5 demonstrates that the importance of tidal straining over tidal mixing increases as the axial tidal velocity decreases and the freshwater discharge increases, such that SIPS is maximized at neap tide under high discharge conditions. These calculations, in combination with the vertical density difference calculations, suggest that curvature-driven secondary flow would be reduced during high discharge conditions, due to the increase in freshwater input and to SIPS, particularly during the ebb phase of the tide.

6.3.5 Seim and Gregg Curvature-Induced Overturning Model

The Seim and Gregg (1997) overturning model provides a rigorous approach to evaluating the interaction between the depth-varying lateral baroclinic gradient and the barotropic curvature-induced secondary flow. As discussed in Chapter 3, this model is based on a steady-state balance between centrifugal acceleration and the tidally-generated lateral baroclinic density gradient in a channel bend. In a curved reach, this model determines the minimum axial velocity necessary to overcome the lateral baroclinic density gradient and mix the water column by turbulent exchange. It is expressed by

$$\overline{u_s^2} \geq \frac{1}{\alpha}\frac{R}{B} g'h \quad \textbf{(6.5)}$$

where $\overline{u}_s$ is the depth-average streamwise velocity, R is the local radius of curvature, B is the effective channel width (the lesser of bank to bank or bank to shoal), g′ is reduced gravity, h is the depth of the *thalweg*, and alpha, α , is a measure of the vertical shear (*cf.* Section 6.3.4). As demonstrated in Chapter 5, the Seim and Gregg (1997) model can explain the observed fortnightly changes in secondary flow driven by centrifugal acceleration, the dominant mechanism for driving lateral flows in the Satilla River. The focus of this section is to apply and determine the applicability of the Seim and Gregg (1997) model to the moorings at Station 3, 4, 5, and 6, a series of different channel reaches (*cf.* Figure 6.2), with local curvature ranging from highly curved (R/B ≈ 4.6) to nearly straight (R/B ≈ 9.5). Using a representative value of α ($\alpha \approx 0.55$), h = 10 m, and observed values for reduced gravity, g′, associated with neap and spring tides (rows 7 and 8 of Table 6.6), the *minimum axial overturning velocity*, $\overline{u}_{s,over}$ **,** for Stations 3, 4, 5, and 6, varies between 1.69 m s^{-1} and 2.00 m s^{-1} for neap tides and between 0.82 m s^{-1} and 1.50 m s^{-1} for spring tides. The calculated results using the Seim and Gregg (1997) curvature-induced overturning model and the *observed axial velocity*, u_s **,** at Stations 3, 4, 5, and 6 are summarized in rows 12 through 17 of Table 6.6.

As discussed in Chapter 5, given sufficient vertical stratification, it is possible for the lateral baroclinic pressure gradient to temporarily shut down part or all of the barotropic curvature driven secondary circulation. This result implies that during neap tides, overturning can be reduced, if not halted, by the interaction of the baroclinic vertical density gradient and the barotropic centrifugal acceleration, thereby maintaining a coherent density structure in the deep channel around the channel bend. From the calculated results of Equation 6.5 shown in Table 6.6, it appears that the observed axial

velocity shown in rows 16 and 17 is insufficient to overcome the lateral baroclinic density gradient, the calculated equivalent of the overturning velocity shown in rows 13 and 14, such that curvature-induced secondary flow can be halted at neap tides for Stations 3, 4, 5, and 6, and not at spring tides, except for Station 5. Unlike Stations 3, 4, and 6, the Seim and Gregg (1997) model at Station 5 suggests that the lateral baroclinic pressure gradient is sufficient to halt curvature-induced secondary flow during both neap and spring tides. This unusual result is due to a limitation of the Seim and Gregg (1997) model, which was developed for moderately curved domains (R/B $\leq \sim 8$). The mooring at Station 5 is located in the *thalweg* of a straight reach in the Satilla River, with R/B $\approx$ 9.5. While the Seim and Gregg (1997) model explains the general differences observed in curvature-driven secondary flow on the fortnightly time scale, additional processes that govern secondary flow (i.e., density and friction) must be considered when applying it to either weakly curved channels or straight reaches. The next section explores scales estimates of secondary flow, as a first step in extending the Seim and Gregg (1997) model to include the effects of either weakly curved channels or straight reaches.

6.3.6 Scale Estimates of Secondary Circulation

Scale estimates are useful first-order approximations in evaluating the strength of secondary flows as well as determining the relative importance of mechanisms that drive such flows. As developed in Chapter 3, the revised scale parameter formulas for determining the strength of secondary flow by Coriolis and centrifugal accelerations, the differential advection of density, and frictional steering are given respectively as follows:

$$U_{n,Coriolis} \approx 6fh \quad \textbf{(6.6)}$$

$$U_{n,curve} \approx \frac{12\left|\bar{U}_s\right|h}{R} \quad \textbf{(6.7)}$$

$$U_{n,density} \approx \frac{1}{16}\left(\sqrt{\frac{g'h}{C_D B}}\right) \quad \textbf{(6.8)}$$

$$U_{n,friction} \approx \frac{1}{16}\frac{1}{fh} C_D u_{s,1mab}^2 \quad \textbf{(6.9)}$$

where f is the Coriolis parameter and h is the depth of the *thalweg*, $\bar{U}_s$ is the depth-averaged streamwise velocity, R is the local radius of curvature, g′ is reduced gravity, C_D is the drag coefficient, B is the effective channel width (the lesser of bank to bank or bank to shoal distance), and $u_{s,1mab}$ is the axial velocity at one meter above the bottom (mab). The results of Equations 6.6 through 6.9 applied to the mooring data at Stations 3, 4, 5, and 6 are shown in rows 18 – 27 of Table 6.6, by using the values of R, B, and g′ as given in Table 6.6 for each Station, by assuming that h = 10 m, f = 7.5114 x 10^{-5} s^{-1}, and C_D = 2.5 x 10^{-3}, and that $\bar{U}_s$ and $u_{s,1mab}$ are the calculated average value at each mooring over a three day period for both neap and spring tides.

As depicted in Table 6.6, the revised analytical scaling formulas suggest that the primary mechanisms for driving secondary circulation at Stations 3, 4, 5, and 6 are curvature, friction, and the differential advection of density. These results show that Coriolis-driven secondary flow is an order of magnitude smaller than secondary flow driven by curvature, friction, or density at all Stations for both neap and spring tides, which implies that Coriolis acceleration is not an important mechanism for driving secondary circulation in these reaches of the Satilla River. In contrast, secondary circulation driven by curvature dominates at all Stations for spring tide and at Stations 4 and 5 for neap tide, while secondary circulation driven by friction dominates for neap tide at Stations 3 and 6. Based on the scale estimate results in Table 6.6, friction (rows 25-27)

is the second most important mechanism for driving secondary flow at Stations 3, 5, and 6 for both spring and neap tides as well as for Station 4 during spring tides, whereas density (rows 22-24) is the most important mechanism for driving secondary flow at Station 4 for neap tides. The strength of curvature-driven (rows 19-21) and frictionally-driven (rows 25-27) secondary flow are approximately twice as strong during spring tides as during neap tides, in contrast to density-driven secondary flow (rows 22-24) which changes by only a few centimeters per second between spring and neap tides and is similar in magnitude to secondary flows during neap tide driven by channel curvature and friction.

Based on the results of the analytical scale formulas for secondary flow (Equations 6.6 through 6.9), it appears that there is a shift between neap and spring tides on the relative importance of mechanisms that drive secondary flow, from a two-way balance between curvature and friction during neap tides to a three-way balance between curvature, friction, and density during spring tides. While the scale estimate results suggest that there is a three-way balance of mechanisms that drive secondary flow at spring and a two-way balance of mechanisms that drive secondary flow at neap, it is clear that some knowledge of the site location is necessary *apriori* for properly interpreting scale estimate results and that such scaling formulas should be used to assess the 'relative' importance of physical processes that drive secondary flow. For example, the mooring at Station 5 is located in a straight reach of the Satilla River, and as discussed in the previous section, is not subject to strong curvature effects. However, without prior knowledge of this site, the scaling parameter, which is only a function of R, not a relative ratio such as R/B, suggests that secondary flow in this reach driven by centrifugal

acceleration would dominate over both friction and density effects and would be stronger than at any other mooring location. Consequently, it is more plausible to expect a shift from a two-way balance between curvature and friction at spring tide when density effects are less important, unless under high discharge conditions, to a three-way balance between curvature, friction, and density at neap tide when density effects, as seen earlier in Section 6.3.4, can play a significant role in modifying the character of secondary flows.

Despite the limitations in using analytical scaling formulas, they provide a useful tool in quickly evaluating the strength and the physical importance of secondary flows driven by channel curvature, the Coriolis effect, friction, and the differential advection of density. These simple scaling parameters can be easily applied to a number of different channel reaches or to a number of different estuaries for direct comparison in a consistent straightforward manner. The next section uses the secondary flow scaling results from the Satilla as a basis to extend the combined work of Geyer (1993b), Dronkers (1996), and Seim and Gregg (1997). This extension is done by developing a more inclusive model based on the lateral momentum balance, the terms of which are determined by the relative importance of the secondary flow scaling values, in an effort to better describe the lateral dynamics under a wide variety of conditions in the Satilla River estuary.

6.3.7 Lateral Momentum Balance Model for the Satilla River, Georgia

While the Seim and Gregg (1997) curvature-induced overturning model is a good first-order approximation to explain the lateral dynamics in the highly curved reaches of the Satilla River, it does not apply equally well to all sections of the river (particularly straight reaches) or at all places in a channel cross-section (away from the *thalweg*). For

this reason and based on scale estimates for secondary flow in the Satilla River (*cf.* Table 6.6), a balance between the centrifugal acceleration (CA), the lateral pressure gradient force (LBC), and vertical shear stress divergence (VSS) is explored as a more versatile lateral momentum balance for this river. The effect of the Coriolis acceleration (CF) is added to this balance, despite its weak nature in the Satilla, for model portability. It is expected that there will be a shift in the balance of terms (from CA ≈ LBC and/or CA ≈ LBC + VSS at neap tides to CA ≈ VSS at spring tides) in the lateral momentum balance model for the Satilla, because of the river's sinuous nature, its variable density structure, and its bathymetric features. Formulated in this manner, the results of this investigation can be directly compared with other estuarine studies that use the lateral momentum balance for their framework.

The lateral momentum balance model (LMBM) extends the work of Geyer (1993b), Dronkers (1996), and Seim and Gregg (1997) by combining the effects of the lateral density gradient, bottom stress, channel curvature, and planetary rotation to enhancing or limiting secondary circulation. This model formulation was chosen because it combines the effects of the deep channel (where most of the momentum is captured in the *thalweg* and subject to the strongest lateral baroclinic gradient) and the effects away from the deep channel in the region of the shoals and shallows as well as being applicable in straight or highly curved channel reaches. An attractive feature of this model formulation is that it accounts for the effects of secondary flow regardless of instrument position in a channel cross-section of variable curvature: either in the deep channel or in the shoal region. In practical application, an additional benefit, as it is often difficult to precisely determine the location of a submerged instrument.

The depth-dependent lateral momentum balance in natural coordinates for stratified flow in a curving channel is given by Equation 6.10 as follows:

$$\frac{\partial u_n}{\partial t} + u_s \frac{\partial u_n}{\partial s} + f u_s - \frac{u_s^2}{R} + g \frac{\partial \eta}{\partial n} = -\frac{g}{\rho_o} \int_z^\eta \frac{\partial \rho}{\partial n} dz + \frac{\partial}{\partial z}\left(A_z \frac{\partial u_n}{\partial z} \right) \quad \textbf{(6.10)}$$

Depth-averaging (indicated by the overbar) Equation 6.10 yields Equation 6.11.

$$\frac{\partial \overline{u}_n}{\partial t} + \overline{u_s \frac{\partial u_n}{\partial s}} + f\overline{u}_s - \frac{\overline{u_s^2}}{R} + g \frac{\partial \eta}{\partial n} = -\frac{g}{\rho_o} \frac{\partial \overline{\rho}}{\partial n} h - \frac{\tau_{n,b}}{\rho_o h} \quad \textbf{(6.11)}$$

Subtracting Equation 6.11 from Equation 6.10 and substituting

$$\frac{\tau_n}{\rho_o} = \left[A_z \frac{\partial u_n}{\partial z} \right]_{z=-h} \quad \textbf{(6.12)}$$

yields Equation 6.13, which eliminates the contribution of the barotropic water slope, a difficult parameter to measure or estimate accurately.

$$\frac{\partial \left(u_n - \overline{u}_n \right)}{\partial t} + u_s \frac{\partial u_n}{\partial s} - \overline{u_s \frac{\partial u_n}{\partial s}} + f\left(u_s - \overline{u}_s \right) - \frac{\left(u_s - \overline{u_s^2} \right)}{R} =$$

$$= -\frac{g}{\rho_o} \int_z^\eta \frac{\partial \rho}{\partial n} dz + \frac{g}{\rho_o} \frac{\partial \overline{\rho}}{\partial n} h + \frac{\partial}{\partial z}\left(\frac{\tau_n}{\rho_o} \right) + \frac{\tau_{n,b}}{\rho_o h} \quad \textbf{(6.13)}$$

The potential for steady-state conditions is determined by T_{bc}, the baroclinic adjustment time, the time scale associated with an inviscid balance between centrifugal acceleration and the lateral baroclinic gradient. T_{bc} can be evaluated using the expression:

$$T_{bc} = \frac{B}{\sqrt{g'h}} \quad \textbf{(6.14)}$$

where B is the channel width, *g'* is reduced gravity, and h is the depth of the *thalweg*

(Chant and Wilson 1997; Lacy and Monismith 2001). Likewise, the potential to neglect advective acceleration is determined by comparing the frictional relaxation time scale,

$$T_f = \frac{L_s}{\overline{u}_s} \quad \textbf{(6.15)},$$

the time associated with the generation or destruction of a secondary circulation (Kalkwijk and Booij 1986; Geyer 1993), to the advective time scale,

$$T_{adv} = \frac{L_s}{\overline{u}_s \Delta u_n} \quad \textbf{(6.16)},$$

the time associated with the advection of the secondary circulation downstream. In Equations 6.15 and 6.16, L_s is the length scale of the axial flow field, $\overline{u}_s$ is the depth-average streamwise velocity, and Δu_n is the change in the normal (lateral) velocity over the distance L_s (Geyer 1993).

For the Satilla River, T_{bc} ranges between 10 minutes at spring tides and 19 minutes at neap tides, indicating that a steady-state assumption is possible and that the secondary circulation is quasi-stationary with respect to semidiurnal forcing. Similarly, $T_f \approx 24$ minutes and $T_{adv} \approx$ 96 minutes, indicating that secondary circulations are generated more quickly than they are advected downstream ($T_f > T_{adv}$), and in this model formulation, advective accelerations can be neglected.

Assuming steady-state conditions and neglecting advective acceleration, the lateral momentum balance model (LMBM) for stratified flow in a curving channel in natural coordinates reduces to the following expression:

$$f\left(u_s - \overline{u}_s\right) - \frac{\left(u_s^2 - \overline{u_s^2}\right)}{R} = -\frac{g}{\rho_o}\int_z^\eta \frac{\partial \rho}{\partial n} dz + \frac{g}{\rho_o}\frac{\partial \overline{\rho}}{\partial n} h + \frac{\partial}{\partial z}\left(\frac{\tau_n}{\rho_o}\right) + \frac{\tau_{n,b}}{\rho_o h} \quad \textbf{(6.17)}$$

where the first and second terms in Equation 6.17 are secondary flow driven by the imbalance between the depth-dependent and the depth-average Coriolis and centrifugal acceleration, respectively, the third term is the lateral baroclinic pressure gradient, the fourth term is the depth-average lateral baroclinic pressure gradient, the fifth term is a Reynolds parameterization of vertical shear stress divergence, and the sixth term is bottom shear stress. In Equation 6.17, bottom shear stress is expressed as

$$\tau_{n,b} = \rho_o C_D \left| u_{n,1mab} \right| u_{n,1mab} = \frac{1}{16} \rho_o C_D \left| u_{s,1mab} \right| u_{s,1mab} \quad \textbf{(6.18)}$$

to account for the contributions of the lateral velocity (which can be approximated by scaling the axial velocity) to the observed shear stress. A full development of the lateral momentum balance model for the Satilla River is detailed in Appendix A.

Equation 6.17 is used to investigate and evaluate the lateral momentum balance at Stations 3 over a 32.5-day period and over a 38.7-day period at Stations 4, 5, and 6, each covering two full neap and two full spring tides. In Equation 6.17, the depth-average lateral baroclinic gradient and bottom shear stress are assumed to represent respectively, the importance of the depth-dependent lateral baroclinic gradient and vertical shear stress. Thus, Equations 6.17 and 6.18 are used to directly evaluate the calculated balance between the centrifugal acceleration (term 2) and the sum of the Coriolis acceleration (term 1), the depth-average lateral baroclinic gradient (term 4), and the bottom shear stress (term 6) with the Satilla River data sets. The results of the lateral momentum balance model applied to the mooring data at Stations 3, 4, 5, and 6 are illustrated by Figures 6.11 through 6.14. The link between changes in freshwater discharge to changes in the density field is illustrated by the scaled black line (Q_f/1 x 10^7) plotted on Figures 6.11 through 6.14.

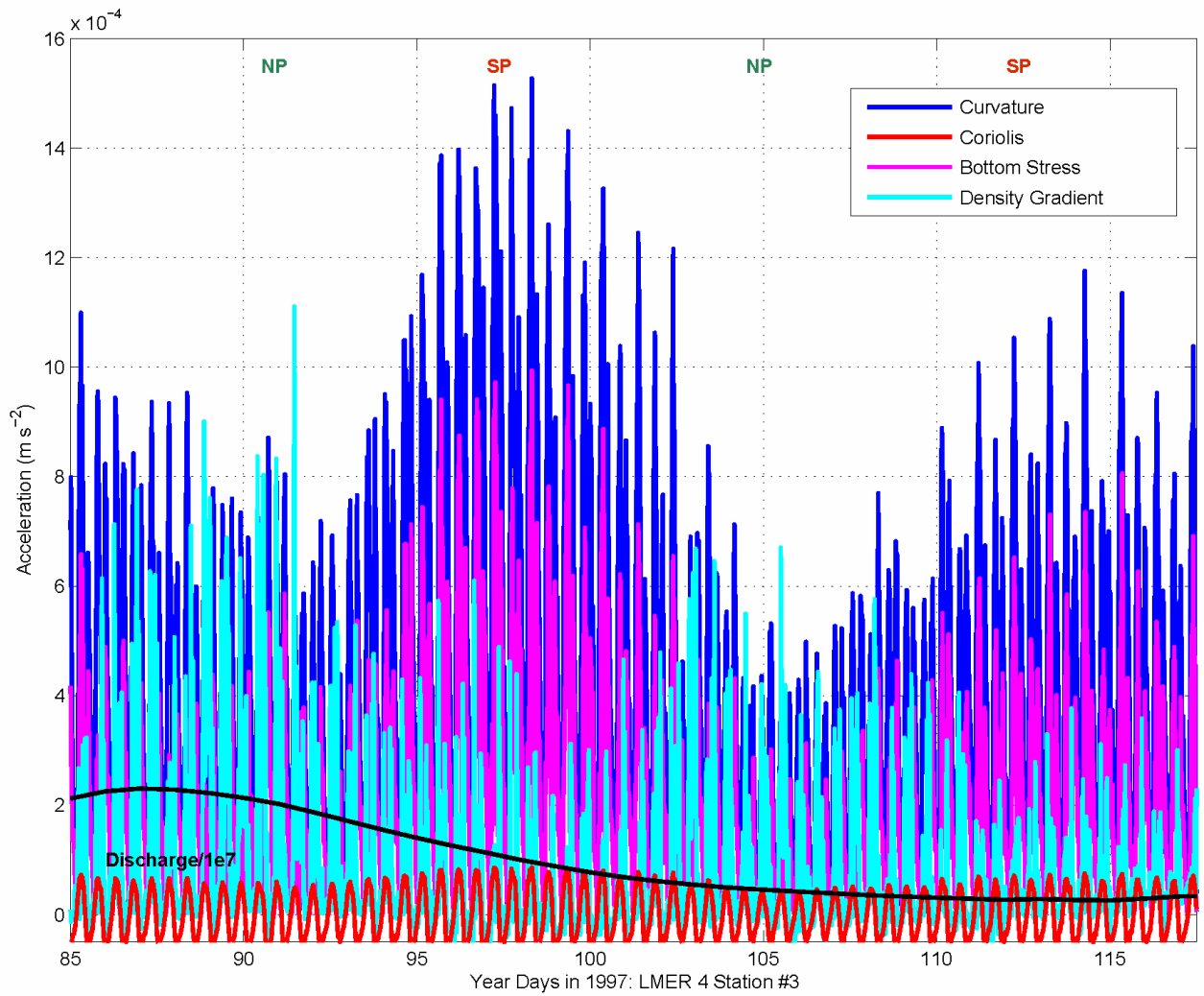

Figure 6.11: Satilla River lateral momentum balance terms for LMER 4 Station #3. Freshwater discharge has been divided by 1 x 10^7 and plotted as a solid black line. Neap and spring tides are indicated by NP and SP, respectively.

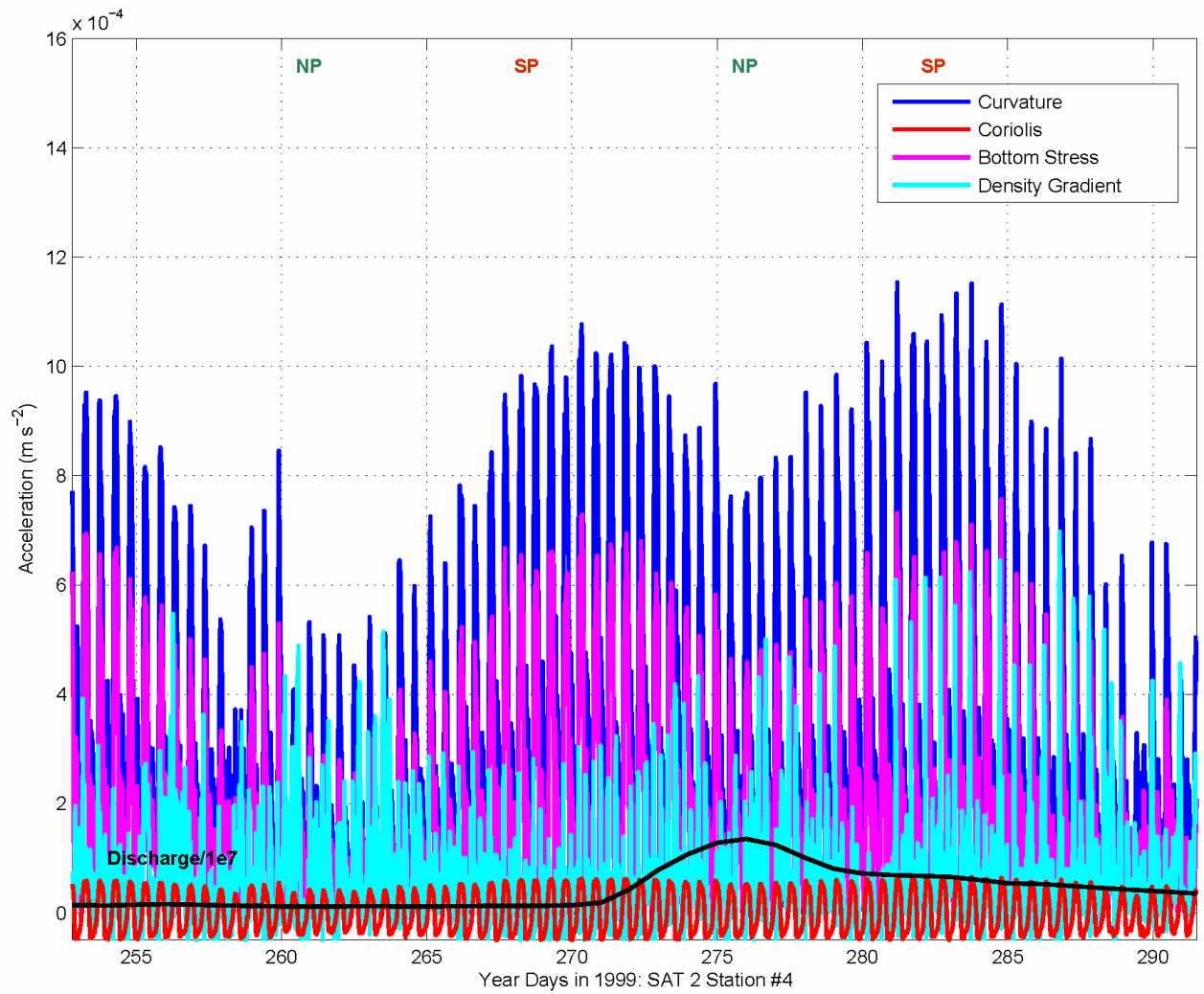

Figure 6.12: Satilla River lateral momentum balance terms for SAT 2 Station #4. Freshwater discharge has been divided by 1 x 10^7 and plotted as a solid black line. Neap and spring tides are indicated by NP and SP, respectively.

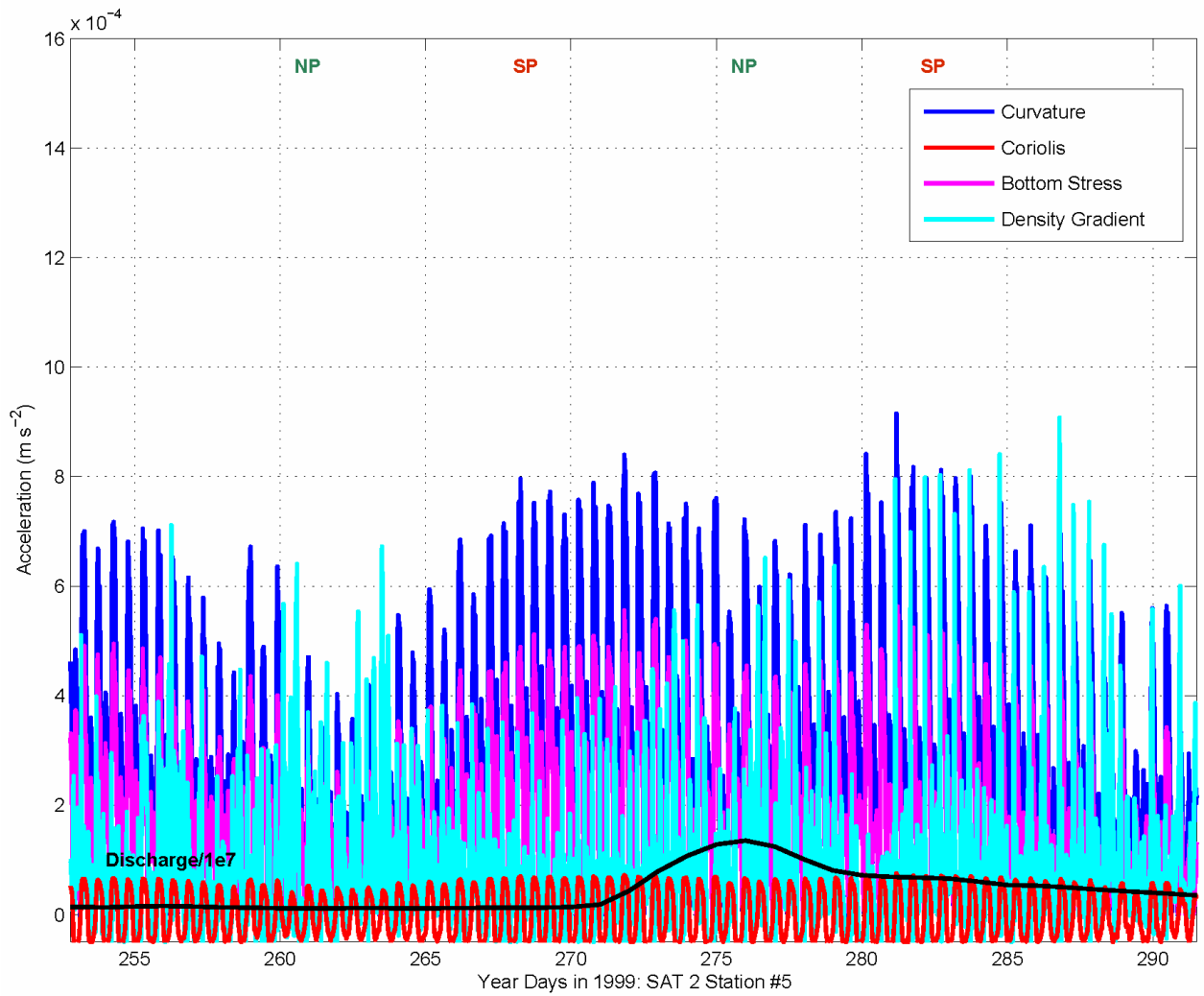

Figure 6.13: Satilla River lateral momentum balance terms for SAT 2 Station #5. Freshwater discharge has been divided by 1 x 10^7 and plotted as a solid black line. Neap and spring tides are indicated by NP and SP, respectively.

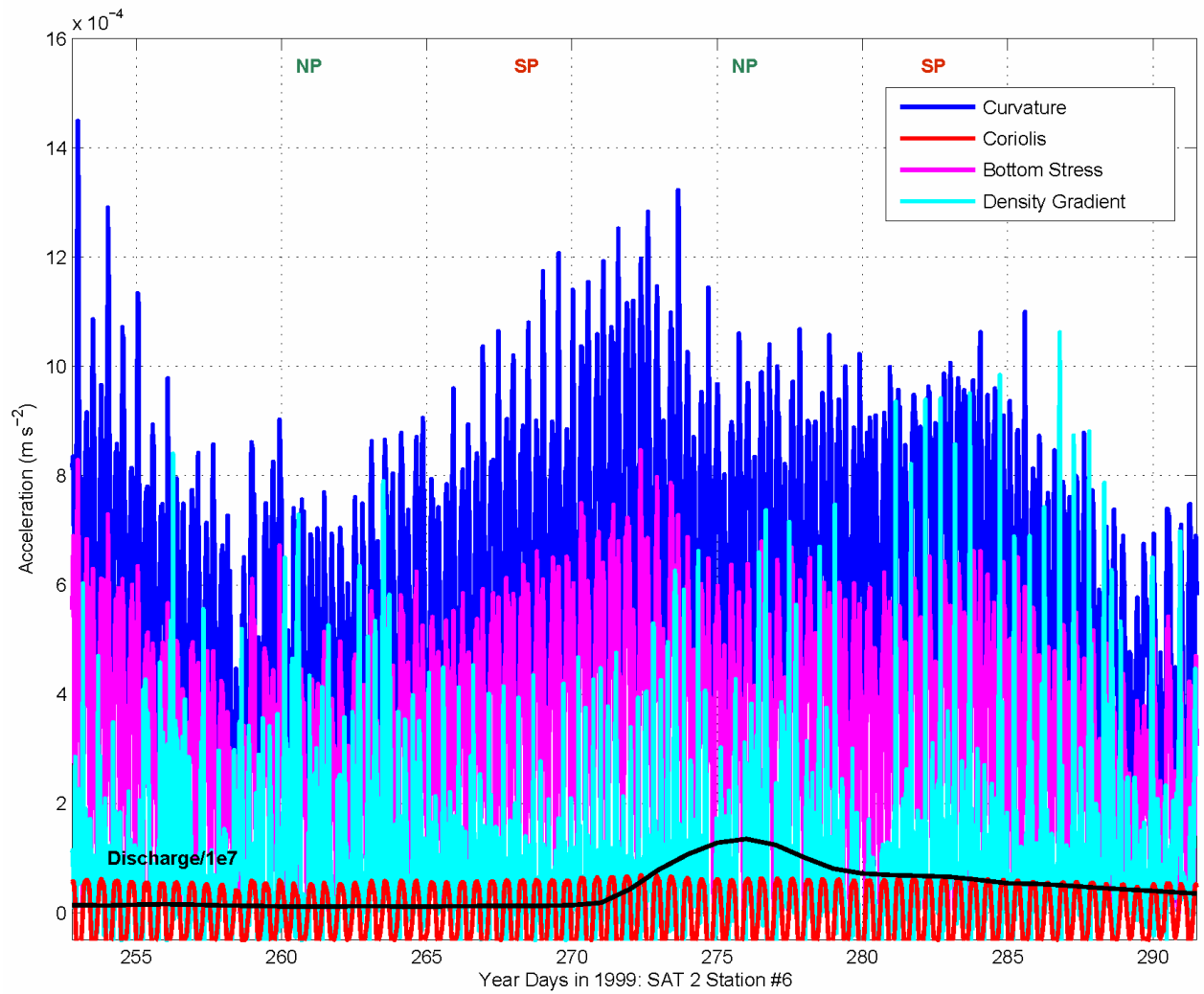

Figure 6.14: Satilla River lateral momentum balance terms for SAT 2 Station #6. Freshwater discharge has been divided by 1 x 10^7 and plotted as a solid black line. Neap and spring tides are indicated by NP and SP, respectively.

Table 6.7: Summary of calculated values and 95% confidence intervals for the lateral momentum balance model applied to the LMER 4 and the SAT 2 mooring data. The bold highlighted values indicate the balance of terms for a given choice of C_D.

STATION	$\left(\frac{u_s^2 - \overline{u_s^2}}{R}\right) =$	$f\left(u_s - \overline{u}_s\right) +$	$\frac{g}{\rho_o}\frac{\partial \overline{\rho}}{\partial n} +$	$\frac{\tau_{n,b}}{\rho_o h}$
LMER 4 Station 3				
Spring – low C_D (m s^{-2})	**4.2e-4 ± 1.5e-4**	7.2e-6 ± 2.7e-6	**5.6e-5 ± 6.5e-5**	**1.3e-4 ± 4.2e-5**
Neap – low C_D (m s^{-2})	**2.5e-4 ± 8.1e-5**	4.3e-6 ± 2.1e-6	**1.9e-4 ± 1.1e-4**	6.4e-5 ± 2.0e-5
Neap – adj low C_D (m s^{-2})	**2.5e-4 ± 8.1e-5**	4.3e-6 ± 2.1e-6	**1.9e-4 ± 1.1e-4**	**1.1e-4 ± 2.4e-5**
SAT 2 Station 4				
Spring – low C_D (m s^{-2})	**2.3e-4 ± 9.0e-5**	3.7e-6 ± 2.1e-6	3.7e-5 ± 3.1e-5	**9.6e-5 ± 3.1e-5**
Neap – low C_D (m s^{-2})	**1.2e-4 ± 5.4e-5**	1.3e-6 ± 1.5e-6	**7.8e-5 ± 6.6e-5**	4.8e-5 ± 1.8e-5
Neap – adj low C_D (m s^{-2})	**1.2e-4 ± 5.4e-5**	1.3e-6 ± 1.5e-6	**7.8e-5 ± 6.6e-5**	**8.2e-5 ± 2.2e-5**
SAT 2 Station 5				
Spring – low C_D (m s^{-2})	**1.7e-4 ± 5.8e-5**	2.7e-6 ± 2.5e-6	4.2e-5 ± 3.5e-5	**1.1e-4 ± 2.8e-5**
Neap – low C_D (m s^{-2})	**9.4e-5 ± 4.1e-5**	4.7e-7 ± 1.8e-7	**8.8e-5 ± 7.5e-5**	6.1e-5 ± 2.1e-5
Neap – adj low C_D (m s^{-2})	**9.4e-5 ± 4.1e-5**	4.7e-7 ± 1.8e-7	**8.8e-5 ± 7.5e-5**	**1.1e-4 ± 2.6e-5**
SAT 2 Station 6				
Spring – low C_D (m s^{-2})	**3.4e-4 ± 9.2e-5**	7.1e-7 ± 2.5e-7	**6.0e-5 ± 5.1e-5**	**1.3e-4 ± 2.9e-5**
Neap – low C_D (m s^{-2})	**2.4e-4 ± 7.9e-5**	1.4e-6 ± 2.1e-6	**1.3e-4 ± 1.1e-4**	**9.1e-5 ± 2.4e-5**
Neap – adj low C_D (m s^{-2})	**2.4e-4 ± 7.9e-5**	1.4e-6 ± 2.1e-6	**1.3e-4 ± 1.1e-4**	**1.5e-4 ± 3.0e-5**
Station Parameters	***LMER 4 Stn 3***	***SAT 2 Stn 4***	***SAT 2 Stn 5***	***SAT 2 Stn 6***
Minimum Depth (m)	7.9	6.4	8.0	7.0
Mean Depth (m)	9.5	7.9	9.6	8.5
Maximum Depth (m)	11.0	9.2	10.8	9.6
Station Channel Width (m)	292	250	271	167
Station Radius of Curvature (m)	1333	1375	2583	1250
Ratio of B/R	0.22	0.18	0.10	0.13

*low C_D = 3.1 x 10-3 is from Geyer et al. (2000) and Soulsby (1990) for muddy bottom estuaries;
adjusted low $C_D = 5.0 \times 10^{-3}$ is from Fischer et al. (1979) for flow over rough topography

As expected, the contribution of the Coriolis effect to the lateral momentum balance model is weak at all Stations (Figures 6.11 – 6.14). All Stations show a clear fortnightly shift, most prominent at Station 3, in the strength of the curvature, bottom stress, and the lateral density gradient terms of the lateral momentum balance. At Station 3, the dominant terms during both the first and second spring tides are curvature and bottom stress, while during the two neap tides; the dominant terms, which are in near balance, are curvature and the lateral density gradient, as predicted by the Seim and Gregg (1997) model. Likewise, a change in the duration and modulation of the lateral density gradient between spring and neap tides is the strongest at Station 3, as was expected from observations of the subtidal lateral velocity data (Figure 6.11). Changes in freshwater discharge at this Station do not appear to significantly affect the strength of either the curvature term or the lateral density gradient term. At Station 4, as predicted by the analytical scale analysis, the primary balance during both spring tides is between curvature, bottom stress, and the lateral density gradient, with a stronger response in the lateral density gradient during the second spring tide. In contrast, during the first neap tide, the dominant terms are curvature and the lateral density gradient when river discharge was low, while during the second neap tide, when there was an increase in the freshwater input, the primary balance shifted to one between curvature, bottom stress, and the lateral density gradient. From Figure 6.12, changes in freshwater input at Station 4 appear to have nearly doubled the strength of the curvature term, (which is likely a function of increased water volume), while only slightly reducing the lateral density gradient, such that there was a shift from two dominant terms to three. At Station 5, located in the nearly straight reach of the Satilla, the primary balance during the first

spring tide is between curvature, bottom stress, and the lateral density gradient, while during the second spring tide, shortly after an increase in river discharge, the dominant terms, curvature and the lateral density gradient nearly balance which is puzzling. It is likely that the increase in freshwater discharge enhanced the lateral density gradient term, which as a result, masked the contribution to the acceleration due to bottom stress. Similarly, during the first neap tide, the dominant terms are curvature and the lateral density gradient are nearly in balance, in contrast to the second neap tide when the dominant terms shift over the tidal cycle from curvature, bottom stress, and the lateral density gradient to curvature and the lateral density gradient. The impact of freshwater discharge at this Station is difficult to determine, however, it appears as with Station 4, that the increase in river discharge enhances the strength of the curvature term, while weakly modifying the lateral density gradient term. As discussed in the previous section, neither the Seim and Gregg (1997) model nor the analytical scale estimates suitably describe the observed lateral dynamics at Station 5. However, the results of the lateral momentum balance model (LMBM) agree reasonably well with the weakly curved observed flows at this site (*cf.* Figure 6.10), thereby making it a candidate for assessing secondary flows under a wide variety of conditions. At Station 6, the curved narrow reach beyond the triple junction just past Station 5 (*cf.* Figure 6.1), the primary balance during the first spring tide is between curvature, bottom stress, and the lateral density gradient, while during the second spring tide, the dominant terms shift over the tidal cycle from a balance between curvature and the lateral density gradient to a balance between curvature, bottom stress, and the lateral density gradient, as expected from scale estimates. Alternatively, during both neap tides the dominant terms are curvature, bottom

stress, and the lateral density gradient, as estimated by the analytical scaling formulas, with a reduced contribution by the lateral density gradient term during the second neap tide. At Station 6, the influence of river discharge is uncertain, but it appears that a freshwater pulse at this site during the second neap tide initially weakens the lateral density gradient and subsequently enhances it during the second spring tide, which is in agreement with the estimated impact of tidal straining and changes in freshwater input as discussed in Section 6.3.4.

A summary of the calculated results and error analysis by applying the lateral momentum balance model (LMBM) to the BB ADCP and the WH ADCP data at Stations 3 – 6 during neap and spring tides is shown in Table 6.7, where columns 2 and 3 are respectively the acceleration due to curvature and the Coriolis effect, column 4 is the acceleration due to the lateral baroclinic density gradient, and column 5 is the acceleration due to bottom stress. The bold highlighted values in Table 6.7 indicate the balance of terms for a given choice of C_D. The selection of 'best fit' values for R, B, and C_D and the limitations of the LMBM are discussed in the next section.

As seen in Table 6.7, there is a shift in the balance of terms at each Station between spring and neap tides relative to the choice of the drag coefficient. At Stations 3 and 6, there is a three-way balance at spring tides between curvature, a weak lateral density gradient, and bottom stress, while for spring tides at Stations 4 and 5, there is a two-way balance between curvature and bottom stress. In contrast, at neap tide, there is a shift at Stations 3, 4, and 5 from a two-way balance given a 'low C_D' value to a three-way balance for a higher 'adjusted low C_D' value, found necessary to close the lateral momentum balance. The balance of terms at Station 6 does not shift with a change in the

choice of C_D, as there is a three-way balance between curvature, the lateral density gradient, and bottom stress for both the 'low' and 'adjusted low' values of C_D. The variations in the balance of terms between neap and spring tides and with changes in the drag coefficient are likely due to the influence of form drag in a stratified fluid (MacCready et al. 2003; Sutherland et al. 2004). Recall, that C_D, incorporates the effects of both skin friction and form drag, and that the latter, rather than the former, has been found to be more important in modifying flow fields (Coleman et al. 2000; Nash and Moum 2001; MacCready et al. 2003). Further discussion of the LMBM and its sensitivity to the choice of C_D will follow after a brief discussion of the associated error analysis.

The 95% confidence intervals included in Table 6.7 for each term in the lateral momentum balance model were calculated separately for neap and spring tide at each Station. At Station 3, the 95% confidence interval was calculated with 576 samples per neap and per spring tide, and at Stations 4, 5, and 6, the 95% confidence interval was calculated with 720 samples per neap and per spring tide.

6.3.8 Lateral Momentum Balance Model Sensitivity Analyses and Limitations

The simple lateral momentum balance model (LMBM) evaluated at Station moorings 3, 4, 5, and 6, and expressed by the following:

$$f\left(u_s - \overline{u}_s\right) - \frac{\left(u_s^2 - \overline{u_s^2}\right)}{R} = \frac{g}{\rho_o}\frac{\partial \overline{\rho}}{\partial n}h + \frac{\tau_{n,b}}{\rho_o h} \quad \textbf{(6.19)}$$

appears sufficient to explain the observed changes in secondary flow on the fortnightly time scale in the Satilla in a variety of differently curved channel reaches. Nonetheless, it is important to explore the limitations of this model for three primary reasons: first, to

assess how small changes in the choice of scalar quantities (R, B, $\partial\overline{\rho}_z$, and C_D) affect the results of the LMBM, second, to determine and evaluate the appropriate choice of the scalar variables R, B, and C_D, and third, to explore the validity of neglecting other physical processes (such as advective accelerations) in this model formulation of the lateral momentum balance.

Sensitivity analyses were done to determine the impact of small changes in the values of R, B, $\partial\overline{\rho}$, and C_D on the resultant estimated terms of the lateral momentum balance model. Four values of the drag coefficient, C_D, were tested at each station location: $C_D = 2.5 \times 10^{-3}$ from Seim et al. (2002) a 'classical value' and referred to as the 'original C_D', $C_D = 3.1 \times 10^{-3}$ from Geyer et al. (2000) and Soulsby (1990) for muddy bottom estuaries referred to here as the 'low C_D', $C_D = 5.0 \times 10^{-3}$ from Fischer et al. (1979), referred to as the 'adjusted low C_D', and $C_D = 8.1 \times 10^{-3}$ chosen as an arbitrary high value, referred to here as the 'adjusted C_D'. Likewise, four values of the radius of curvature, R, were tested for each location: the 'original R' measured as the local radius of curvature referencing the channel center-line relative to the bank to bank distance on a bathymetric chart, one-half R calculated as half of the original R value, three-quarters R calculated as three-quarters of the original R value, and the *thalweg* R measured as the local radius of curvature referencing the *thalweg* center-line relative to the lesser of the bank to bank or bank to shoal distance across the deep channel on a bathymetric chart. A similar set of four values for the channel width, B, were tested at each station location: the 'original' B measured from bank to bank on a bathymetric chart at the bend inflection point, one-half B calculated as half of the original B value, three-quarters B calculated as three-quarters of the original B value, and the *thalweg* B, measured as the lesser of bank

to bank or bank to shoal distance across the deep channel on a bathymetric chart at the *thalweg* inflection point. Lastly, two values of the mean density difference, $\overline{\partial\rho}$, were tested at each station: the mean value of the density at a Station for the entire deployment period and the instantaneous density difference at each Station for the deployment period. Results of the sensitivity analyses indicate that the LMBM is most sensitive to changes in C_D, followed next by changes in R or the ratio of R/B, and lastly by changes in the density structure.

The definition and the selection of the R and B test values were not trivial. Conventionally, the radius of curvature, R, is defined as the arc between the inflection points in a channel bend down the channel center-line axis, and the corresponding channel width, B, is defined as the channel width from bank to bank at the downstream inflection point (Callander 1978; Dunne and Leopold 1978; Smith and McLean 1984; Nelson and Smith 1989; Leopold et al. 1995; Knighton 1998; and Ritter et al. 2002). In addition, R and B defined in the preceding manner correspond to uni-directional flows, an aspect not often discussed in the literature. Recent studies focusing on observing and modeling complex uni- and bi-directional flows (Demuran 1993; Boxall and Guymer 2003; Boxall et al. 2003; and Fagherazzi et al. 2004) have found that using R and B associated with the natural channel axis, the *thalweg*, allows for the channel geometry to evolve naturally (in either a laboratory setting or numerically using 'natural coordinates') and to be uniquely defined at each channel cross-sectional location. Fagherazzi et al. (2004) included an additional velocity term, u_b, the bank velocity increment, associated with the *thalweg* R, to the average velocity, u_o, associated with the center-line R, to account for the curvature-induced secondary current at the outer bank and found that this

inclusion lead to better agreement between observational data and model results. In addition to accounting for the bi-directional flow that occurs in estuaries and in tidal channels, the approach by Fagherazzi et al. (2004) found that the relative velocities of the ebb and flood tides could be remotely determined by planform geometry using a simplified shallow water equation model reflecting both the center-line and *thalweg* definitions of R and B. A schematic of the center-line and *thalweg* definitions of R and B are shown in Figure 6.15.

The 'best fit' R and the associated B value were chosen initially by determining at each mooring location which of the four pre-selected R values minimized the variance between the observed cross-channel current and the estimated cross-channel current as given by the scale estimate for curvature-driven secondary flow (Equation 6.7). The 'best fit' R and associated B value were later re-evaluated after the 'best fit' C_D was determined by assuming that the density-driven scale estimate for secondary flow (Equation 6.8) could be approximated by the curvature-driven secondary flow scale estimate (Equation 6.7) minus the sum of the frictional-driven (Equation 6.9) and Coriolis-driven (Equation 6.6) secondary flow scale estimates. The density-driven scale estimate for secondary flow (Equation 6.8) was then solved for B and this value was compared to the 'best fit' value for B chosen using the associated R approach. The 'best fit' C_D was chosen by determining which of the four pre-selected values of C_D that minimized the least-squares difference between the curvature term and the sum of the Coriolis, density, and friction terms in the LMBM.

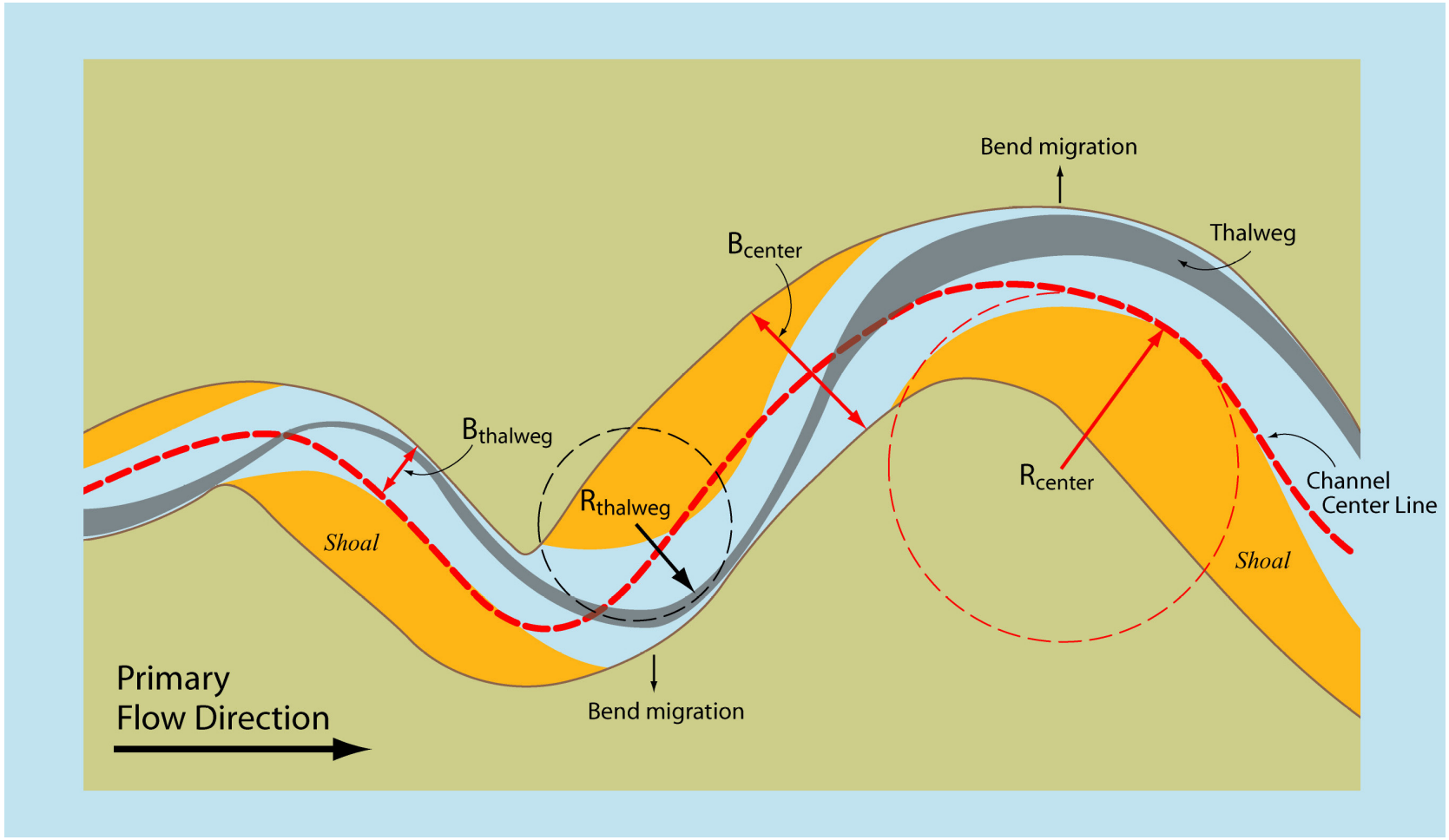

Figure 6.15: Channel curvature and channel width defined with respect to the channel center-line (indicated by red) and with respect to the *thalweg* (indicated by black).

Results of the sensitivity analyses determined the best fit for R and B at each Station was the *thalweg* R and the *thalweg* B. And likewise, the sensitivity analyses determined that the best fit for the drag coefficient, C_D, at each Station, done independently for neap and spring tides, was the value of C_D that achieved a balance in the LMBM. The best fit value of C_D at Stations 3, 4, and 6, where curvature effects are known to be important, was found to be the 'adjusted low C_D' value ($C_D = 5.0 \times 10^{-3}$) for neap tides and was found to be the 'low C_D' value ($C_D = 3.1 \times 10^{-3}$) for spring tides. Correspondingly, the best fit value of C_D at Station 5, in the straight reach of the river, was found to be the 'low C_D' value ($C_D = 3.1 \times 10^{-3}$) for both neap and spring tides. These results are similar to those of Li et al. (2004), who found that the best value of C_D, using the 'phase matching' method, was slightly higher during neap tides ($C_D = 2.3 \times 10^{-3}$) than during spring tides ($C_D = 2.2 \times 10^{-3}$). Li et al. (2004) surmised that the change in the drag coefficient value between neap and spring tides was due to the increased frictional influence of the bottom and lateral boundaries. However, their result of a variable C_D (Li et al. 2004) originated from a barotropic model that did not account for the effects of stratification. In contrast, the necessary changes in the value of C_D to close the LMBM between spring and neap tides in the Satilla are likely due to the influence of form drag distorting the flow field (MacCready et al. 2003).

Recent work by Sutherland et al. (2004) found that in a continuously stratified fluid, form drag could easily distort the ambient flow field, excite internal waves (e.g., an internal seiche such as seen at Stations 3 and 4), and reduce turbulent mixing. Earlier work by Nash and Moum (2001) found bottom stress during stratified conditions (akin to neap tide conditions in the Satilla) could be 5-10 times higher than during barotropic-like

conditions (akin to spring tide conditions in the Satilla). Nash and Moum (2001) also found that the distortion of the flow field by form drag was even larger during stratified conditions, such that form drag was twice as effective at reducing local momentum transfer as the enhanced bottom friction, and served as a feedback mechanism to locally generate or sustain internal waves. Therefore, it seems plausible that increasing the value of C_D during neap tides in the LMBM accounts for the increase in bottom stress and form drag under such stratified conditions.

A major limitation of the LMBM is the singular choice of the drag coefficient, C_D, as one representative value for all Stations and for all conditions during either neap or spring tides. Clearly, a variable drag coefficient is likely to give better results, but presently, due to restrictions of the data set, it is not possible to assess the contribution of a variable C_D to the LMBM results. Another limitation of the LMBM as formulated by Equation 6.19 is the omission of the depth-dependent lateral baroclinic gradient and the vertical shear stress divergence terms. While the importance of these two terms are approximated respectively by the depth-average lateral baroclinic gradient and bottom stress, sensitivity analyses suggest that neglecting the depth-dependent lateral baroclinic term is less likely to impact the results from LMBM calculations than by neglecting the vertical shear stress divergence term. Reliable calculations of the vertical shear stress divergence term are not possible with the current data set. As a result, assessing the impact of retaining the vertical shear stress divergence term in the LMBM is also not possible. However, the Satilla is a shallow estuary which responds to wind stress only under extreme weather conditions, like hurricanes or nor'easters (Elston 1998, unpublished data), such that the bottom stress term would likely dominate over the

vertical shear stress divergence term. Lastly, the current LMBM was developed assuming steady-state conditions and neglecting advective accelerations. While suitable for this application, these assumptions in the formulation of the LMBM may not be appropriate in all cases. As an example, if understanding the evolution of secondary flow was the goal, the assumption of steady-state conditions would be incorrect. Recent research (Geyer 1993; Chant and Wilson 1997; Seim and Gregg 1997; and Lacy and Monismith 2001) suggests that the assumption of steady-state conditions is more applicable than neglecting advective accelerations. Chant and Wilson (1997) found that it was necessary to include advective accelerations to close the lateral momentum balance and to account for changes in the flow field around a headland near the George Washington Bridge in the Hudson River. Likewise, Lacy and Monismith (2001) found that the addition of lateral advection was necessary to close the momentum balance when the channel configuration was complex producing large lateral gradients or in areas where the bathymetry changes rapidly, such as an area with broad shoals like Grizzly Bay. Despite these limitations, the LMBM does well to describe changes in the lateral momentum balance of the Satilla River in a variety of channel reaches driven by secondary flows in a simple straightforward manner.

6.4 Conclusions

This chapter explores the changes in the strength, signal, and balance of mechanisms that drive secondary circulation in four different channel reaches, from highly curved to nearly straight, the changes in the strength of secondary flow in relation to changes in freshwater discharge, and the ability to describe these changes with a simple lateral momentum balance model. As in Chapter 5, current profiles are used to

quantify the strength, direction, and duration of secondary flows driven by channel curvature, Coriolis acceleration, friction, and the differential advection of density. Likewise, secondary circulation driven by channel curvature dominates at three of the four mooring locations, located in channel bends, while secondary circulation driven by the differential advection dominates at the fourth location, a nearly straight reach of the Satilla River.

The structure of the curvature driven secondary flow in the study area, as seen also in Chapter 5, fluctuates fortnightly between a classical single cell configuration at spring to a more complicated stacked double-cell configuration at neap. At neap, the uppermost circulation cell is driven by channel curvature while the lowermost cell is the result of lateral seiching in response to internal adjustments of the density field between ebb and flood tides. Lateral seiching is a local feature and is likely to be detected only in nearby downstream bends within close proximity (1500 m).

Changes in freshwater discharge were found to greatly modify the strength and the character of secondary flows in the Satilla. Though the LMER 4 and SAT 2 experiments did not cover the full dynamic range of river discharge conditions, it is possible to estimate the contribution of changes in freshwater input to the strength of secondary flows. During low discharge conditions, the strength of secondary flow is relatively unaffected, the result of either a weak vertical salinity gradient or a shift in the location of the maximum vertical salinity gradient upriver. Conditions necessary to limit or halt secondary flow driven by centrifugal acceleration are less frequent and secondary flow acts unimpeded as a vertical mixing mechanism. In contrast, during high discharge conditions, the strength of secondary flow driven by channel curvature was found to be

reduced by the addition of sufficient freshwater discharge, especially during ebb tides due to tidal straining, which enhances vertical stratification on ebb and reduces vertical stratification on flood. Tidal straining is most effective at enhancing vertical stratification under high discharge conditions and/or when the average axial velocity is high, as during spring tides. Conditions necessary to limit or halt secondary flow are more common during times of high discharge and there is a noticeable decrease in the effectiveness of secondary circulation as a vertical mixing agent. Consequently, secondary flow driven by centrifugal acceleration, in addition to being sensitive to changes in river discharge, is modified by tidal straining during the ebb phase of the tidal cycle.

As demonstrated, the Seim and Gregg (1997) model is effective at explaining the observed fortnightly changes in secondary flow driven by centrifugal acceleration, the dominant mechanism for driving lateral flows in the Satilla River. While this model explains the general differences observed in curvature-driven secondary flow on the fortnightly time scale, additional processes that govern secondary flow (i.e., density and friction) must be considered when applying it to either weakly curved channels or straight reaches. As a result, analytical scale estimate formulas, adjusted to observed secondary flows, are used as first order estimates to determine the relative importance of curvature, Coriolis, friction, or density driven secondary flows, and to assess the dominant terms in a simple lateral momentum balance at a number of locations, under a variety of conditions.

The balance of mechanisms responsible for the strength and location of secondary flows in the Satilla River varies with changes in the axial current speed, the lateral baroclinic gradient, neap-to-spring variations in salinity, channel curvature, and freshwater discharge. A simple steady-state lateral momentum balance model between the Coriolis acceleration, centrifugal acceleration, the lateral baroclinic gradient, and bottom stress is sufficient to explain the observed changes in secondary flow on the fortnightly time scale in the Satilla in a variety of differently curved channel reaches. Sensitivity analyses on the lateral momentum balance model determined that the best choice values for the local radius of curvature and channel width are those associated with the *thalweg* and that the best choice value for the drag coefficient, C_D, depends on the local stratification conditions and the phase of the fortnightly tidal cycle, with the choice of C_D at neap tides being slightly higher than the choice of C_D at spring tides. The increase in C_D necessary to close the lateral momentum balance model in the Satilla between spring and neap tides is likely due to the influence of form drag distorting the flow field. The lateral momentum balance model results shows that there is a shift in the primary momentum balance between neap and spring tides. At spring tide, the primary momentum balance is between centrifugal acceleration and bottom stress. At neap tide, depending on local stratification and form drag, the primary momentum balance shifts from a two-way balance between centrifugal acceleration and the lateral baroclinic gradient at low drag states to a three-way balance between centrifugal acceleration, the lateral baroclinic gradient, and bottom stress at high drag states.

This chapter demonstrates that the balance of mechanisms that drive a secondary circulation is different between straight and curving reaches and varies on the fortnightly tidal cycle. It is important to be able to estimate the relative magnitude of mechanisms that drive secondary flow in order to clarify their role in local and estuarine-wide mixing. Knowledge of this role will better able us to predict important parameters such as the length of the salt intrusion and to determine the dispersion and distribution of various waterborne properties (e.g., larvae, sediment, and pollutants) in the estuarine environment.

7. SECONDARY CIRCULATION SIGNATURE IN SPACE AT TWO BENDS

7.1 Introduction

Estuaries have always been important in the development and growth of human societies. These unique transitional environments are among the most biologically productive areas in the world and often provide a major source of drinking and industrial water for many communities. As an important resource, understanding the dispersion and distribution of various properties in an estuary (i.e., larvae, momentum, pollutants, salt, and sediments) is vitally important for both human health and scientific discovery.

Understanding the relationship between secondary circulation and its role in the transfer and distribution of momentum, and its connection with the spatial variations in the lateral structure of the axial current is fundamental to the study of estuarine dynamics. Little advancement has been made on this topic until recently, a result of the continued development and refinement of modern acoustic current sensors, which yield highly detailed observational data, in conjunction with better computational techniques. Despite a resurgent interest in comprehending such connections and technical advances, only two studies have been done (Kjerfve and Proehl 1979; Valle-Levinson and Atkinson 1999) which detail or quantify such interactions in lateral space (i.e., in a channel cross-section) and most notably, such interactions in partially mixed estuaries. This is in direct contrast to the suggestion by several authors (Seim and Gregg 1997; Trowbridge et al. 1999; Geyer et al. 2000; and Peters 2003) that secondary flow is the link to understanding the transfer of axial momentum downstream and a key physical process necessary to include when determining or evaluating an estuarine momentum balance.

Several mechanisms can generate a secondary flow. Most commonly, secondary flow can be attributed to one or more of the following mechanisms: channel curvature, planetary rotation (the Coriolis effect), frictional effects of irregular channel bathymetry or geometry, and/or the interaction between the lateral shear of the axial current with the axial salinity gradient (the differential advection of density) associated with the tides, making the structure of the secondary circulation locally complex and significantly modulating the strength of the secondary flow between ebb and flood tides. Secondary circulation resulting from channel curvature is driven by a local imbalance between the vertically varying centrifugal acceleration and the cross-channel pressure gradient (Bathurst et al. 1977). While the direction of cross-channel flow is invariant during flood and ebb, its strength differs depending on the orientation of the along-axis flow (cyclonic vs. anticyclonic) in the channel bend (Dyer 1997) and vertical shear, which can be enhanced or limited due to tidal straining (Simpson et al. 1990). A Coriolis-driven secondary circulation, however, is unidirectional and oriented to the right of the axial current in the Northern Hemisphere. Though Coriolis-driven secondary flow is typically weak in estuaries the size of the Satilla River, in large estuaries, such as the Chesapeake, the contribution to the overall strength of a local secondary circulation by the Coriolis acceleration may be significant (Kasai et al. 2000). In contrast to a curvature-driven or a Coriolis-driven transverse circulation, a secondary circulation due to the frictional interaction with lateral and/or bottom boundaries is complex and often difficult to determine its initial source (lateral or bottom boundaries) and to quantitatively separate it from the other mechanisms that drive secondary flow. Most often, frictional effects are parameterized and modeled by an eddy viscosity that may have several forms and values

(Falcón 1984; Nunes and Simpson 1985; Mertz and Gratton 1995; Swift et al. 1996; Turrell et al. 1996). By comparison, secondary circulation driven by the differential advection of density is a process whereby the axial density gradient interacts with the lateral shear of the axial current generated by boundary friction to produce transverse density gradients. Diagnostically, it is assumed that density-driven secondary flow arises as a result of an equilibrium balance between the laterally directed baroclinic forces and friction. When the current velocities are slow and the lateral salinity gradients are maximized, as is often characteristic of late flood to early ebb, the lateral density gradients induce a gentle density driven 'secondary' vertical and horizontal circulation, the presence of which is marked by axial fronts or slicks on the water's surface. The actual appearance and particular timing of axial fronts and slicks most likely depends on the local estuarine characteristics that maximize the lateral salinity and velocity gradients.

The results of Chapter 6 show that the balance of forces that regulate the strength and orientation of secondary flow changes on the fortnightly tidal cycle. The objective of this chapter is to explore the spatial transition in the balance of mechanisms responsible for generating observed transverse circulations in two opposing channel bends of the Satilla River and to demonstrate how secondary circulation contributes to a change in the distribution and transfer of longitudinal momentum in the downstream direction. Specifically, the focus of Chapter 7 is to examine and to quantify the observed secondary circulation patterns in four lateral cross-sections, two cross-sections in a bend to the north, and two cross-sections in the adjacent bend to the south during maximum ebb and maximum flood conditions, when axial acceleration is at a minimum and the lateral structure of the axial flow is assumed to be in steady-state conditions.

7.2 Materials and Methods

7.2.1 Experiment Site and Environmental Conditions

A shallow coastal plain river in Georgia, the Satilla is a partially mixed estuary which experiences 1 to 2.5 meter range semidiurnal tides. It has a drainage basin of 9143 km^2 and a length of about 362 kilometers from its headwaters to the Atlantic Ocean (Dame et al. 2000; Blanton et al. 2001). Confined to a 120 mile segment of the coast, the Satilla offers a unique look at understanding the link between differing landscape characteristics, geologic setting, and flow rate. Axial currents at spring tide are on the order of 1.0 m s^{-1} to 1.5 m s^{-1} while axial currents at neap tide are weaker and vary between 0.30 m s^{-1} and 0.65 m s^{-1}. The Satilla has an average discharge of less than 80 m^3 s^{-1} but can vary from 0 to 150 m^3 s^{-1} over an annual cycle (Blanton et al. 2001; USGS 2004). Fortnightly variations in the observed density structure in the Satilla River are primarily the result of changes in salinity.

Bordered by extensive salt marshes, the Satilla is known as a 'blackwater' river due to the large amounts of decaying humic substances which produce tannic acids. A triple junction near river kilometer 26 divides the flow of the Satilla River between its main branch to the south and White Oak Creek (WOC), a tidal creek to the north. Upriver, beyond the triple junction at river kilometer 26, the Satilla is a nearly fresh river where crawfish farms and old rice plantations still thrive.

The main channel of the Satilla is marked by nine channel bends and two short straight reaches that extend from its mouth between Jekyll and Cumberland Islands to 38 kilometers upriver. The majority of these bends are broadly concave (bends to the north, radius of curvature ~ 1200 m) each followed by more sharp convex bends (to the south,

radius of curvature ~ 800 m). The bends have a channel width between 200 – 500 meters and are roughly three to four kilometers apart, starting six kilometers from the ocean (0 km) and extending 33 kilometers upriver (Figure 7.1).

This experiment focuses on two differently curved domains (A and B) during spring and neap tide at maximum ebb and maximum flood tide conditions during the Spring of 1999. Domain A is a concave reach (bend to the north) located just past the Alternate IntraCoastal Waterway between 12 and 16 kilometers upriver from the estuary mouth at St. Andrews Sound with an average bank-to-bank radius of curvature of approximately 1200 m and an effective channel width of 290 m. Domain B is a convex reach (bend to the south) adjacent to Domain A, and is located between 16 and 20 kilometers upriver from the ocean with an average bank-to-bank radius of curvature of approximately 940 m and effective channel width of 200 m. In an effort to discern changes in the flow field between the two channel bends, Domains A and B were each further subdivided into two lateral cross-sections, each approximately 1 to 2 kilometers apart: Domain cross-sections A 4/5, A 9/10, B 5/6, and B 10/11 (Figure 7.2).

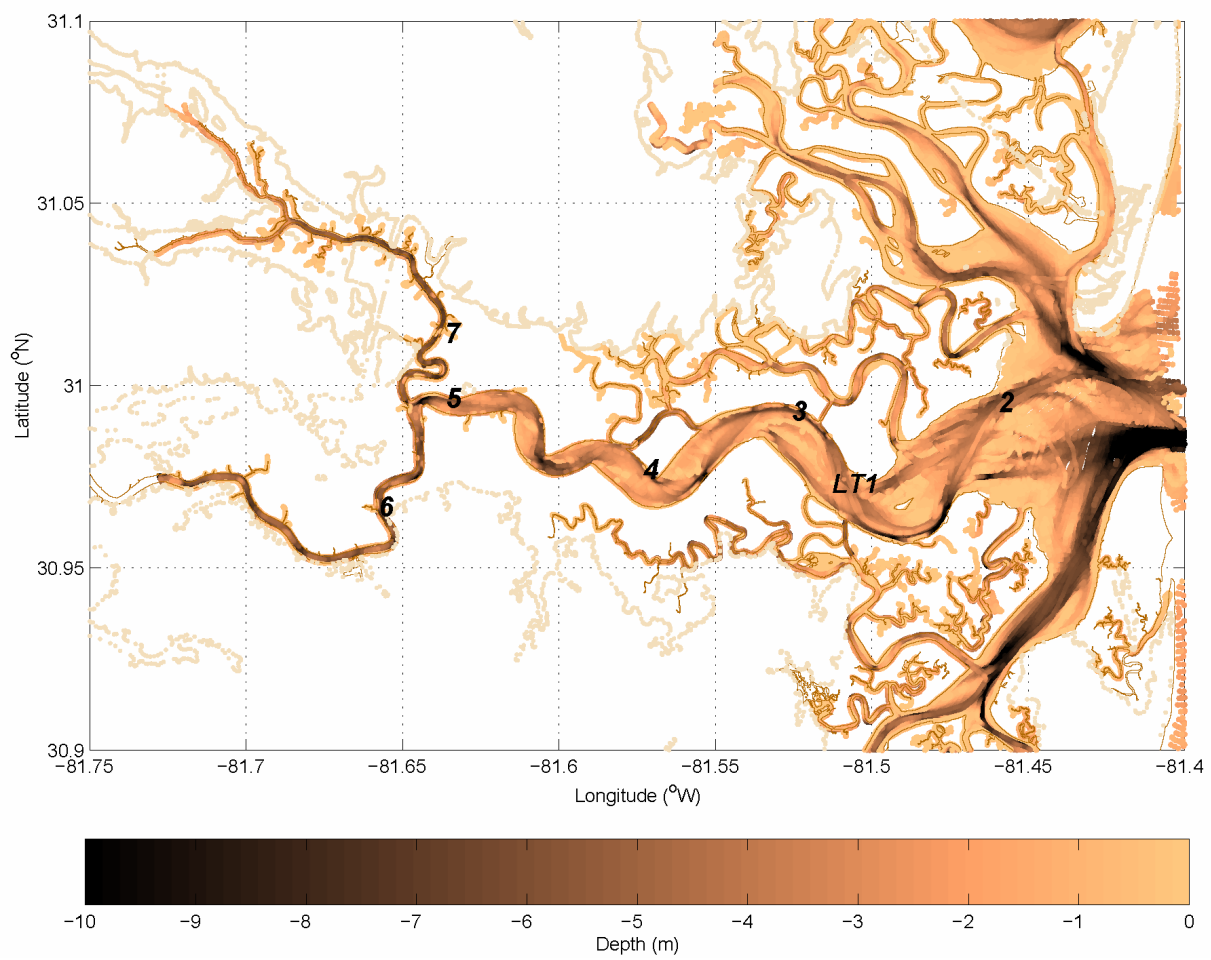

Figure 7.1: Map of the Satilla River in southeast Georgia near the Florida border. The mooring locations for the SAT 1 (January – March 1999) field survey are indicated by bold numbers 2 through 7. LT 1 refers to the long-term mooring (March 1999 – April 2000) near St. Andrews Sound. Darker colors indicate deeper depths.

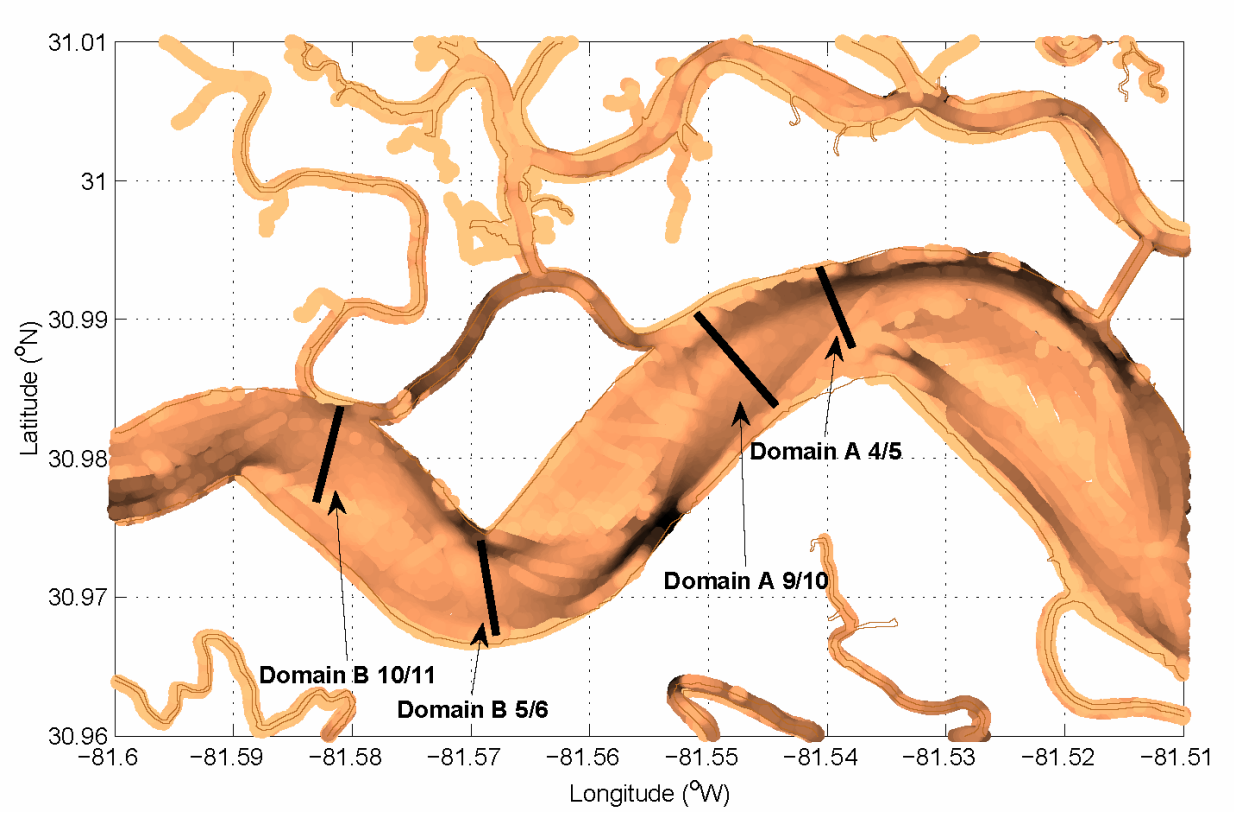

Figure 7.2: Map of Domain A and Domain B in first bend of the Satilla River. Black lines indicate roving transect cross-sections. The depth variations (colorbar) in this figure are the same as shown in Figure 7.1.

Meteorological data from Brunswick, Georgia (091340) show that the atmospheric conditions during the SAT 1 experiment (20 January – 23 March 1999) were cold and wet. These three 'major climatic' events (National Weather Service Records 1999) occurred in early 1999, producing a record number of tornadoes for the month of January (169 reported tornadoes in January 1999 surpassing the 52 reported tornadoes in January 1975), widespread crop damage in several states due to multiple severe hail storms, and widespread power outages for the eastern United States. Average daily temperatures ranged from 8.5°C to 20.2°C, with a drop in the daily maximum temperature below 3.3°C associated with the severe weather outbreaks. Three major

precipitation events occurred in January – March 1999: the first event occurred on January 9, 1999 (17.8 mm of recorded precipitation), the second occurred on January 23, 1999 (35 mm of recorded precipitation), and the third occurred over the end of January and the beginning of February 1999 (60.3 mm of total recorded precipitation).

The 1999 Satilla SAT 1 experiment occurred shortly before a period of extended drought for coastal Georgia, beginning in April 1999 and lasting until nearly June 2003. The SAT 1 data was collected shortly after a large freshet event (February 8, 1999) with a peak discharge of near 118 m^3 s^{-1} followed by a steady decline to approximately 20 m^3 s^{-1}. Discharge conditions remained steady around 20 m^3 s^{-1} for the duration of the SAT 1 mooring deployment.

7.2.2 Rapid Spatial Survey System – Spring 1999

Data for the SAT 1 experiment was collected in one of five operational modes: spatially detailed 'rapid surveys' aboard the R/V Gannet (a 5.5 meter-long maneuverable catamaran), an array of moored surface and bottom instruments, 13-hour anchor stations aboard the R/V Blue Fin (the 24 meter-long primary research vessel), synoptic surveys throughout the estuary, and a long term monitoring site. Anchor stations and rapid surveys were conducted simultaneously, at neap and at spring tide in Domains A and B (Figure 7.2), for a continuous 13-hour period in order to resolve temporal changes in the three-dimensional velocity and density structure of the Satilla on the tidal time scale. Anchor station data consisted of hourly Conductivity-Temperature-Depth (CTD) profiles, which included temperature, salinity, pressure, optical backscatterance (OBS), and fluorescence. Rapid survey and anchor station depths were determined in-situ from a subsurface recording fathometer while latitude and longitude positions were obtained

from a shipboard Differential Global Positioning System (DGPS), respectively, on the R/V Gannet and the R/V Blue Fin. Synoptic surveys were conducted periodically at low and high water in an effort to define the longitudinal salinity (density) structure throughout the Satilla. The primary data sources for this Chapter are a composite of the 'rapid surveys' conducted aboard the R/V Gannet, the mooring field, and a near-ocean long-term monitoring site (LT 1 in Figure 7.1).

Rapid surveys were conducted while underway on the R/V Gannet. In the 'rapid survey' mode, high-resolution surface temperature and salinity, OBS, velocity, depth, and position were collected continuously at a sampling interval of 1, 5, and 15 seconds over a tidal cycle in a predetermined zigzag pattern covering a 4 kilometers reach (Figure 7.3). The R/V Gannet surveys were conducted at an average boat speed of 3 m s^{-1} to ensure high data quality. The towing speed of 3 m s^{-1} allowed coverage of the 4 kilometer transects in approximately 1.5 hours. Survey data was acquired using a surface pumped Sea-Bird Electronics, Inc., Thermosalinograph (SBE-21) system linked to two fathometers and DGPS unit, a side-towed 600 kHz RD Instruments, Inc., (RDI) Broad Band Acoustic Doppler Current Profiler (BB ADCP) mounted on a floating sled to resolve three-dimensional currents in the axial, lateral, and vertical directions, and a frame suspended Falmouth Scientific Instruments (FSI) CTD for stop and drop CTD casts at predetermined side channel locations and at predetermined locations over the mooring field. While the stop and drop CTD data collected had discrete (rather than continuous) spatial coverage, it nicely complimented the surface temperature and salinity data from the SBE-21 unit by indicating cross-channel changes in vertical stratification.

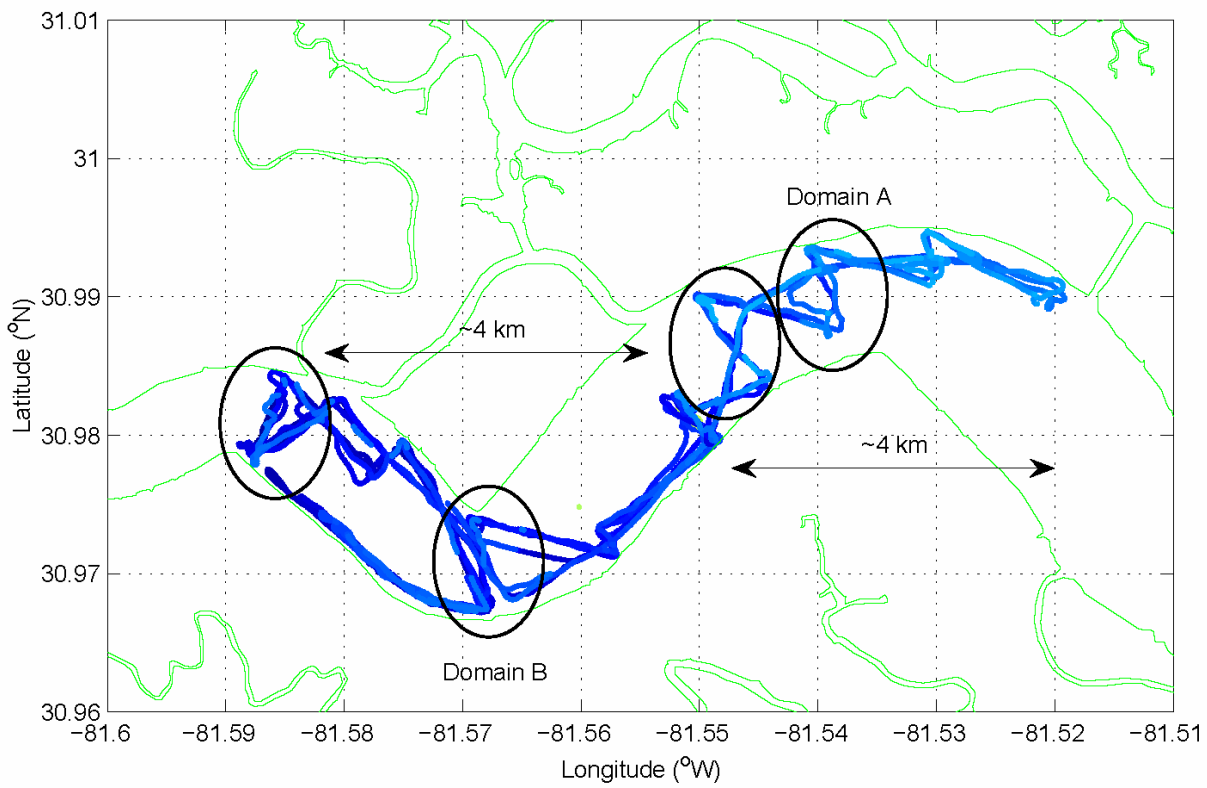

Figure 7.3: The R/V Gannet boat tracks during the 13-hour Domain A and B rapid surveys. Circles indicate the location of the cross-sectional data as shown in Figure 7.2.

Domain A was surveyed for a 13-hour period (March 10, 1999) followed by a 13-hour survey of Domain B (March 11, 1999). One full tidal cycle was skipped between roving surveys in order to eliminate the small diurnal inequality in the tidal amplitude and to insure that the tidal amplitude in the adjacent Domain was approximately the same during the course of the surveys (Figures 7.4 and 7.5). Sampling was initially done at neap tide in each Domain and the entire survey procedure was repeated seven days later for spring tide (18 March 1999 for Domain A and 20 March 1999 for Domain B). There were 8 to 10 circuits (cross-section realizations) in each Domain per tidal cycle, yielding more than enough data for a harmonic analysis of the currents for the M_2 semi-diurnal tidal species.

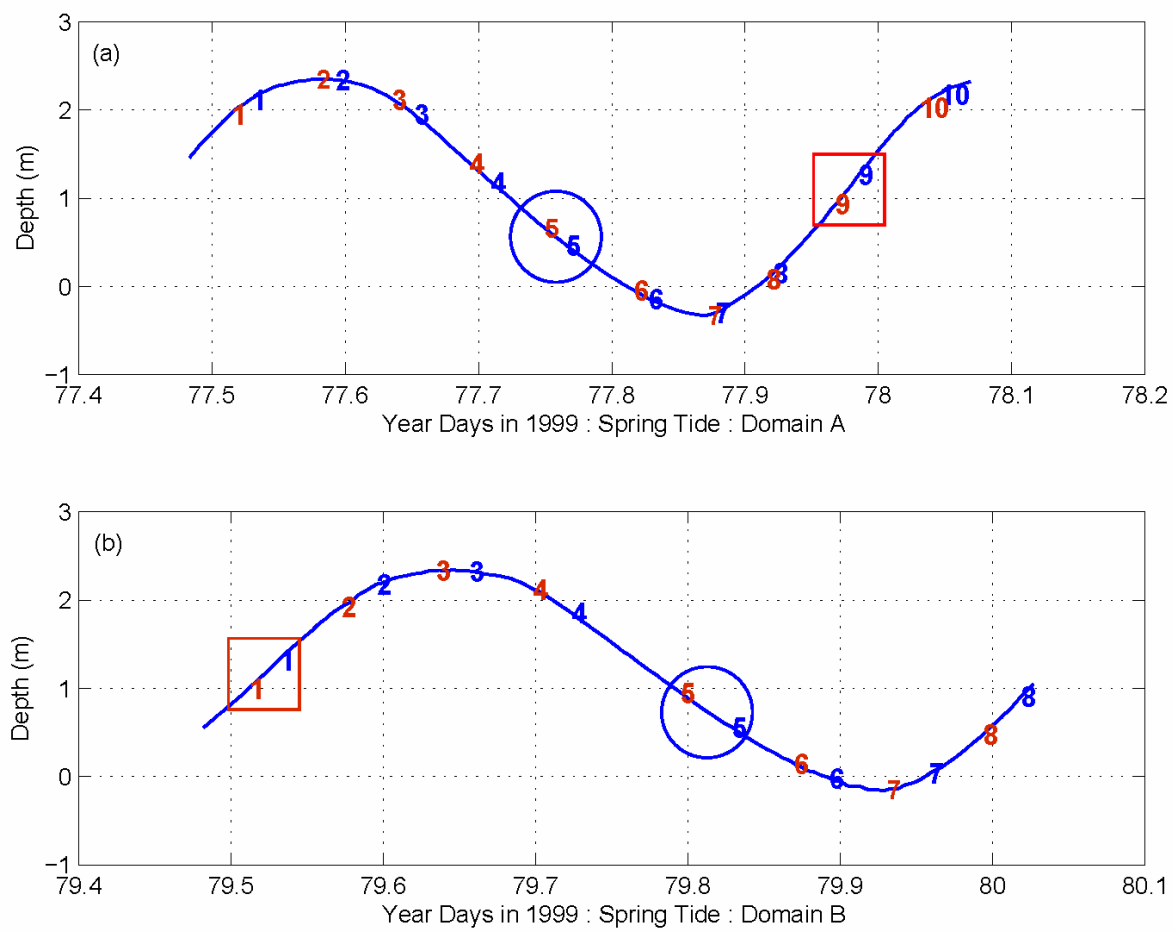

Figure 7.4: Tidal stage relative to MLLW during the (a) Domain A and (b) Domain B rapid surveys at spring tide. Circles indicate comparative maximum ebb tide conditions while squares indicate comparative maximum flood tide conditions. Numbers correspond to the beginning and end of the CTD casts taken during each Domain survey.

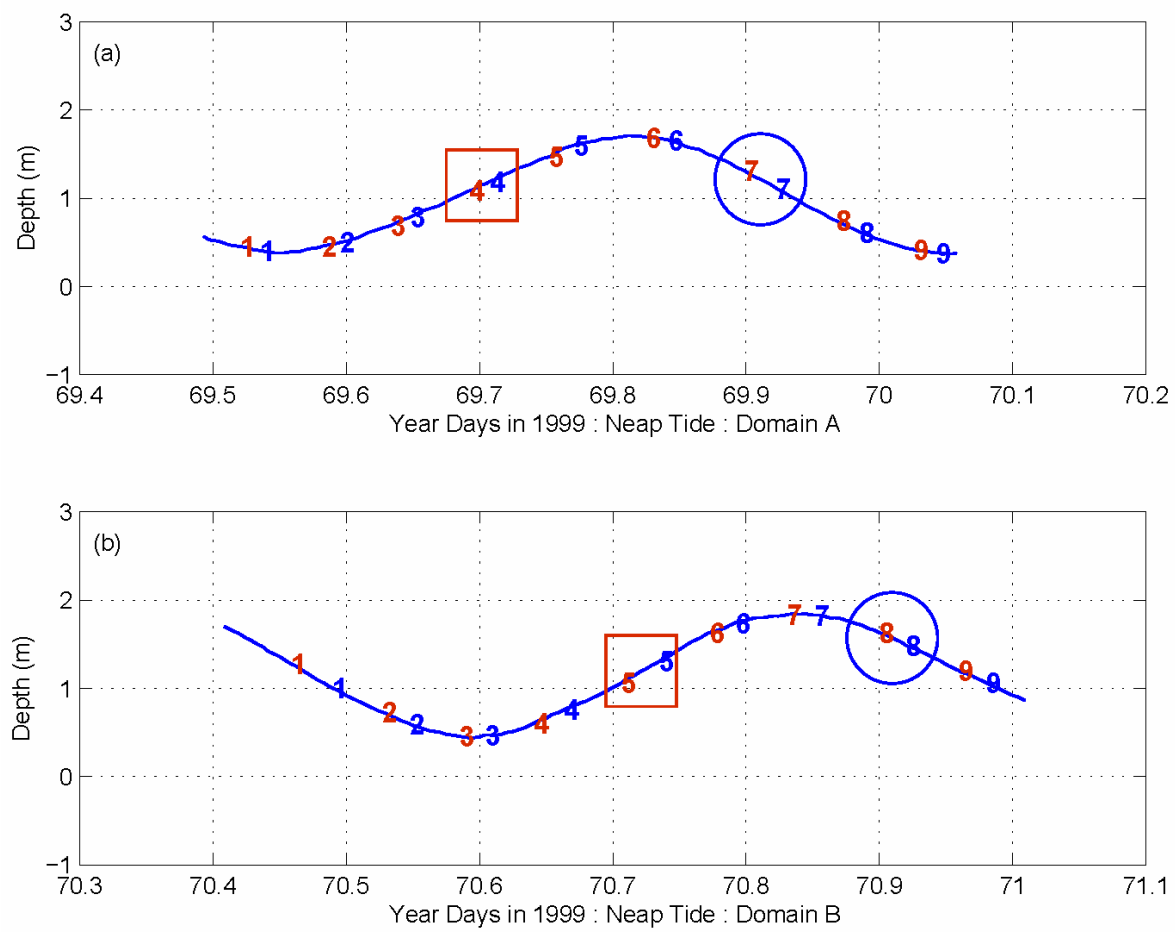

Figure 7.5: Tidal stage relative to MLLW during the (a) Domain A and (b) Domain B rapid surveys at neap tide. Circles indicate comparative maximum ebb tide conditions while squares indicate comparative maximum flood tide conditions. Numbers correspond to the beginning and end of the CTD casts taken during each Domain survey.

The rapid survey data was collected while the mooring field was in place in an effort to ground truth the roving data with the fixed mooring locations and to relate the changes between the tidal and 'seasonal' time scales. The mooring deployment locations, the roving transect locations, and the roving ADCP setup conditions for the SAT 1 experiment are respectively summarized in Tables 7.1, 7.2, and 7.3. Figure 7.6 shows a schematic of the rapid spatial survey system while Figure 7.7 shows a photograph of the R/V Gannet in rapid spatial survey mode.

Table 7.1: SAT 1 mooring deployment locations.

Station	Sensor Depth (mab)	Water Depth (m)	Instrument (serial #)	Parameters Measured	Latitude (°N)	Longitude (°W)
2	Floating	8.9	SC 296	C, T	30° 59.75′	81° 27.53′
2	1.00	8.9	WH 722	V+	30° 59.75′	81° 27.53′
2	0.74	8.9	SC 2722	C, Obs, P, T	30° 59.75′	81° 27.53′
3	Floating	9.3	MC 672	C, T	30° 59.59′	81° 31.56′
3	1.00	9.3	S4 2099	D, V	30° 59.59′	81° 31.56′
3	0.89	9.3	SC 849	C, Obs, P, T	30° 59.59′	81° 31.56′
4	Floating	7.9	MC 673	C, T	30° 58.59′	81° 34.37′
4	0.40	7.9	WH 721	V+	30° 58.59′	81° 34.37′
4	0.66	7.9	SC 337	C, P, T	30° 58.59′	81° 34.37′
5	Floating	9.6	MC 703	C, T	30° 59.80′	81° 38.18′
5	0.40	9.6	S4 2098	D, V	30° 59.80′	81° 38.18′
5	0.71	9.6	SC 1836	C, Obs, P, T	30° 59.80′	81° 38.18′
6	Floating	8.5	MC 704	C, T	30° 58.04′	81° 39.47′
6	0.40	8.5	S4 1530	C, T, V	30° 58.04′	81° 39.47′
6	0.66	8.5	SC 1834	C, Obs, P, T	30° 58.04′	81° 39.47′
7	Floating	10.2	MC 705	C, T	31° 00.87′	81° 38.40′
7	1.00	10.2	S4 909	C, T, V	31° 00.87′	81° 38.40′
7	0.64	10.2	SC 848	C, Obs, P, T	31° 00.87′	81° 38.40′
LT 1	Piling	1.1	MC 757	C, P, T	30° 58.40′	81° 30.78′

* mab = meters above bottom; C = conductivity; Obs = optical backscatterance; D = depth
P = pressure; T = temperature; V = current velocity; V+ = current velocity profile

Table 7.2: SAT 1 Roving transect locations.

Station	Sensor Depth (mab)	Water Depth (m)	Instrument (serial #)	Parameters Measured	Latitude (°N)	Longitude (°W)
A 4/5	Profiling	8.0	FSI CTD	C, Obs, P, T	30° 59.43′	81° 32.32′
A 4/5	Roving	8.0	ADCP	V+	30° 59.43′	81° 32.32′
A 9/10	Profiling	8.3	FSI CTD	C, Obs, P, T	30° 59.19′	81° 32.82′
A 9/10	Roving	8.3	ADCP	V+	30° 59.19′	81° 32.82′
B 5/6	Profiling	7.8	FSI CTD	C, Obs, P, T	30° 58.22′	81° 34.11′
B 5/6	Roving	7.8	ADCP	V+	30° 58.22′	81° 34.11′
B 10/11	Profiling	8.2	FSI CTD	C, Obs, P, T	30° 58.87′	81° 35.17′
B 10/11	Roving	8.2	ADCP	V+	30° 58.87′	81° 35.17′
LT 1	Piling	1.1	MC 757	C, P, T	30° 58.40′	81° 30.78′

* mab = meters above bottom; C = conductivity; Obs = optical backscatterance; P = pressure; T = temperature; V = current velocity; V+ = current velocity profile

Table 7.3: Broad Band ADCP setup specifications for the SAT 1 experiment.

SAT Satilla River, Georgia	Experiment 1 10 March to 20 March 1999
Acoustic Frequency	600 kHz (BB ADCP)
Beam Angle	20 degrees
Transducer Depth	0.5 m
Bin Length	0.5 m
Sampling Interval	15 seconds
Pulse Length	0.72 m
Blanking Interval	0.5 m
Center of First Bin	1.23 m
Profiling Mode	4
Pings per Ensemble	4
Pings per Ensemble Average	8.4
Single Ping Velocity Error	1.38×10^{-2} m s^{-1}
Dynamic Velocity Error	3.06×10^{-4} m s^{-1}
Bottom Track	Yes, though no NAV on 10 March 1999
Data Acquisition	RD Instruments Software (Transect)
Navigation	Global Positioning (DGPS)
Ship Speed	6 .5 knots ≈ 3.3 m s^{-1}

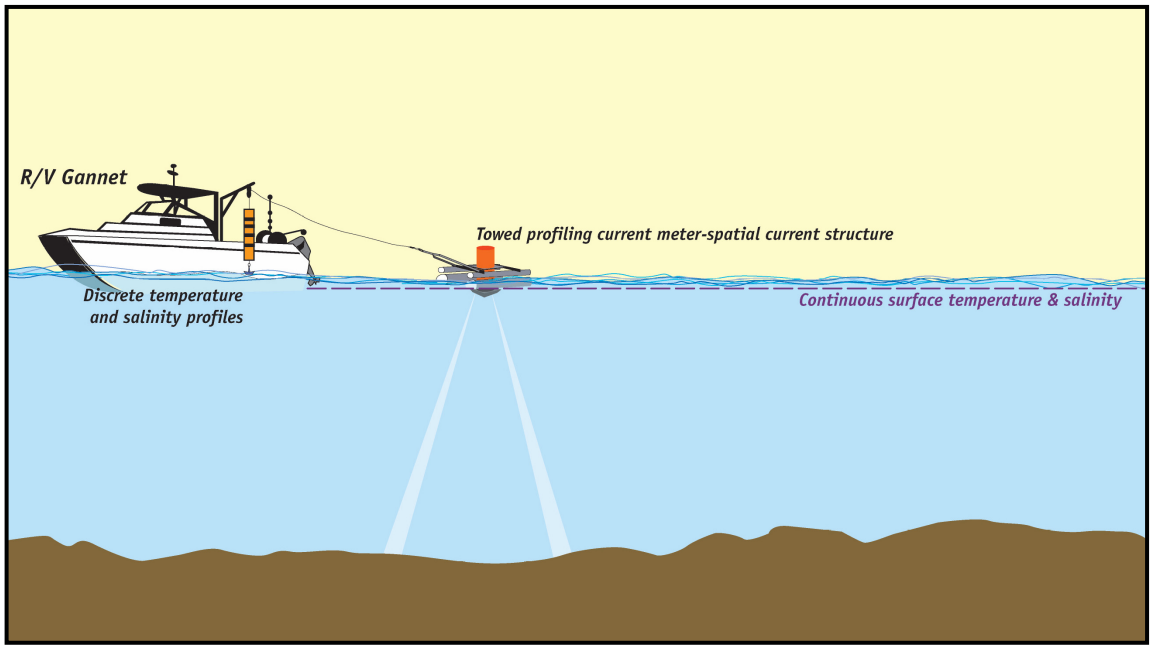

Figure 7.6: A schematic of the rapid spatial survey system aboard the R/V Gannet.

Figure 7.7: A photograph of the R/V Gannet active in a rapid spatial survey.

Moored data for the SAT 1 experiment (*cf.* Figure 7.1) was collected for a sixty day period (20 January to 23 March 1999), at seven sites, from near the mouth of the Satilla River to up beyond the triple junction at White Oak Creek (WOC). A pyramid shaped stainless steel frame was placed at each mooring location on which a subsurface (1-m off the bottom) Sea-Bird Electronics, Inc., (SBE) SeaCAT, measuring temperature, salinity, pressure, and OBS, and a 600 kHz RDI Workhorse ADCP (WH ADCP), measuring depth, velocity, and acoustic backscatter, were mounted. A SBE MicroCAT was tethered to each pyramid to measure surface temperature and salinity. InterOcean S4 current meters were used alternately with RDI WH ADCPs at a few mooring locations (*cf.* Table 7.1). River bathymetry and mooring deployments locations were determined in-situ by a subsurface fathometer, while latitude and longitude positions were determined using a DGPS unit installed on the R/V Blue Fin.

Additional supplementary data was collected for a one year period (early March 1999 through early April 2000) at a fixed long-term monitoring site. A US Coast Guard channel marker (USCG A14), located downstream of Domain A, near river kilometer 8, was used as the long-term fixed site onto which a small CTD was attached. Temperature, salinity, and pressure data were collected at this site (LT 1) for a thirteen month period (9 March 1999 to 6 April 2000) at a 6 minute interval. Pressure data collected at this location was used to adjust the depth component of the roving BB ADCP, the moored WH ADCPs, and the depth component of the moored CTDs to the prescribed datum of mean lower low water (MLLW), hereafter referred to as the de-tiding process.

In general, salinity data from the SBE-21 system, the FSI CTD, and velocity data from the moored WH ADCPs, and the BB ADCP were of excellent quality. The SBE-21

unit sampled every 5 seconds and measured approximately 1 liter of water per sample. During long surveys, significant timing errors were diagnosed in the spatial position of the SBE-21 data file. This error was determined to be due to a combination of an incorrect time interval calculation and a delayed response in the SBE-21 unit when writing data to a log file. A redundant fathometer on the R/V Gannet which recorded depth, spatial position, and time at 2 second intervals linked to the same DGPS unit as the SBE-21 was used to correct the data delay of 0.21 seconds per sample. The FSI CTD, due to inconsistencies in the sampling frequency of the onboard thermistor (varying between 2.8 Hz and 3.9 Hz for each cast) showed a large hystersis in the temperature, conductivity, and salinity data between upcasts and downcasts when operated at the manufacturer's suggested baud rate of 9600. The FSI CTD sample rate was adjusted to a higher baud rate of 19200, which decreased the hystersis, but did not eliminate the problem. As a result, cross-calibration casts were performed between the FSI CTD and a SeaCAT 19 CTD (reliably recording at 1 Hz and 4 Hz and used during the 13-hour anchor stations aboard the R/V Blue Fin) and were used to correct and process the FSI CTD data following the accepted UNESCO protocol (1985) for temperature, salinity, density, and depth.

Velocity data from the WH ADCPs were of excellent quality. Bio-fouling was nearly eliminated on the WH ADCPs by applying a thin mixture of cayenne pepper and marine grade silicon grease to each of the transducer faces before deployment. The WH ADCPs likely due to fauna interference or a glass-like water surface, sporadically failed to detect, respectively, the water column velocities and/or the water surface level (Emery and Thompson 1998; Ott 2000). Pressure data from the lower CTD at each

WH ADCP station was used to uniformly correct the acoustic data for missing surface returns, to remove the near surface side lobe energy returns, and to adjust the depth of the velocity observations to a standard datum. Contaminating side lobe energy generated by transducer beam interference near the 'reflecting surface' (for an upward-looking ADCP, the water surface) was removed using the data range expression

$$R_{valid} = H_r \cos\varphi \quad (\mathbf{7.1})$$

where H_r is the range depth and φ is the beam angle (generally 20°) of the transducer faces with the horizontal plane (Emery and Thompson 1998). Removing side lobe energy from the WH ADCP data reduced the vertical data range near the reflecting surface by approximately 6% (60 centimeters for H_r = 10 m). Because the SAT 1 WH ADCP bins were 0.5 m in size, it was necessary to remove the first two bins (totaling 1 meter) near the water surface to account for and eliminate side lobe energy from the observed data. The WH ADCP data at Station 2 and 4 were each respectively rotated through an angle of 19º (counter-clockwise) and -54º (clockwise) to align the U and V components of velocity with the streamwise (U_s) and normal (U_n) flow directions.

The roving ADCP during the SAT 1 experiment was configured to operate in a downward looking, vessel towed fast ping mode, sampling the entire three-dimensional water column every second in raw single ping format and every 15 seconds in ensemble average ping format. Navigational input and bottom tracking failed for the roving ADCP on March 10, 1999, yielding only the raw single ping data file and a partial ensemble average ping data file. Correct depth and navigational data was derived and appended to the March 10, 1999 ADCP raw data file from a combination of the redundant fathometer recording at 1 Hz and the corrected SBE-21 data file. Navigational input and bottom

tracking functioned properly on the remaining roving survey days (March 11, March 18, and March 20, 1999). The BB ADCP velocity determined from bottom tracking was used to correct the profile of the apparent water velocity to the actual measured values, by measuring both the ambient water motion and its own motion in the same reference frame, and was used to back correct the profile of the apparent water velocity to the actual measured values on March 10, 1999. The variation between true north and magnetic north was calculated for each survey day using the Geomagnetic Declination Online Calculator from the National Geophysical Data Center (NGDC) and incorporated into the BB ADCP processing protocol. The internal compass corrections were done following Pollard and Read (1989). Echo intensity, a proxy for acoustic backscatter, was corrected using MATLAB code provided by Luke Stearns at the University of North Carolina – Chapel Hill based on a method by Deines (1999).

7.2.3 Reduction of ADCP data to Mean Lower Low Water

In order to systematically analyze and describe the cross-channel BB ADCP measurements from Domains A and B, it was necessary to develop a technique to register and reduce the recorded bathymetry and velocity data from the SAT 1 moorings and from the roving BB ADCP to the prescribed mean lower low water (MLLW) datum. Depths relative to MLLW were generated by using the 6-minute interval long-term data collected at USCG Marker A14 (*cf.* LT 1 in Figure 7.1). The depth data at the LT 1 site was registered to the MLLW datum by the following process:

$$H_{MLLW} = H_{LT1} - \bar{H}_{LT1} + \bar{H}_{tide\ prediction\ to\ MLLW} \quad \textbf{(7.2)}$$

where H_{MLLW} is the LT 1 depth relative to MLLW, H_{LT1} is the original LT 1 depth data, $\bar{H}_{LT1}$ is the demeaned LT 1 depth data, and $\bar{H}_{tide\ prediction\ to\ MLLW}$ is the mean water depth

from tidal predictions for Bailey Cut (*cf.* Figure 2.6) relative to MLLW over the LT 1 deployment period. The LT 1 depths adjusted to MLLW were then used to reduce the roving BB ADCP depth and velocity data for each survey day (10 – 11 March 1999, 18 March 1999, and 20 March 1999) to the standard MLLW datum. The process of registering the BB ADCP data to the MLLW datum is not trivial. However, this method is advantageous because it minimizes the distortions of the BB ADCP data by numerical processing techniques and a larger portion of good quality velocity data can be retained, particularly in the intertidal region, a region whose dynamical contribution to the lateral momentum balance is usually neglected or omitted due to data processing complexities.

7.2.4 Idealized Channel Cross-Sections and Principle Axis Determination

In order to comparatively describe and quantify the spatially changing distribution of momentum in a lateral channel cross-section and between lateral cross-sections, it is necessary to consistently grid the MLLW registered irregularly spaced roving BB ADCP data and to appropriately determine a principle axis on which to rotate the data for each cross-sectional location (Domain A 4/5, A 9/10, B 5/6, and B 10/11). After its reduction to MLLW, the registered BB ADCP data for each transect realization (8 – 10 depending on weather and tidal conditions, *cf.* Figures 7.4 and 7.5) per Domain cross-section was interpolated onto a regular grid of 8 m bins horizontally and 0.5 m bins vertically to form an 'idealized cross-section' at each survey location as illustrated in Figure 7.8. The 8 meter horizontal grid size was chosen such that when the channel width was at a minimum (~ 160 m) and/or when the tide was at low water (LW), there would be at a minimum 20 lateral grid points. The 0.5 meter vertical bin size was selected to match the size of the roving BB ADCP depth bins as configured for the SAT 1 Domain surveys. By

converting the roving BB ADCP velocity profiles to gridded idealized cross-sections, the erstwhile irregularly spaced BB ADCP velocity profiles with variable bottom depths, were now a series of equally spaced velocity profiles that reference the same pre-defined (MLLW) fixed bottom. In addition, as all the cross-section realizations were gridded similarly, the change in the water volume over the tidal cycle in the lateral cross-sections was now represented by the total number of filled boxes at each stage of the tide. The benefits of this approach were that it reduced the distortion of the BB ADCP data, the lateral cross-sections can be directly compared and easily quantified, and this method provides a clear picture of changes in the lateral flow structure, including the structure of the intertidal zone, over the entire tidal cycle.

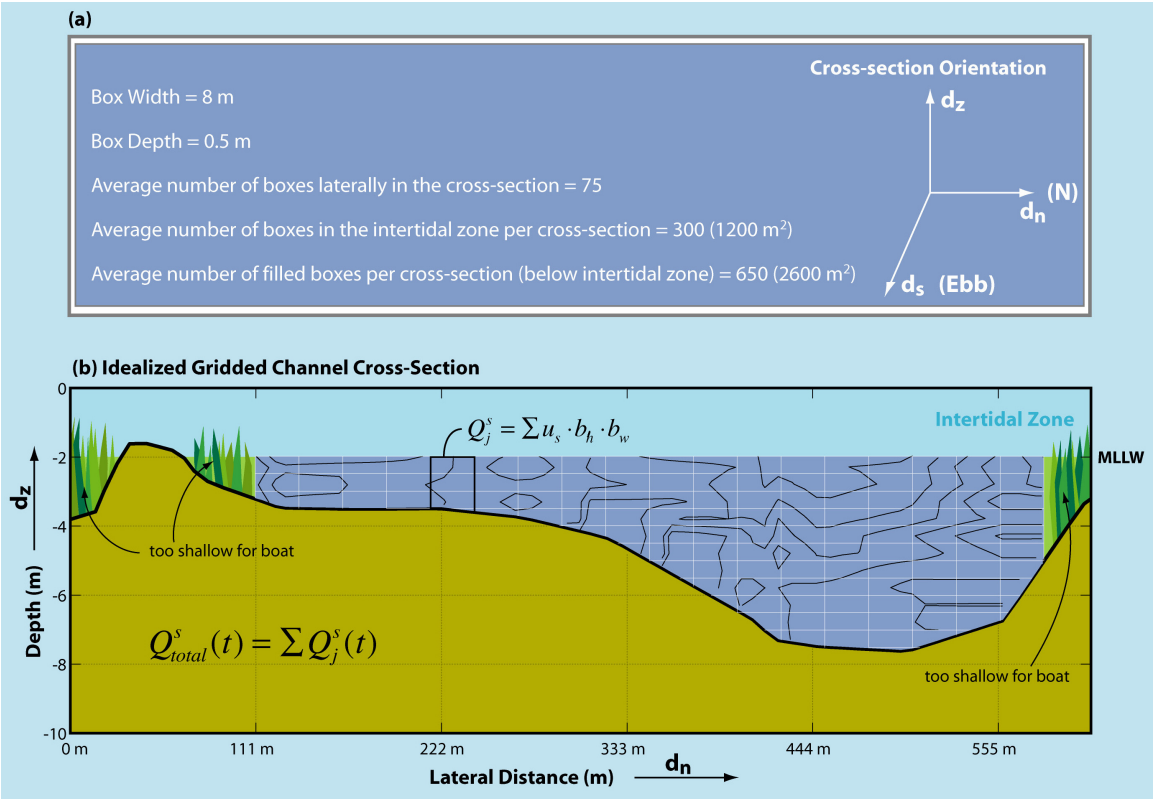

Figure 7.8: (a) Cross-section grid dimensions and orientation. (b) Idealized cross-section.

As the Satilla has a widely variable and rapidly changing bathymetry (*cf.* Figure 7.1 and 7.2), the most appropriate method for determining the principle axis is by minimizing the variability in the lateral component, $Q^{n}_{total}(t)$, of the total transport vector, $Q_{total}(t) = Q^{s}_{total}(t) + Q^{n}_{total}(t)$ where $Q^{s}_{total}(t) = \sum Q^{s}_{j}(t)$ and $Q^{n}_{total}(t) = \sum Q^{n}_{j}(t)$ and s, n, and j respectively indicate the streamwise component, the lateral component, and the j-th lateral increment. The degree of rotation for the new principle axes (Figure 7.9) is calculated at each cross-sectional location (illustrated in Figure 7.8b) by determining the average value over the tidal cycle, i.e. for the cross-sectional realizations (8 – 10 at each location), of the spatial mean of the cross-sectional depth-average (Lagrangian) transport, $\left[\left\langle \overline{Q^{s}_{j}} + \overline{Q^{n}_{j}} \right\rangle\right]_{realizations}$ referred to herein as the 'global mean of the cross-sectional depth-average transport' or the 'global mean transport', where the pair of square brackets, $[\ ]$, indicates the average of the interior quantity over time, the pair of angular brackets, $\langle\ \rangle$, indicates the average of the interior quantity over space, the overbar represents depth-averaging, and where $Q^{s}_{j} = \sum u_s b_h b_w$ and $Q^{n}_{j} = \sum u_n b_h b_w$, u_n and u_s are respectively the normal and streamwise velocity, b_h is the idealized cross-section box height (0.5 m), and b_w is the idealized cross-section box width (8 m). The 'global mean transport' is used, in contrast to the commonly used Rozovskii method (Bathurst et al. 1977; Thorne and Hey 1983; Geyer 1993b; Rhoads and Kenworthy 1995; Chant and Wilson 1997; Valle-Levinson and Atkinson 1999; Lacy and Monismith 2001), which uses the velocity field to determine the principle axes, because as a volume per unit time, the Langrangian transport vector properly weights the flow field that is

influenced by local bathymetry, irrespective of nearby river confluences or of channel bend orientation, to uniquely define a lateral transect (Lane et al. 2000). An additional benefit to using the transport principle axes method is that it does not mathematically restrict a transfer of mass or momentum downstream, unlike the Rozovskii method, which assumes that a secondary circulation cell is completed within one lateral transect (Lane et al. 2000). By the simple choice of principle axes methodology, it is possible to directly observe the downstream transfer of momentum due to secondary circulation, as will be shown in Section 7.3.3. The new axes and the degree of rotation for each of the lateral cross-sections B 10/11, B 5/6, A 9/10, and A 4/5, along with the normalized average transport associated with the registered gridded idealized cross-sections at each Domain location are shown in Figure 7.9.

After reducing the roving BB ADCP data to the MLLW datum, systematically gridding it onto the 'idealized' cross-sections, and rotating it to a new set of principle axes, it is possible to directly calculate and investigate changes in the impact, structure, and character of secondary circulation in the two lateral cross-sections for each Domain. The calculations in the following sections are focused on maximum ebb and maximum flood tide, when axial acceleration is at a minimum, and the lateral structure of the axial flow can be examined assuming steady-state conditions.

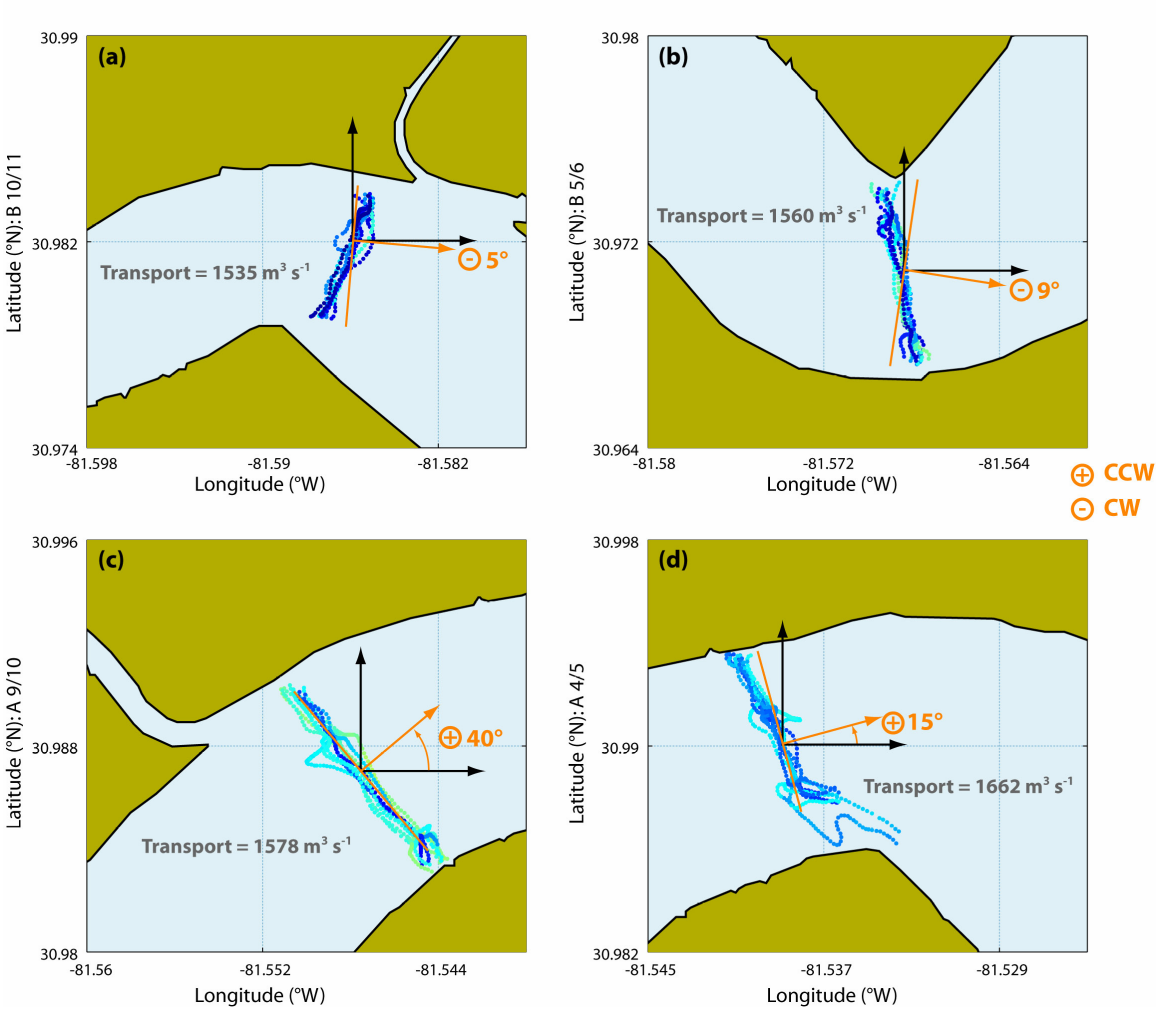

Figure 7.9: Principle axis determination based on the global mean of the depth-average lateral transport at cross-sections (a) B 10/11, (b) B 5/6, (c) A 9/10, and (d) A 4/5. The orientation and degrees of rotation are noted by orange lettering at each cross-section location. Likewise, after rotation to the new principle axis, the normalized average transport associated with the registered gridded idealized cross-sections for each location is shown in gray lettering. CCW and CW respectively indicate the counter-clockwise and clockwise directions.

7.3 Results and Discussion

The gross features of the salinity distribution from the R/V Gannet FSI CTD and the onboard SBE-21 system and the velocity profiles from the roving BB ADCP for the SAT 1 experiment are shown respectively in Figures 7.10 and 7.11 in Section 7.3.1 and in Figures 7.12 and 7.13 in Section 7.3.2. Section 7.3.1 presents the spring and neap observations of the salinity distribution during maximum ebb and maximum flood tide. While subsequently, Section 7.3.2 presents the observed three-dimensional velocity profiles for spring and neap during maximum ebb and maximum flood tide.

7.3.1 Spring and Neap Tide Salinity Distributions

For brevity and clarity, Figures 7.10 and 7.11 show the salinity distribution during maximum ebb for the representative lateral cross-section A 4/5 collected during the spring and neap rapid spatial surveys. As discussed previously in Chapter 5, the signature of secondary circulation is the strongest and the most apparent during ebb tides, when both the axial velocity and the vertical shear of the axial current are at a maximum (Ott 2000; Blanton et al. 2002; Ott 2002). As a result, the salinity and velocity distributions associated with spring and neap ebb tides reflect the maximum range of conditions, while the salinity and velocity distributions associated with spring and neap flood tides fall within the range of the spring and neap ebb tide conditions. As a result, only the maximum ebb tide conditions will be presented and discussed accordingly.

At spring tide, for both maximum ebb and maximum flood, the salinity structure in Domains A and B of the Satilla River reflects a laterally stratified system (Figure 7.10) of about a $(\Delta s)_h$ = 2 PSU difference (2 to 4 PSU) from bank-to-bank with a stratified vertical structure ranging from a $(\Delta s)_z$ = 3 PSU difference in the deep channel to

vertically well-mixed area, $(\Delta s)_z = 0$, over the shoal region. The mixing power associated with the high velocity axial current at spring tide easily overturns the water column, especially in the shallows, weakening the vertical density gradient and vertically homogenizing the water column. These results are consistent with the salinity distribution as expected from the Seim and Gregg (1997) model and suggest the presence of a single vertical secondary circulation cell in the *thalweg* (deep channel). However, the same axial current at spring tide increases the horizontal shear and the lateral density gradients as the water flows around the numerous channel bends in the river. Consequently, less dense water is often found in the *thalweg*. The lighter water is separated from the heavier water which is forced into the shoal region near the channel center leading to a greater degree of lateral stratification. Surface fronts are often observed upriver of the shoal region during an incoming flood tide where waters of different salinities collide and partially re-mix before entering the next channel bend.

In contrast, the salinity structure at neap tide during maximum ebb and maximum flood reflects a vertically stratified system (Figure 7.11) ranging from a $(\Delta s)_z = 2$ PSU difference (5 to 7 PSU) in the deep channel to a $(\Delta s)_z = 3$ PSU difference (2 to 5 PSU) over the shoal region with a laterally stratified structure of about $(\Delta s)_h = 2$ PSU across the channel, from bank to bank. Not surprisingly, due to the slower axial currents associated with neap tides and the sinuous nature of the Satilla, the vertical density gradient is significantly greater than the horizontal density gradient. Currents at neap do not provide enough mixing energy to overcome the moderate to strong vertical stratification, which agrees with the results from Chapter 5, suggesting a sufficient vertical salinity difference (≥ 3 PSU in this case) can halt curvature-driven secondary

flow, which in turn reduces vertical mixing. The shoal area is shallow, requiring less energy input locally to mix the water column, but the energy input is often insufficient to completely vertically homogenize the water column, resulting in only a slightly weaker vertical density gradient in that region. The average salinity in the shoal area is approximately equal to the mean value of the salinity in the deep channel, indicating that there is communication across the channel transect during neap tides.

The salinity structure of the Satilla River appears to shift from a laterally stratified two-channel system at spring tides to a vertically stratified two layer system at neap tides. The tidal and fortnightly variations in salinity for Satilla River are known to be primarily affected by changes in tidal amplitude and river discharge (Blanton et al. 2001), though some changes in the lateral and vertical salinity structure between spring and neap tides are likely related to the geomorphology of the Satilla River. Similar to ebb dominant estuaries of coastal South Carolina, the Satilla features a sinuous *thalweg* (deep channel) that is separated from a secondary shallow channel by a series of shoals (Sexton and Hayes 1996). At spring tides, communication is limited between the two channels to times of high water and is virtually non-existent during times of low water, when near surface shoals are exposed, effectively producing two separate tidal channels.

7.3.1.1 Spring Tide – Maximum Ebb

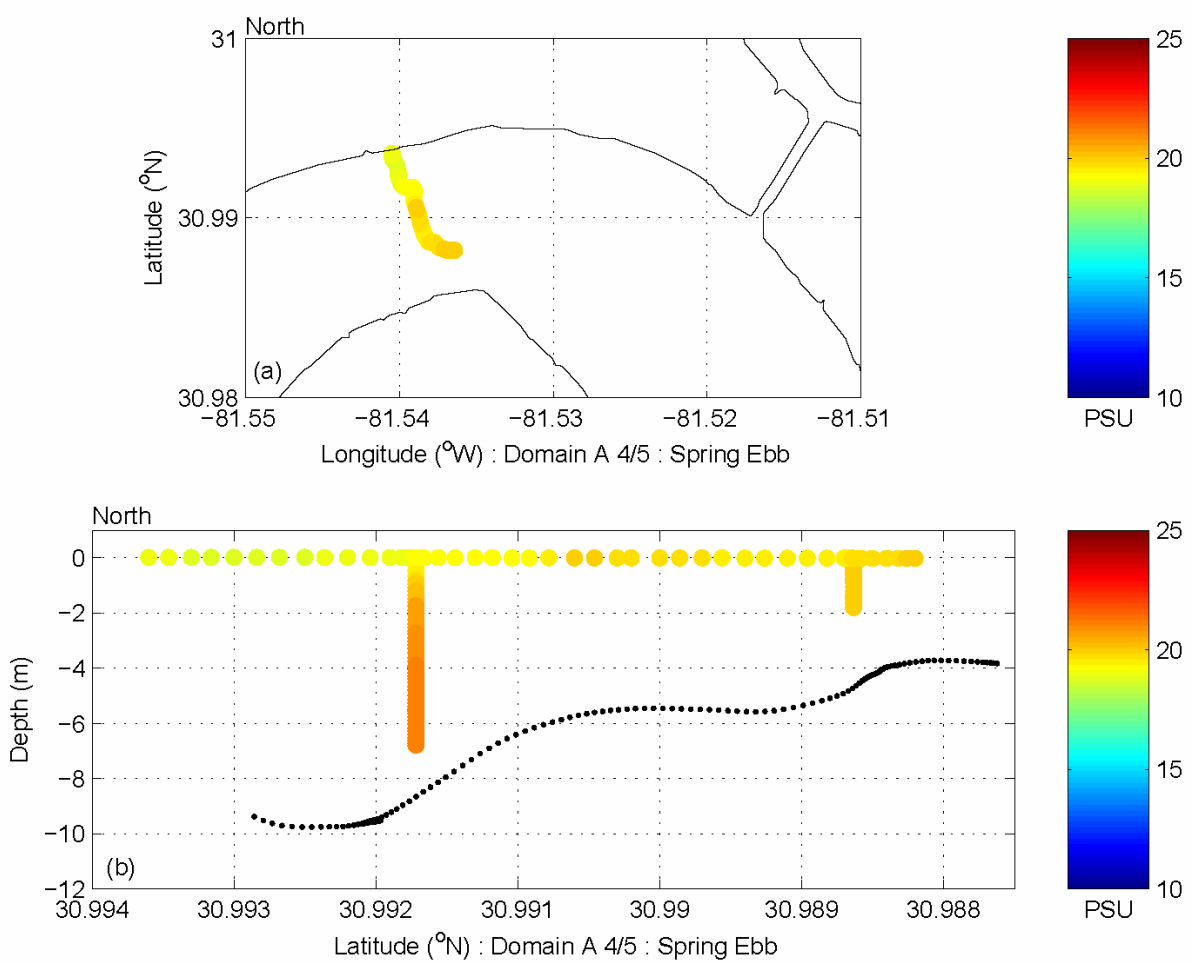

Figure 7.10: (a) Plan view plot of SBE-21 surface track in Domain A 4/5 during maximum ebb at spring tide. (b) YZ plot of the SBE-21 surface track with FSI CTD casts in Domain A 4/5 during maximum ebb at spring tide. The leftmost cast corresponds to the north channel and the rightmost cast corresponds to the south channel. The salinity structure shown is stratified laterally ~ 2 PSU across the channel, stratified ~ 3 PSU vertically in the deep channel, and well-mixed vertically over the shoal.

7.3.1.2 Neap Tide – Maximum Ebb

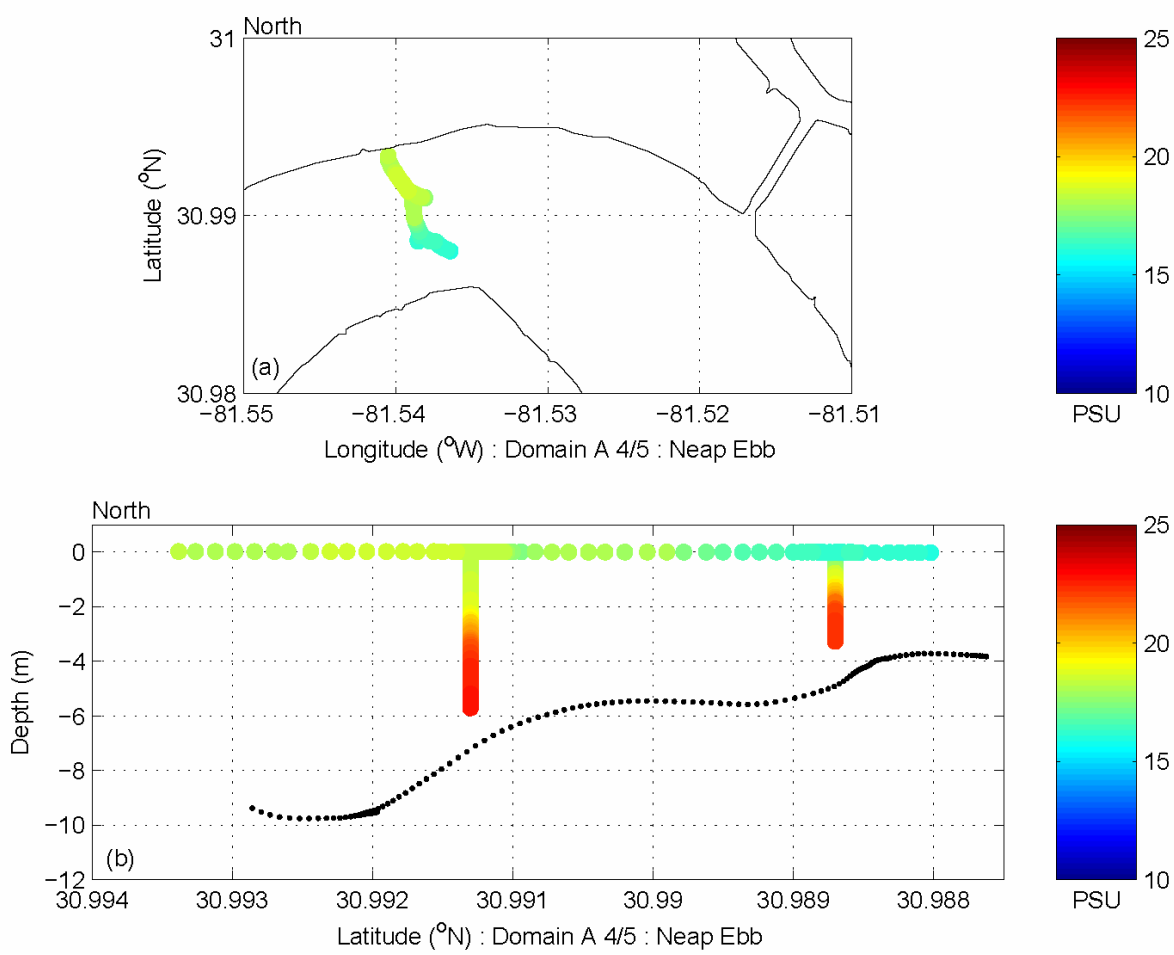

Figure 7.11: (a) Plan view plot of SBE-21 surface track in Domain A 4/5 during maximum ebb at neap tide. (b) YZ plot of the SBE-21 surface track with FSI CTD casts in Domain A 4/5 during maximum ebb at spring tide. The leftmost cast corresponds to the north channel and the rightmost cast corresponds to the south channel. The salinity structure shown is stratified laterally ~ 2 PSU across the channel, stratified ~ 7 PSU vertically in the deep channel, and stratified vertically ~ 5 PSU over the shoal.

7.3.2 Spring and Neap Tide Velocity Distributions

Figures 7.12 and 7.13 respectively show the three observed velocity components from the roving BB ADCP during maximum ebb for the representative lateral cross-section A 4/5 during the spring and neap rapid spatial surveys. A right-handed reference frame is used to describe the BB ADCP data, and is illustrated in Figures 7.12 and 7.13. In both Figures 7.12 and 7.13, subpanel (a) shows the axial velocity, where red indicates ebb flow, subpanel (b) shows the lateral velocity, where red indicates flow toward the outside of the channel bend, and subpanel (c) shows the vertical velocity, where red indicates upward flow.

At spring tide (Figure 7.12), persistent cores of axial and transverse velocity were observed in each lateral cross-section for both maximum ebb and maximum flood tides. As expected, because the Satilla is a weakly ebb-dominant system (Blanton et al. 2002), the axial and lateral currents were stronger during maximum ebb than during maximum flood. The core of maximum axial velocity (circled in Figure 7.12a) was most often located slightly to the inside of the *thalweg* on the flank of the shoal (between Latitudes 30.9905 ºN and 30.9915 ºN) or in the shallows, while the core of transverse velocity (circled in Figure 7.12b) was found shifted to the outside of the axial velocity core, toward the outside of the channel bend and generally centered in the *thalweg* (located between Latitudes 30.9915 ºN and 30.993 ºN). The observed transverse circulation patterns in the Domain A and B lateral cross-sections were consistent with secondary circulation driven by channel curvature in an unstratified fluid (Seim and Gregg 1997), and were similar to those observed by Seim et al. (2002), with flow to the outside of the channel bend at the surface and flow toward the inside of the channel bend below mid-

depth in the *thalweg*. Though the secondary circulation signal was more subtle during maximum flood than during maximum ebb, the single vertical circulation pattern in the *thalweg* was maintained throughout the tidal cycle. Vertical velocity profiles for Domains A and B during maximum ebb and maximum flood at spring tide suggest the presence of two laterally adjacent secondary circulation cells, with one located in the *thalweg* and one located on the flank of the shoal. If reliable, a benefit to retaining vertical velocity data from the BB ADCP is that it could provide a simple method to determine the lateral width of individual secondary circulation cells.

At neap (Figure 7.13), similar persistent but reduced cores of axial and transverse velocity were observed in each lateral cross-section for both maximum ebb and maximum flood tides. During neap, the core of maximum axial velocity (circled in Figure 7.13a) was more diffuse and was most often located in the shallows just beyond the flank of the shoal (between Latitudes 30.990 ºN and 30.9915 ºN), while a weaker, shallower core of transverse velocity (circled in Figure 7.13b) was found shifted to the outside of the axial velocity core in the *thalweg* (between Latitudes 30.9915 ºN and 30.993 ºN). The observed transverse circulation patterns in the Domain A and B lateral cross-sections during neap were more complex, with flow to the outside of the channel bend at the surface, flow toward the inside of the channel bend at approximately mid-depth, and either a weak flow toward the outside of the channel bend around 2 meters above the bottom (mab) or a stagnation zone below this depth, depending on the local stratification conditions. The vertically-stacked secondary flow configuration was observed in all the Domain A and B lateral cross-sections during maximum ebb, while the stagnation zone was most often observed in the Domain A and B lateral cross-

sections during maximum flood. The upper cell in the stacked secondary flow configuration is consistent with secondary circulation driven by channel curvature (Seim and Gregg 1997), while the lower, weaker lateral circulation pattern, as determined in Chapters 5 and 6, is likely the result of internal adjustments to the density field, which initiate an internal lateral seiche (Chant 2002; Seim et al. 2002). The stagnation zone, most often observed during maximum flood, develops when the local lateral baroclinic pressure gradient balances the centrifugal acceleration associated with flow around the channel bend (Seim and Gregg 1997). The presence of the lowermost secondary circulation cell, which may only be detected downstream of bends, reduces the mixing depth of the upper curvature-driven secondary circulation cell by approximately half, from an overall depth of 6 meters at spring tide to approximately 3 meters at neap tide. Vertical velocity profiles for Domains A and B during maximum ebb and maximum flood at neap tide suggest the presence of two weak laterally adjacent secondary circulation cells, with one located in the *thalweg* and one located between the flank of the shoal and in the shallows.

Figures 7.14 and 7.15 show the tidally-averaged mean axial and mean lateral velocity profiles for spring and neap tide in the representative lateral cross-section Domain A 4/5. Figure 7.14 demonstrates that during spring, the axial flow has a two-channel nature with a defined ebb and flood channel, and that during neap, the axial flow has a two-layer structure. Likewise, Figure 7.15 demonstrates that during spring, the lateral flow consists of a single vertical secondary circulation cell, mixing the water column from top to bottom, and that during neap, the lateral flow has a more complex pattern of two vertically-stacked secondary circulation cells.

7.3.2.1 Spring Tide – Maximum Ebb

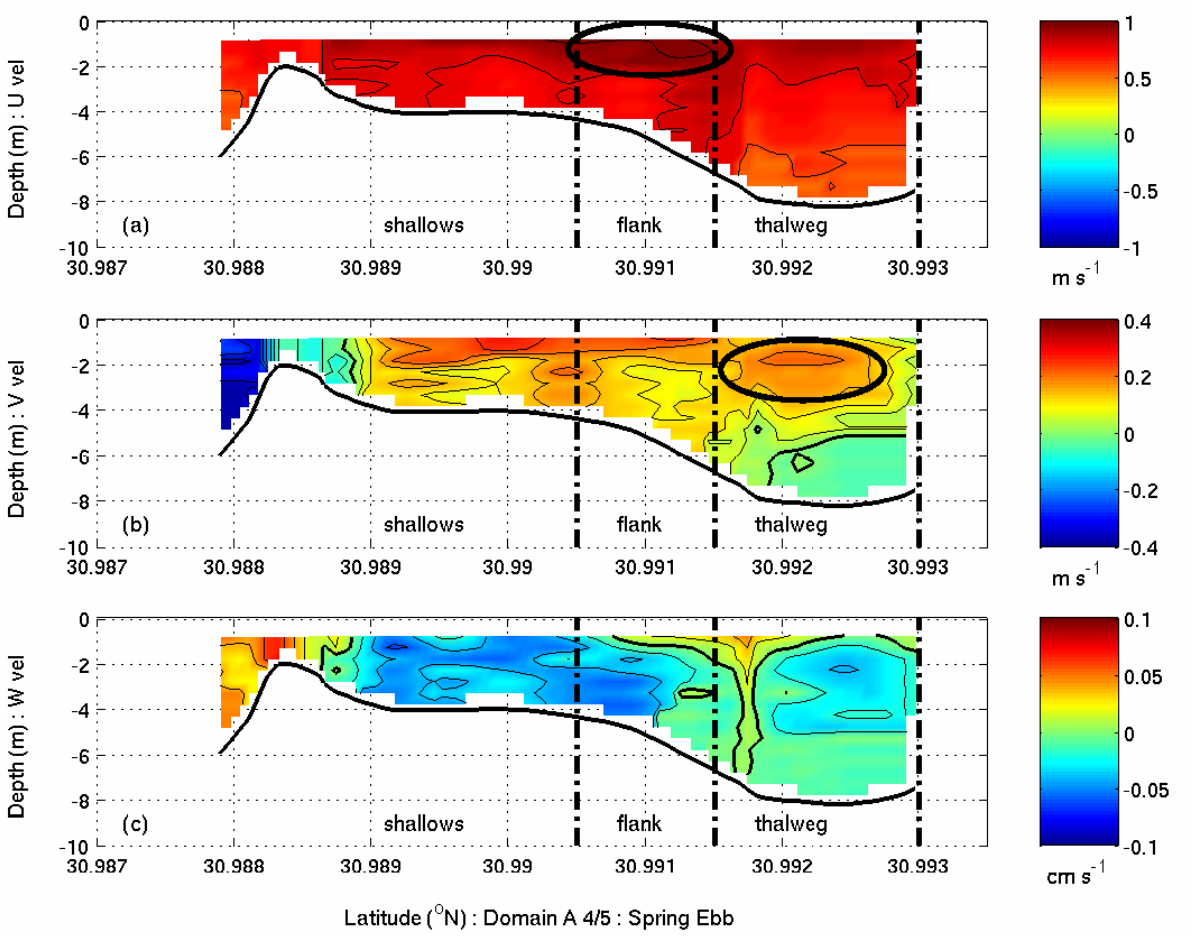

Figure 7.12: The (a) axial, (b) lateral, and (c) vertical velocity structure for maximum ebb at spring tide in Domain A 4/5. Red in subpanel (a) indicates ebb flow, red in subpanel (b) indicates flow to the outside of the channel bend, and red subpanel in (c) indicates upward flow. The bold solid line in the figure subpanels indicates the zero crossing and the approximate locations of the shallows, flank of the shoal (labeled as flank), and the *thalweg* are shown below each subpanel.

7.3.2.2 Neap Tide – Maximum Ebb

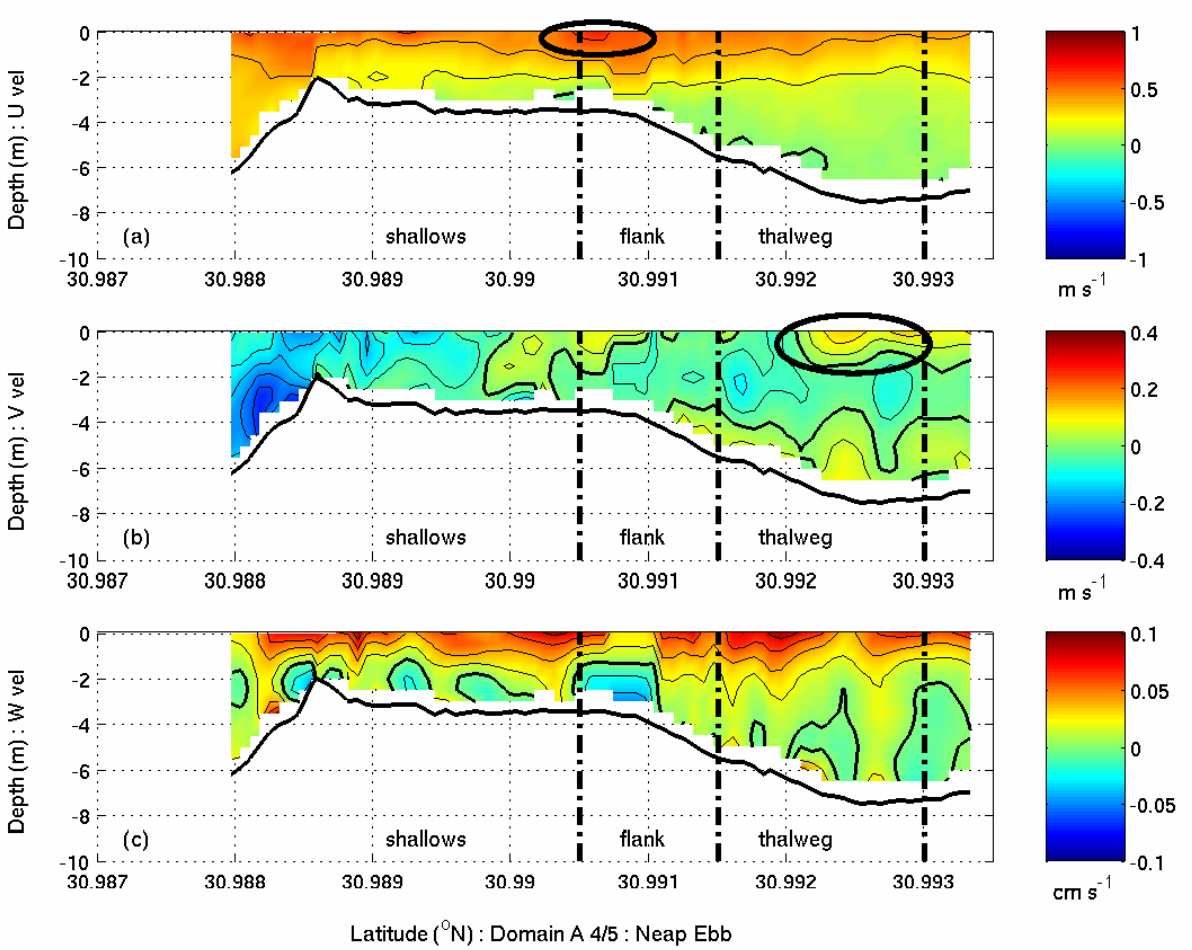

Figure 7.13: The (a) axial, (b) lateral, and (c) vertical velocity structure for maximum ebb at neap tide in Domain A 4/5. Red in subpanel (a) indicates ebb flow, red in subpanel (b) indicates flow to the outside of the channel bend, and red subpanel in (c) indicates upward flow. The bold solid line in the figure subpanels indicates the zero crossing and the approximate locations of the shallows, flank of the shoal (labeled as flank), and the *thalweg* are shown below each subpanel.

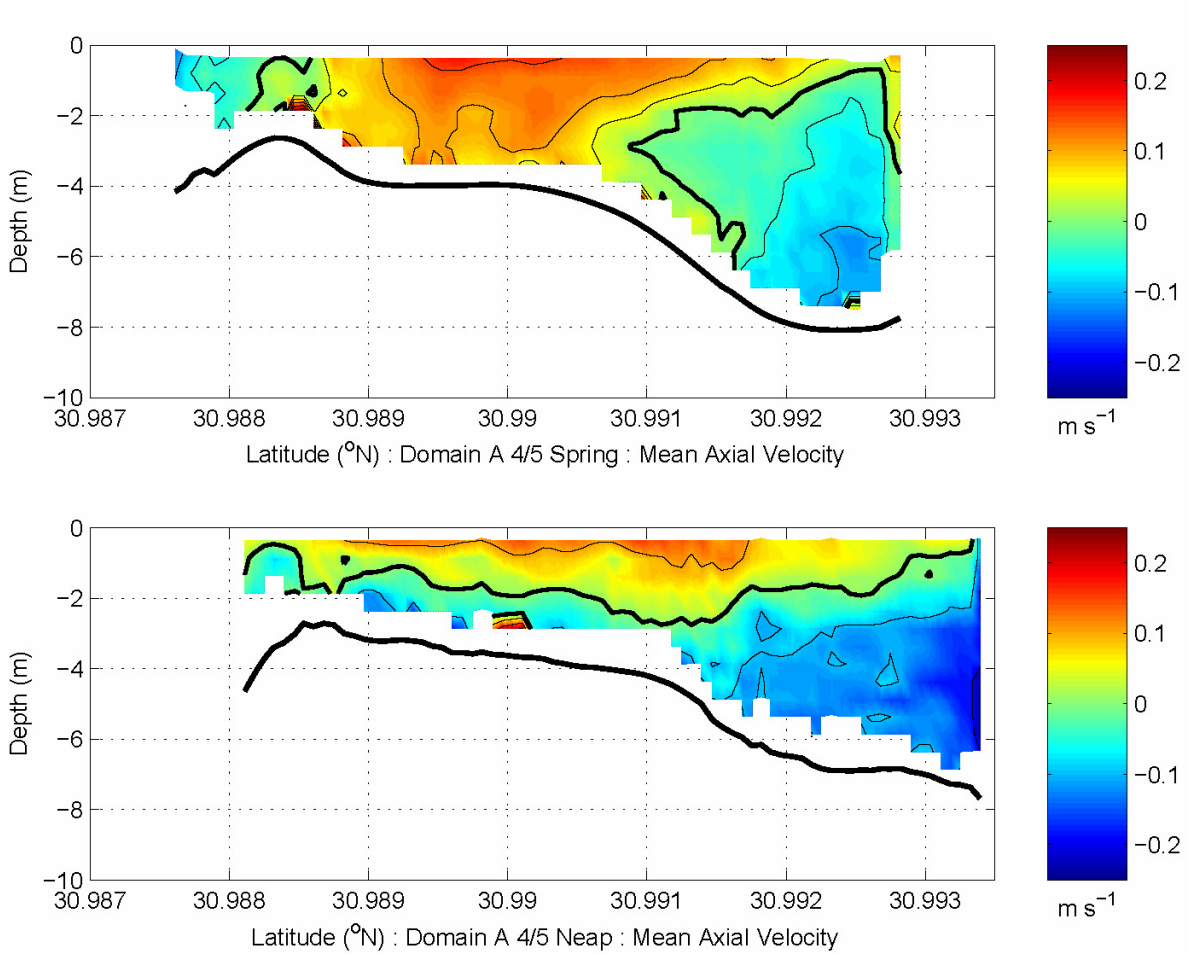

Figure 7.14: The tidally-averaged mean axial velocity in lateral cross-section Domain A 4/5 for (a) spring tide and for (b) neap tide. Seaward flow is indicated by positive values and landward flow is indicated by negative values. The bold solid line in the figure subpanels indicates the zero crossing.

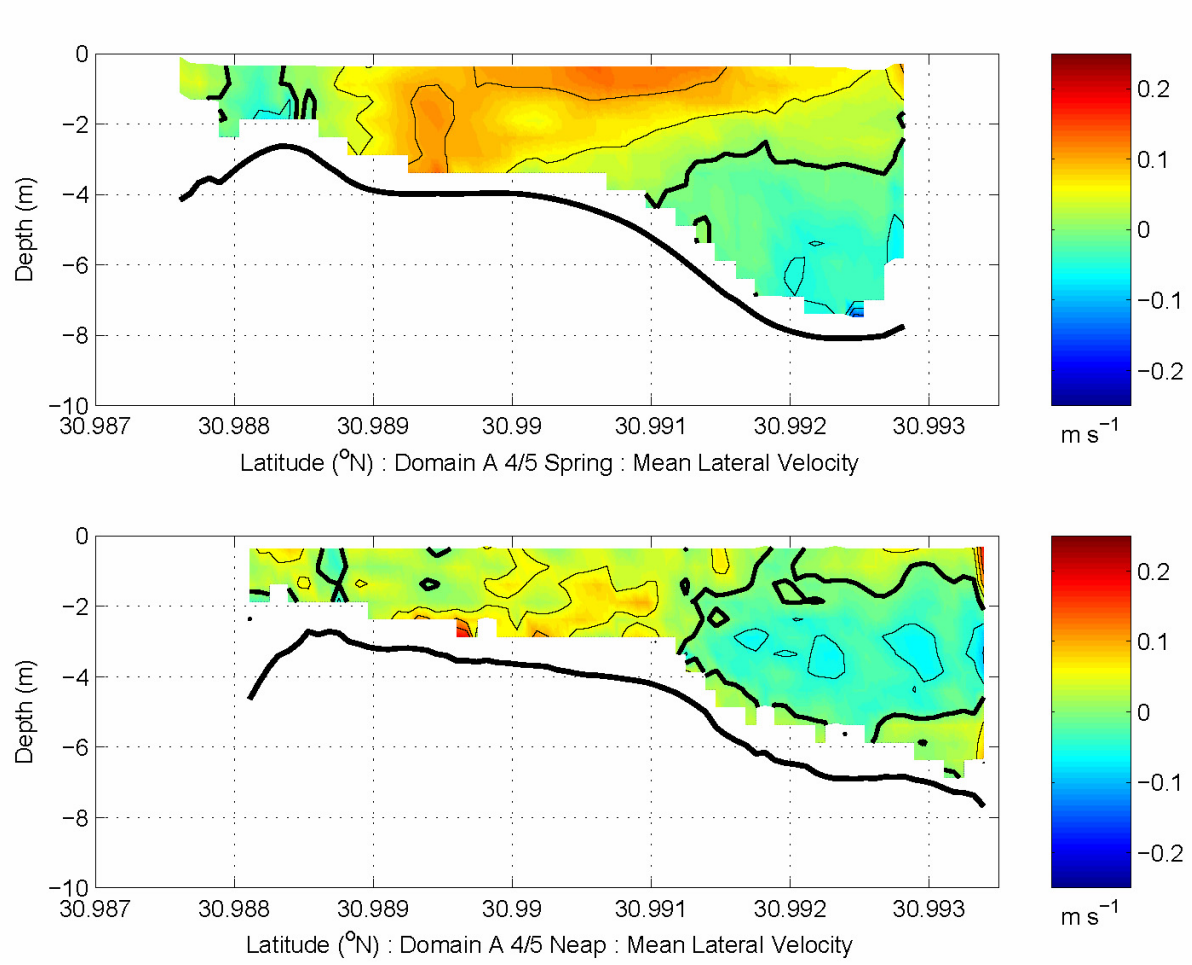

Figure 7.15: The tidally-averaged mean lateral velocity in lateral cross-section Domain A 4/5 for (a) spring tide and for (b) neap tide. Flow toward the outside of the channel bend is indicated by positive values and flow toward the inside of the channel bend is indicated by negative values. The bold solid line in the figure subpanels indicates the zero crossing.

7.3.3. Secondary Circulation and the Axial Transfer of Momentum

During spring tide (Figures 7.16 and 7.17), cores of axial and transverse momentum (the core velocity in each subpanel of Figures 7.16 and 7.17 multiplied by a constant density of $\rho_o = 1014$ kg m^{-3}) were observed in each lateral cross-section that increased in size and decreased in strength in the downstream direction at maximum ebb and maximum flood tides. While more pronounced at maximum ebb than maximum flood, the core of maximum axial momentum was most often located slightly to the inside of the *thalweg* on the flank of the shoal or in the shallows, while the core of transverse momentum was found shifted slightly to the outside of the axial momentum core, toward the outside of the channel bend and generally closer to the *thalweg*. At spring tide, when vertical stratification was weak, cores of axial and transverse momentum were observed at or near the bottom of the water column in each of the lateral transect locations, and are suggested by the axial velocity profiles in Figure 7.18.

Likewise, during neap tide (Figures 7.19 and 7.20), reduced cores of axial and transverse momentum (as above, the core velocity in each subpanel multiplied by a constant density of $\rho_o = 1014$ kg m^{-3}) were observed in each lateral cross-section that increased moderately in size and maintained a relatively constant strength in the downstream direction, at maximum ebb and maximum flood tides. During neap, the core of maximum axial momentum was more diffuse and was most often located in the shallows just beyond the flank of the shoal, while a weaker core of transverse momentum was found shifted slightly to the outside of the axial momentum core and generally closer to the *thalweg*. At neap tide, when vertical stratification was strong, cores of axial and transverse momentum were trapped closer to the surface and penetrated to only

mid-depth in each of the lateral transect locations, and are suggested by the axial velocity profiles in Figure 7.21. For both spring and neap tides, the axial momentum flux in each lateral transect was oriented along the *thalweg*. Likewise, the lateral momentum flux in each lateral transect was directed toward the outer bank and was consistent with the pattern of observed curvature-induced secondary circulation at each of the transect locations.

Seim et al. (2002) and Blanton et al. (2003) have shown that in the first bend of the Satilla River (*cf.* Figure 7.1 near Station 3), ebb currents in the deepest part of the channel were consistently stronger at the seaward end of the bend (downriver) and flood currents were consistently stronger at the landward end of the bend (upriver), with the maximum difference occurring at spring tide. They postulated that the observed increase in bottom currents during spring tide was due to the vertical advection of axial momentum by curvature-driven secondary circulation, which these observations support.

Table 7.4 summarizes the variations between maximum ebb and maximum flood for neap and spring tide in the buoyancy frequency, given here as N_z^2 in radians^2 s^{-2}, the total axial and lateral transport per unit area in m s^{-1}, and the total axial momentum in kg m^{-2} s^{-1} for the lateral cross-sections A 4/5 – B 10/11. As seen in Table 7.4, the buoyancy frequency, the total axial and lateral transport per unit area, and the total axial momentum vary fortnightly and over the tidal cycle. The lowest buoyancy frequencies were observed during spring tide, and the highest buoyancy frequencies were observed during neap tide with one exception at Domain B 5/6 for maximum flood at spring tide. The occurrence of the higher N_z^2 value at Domain B 5/6 for maximum flood at spring tide, more similar to N_z^2 values seen during neap tide, is presently unclear. Excluding

the B 5/6 spring tide maximum flood observation, the average N_z^2 value for spring tide over both maximum ebb and maximum flood was approximately 1.5E-3±3.5E-4 s^{-2}. Likewise, the average N_z^2 value for neap tide over both maximum ebb and maximum flood was approximately 6.1E-3±4.2E-4 s^{-2}. These results are in agreement, though about 6 times larger, with those reported by Friedrichs and Wright (1997) for weak stratification, $(\Delta s)_z \approx 2$ PSU, and for strong stratification, $(\Delta s)_z \approx 3$ PSU. Similarly, the total axial transport per unit area as shown in Table 7.4 was found to be the highest during spring tide, typically during maximum flood, and was found to be the lowest during neap tide, typically during maximum ebb. The total lateral transport per unit area, with a weaker signal and a more variable nature, followed a similar trend to the total axial transport, with the highest observed values occurring during spring tide and the lowest observed values occurring during neap tide.

Changes in the total axial momentum, shown in the last column of Table 7.4, may be a revealing assessment in the connection between secondary circulation and the transfer of axial momentum in the downstream direction. Similar to Seim et al (2002) and Blanton et al. (2003), the total axial momentum was found to be generally stronger at the channel bend furthest downstream, with the maximum difference occurring at spring tide. Variations in the total axial momentum suggest that during both ebb and flood tide there is a local acceleration into the channel bend and a local deceleration out of the channel bend. In this manner, while total axial momentum is conserved, secondary circulation may provide a source mechanism for enhancing the transfer axial momentum as the fluid travels into the bend and a sink mechanism for reducing the transfer of axial momentum as the fluid exits the bend. These results, as the previous observations,

support the hypotheses of Seim et al. (2002) and Blanton et al. (2003) in that curvature-driven secondary circulation acts to redistribute axial momentum in the downstream direction by advecting higher momentum fluid toward the bottom boundary layer.

Spring and neap observations of the cores of axial and transverse momentum are used in Section 7.3.4 to determine the reasonableness of the spatial and temporal characteristics of secondary flow within and between the Domain A and B lateral transect locations.

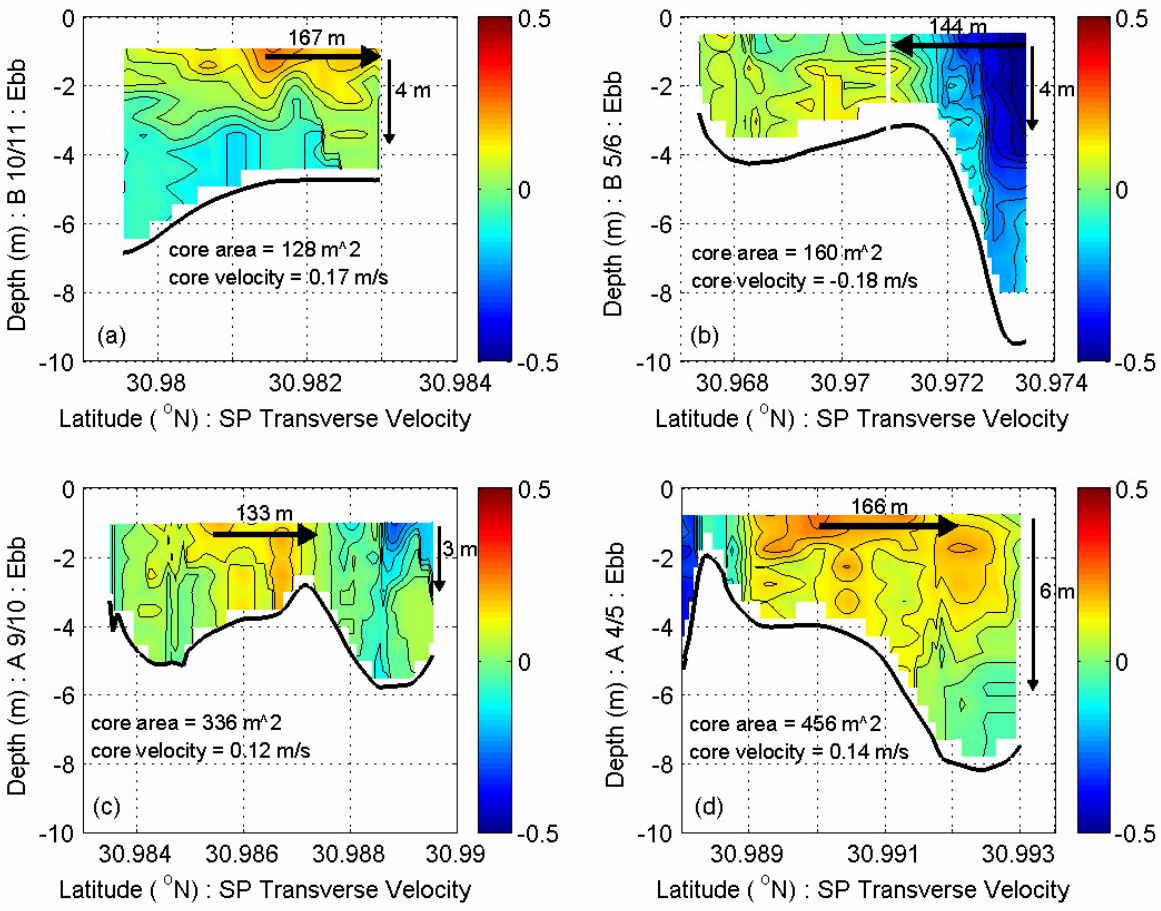

Figure 7.16: The spatial scales of secondary circulation and the transfer of axial momentum downstream (the core velocity in each subpanel multiplied by a constant density, $\rho_o = 1014$ kg m^{-3}) during maximum ebb at spring tide for sections (a) Domain B 10/11, (b) Domain B 5/6, (c) Domain A 9/10, and (d) Domain A 4/5.

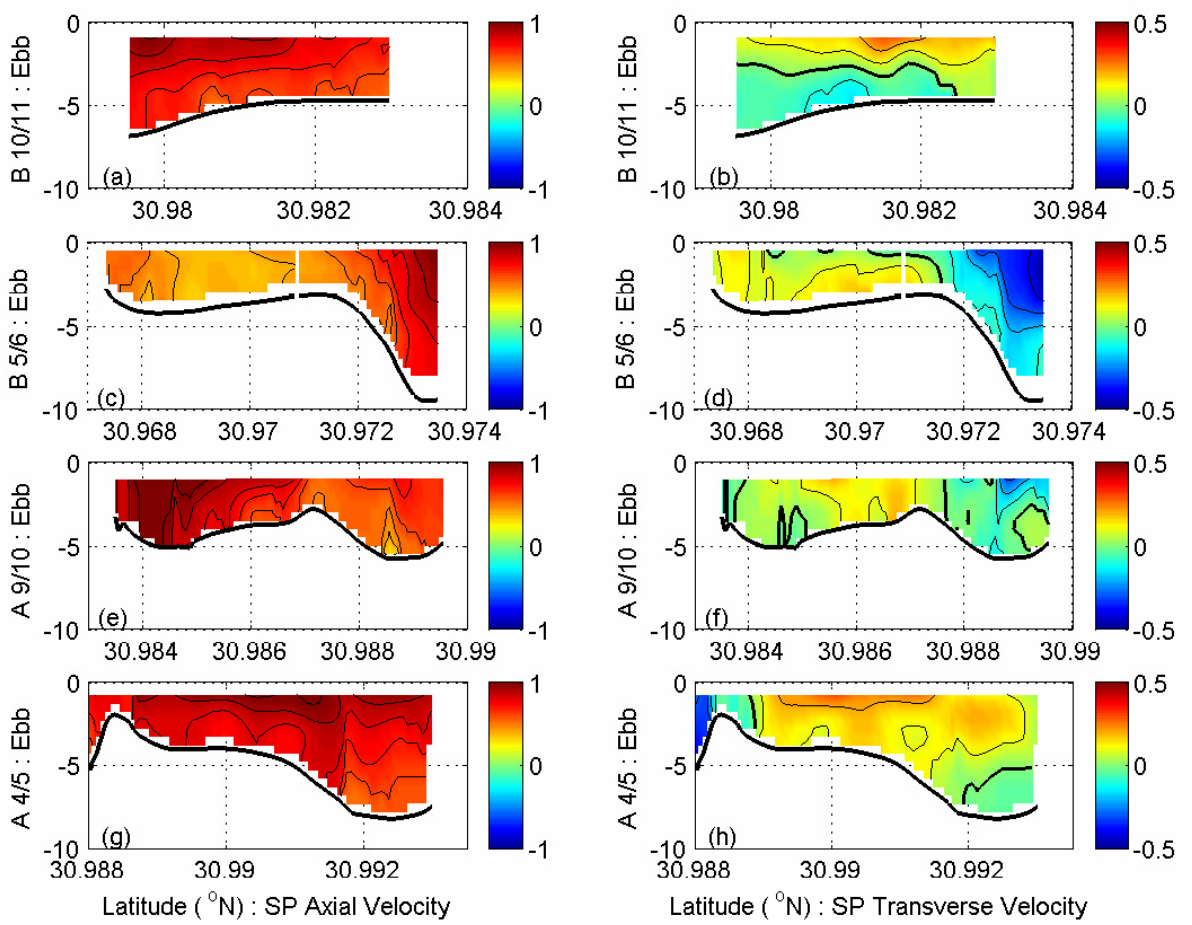

Figure 7.17: The spatial scales of secondary circulation and respectively, the transfer of axial and lateral momentum in the downstream direction (the core velocity in each subpanel multiplied by a constant density, $\rho_o = 1014$ kg m^{-3}) during maximum ebb at spring tide for sections (a & b) Domain B 10/11, (c & d) Domain B 5/6, (e & f) Domain A 9/10, and (g & h) Domain A 4/5.

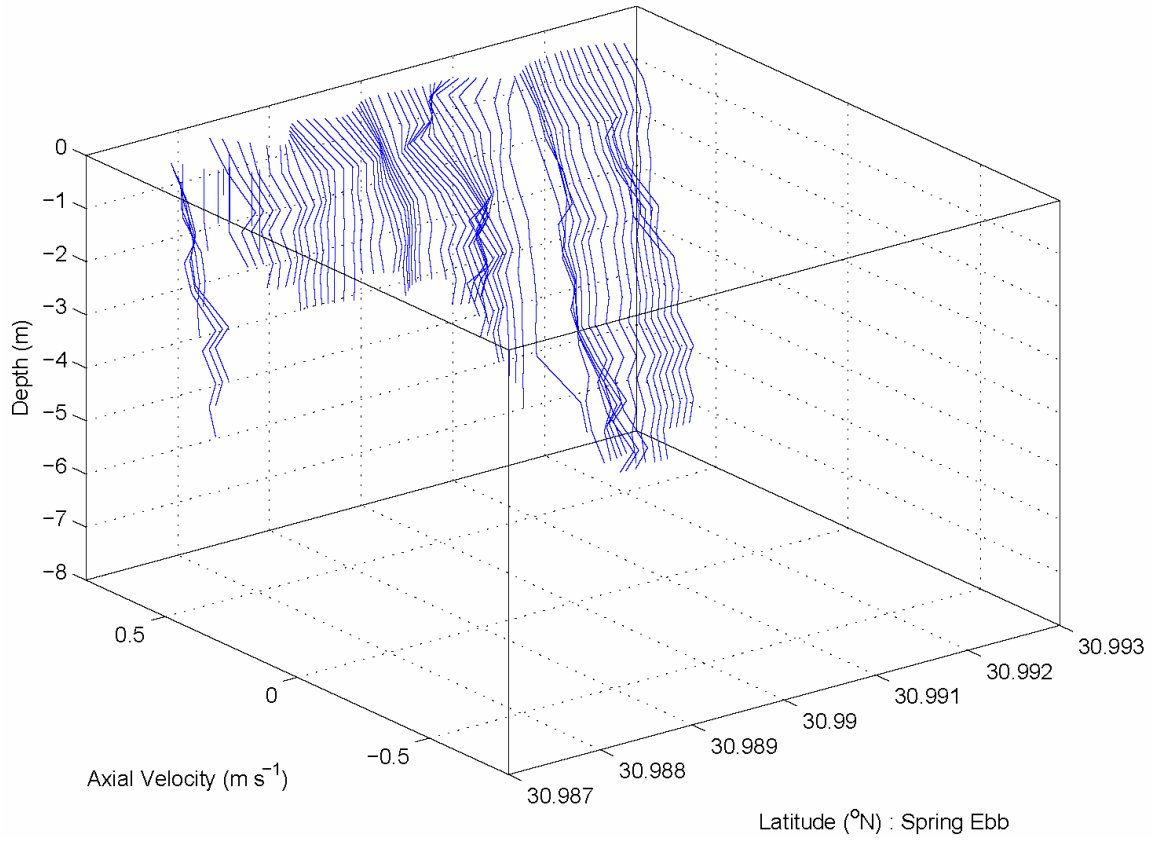

Figure 7.18: Axial velocity profiles at maximum ebb for spring tide conditions in the representative lateral cross-section Domain A 4/5.

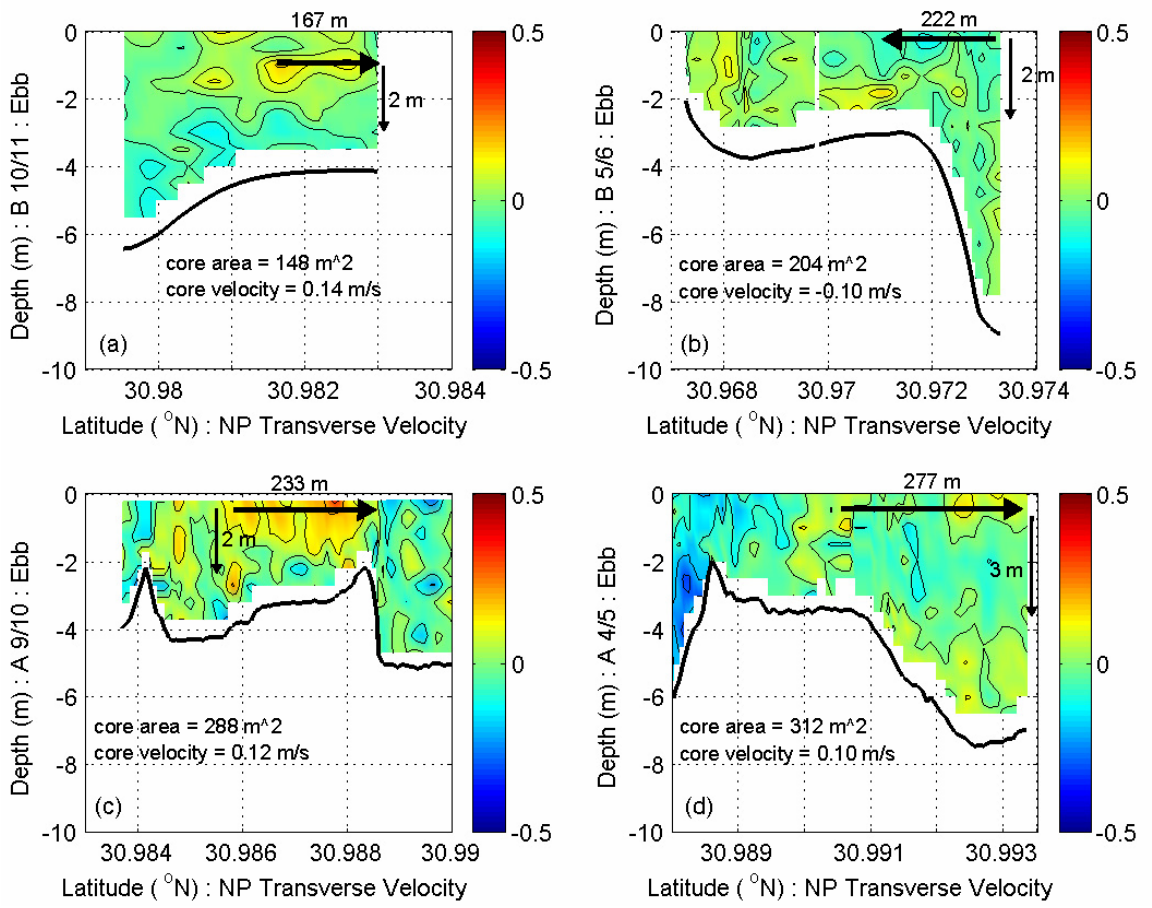

Figure 7.18: The spatial scales of secondary circulation and the transfer of axial momentum downstream (the core velocity in each subpanel multiplied by a constant density of $\rho_o = 1014$ kg m^{-3}) during maximum ebb at neap tide for sections (a) Domain B 10/11, (b) Domain B 5/6, (c) Domain A 9/10, and (d) Domain A 4/5.

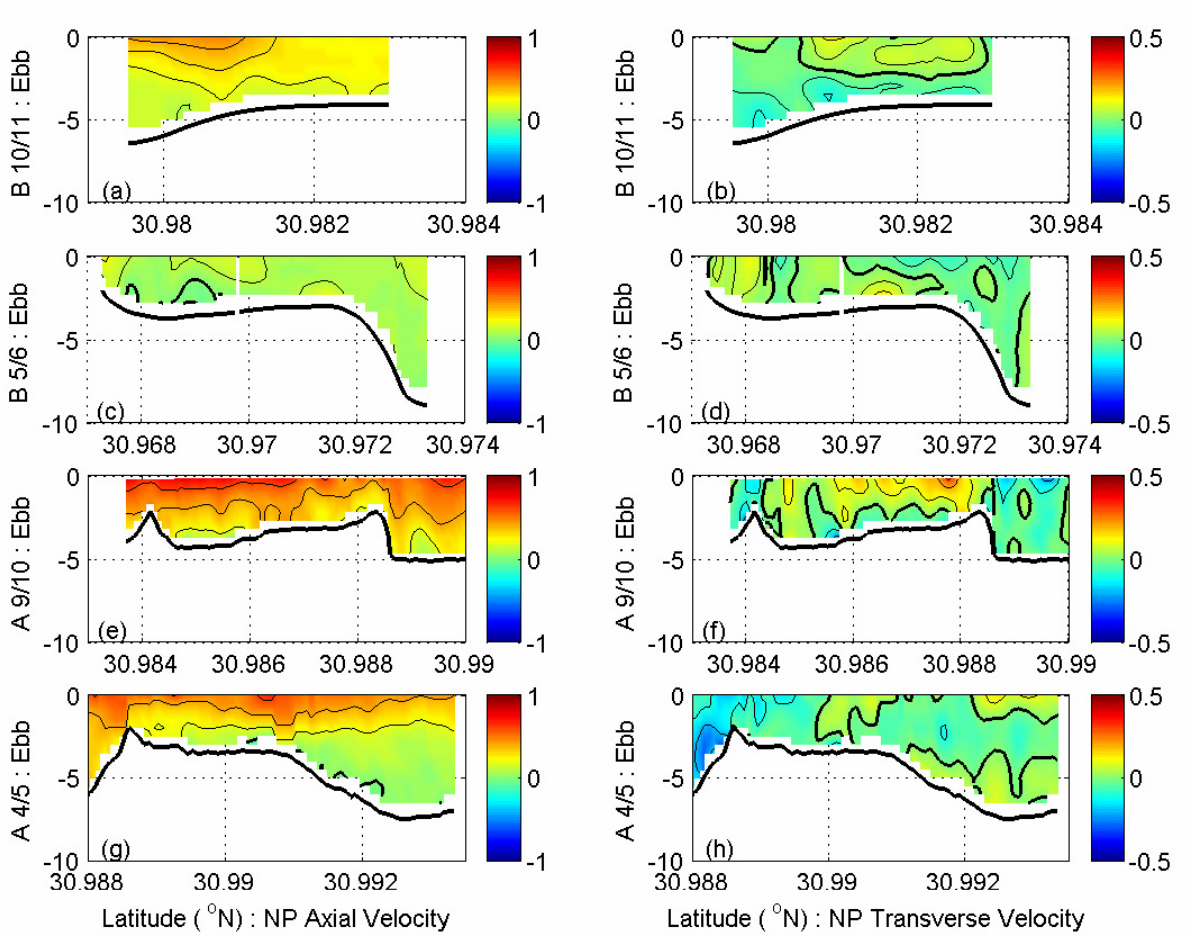

Figure 7.19: The spatial scales of secondary circulation and respectively, the transfer of axial and lateral momentum in the downstream direction (the core velocity in each subpanel multiplied by a constant density, $\rho_o = 1014$ kg m^{-3}) during maximum ebb at neap tide for sections (a & b) Domain B 10/11, (c & d) Domain B 5/6, (e & f) Domain A 9/10, and (g & h) Domain A 4/5.

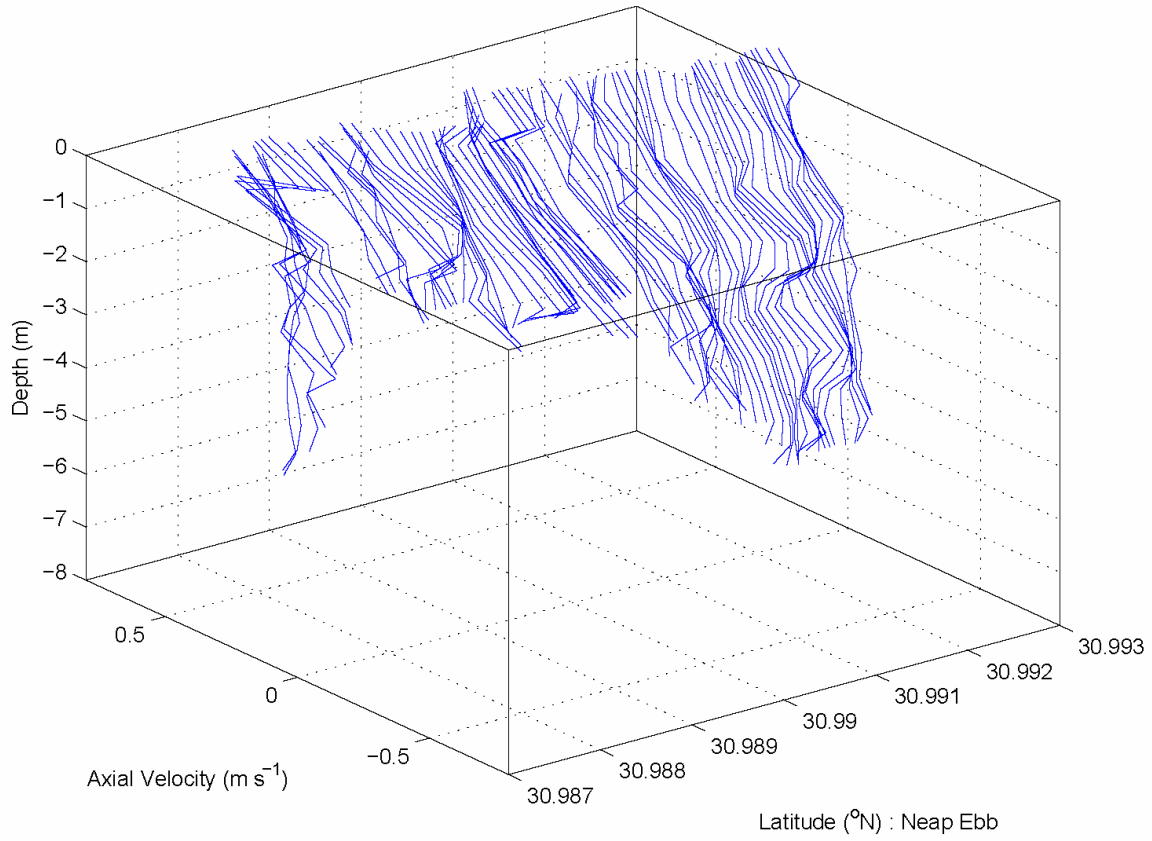

Figure 7.21: Axial velocity profiles at maximum ebb for neap tide conditions in the representative lateral cross-section Domain A 4/5.

Table 7.4: The buoyancy frequency, the total axial transport per unit area, the total lateral transport per unit area, and the total axial momentum for the lateral cross-sections: Domain A 4/5 – Domain B 10/11. To assess acceleration and deceleration into and out of the channel bends, read down the table from A 4/5 – B 10/11 for flood tide and read up the table from B 10/11 – A 4/5 for ebb tide.

STATION	N_z^2	$\frac{Q^s_{total}}{b_h \cdot b_w}$	$\frac{Q^n_{total}}{b_h \cdot b_w}$	$\Sigma U_{momentum}$
Domain A Cross-section 4/5				
Spring - Max Ebb	1.0e-3 ±8.0e-4 s^{-2}	1658.50 m s^{-1}	239.75 m s^{-1}	3.72E+05 kg m^{-2} s^{-1}
Spring - Max Flood	1.4e-3 ±1.0e-4 s^{-2}	-1779.14 m s^{-1}	-177.11 m s^{-1}	-4.08E+05 kg m^{-2} s^{-1}
Neap – Max Ebb	6.4e-3 ±1.0e-4 s^{-2}	489.60 m s^{-1}	-40.80 m s^{-1}	1.20E+05 kg m^{-2} s^{-1}
Neap – Max Flood	6.5e-3 ±4.0e-4 s^{-2}	-659.24 m s^{-1}	9.79 m s^{-1}	-1.54E+05 kg m^{-2} s^{-1}
Domain A Cross-section 9/10				
Spring - Max Ebb	1.4e-3 ±7.0e-4 s^{-2}	1578.80 m s^{-1}	64.33 m s^{-1}	2.78E+05 kg m^{-2} s^{-1}
Spring - Max Flood	2.0e-3 ±1.0e-4 s^{-2}	-1669.70 m s^{-1}	-57.27 m s^{-1}	-2.96E+05 kg m^{-2} s^{-1}
Neap - Max Ebb	1.1e-2 ±1.9e-3 s^{-2}	532.43 m s^{-1}	38.07 m s^{-1}	9.08E+04 kg m^{-2} s^{-1}
Neap - Max Flood	7.8e-3 ±4.0e-4 s^{-2}	-664.24 m s^{-1}	-56.63 m s^{-1}	-1.15E+05 kg m^{-2} s^{-1}
Domain B Cross-section 5/6				
Spring - Max Ebb	1.0e-3 ±1.0e-4 s^{-2}	1560.60 m s^{-1}	-36.50 m s^{-1}	3.66E+05 kg m^{-2} s^{-1}
Spring - Max Flood	3.5e-3 ±1.0e-4 s^{-2}	-1607.86 m s^{-1}	-60.83 m s^{-1}	-3.78E+05 kg m^{-2} s^{-1}
Neap - Max Ebb	2.0e-3 ±2.0e-4 s^{-2}	382.73 m s^{-1}	-4.66 m s^{-1}	9.06E+04 kg m^{-2} s^{-1}
Neap - Max Flood	4.2e-3 ±1.0e-4 s^{-2}	-752.54 m s^{-1}	-14.88 m s^{-1}	-1.78E+05 kg m^{-2} s^{-1}
Domain B Cross-section 10/11				
Spring - Max Ebb	2.1e-3 ±1.3e-4 s^{-2}	1535.55 m s^{-1}	57.91 m s^{-1}	3.67E+05 kg m^{-2} s^{-1}
Spring - Max Flood	1.4e-3 ±8.0e-4 s^{-2}	-1528.68 m s^{-1}	132.36 m s^{-1}	-3.56E+05 kg m^{-2} s^{-1}
Neap - Max Ebb	5.0e-3 ±1.9e-4 s^{-2}	453.91 m s^{-1}	-12.41 m s^{-1}	1.09E+05 kg m^{-2} s^{-1}
Neap - Max Flood	5.7e-3 ±1.0e-4 s^{-2}	-719.58 m s^{-1}	140.85 m s^{-1}	-1.67E+05 kg m^{-2} s^{-1}

7.3.4. Spatial Characteristics of Secondary Circulation

The spatial and temporal scales of secondary flow can be estimated using a two-dimensional form of the mass continuity equation in natural coordinates, given as:

$$\frac{d\overline{v}}{d\overline{n}} = -\frac{d\overline{w}}{d\overline{z}} \quad \textbf{(7.3)}$$

which assumes that $\frac{d\overline{u}}{d\overline{s}} = 0$ and where $d\overline{v}$ is the average difference in the lateral velocity, $d\overline{w}$ is the average difference in the vertical velocity, $d\overline{n}$ is the average lateral distance over which the lateral velocity changes, and $d\overline{z}$ is the average vertical distance over which the vertical velocity changes. Solving Equation 7.3 for $\overline{w}$, assuming an average axial and transverse velocity, respectively $\overline{u}$ and $\overline{v}$, for the Satilla River during spring and neap tides, $\overline{u}$ = 1.00 m s^{-1} and $\overline{v}$ = 0.30 m s^{-1} for spring tide and $\overline{u}$ = 0.60 m s^{-1} and $\overline{v}$ = 0.16 m s^{-1} for neap tide, and assuming $d\overline{u}$ and $d\overline{v}$ are approximately half, respectively, of $\overline{u}$ and $\overline{v}$ ($d\overline{u}$ = 0.50 m s^{-1} and $d\overline{v}$ = 0.15 m s^{-1} at spring tide and $d\overline{u}$ = 0.30 m s^{-1} and $d\overline{v}$ = 0.08 m s^{-1} at neap tide) and using the average spatial dimensions of a secondary circulation cell for spring and neap tides (*cf.* Figures 7.16 and 7.18) in Equation 7.3 gives the resultant average vertical velocity, $\overline{w}$ = 2.3 x 10^{-3} m s^{-1} for spring tide and $\overline{w}$ = 1.2 x 10^{-3} m s^{-1} for neap tide. These calculations are reasonable and consistent with the observations of $\overline{w}$ for spring and neap as given in Figures 7.12 and 7.13, though higher than the maximum observation of $\overline{w}$ at spring tide.

Setting Equation 7.3 equal to zero, inverting, and multiplying by two for a full secondary circulation cell, yields Equation 7.4. Using Equation 7.4, it is possible to calculate the time necessary for a secondary circulation to complete one full revolution:

$$t_{revolution} = 2\left(\frac{d\overline{n}}{\overline{v}} + \frac{d\overline{z}}{\overline{w}}\right) \quad \textbf{(7.4)}$$

Given $\overline{w}$ = 2.3 x 10^{-3} m s^{-1} for spring tide and $\overline{w}$ = 1.2 x 10^{-3} m s^{-1} for neap tide, the time for a water parcel in the secondary circulation to complete one full revolution at spring tide is $t_{revolution}$ = 4000 seconds (~ 67 minutes), while at neap tide, the revolution time is nearly twice as long with $t_{revolution}$ = 7500 seconds (~ 125 minutes). Correspondingly, the axial distance that a water parcel would travel while completing one full revolution can be estimated by multiplying $t_{revolution}$ by the average axial velocity at spring and at neap tide. At spring, the water parcel travels approximately 4.0 kilometers to complete one full revolution, while at neap; the water parcel travels approximately 4.5 kilometers to complete one full revolution. Table 7.5 summarizes the spatial and temporal characteristics of secondary flow for spring and neap tides.

Table 7.5: The spatial and temporal characteristics of secondary circulation during spring and neap tides.

PARAMETER	SPRING	NEAP
$\overline{u}$	1.00 m s^{-1}	0.60 m s^{-1}
$d\overline{u}$	0.50 m s^{-1}	0.30 m s^{-1}
$\overline{v}$	0.30 m s^{-1}	0.16 m s^{-1}
$d\overline{v}$	0.15 m s^{-1}	0.08 m s^{-1}
$\overline{w}$	2.3 x 10^{-3} m s^{-1}	1.2 x 10^{-3} m s^{-1}
$d\overline{s}$	1500 m	1500 m
$d\overline{n}$	200 m	200 m
$d\overline{z}$	3 m	3 m
REVOLUTION TIME	4000 s (~ 67 minutes)	7500 s (~ 125 minutes)
REVOLUTION DISTANCE	4000 m	4500 m

Given the distance between the lateral cross-sections, (0.91 km between A 4/5 and A 9/10, 2.7 km between A 9/10 and B 5/6, and 2.1 km between B 5/6 and B 10/11) it is likely that the effect of secondary circulation in Domain A 4/5 will be seen in Domain A 9/10 and likewise, the effect of secondary circulation in Domain B 5/6 will be seen in Domain B 10/11. In addition, these results suggest that a secondary circulation can best be described as helical in the axial direction, in contrast to a closed circulation cell at a fixed location in space or in a single lateral transect. Likewise, the helical flow pattern confirms the choice of using the global mean of the depth-average transport to determine the principle axes in each of the lateral cross-sections.

The calculations presented here and summarized in Table 7.5, for the transit time and the axial distance traveled by the secondary circulation as it makes one complete revolution, are of the same order as those calculations from Seim et al. (2002). They estimated that a water parcel starting near the center-line of the channel would take approximately 100 minutes to complete one full revolution and would travel approximately 3 kilometers downstream before returning to its starting point in a lateral circulation pattern. Likewise, the results of the two-dimensional continuity model (Equation 7.3) supports the conclusions of Seim et al. (2002) that the shape of the secondary circulation pattern is helical in nature, and that when secondary flow is super-imposed on the axial flow field, it leads to a transfer in the vertical flux of momentum toward the bottom boundary layer. Secondary circulation is a mechanism to transfer (by vertical advection) high velocity fluid into the bottom boundary layer.

Figures 7.22 through 7.24 show the three-dimensional velocity structure and the three-dimensional spatial relationship of the Domain A and B lateral channel cross-

sections during maximum ebb at spring tide. For reference, the orientation in Figures 7.22 through 7.24 is looking down the axis of the estuary toward the ocean. In Figure 7.22 (axial velocity), the alternating location of the *thalweg* can be observed by noting the location of the circles in the deep channel. Likewise, by noting the arrows drawn on the lateral transects in Figure 7.23 (lateral velocity), it is possible to observe the alternating direction of the curvature-induced secondary flow as it switches from bank to bank between the channel cross-sections. At B 10/11, the flow toward the outer bank is directed to the north and switches toward the south in B 5/6. The curvature-induced secondary flow switches directions again between B 5/6 and A 9/10, where a small rise in bathymetry acts as a dynamical barrier to the northward moving secondary circulation. Surface fronts are often observed during field surveys at the location above the small topographic feature in Domain A 9/10. Unimpeded by bathymetry in A 4/5, the secondary circulation reaches the north bank. It is clear from Figure 7.24 (vertical velocity), that in general, two or more adjacent vertical secondary circulation cells occur simultaneously in any given channel cross-section. Recalling that red indicates upward flow and blue indicates downward flow, it can be seen in Figure 7.22 that there are approximately 3 distinct adjacent circulation cells in B 10/11, 2 distinct adjacent circulation cells in B 5/6, ~ 3 distinct adjacent circulation cells in A 9/10, and 2 distinct adjacent circulation cells in A 4/5.

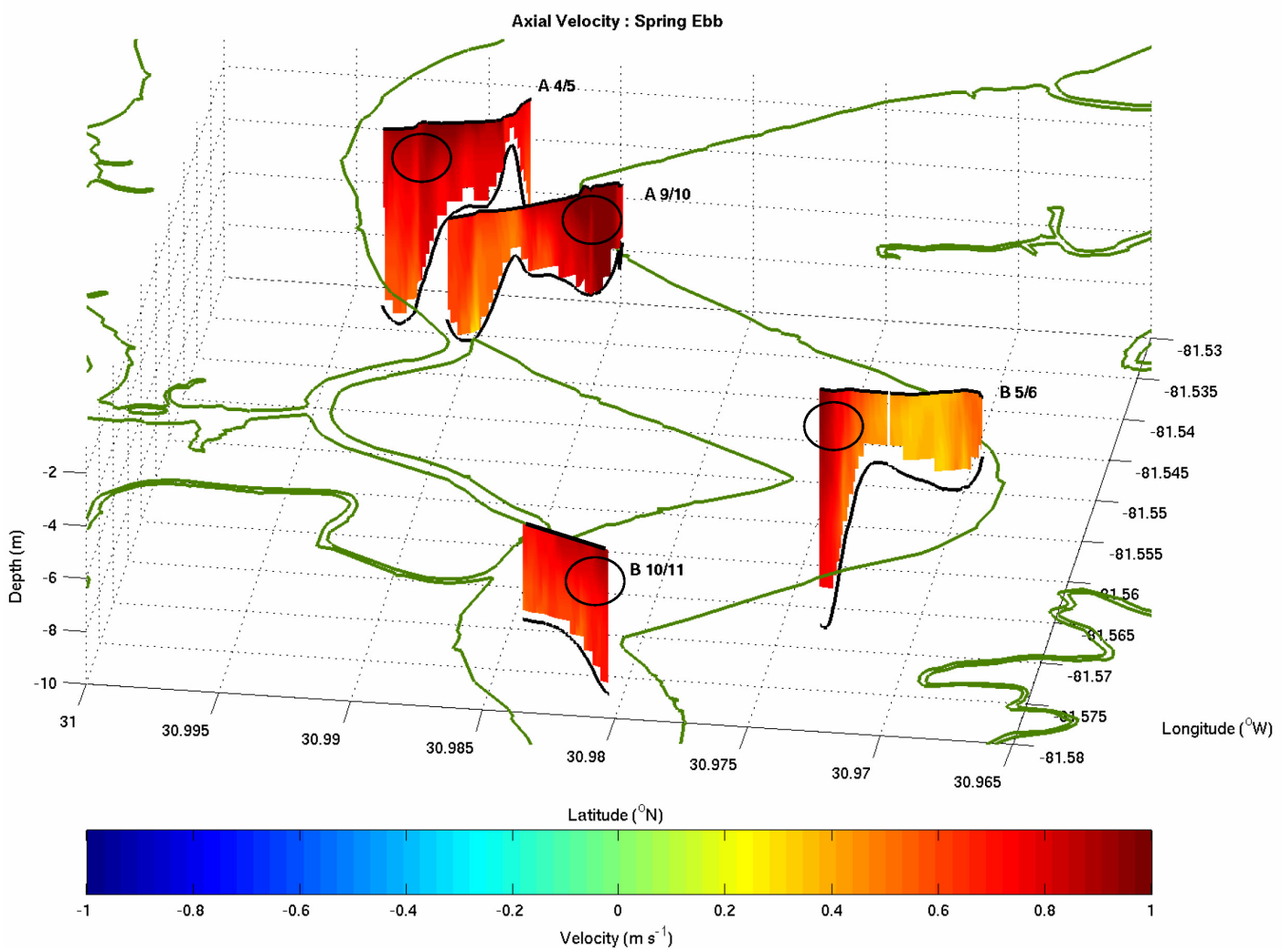

Figure 7.18: The axial velocity structure for cross-sections B 10/11 through A 4/5 during maximum ebb at spring tide. The darker red color indicates the location of the maximum axial velocity. Ovals indicate the location of the sinuous *thalweg*.

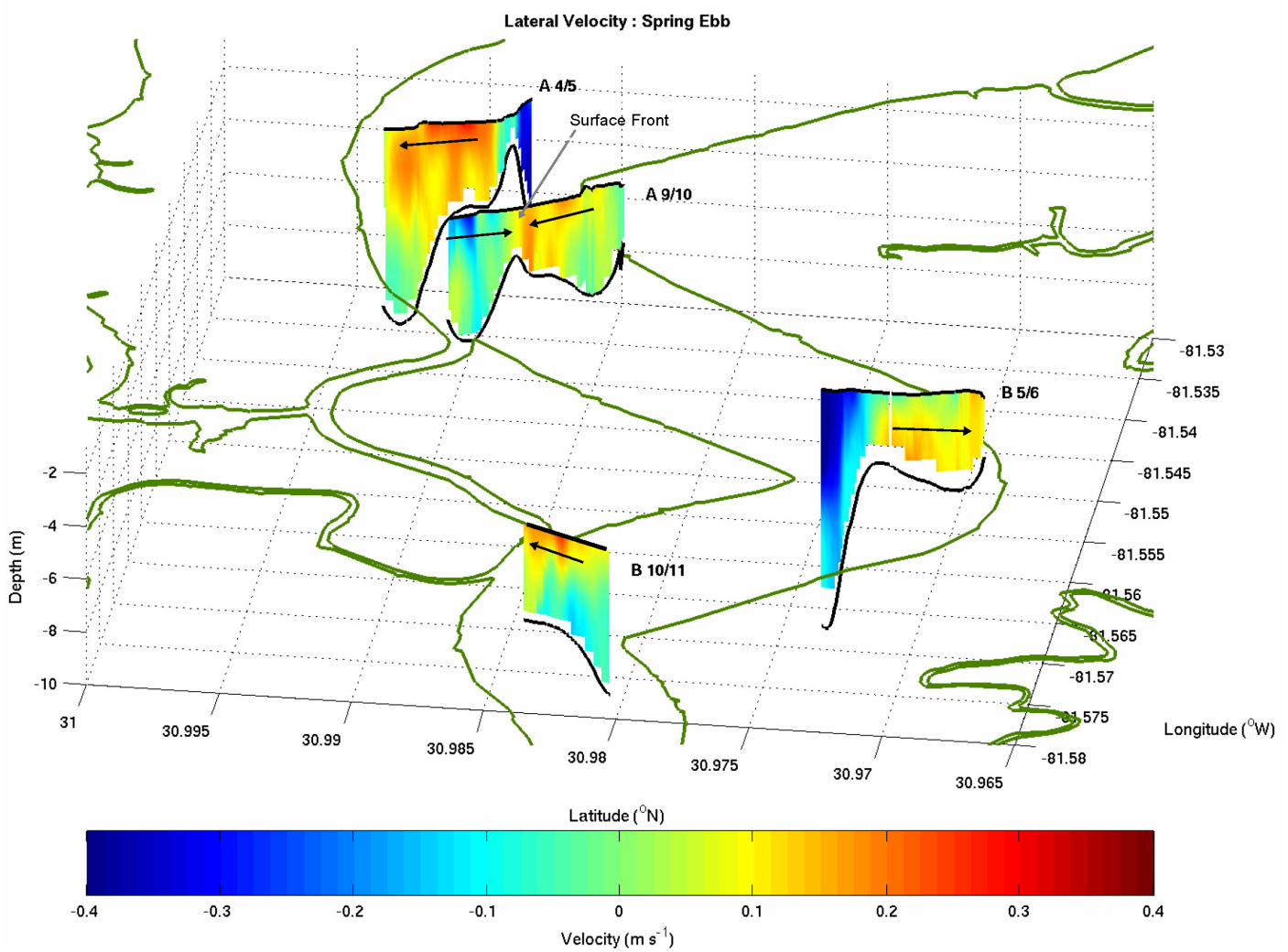

Figure 7.19: The lateral velocity structure for cross-sections B 10/11 through A 4/5 during maximum ebb at spring tide. The orange color indicates flow to the outside of the channel bend. Arrows indicate an orientation shift in the flow between lateral cross-sections.

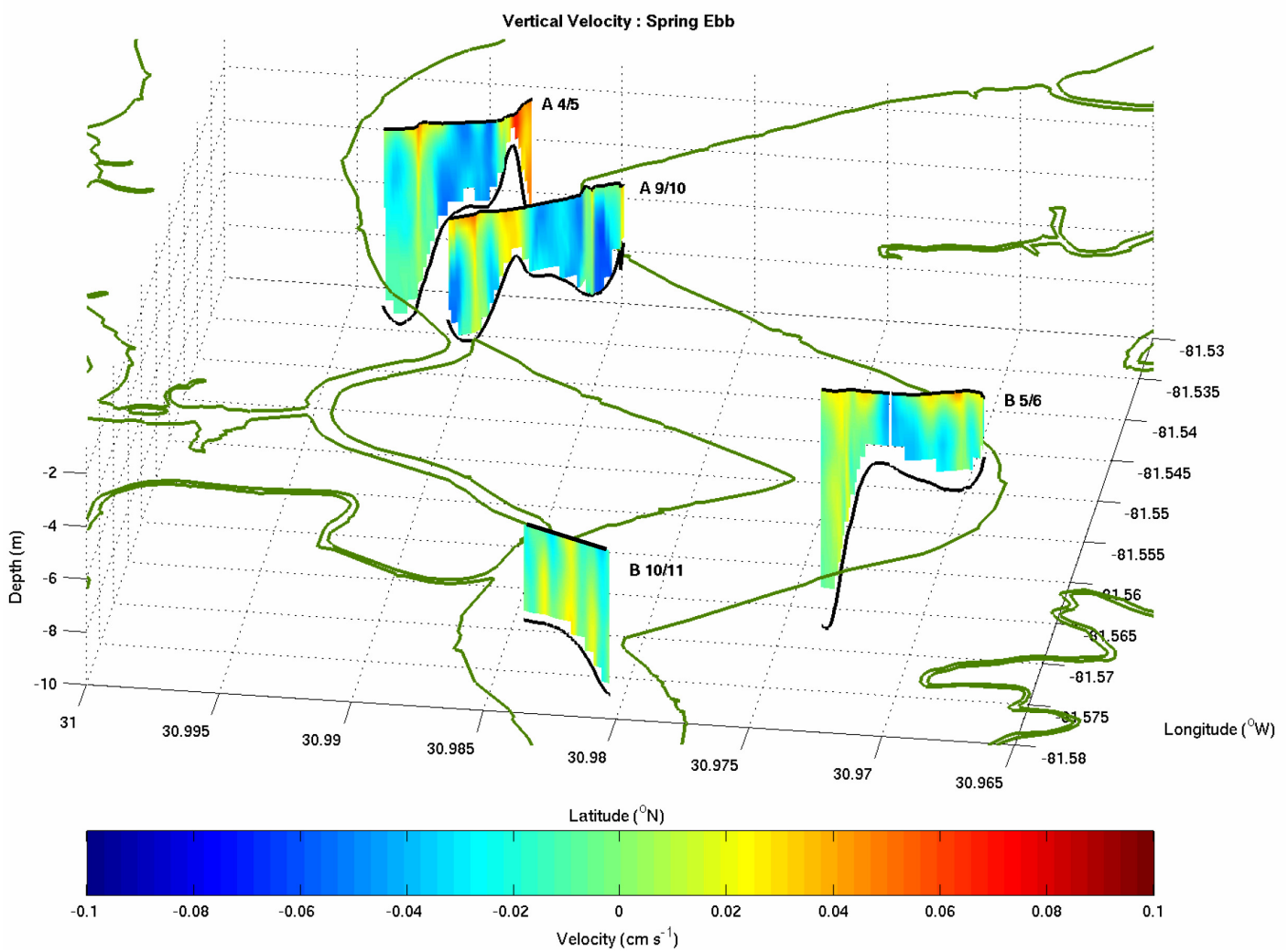

Figure 7.20: The vertical velocity structure for cross-sections B 10/11 through A 4/5 during maximum ebb at spring tide. The red color indicates upward flow. Note the multiple appearances of vertical circulation cells.

7.3.5 Lateral Momentum Balance Model for the Satilla River, Georgia

While the Seim and Gregg (1997) curvature-induced overturning model is a good first-order approximation to explain the lateral dynamics in the highly curved reaches of the Satilla River, as seen in Chapter 6, it does not apply equally well to all sections of the river (particularly in straight reaches) or at all places in a channel cross-section (away from the *thalweg*). For this reason and based on scale estimates for secondary flow in the Satilla River (*cf.* Table 6.6, Chapter 6), a balance between the centrifugal acceleration (CA), the lateral pressure gradient force (LBC), and vertical shear stress divergence (VSS) is used as a more versatile lateral momentum balance for this river. The effect of the Coriolis acceleration (CF) is added to this balance, despite its weak nature in the Satilla, for model portability. It is expected that there will be a shift in the balance of terms (bank to bank in a channel cross-section from CA ≈ LBC in the deep channel to CA ≈ LBC + VSS near the flank of the shoal regions to CA ≈ VSS in the shallows) in the lateral momentum balance model for the Satilla, because of the river's sinuous nature, its variable density structure, and its bathymetric features. Formulated in this manner, the results of this investigation can be directly compared with other estuarine studies that use the lateral momentum balance for their framework.

The lateral momentum balance model (LMBM) extends the work of Geyer (1993b), Dronkers (1996), and Seim and Gregg (1997) by combining the effects of the lateral density gradient, bottom stress, channel curvature, and planetary rotation to enhancing or limiting secondary circulation. This model formulation was chosen because it combines the effects of the deep channel (where most of the momentum is captured in the *thalweg* and subject to the strongest lateral baroclinic gradient) and the effects away

from the deep channel in the region of the shoals and shallows as well as being applicable in straight or highly curved channel reaches with variable channel bathymetry. An attractive feature of this model formulation is that it accounts for the effects of secondary flow regardless of instrument position in a channel cross-section of variable curvature: either in the deep channel or in the shoal region. In practical application, using a model that does not consider a variable instrument location or a model which is sensitive to changes in bathymetry could lead to biased results, as it is often difficult to precisely determine the location of a submerged instrument.

The depth-dependent lateral momentum balance in natural coordinates for stratified flow in a curving channel is given by Equation 7.5 as follows:

$$\frac{\partial u_n}{\partial t} + u_s \frac{\partial u_n}{\partial s} + f u_s - \frac{u_s^2}{R} + g \frac{\partial \eta}{\partial n} = -\frac{g}{\rho_o} \int_z^\eta \frac{\partial \rho}{\partial n} dz + \frac{\partial}{\partial z}\left(A_z \frac{\partial u_n}{\partial z} \right) \quad \textbf{(7.5)}$$

Depth-averaging (indicated by the overbar) Equation 7.5 yields Equation 7.6.

$$\frac{\partial \overline{u}_n}{\partial t} + \overline{u_s \frac{\partial u_n}{\partial s}} + f\overline{u}_s - \frac{\overline{u_s^2}}{R} + g \frac{\partial \eta}{\partial n} = -\frac{g}{\rho_o} \frac{\partial \overline{\rho}}{\partial n} h - \frac{\tau_{n,b}}{\rho_o h} \quad \textbf{(7.6)}$$

Subtracting Equation 7.6 from Equation 7.5 and substituting

$$\frac{\tau_n}{\rho_o} = \left[A_z \frac{\partial u_n}{\partial z} \right]_{z=-h} \quad \textbf{(7.7)}$$

yields Equation 7.8, which eliminates the contribution of the barotropic water slope, a difficult parameter to measure or estimate accurately.

$$\frac{\partial \left(u_n - \overline{u}_n \right)}{\partial t} + u_s \frac{\partial u_n}{\partial s} - \overline{u}_s \frac{\partial \overline{u}_n}{\partial s} + f\left(u_s - \overline{u}_s \right) - \frac{\left(u_s - \overline{u_s^2} \right)}{R} =$$

$$= -\frac{g}{\rho_o} \int_z^\eta \frac{\partial \rho}{\partial n} dz + \frac{g}{\rho_o} \frac{\partial \overline{\rho}}{\partial n} h + \frac{\partial}{\partial z}\left(\frac{\tau_n}{\rho_o} \right) + \frac{\tau_{n,b}}{\rho_o h} \quad \textbf{(7.8)}$$

The potential for steady-state conditions is determined by T_{bc}, the baroclinic adjustment time, the time scale associated with an inviscid balance between centrifugal acceleration and the lateral baroclinic gradient. T_{bc} can be evaluated using the expression:

$$T_{bc} = \frac{B}{\sqrt{g'h}} \quad \textbf{(7.9)}$$

where B is the channel width, *g'* is reduced gravity, and h is the depth of the thalweg (Chant and Wilson 1997; Lacy and Monismith 2001). Likewise, the potential to neglect advective acceleration is determined by comparing the frictional relaxation time scale,

$$T_f = \frac{L_s}{\overline{u}_s} \quad \textbf{(7.10)},$$

the time associated with the generation or destruction of a secondary circulation (Kalkwijk and Booij 1986; Geyer 1993), to the advective time scale,

$$T_{adv} = \frac{L_s}{\overline{u}_s \Delta u_n} \quad \textbf{(7.11)},$$

the time associated with the advection of the secondary circulation downstream. In Equations 7.10 and 7.11, L_s is the length scale of the axial flow field, $\overline{u}_s$ is the depth-average streamwise velocity, and Δu_n is the change in the normal (lateral) velocity over the distance L_s (Geyer 1993).

For the Satilla River, T_{bc} ranges between 10 minutes at spring tides and 19 minutes at neap tides, indicating that a steady-state assumption is possible and that the secondary circulation is quasi-stationary with respect to semidiurnal forcing. Furthermore, this chapter focuses on maximum ebb and maximum flood tide conditions,

when acceleration is at a minimum, providing additional circumstances when the steady-state assumption is most valid. Likewise, advective accelerations can be neglected, as $T_f \approx 24$ minutes and $T_{adv} \approx$ 96 minutes, indicating that secondary circulations are generated more quickly than they are advected downstream.

Assuming steady-state conditions and neglecting advective acceleration, the lateral momentum balance model (LMBM) for stratified flow in a curving channel in natural coordinates reduces to the following expression:

$$f\left(u_s - \overline{u}_s\right) - \frac{\left(u_s^2 - \overline{u_s^2}\right)}{R} = -\frac{g}{\rho_o}\int_z^\eta \frac{\partial \rho}{\partial n} dz + \frac{g}{\rho_o}\frac{\partial \overline{\rho}}{\partial n} h + \frac{\partial}{\partial z}\left(\frac{\tau_n}{\rho_o}\right) + \frac{\tau_{n,b}}{\rho_o h} \quad \textbf{(7.12)}$$

where the first and second terms respectively in Equation 7.12 are secondary flow driven by the imbalance between the depth-dependent and the depth-average Coriolis and centrifugal acceleration, the third term is the lateral baroclinic pressure gradient, the fourth term is the depth-average lateral baroclinic pressure gradient, the fifth term is a Reynolds parameterization of vertical shear stress divergence, and the sixth term is bottom shear stress. In Equation 7.12, bottom shear stress is expressed as

$$\tau_{n,b} = \rho_o C_D \left|u_{n,1mab}\right| u_{n,1mab} = \frac{1}{16}\rho_o C_D \left|u_{s,1mab}\right| u_{s,1mab} \quad \textbf{(7.13)}$$

to account for the contributions of the lateral velocity (which can be approximated by scaling the axial velocity) to the observed shear stress.

Equation 7.12 is used to investigate and evaluate the lateral momentum balance at Domain cross-sections A 4/5, A 9/10, B 5/6, and B 10/11, for maximum ebb and maximum flood tide conditions during a spring-to-neap fortnightly cycle (*cf.* Figures 7.4 and 7.5, where circles indicate maximum ebb and boxes indicate maximum flood).

In Equation 7.12, the depth-average lateral baroclinic gradient and bottom shear stress are assumed to represent respectively, the importance of the depth-dependent lateral baroclinic gradient and vertical shear stress. Thus, Equations 7.12 and 7.13 are used to directly evaluate the calculated balance between the centrifugal acceleration (term 2) and the sum of the Coriolis acceleration (term 1), the depth-average lateral baroclinic gradient (term 4), and the bottom shear stress (term 6) with the Satilla River data sets. The results of the lateral momentum balance model applied to the lateral cross-sections in Domains A and B: A 4/5, A 9/10, B 5/6, and B 10/11 (*cf.* Figure 7.2), for maximum ebb and maximum flood conditions for both spring and neap tides, are illustrated by Figures 7.25 through 7.28 and are summarized in Table 7.6. In the LMBM figures, as in Table 7.6, the 'original' drag coefficient, $C_D = 2.5 \times 10^{-3}$ is from Seim et al. (2002) and is considered a 'classical' value, while the 'low' drag coefficient, $C_D = 3.1 \times 10^{-3}$ is from Geyer et al. (2000) and Soulsby (1990) for muddy bottom estuaries.

7.3.5.1 Spring Tide – Maximum Ebb

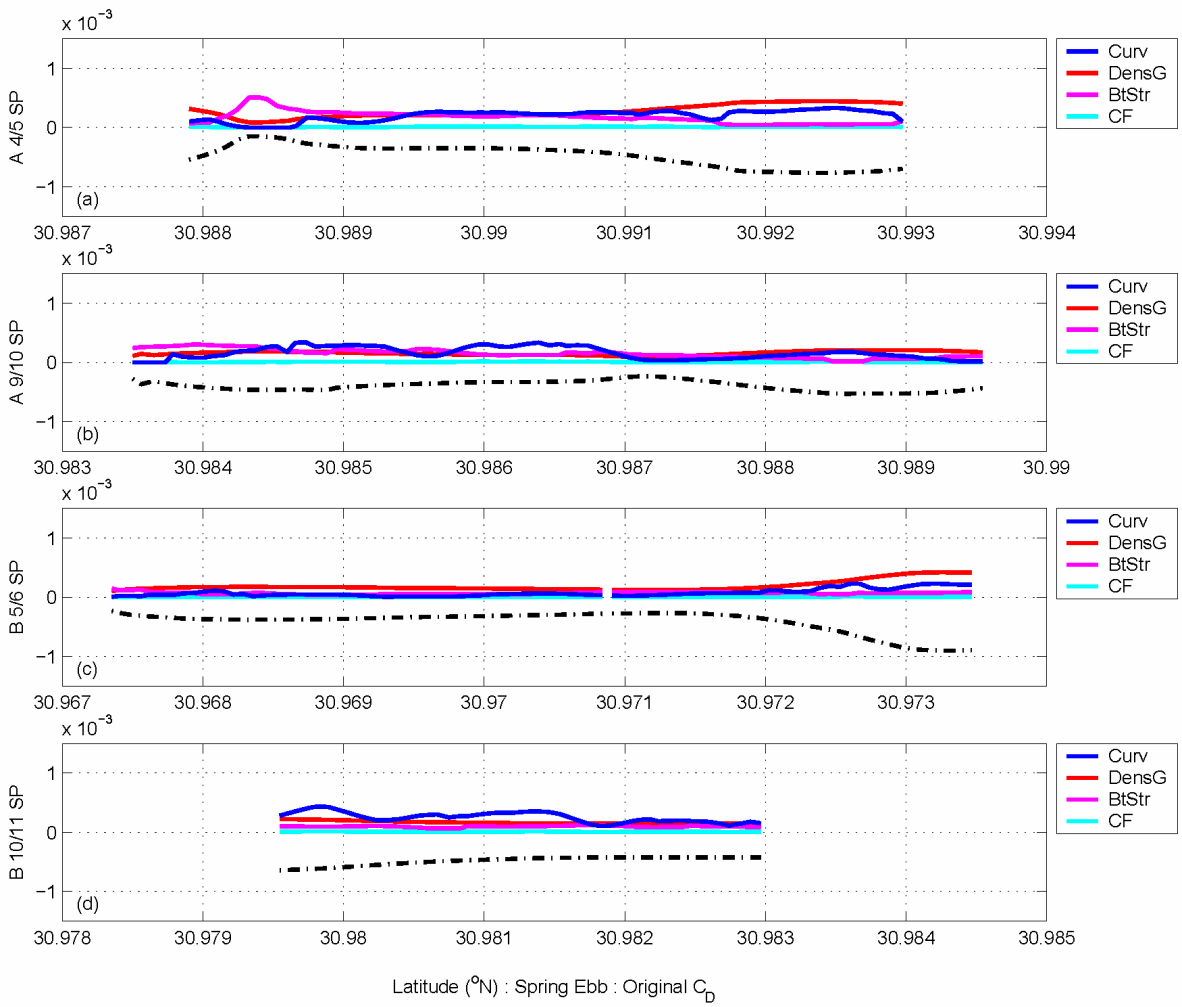

Figure 7.25: Satilla River lateral momentum balance terms (blue curvature, red density, magenta bottom stress, and cyan Coriolis) during maximum ebb at spring tide for sections (a) Domain A 4/5, (b) Domain A 9/10, (c) Domain B 5/6, and (d) Domain B 10/11. The black dashed line in each subpanel represents the lateral cross-section bathymetry. The bottom stress term was calculated using the original drag coefficient, $C_D = 2.5 \times 10^{-3}$.

7.3.5.2 Spring Tide – Maximum Flood

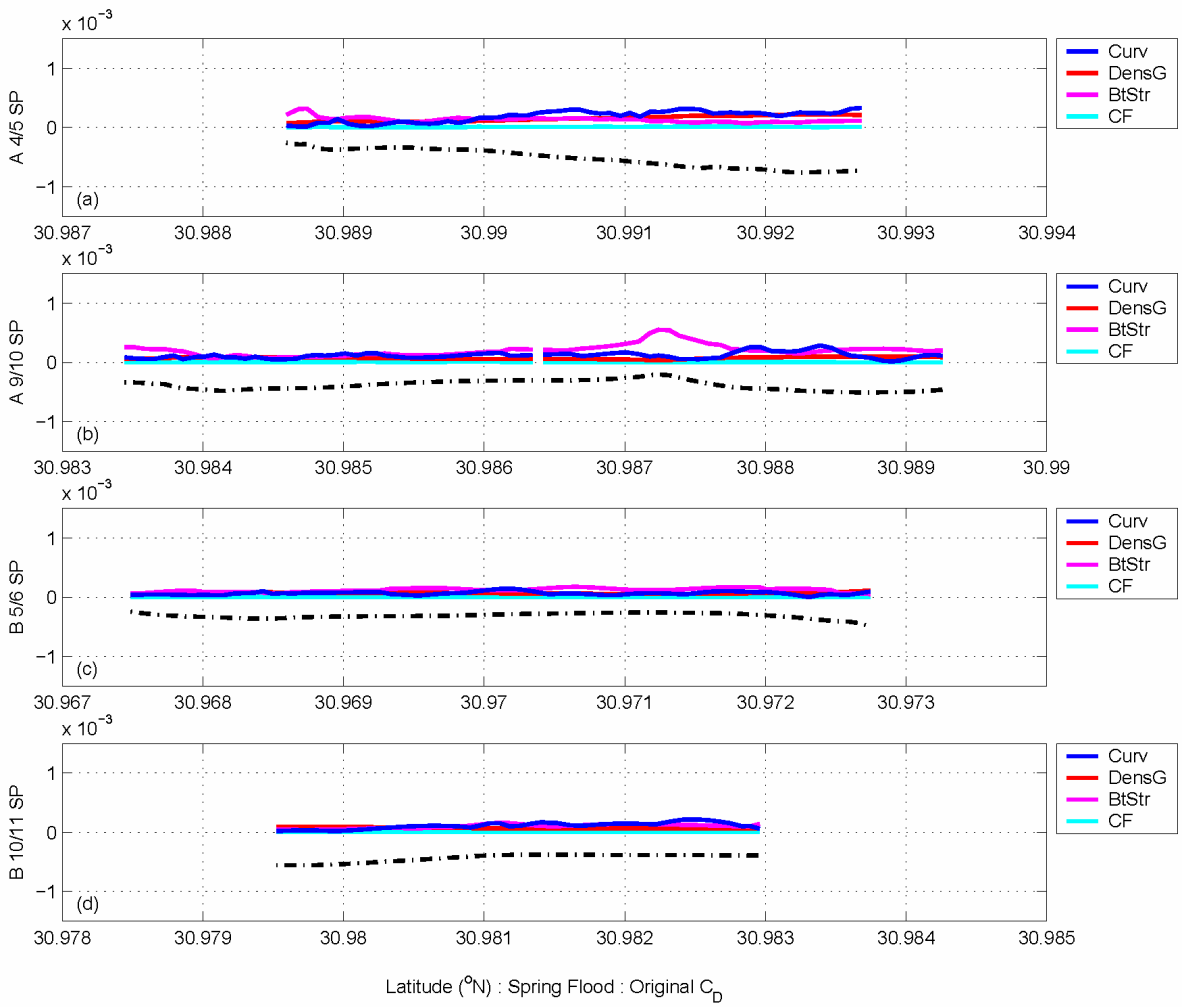

Figure 7.26: Satilla River lateral momentum balance terms (blue curvature, red density, magenta bottom stress, and cyan Coriolis) during maximum flood at spring tide for sections (a) Domain A 4/5, (b) Domain A 9/10, (c) Domain B 5/6, and (d) Domain B 10/11. The black dashed line in each subpanel represents the lateral cross-section bathymetry. The bottom stress term was calculated using the original drag coefficient, $C_D = 2.5 \times 10^{-3}$.

7.3.5.3 Neap Tide – Maximum Ebb

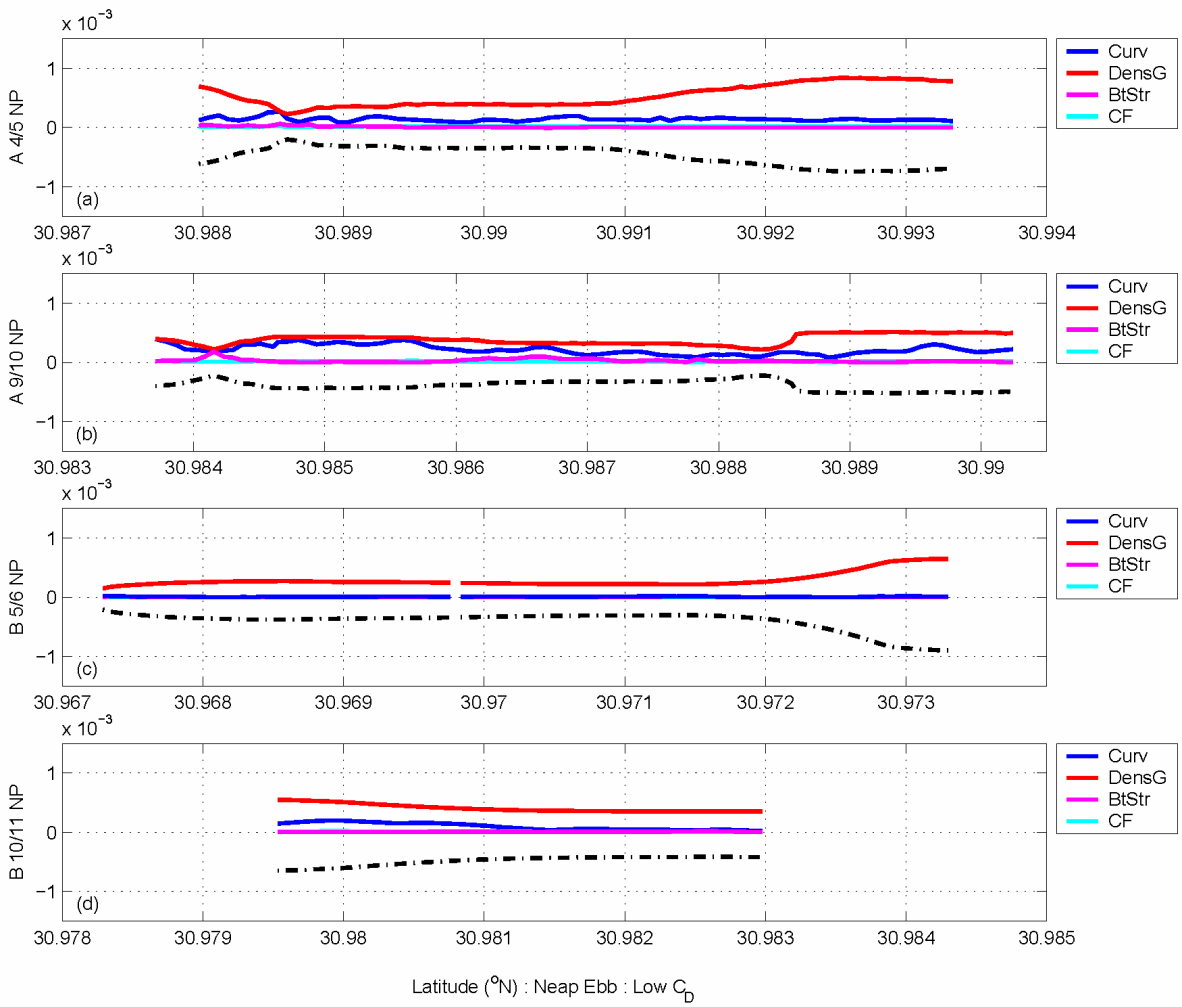

Figure 7.27: Satilla River lateral momentum balance terms (blue curvature, red density, magenta bottom stress, and cyan Coriolis) during maximum ebb at neap tide for sections (a) Domain A 4/5, (b) Domain A 9/10, (c) Domain B 5/6, and (d) Domain B 10/11. The black dashed line in each subpanel represents the lateral cross-section bathymetry. The bottom stress term was calculated using the low drag coefficient, $C_D = 3.1 \times 10^{-3}$.

7.3.5.4 Neap Tide – Maximum Flood

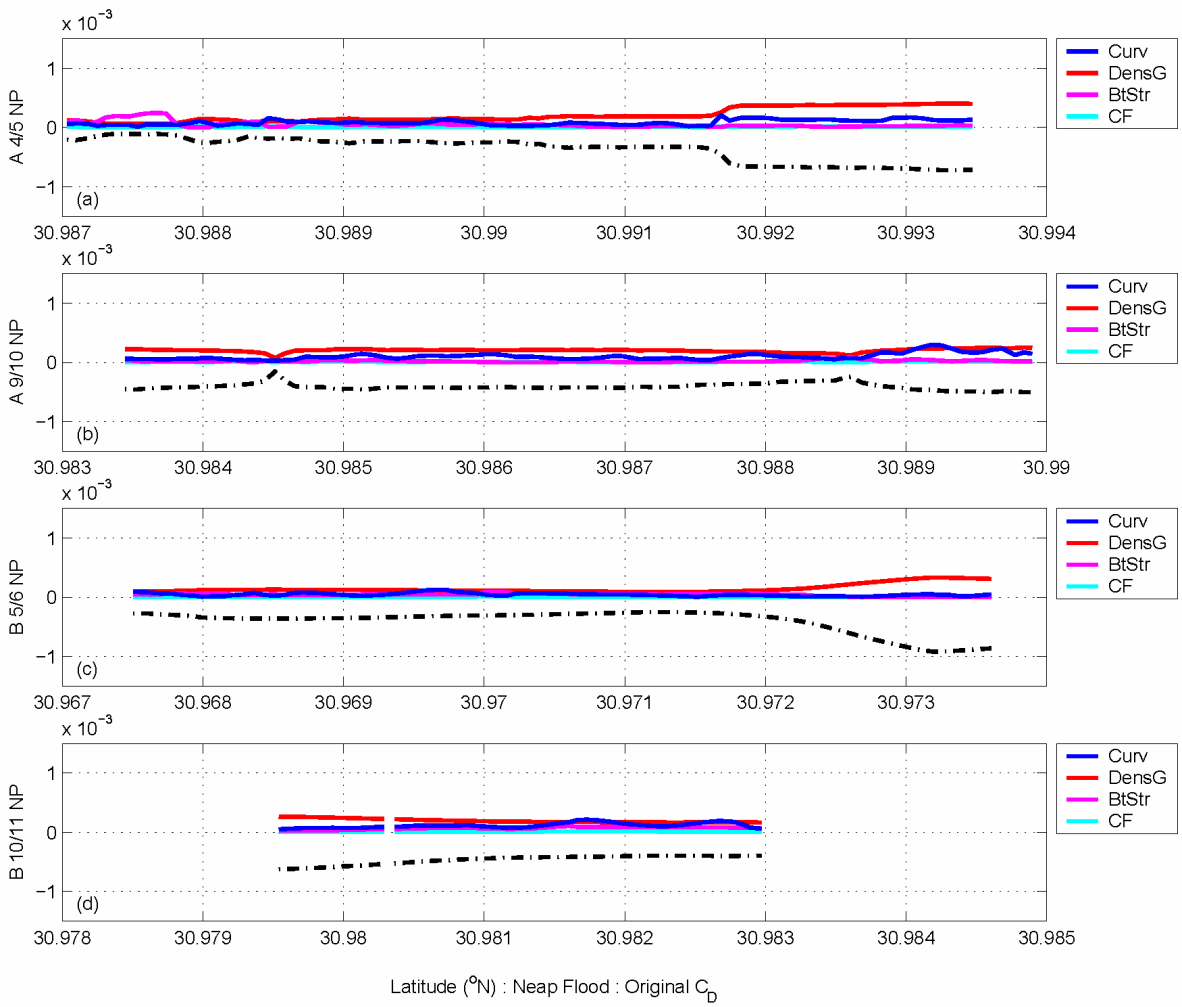

Figure 7.28: Satilla River lateral momentum balance terms (blue curvature, red density, magenta bottom stress, and cyan Coriolis) during maximum flood at neap tide for sections (a) Domain A 4/5, (b) Domain A 9/10, (c) Domain B 5/6, and (d) Domain B 10/11. The black dashed line in each subpanel represents the lateral cross-section bathymetry. The bottom stress term was calculated using the original drag coefficient, $C_D = 2.5 \times 10^{-3}$.

Table 7.6: Calculated values and 95% confidence intervals for the LMBM at the lateral sections: Domain A 4/5 – Domain B 10/11.

STATION	$\left(\frac{u_s^2}{R}\right) =$	$f(u_s) +$	$\frac{g}{\rho_o}\frac{\partial \overline{\rho}_z}{\partial n} +$	$\frac{\tau_{n,b}}{\rho_o h}$
Domain A Cross-section 4/5				
Spring - Max Ebb orig C_D (m s^{-2})	**5.2e-4 ±4.4e-5**	5.9e-5 ±2.6e-6	**3.5e-4 ±7.1e-5**	**3.5e-4 ±1.1e-4**
Spring - Max Flood orig C_D (m s^{-2})	**5.8e-4 ±7.4e-5**	6.2e-5 ±4.2e-6	**2.0e-4 ±3.0e-5**	**2.7e-4 ±4.7e-5**
Neap – Max Ebb orig C_D (m s^{-2})	**8.8e-5 ±2.2e-5**	2.0e-5 ±3.4e-6	**6.9e-4 ±1.2e-4**	1.6e-5 ±1.2e-5
Neap – Max Ebb low C_D (m s^{-2})	**8.8e-5 ±2.2e-5**	2.0e-5 ±3.4e-6	**6.9e-4 ±1.2e-4**	2.0e-5 ±1.5e-5
Neap – Max Flood orig C_D (m s^{-2})	**1.5e-4 ±3.1e-5**	3.0e-5 ±2.6e-6	**2.6e-4 ±7.5e-5**	**1.1e-4 ±5.4e-5**
Domain A Cross-section 9/10				
Spring - Max Ebb orig C_D (m s^{-2})	**5.3e-4 ±1.2e-4**	5.4e-5 ±6.4e-6	**2.0e-4 ±2.2e-5**	**3.1e-4 ±7.5e-5**
Spring - Max Flood orig C_D (m s^{-2})	**6.3e-4 ±1.0e-4**	6.0e-5 ±5.0e-6	**9.8e-5 ±1.1e-5**	**4.1e-4 ±1.0e-4**
Neap - Max Ebb orig C_D (m s^{-2})	**1.8e-4 ±2.2e-5**	3.0e-5 ±2.1e-6	**5.0e-4 ±5.6e-5**	5.2e-5 ±2.5e-5
Neap - Max Ebb low C_D (m s^{-2})	**1.8e-4 ±2.2e-5**	3.0e-5 ±2.1e-6	**5.0e-4 ±5.6e-5**	6.4e-5 ±3.1e-5
Neap - Max Flood orig C_D (m s^{-2})	**1.2e-4 ±3.7e-5**	2.4e-5 ±4.1e-6	**2.6e-4 ±1.9e-5**	5.0e-5 ±1.8e-5
Domain B Cross-section 5/6				
Spring - Max Ebb orig C_D (m s^{-2})	**2.6e-4 ±7.5e-5**	3.7e-5 ±4.8e-6	**2.5e-4 ±5.7e-5**	**1.5e-4 ±2.1e-5**
Spring - Max Flood orig C_D (m s^{-2})	**3.3e-4 ±2.7e-5**	4.3e-5 ±1.8e-6	**9.4e-5 ±7.0e-6**	**2.5e-4 ±3.1e-5**
Neap - Max Ebb orig C_D (m s^{-2})	**9.0e-5 ±3.1e-5**	5.8e-6 ±1.2e-6	**3.8e-4 ±8.0e-5**	4.7e-5 ±3.5e-6
Neap - Max Ebb low C_D (m s^{-2})	**9.0e-5 ±3.1e-5**	5.8e-6 ±1.2e-6	**3.8e-4 ±8.0e-5**	5.8e-5 ±4.3e-6
Neap - Max Flood orig C_D (m s^{-2})	**1.3e-4 ±2.0e-5**	2.6e-5 ±2.3e-6	**1.9e-4 ±4.7e-5**	**9.0e-5 ±2.1e-5**
Domain B Cross-section 10/11				
Spring - Max Ebb orig C_D (m s^{-2})	**6.0e-4 ±4.0e-5**	5.4e-5 ±1.8e-6	**2.2e-4 ±1.6e-5**	**2.0e-4 ±1.3e-5**
Spring - Max Flood orig C_D (m s^{-2})	**4.4e-4 ±8.2e-5**	4.5e-5 ±4.5e-6	**9.6e-5 ±7.5e-6**	**2.1e-4 ±3.7e-5**
Neap - Max Ebb orig C_D (m s^{-2})	**7.6e-5 ±3.3e-5**	1.8e-5 ±1.1e-6	**5.3e-4 ±4.3e-5**	1.5e-5 ±3.8e-6
Neap - Max Ebb low C_D (m s^{-2})	**7.6e-5 ±3.3e-5**	1.8e-5 ±1.1e-6	**5.3e-4 ±4.3e-5**	1.9e-5 ±4.7e-6
Neap - Max Flood orig C_D (m s^{-2})	**2.0e-4 ±2.2e-5**	3.1e-5 ±1.7e-6	**2.5e-4 ±2.1e-5**	**1.4e-4 ±2.2e-5**

As it is difficult to describe the exact balance of terms for each grid point in the lateral cross-sections, after a brief description of the lateral momentum balance model results shown in Figures 7.25 through 7.28, the remainder of this Section will focus on the overall balance of terms for each lateral cross-section as given in Table 7.6. All channel cross-sections show a clear lateral shift, most prominent during maximum ebb for spring tide (Figure 7.25), in the strength of the curvature, bottom stress, and the lateral density gradient terms of the lateral momentum balance. Likewise, all channel cross-sections show a peak in bottom stress at locations where there is an abrupt change in the bathymetry. Lastly, as expected from scale estimates in Chapter 6 and shown in Figures 7.25 – 7.28, the contribution of the Coriolis acceleration to the lateral momentum balance is weak in all channel cross-sections for both spring and neap tides during maximum ebb and maximum flood.

During maximum ebb at spring tide (Figure 7.25), the balance of terms varies in the deep channel from a two-way balance between curvature and the lateral density gradient to a three-way balance between curvature, the lateral density gradient, and bottom stress. Away from the deep channel, between the flank of the shoal and the shallows, there is generally a three-way balance between curvature, the lateral density gradient, and bottom stress. The importance of bottom stress is seen in the shallow regions (e.g., Figure 7.25a near Latitude 30.988 ºN) where bathymetry changes rapidly. During maximum flood at spring tide (Figure 7.26), curvature dominates throughout the lateral cross-sections except at locations which have abrupt changes in bathymetry. Away from the deep channel between the flank of the shoal and the shallows, there is typically a two-way balance between curvature and bottom stress. During maximum ebb

at neap tide (Figure 7.27), the lateral density gradient dominates at all four sites across the entire lateral cross-section. Here, the signal of bottom stress is very weak in all of the lateral cross-sections, even in areas of rapidly changing bathymetry. Lastly, at neap tide during maximum flood (Figure 7.28), a comparatively weak lateral density gradient dominates in the deep channel in all of the lateral cross-sections. Weak bottom stress peaks in the shallow areas of the lateral cross-sections, except notably stronger in transect A 4/5 near Latitude 30.987 ºN. Away from the deep channel, between the flank of the shoal and the shallows, there is a three-way balance between curvature, the lateral density gradient, and bottom stress.

A summary of the calculated results and error analysis by applying the lateral momentum balance model (LMBM) to the roving BB ADCP data for Domains A and B during maximum ebb and maximum flood for spring and neap tides is shown in Table 7.6, where columns 2 and 3 are respectively the acceleration due to curvature and the Coriolis effect, column 4 is the acceleration due to the lateral baroclinic density gradient, and column 5 is the acceleration due to bottom stress. The bold highlighted values in Table 7.6 indicate the balance of terms for maximum ebb or maximum flood conditions, the phase of the fortnightly cycle (spring or neap), and a given choice of C_D. The selection of 'best fit' values for R, B, and C_D and the limitations of the LMBM are discussed in the next section.

As seen in Table 7.6, there is a shift in the balance of terms at each lateral cross-section between maximum ebb and maximum flood for spring and neap tides relative to the choice of the drag coefficient. For spring tide during maximum ebb and maximum flood at all the lateral cross-sections, there is a three-way balance between curvature, the

lateral density gradient, and bottom stress. Likewise, for neap tide during maximum flood, at all the stations but A 9/10, the same three-way balance is observed. However, for neap tide during maximum ebb, there is a two-way between curvature and the lateral baroclinic density gradient. At first, these results may seem puzzling, however, the strong lateral density gradient term, likely enhanced by tidal straining, masks the contribution by the acceleration of bottom stress to the lateral momentum balance. The observed shift in the LMBM results from a three-way balance during weakly stratified conditions to a two-way balance during strongly stratified conditions seems reasonable and is consistent with the results of scale estimates and the Seim and Gregg (1997) curvature-induced overturning model as shown in Chapter 6.

In contrast to the results of Chapter 6, the choice of C_D for maximum ebb at neap tide, either as the 'original C_D' or 'low C_D' value does not shift the overall balance in the lateral cross-sections, despite closing the balance in the LMBM in the lateral cross-section space (*cf.* Figures 7.25 – 7.28). As in Chapter 6, the variations in the balance of terms between maximum ebb and maximum flood for spring and neap tides are likely due to the impact of tidal straining during ebb, which enhances vertical stratification and reduces turbulent mixing, and the influence of form drag during times of high stratification (Simpson et al. 1990; MacCready et al. 2003; Sutherland et al. 2004; Fugate and Chant 2005). Recall that C_D, incorporates the effects of both skin friction and form drag, and that the latter, rather than the former, has been found to be dominant in modifying flow fields (Coleman et al. 2000; Nash and Moum 2001; MacCready et al. 2003; Maddux et al. 2003; Sutherland et al. 2004), particularly in stratified fluids.

Further discussion of the LMBM and its sensitivity to the choice of C_D will follow after a brief discussion of its error analysis.

The 95% confidence intervals included in Table 7.6 for each term in the LMBM were calculated separately for the Domain A and B lateral cross-sections during maximum ebb and maximum flood for spring and neap tide. Because each of the lateral transects were mapped on to an idealized cross-section, the variation in the number of samples used in the LMBM calculations and in calculating the 95% confidence intervals during maximum ebb and maximum flood for spring and neap tides varied by no more than 8% and was usually less than 1%. As a result, and for brevity, the 95% confidence interval calculations are given over an average number of samples used at each cross-sectional location during maximum ebb and maximum flood for spring and neap tides. At Domain A 4/5, the 95% confidence interval was calculated over an average of 640 samples, and was calculated over an average of 653 samples for Domain A 9/10. At Domain B 5/6, the 95% confidence interval was calculated over an average of 592 samples, and was calculated over an average of 531 samples for Domain B 10/11.

7.3.6 Lateral Momentum Balance Model Sensitivity Analyses and Limitations

The simple lateral momentum balance model (LMBM) evaluated at the lateral cross-sections A 4/5, A 9/10, B 5/6, and B 10/11, and expressed by Equation 7.14 below,

$$f\left(u_s-\overline{u}_s\right)-\frac{\left(u_s^2-\overline{u_s^2}\right)}{R}=\frac{g}{\rho_o}\frac{\partial\overline{\rho}}{\partial n}h+\frac{\tau_{n,b}}{\rho_o h} \quad \textbf{(7.14)}$$

appears sufficient to explain the observed changes in secondary flow during maximum ebb and maximum flood for spring tide and during maximum flood for neap tide in the Satilla in a variety of differently oriented and curved channel transects. Nonetheless, it is

important to explore the limitations of this model for three primary reasons: first, to assess how small changes in the choice of scalar quantities (R, B, $\partial\overline{\rho}$, and C_D) affect the results of the LMBM, second, to determine and evaluate the appropriate choice of the scalar variables R, B, and C_D, and third, to explore the validity of neglecting other physical processes (such as vertical variations in the lateral baroclinic gradient) in this model formulation of the lateral momentum balance.

Sensitivity analyses were done, as in Chapter 6, to determine the impact of small changes in the values of R, B, $\partial\overline{\rho}$, and C_D on the resultant estimated terms of the lateral momentum balance model. In a similar manner to Chapter 6, four values of the drag coefficient, C_D, were tested in each lateral cross-section: the 'original C_D', $C_D = 2.5 \times 10^{-3}$ from Seim et al. (2002), the 'low C_D', $C_D = 3.1 \times 10^{-3}$ from Geyer et al. (2000) and Soulsby (1990) for muddy bottom estuaries, the 'adjusted low C_D', $C_D = 5.0 \times 10^{-3}$ from Fischer et al. (1979), and the 'adjusted C_D', $C_D = 8.1 \times 10^{-3}$ chosen as an arbitrary high value. Likewise, four values of the radius of curvature, R, were tested in each lateral cross-section: the 'original R', measured as the local radius of curvature referencing the channel center-line, one-half R, calculated as half of the original R value, three-quarters R, calculated as three-quarters of the original R value and the *thalweg* R, measured as the local radius of curvature referencing the *thalweg* center-line. A similar set of four values for the channel width, B, were tested in each lateral cross-section: the 'original B', relative to the 'original R' and measured at the channel bend inflection point, one-half B calculated as half of the original B value, three-quarters B calculated as three-quarters of the original B value, and the *thalweg* B, measured as the lesser of bank to bank or bank to shoal distance across the deep channel on a bathymetric

chart at the *thalweg* inflection point. Lastly, three values of the mean density difference, $\overline{\partial\rho}$, were tested in each lateral cross-section derived from a combination of the FSI CTD profiles and the SBE-21 system on the R/V Gannet (*e.g.,* Figures 7.10 and 7.11): the mean value of the vertical density difference during maximum ebb and maximum flood at spring and neap, half the mean value of the vertical density difference during maximum ebb and maximum flood at spring and neap, and double the mean value of the vertical density difference during maximum ebb and maximum flood at spring and neap. The results of the sensitivity analyses were in agreement with the sensitivity analyses done in Chapter 6, and indicate that the LMBM is most sensitive to changes in C_D, followed next by changes in R or the ratio of R/B, and lastly by changes in the vertical density structure.

The definition and the selection of the R and B test values were not trivial. Conventionally, the radius of curvature, R, is defined as the arc between the inflection points in a channel bend down the channel center-line axis, and the corresponding channel width, B, is defined as the channel width from bank to bank at the downstream inflection point (Callander 1978; Dunne and Leopold 1978; Smith and McLean 1984; Nelson and Smith 1989; Leopold et al. 1995; Knighton 1998; and Ritter et al. 2002). In addition, R and B defined in the preceding manner correspond to uni-directional flows, an aspect not often discussed in the literature. Recent studies focusing on observing and modeling complex uni- and bi-directional flows (Demuran 1993; Boxall and Guymer 2003; Boxall et al. 2003; and Fagherazzi et al. 2004) have found that using R and B associated with the natural channel axis, the *thalweg*, allows for the channel geometry to evolve naturally (in either a laboratory setting or numerically using 'natural coordinates')

and to be uniquely defined at each channel cross-sectional location. Fagherazzi et al. (2004) included an additional velocity term, u_b, the bank velocity increment, associated with the *thalweg* R, to the average velocity, u_o, associated with the center-line R, to account for the curvature-induced secondary current at the outer bank and found that this inclusion lead to better agreement between observational data and model results. In addition to accounting for the bi-directional flow that occurs in estuaries and in tidal channels, the approach by Fagherazzi et al. (2004) found that the relative velocities of the ebb and flood tides could be remotely determined by planform geometry using a simplified shallow water equation model reflecting both the center-line and *thalweg* definitions of R and B. A schematic of the center-line and *thalweg* definitions of R and B are illustrated in Chapter 6 by Figure 6.15.

The 'best fit' R and the associated B value were chosen initially by determining at each mooring location which of the four pre-selected R values minimized the variance between the observed cross-channel current and the estimated cross-channel current as given by the scale estimate for curvature-driven secondary flow (*cf.* Equation 6.7). The 'best fit' R and associated B value were later re-evaluated after the 'best fit' C_D was determined by assuming that the density-driven scale estimate for secondary flow (*cf.* Equation 6.8) could be approximated by the curvature-driven secondary flow scale estimate (*cf.* Equation 6.7) minus the sum of the frictional-driven (*cf.* Equation 6.9) and Coriolis-driven (*cf.* Equation 6.6) secondary flow scale estimates. The density-driven scale estimate for secondary flow (*cf.* Equation 6.8) was then solved for B and this value was compared to the 'best fit' value for B chosen using the associated R approach. The 'best fit' C_D was chosen by determining which of the four pre-selected values of C_D that

minimized the least-squares difference between the curvature term and the sum of the Coriolis, density, and friction terms in the LMBM. Figure 7.29 illustrates the results of the 'best fit' C_D choice for the LMBM during maximum flood at spring tide.

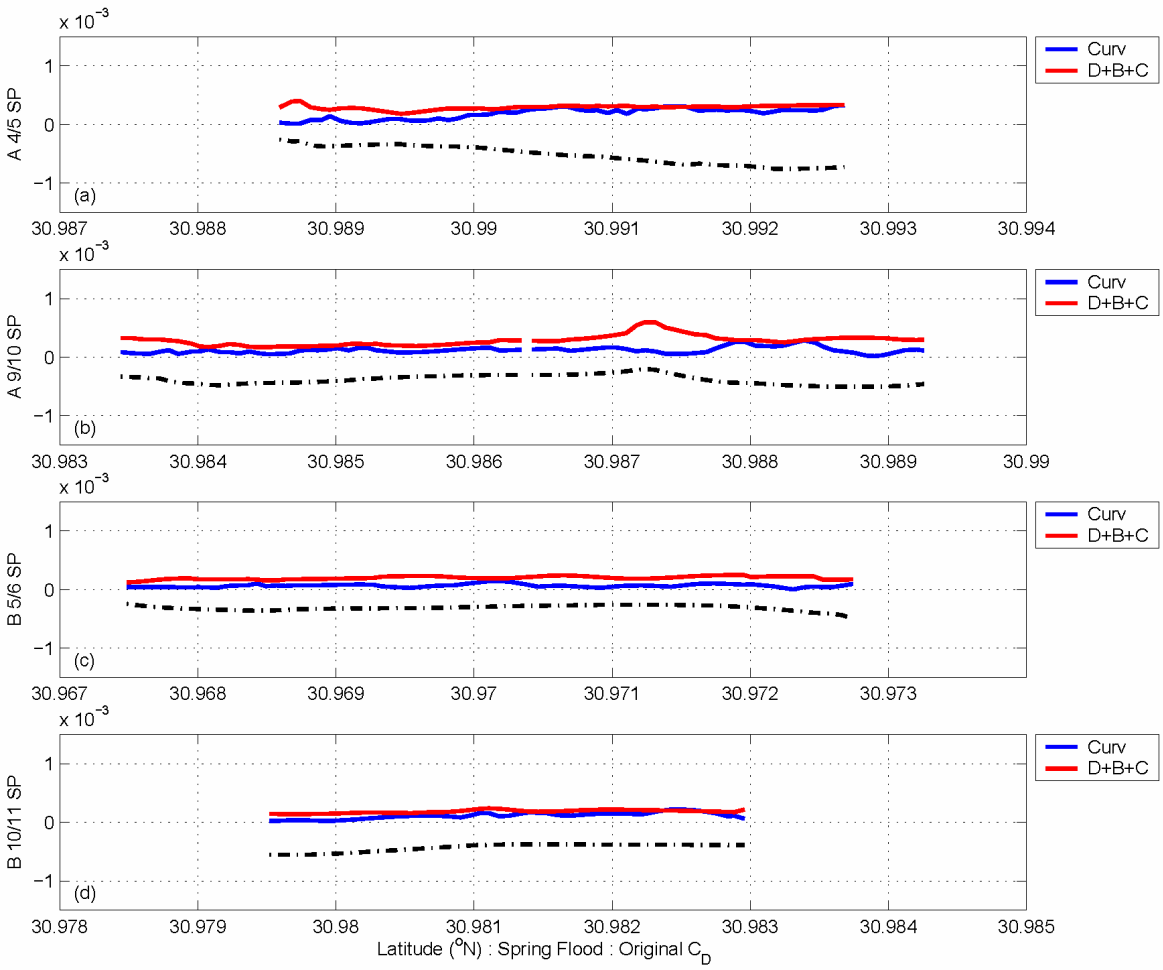

Figure 7.29: Satilla River lateral momentum balance terms (blue curvature, red the sum of density, bottom stress, and Coriolis) illustrating the 'best fit' C_D choice for maximum flood at spring tide for sections (a) Domain A 4/5, (b) Domain A 9/10, (c) Domain B 5/6, and (d) Domain B 10/11. The black dashed line in each subpanel represents the lateral cross-section bathymetry. The bottom stress term was calculated using the original drag coefficient, $C_D = 2.5 \times 10^{-3}$.

Results of the sensitivity analyses determined the best fit for R and B at each Station was the *thalweg* R and the *thalweg* B. And likewise, the sensitivity analyses determined that the best fit for the drag coefficient, C_D, in each lateral cross-section, done independently during maximum ebb and maximum flood for spring and neap tides, was the value of C_D that achieved a balance in the LMBM for a majority of the cross-section in lateral space (*cf.* Figures 7.25 – 7.28). The best fit value of C_D for maximum ebb and maximum flood at spring tide and for maximum flood at neap tide was found to be the 'original C_D' value ($C_D = 2.5 \times 10^{-3}$). Correspondingly, the best fit value of C_D for maximum ebb at neap tide was found to be the 'low C_D' value ($C_D = 3.1 \times 10^{-3}$), when stratification effects were found to be important. However, for an overall cross-sectional choice of C_D during maximum ebb at neap tide, as shown in Table 7.6, there appears to be little difference in the choice between the 'original C_D' and the 'low C_D'. Though no distinction was made between ebb and flood, these results are similar to those of Li et al. (2004) who found that the best value of C_D, using the 'phase matching' method, was slightly higher during neap tides ($C_D = 2.3 \times 10^{-3}$) than during spring tides ($C_D = 2.2 \times 10^{-3}$). Li et al. (2004) surmised that the change in the drag coefficient value between neap and spring tides was due to the increased frictional influence of the bottom and lateral boundaries. However, their result of a variable C_D (Li et al. 2004) originated from a barotropic model that did not account for the effects of stratification. In contrast, the necessary change in the value of C_D to close the LMBM in the Satilla between maximum ebb and flood at spring tide and maximum ebb at neap tide is likely due to the influence of form drag distorting the flow field (MacCready et al. 2003).

Recent work by Sutherland et al. (2004) found that in a continuously stratified fluid, form drag could easily distort the ambient flow field, excite internal waves (e.g., an internal seiche such as seen at neap tides during maximum ebb), and reduce turbulent mixing. Earlier work by Nash and Moum (2001) found bottom stress during stratified conditions (akin to neap tide conditions in the Satilla) could be 5-10 times higher than during barotropic-like conditions (akin to spring tide conditions in the Satilla). Nash and Moum (2001) also found that the distortion of the flow field by form drag was even larger during stratified conditions, such that form drag was twice as effective at reducing local momentum transfer (*cf.* the difference in the core area and core velocity between Figures 7.16 and 7.17) as the enhanced bottom friction, and served as a feedback mechanism to locally generate or sustain internal waves. Therefore, it seems plausible that increasing the value of C_D during maximum ebb at neap tide in the LMBM accounts for the increase in bottom stress and form drag under such stratified conditions. Alternatively, recent work by Fugate and Chant (2005) and Stacey and Ralston (2005) suggest that the observed difference in C_D between ebb and flood for neap tide is related to changes in sediment grain size and cohesiveness and instrument measurements at heights significantly above the bottom boundary layer, which thins at ebb, due to the interaction between tidal straining and the suppression of turbulent mixing by vertical stratification. The observed difference could due to a combination of the above factors.

A major limitation of the LMBM, as seen in Chapter 6, is the singular choice of the drag coefficient, C_D, as one representative value for each lateral cross-section during maximum ebb or maximum flood conditions at either spring or neap tides. Clearly, a spatially varying drag coefficient is likely to give better results, but presently, due to

restrictions of the data set, it is not possible to assess the contribution of a variable C_D to the LMBM results. Another limitation of the LMBM as formulated by Equation 7.12 is the omission of the depth-dependent lateral baroclinic gradient and the vertical shear stress divergence terms. While the importance of the depth-dependent lateral baroclinic gradient and vertical shear stress terms were approximated respectively by the depth-average lateral baroclinic gradient and bottom shear stress, this assumption does not seem suitable especially for maximum ebb at neap tide, when the LMBM does not balance (Figure 7.30), vertical shear stress is maximized, and the depth-dependent vertical density gradient has considerable structure (Figure 7.31c).

Though not done as part of this study, the sensitivity of excluding vertical shear stress in the LMBM as given by Equation 7.12 could be evaluated by considering two different dynamic balances, one assuming well-mixed conditions and the other assuming stratified conditions. In the first case, assuming well-mixed conditions, the lateral dynamic balance would be between the curvature term, the Coriolis term (which is inherently small for the Satilla River), vertical shear stress, and bottom stress. Assuming a quadratic bottom stress as given by Equation 7.13, it would be possible to calculate the vertical shear stress term at each location for the entire lateral cross-section. Likewise, the second case would consider the effect of stratification on the lateral momentum balance, by assuming a balance between the curvature term, the Coriolis term, bottom stress, vertical shear stress, the depth-dependent and the depth-average lateral baroclinic density gradient. As in the previous case, after approximating the bottom shear stress term, the remaining unknown is the vertical shear stress divergence term, which could be inversely determined. A comparison could then be made on the impact of changes in the

density field to the strength of the vertical shear stress term between well-mixed and stratified conditions. For example, comparing the difference in the strength of the lateral density gradient in Figures 7.31c and 7.32c and how these differences might this affect the structure of the calculated vertical shear stress divergence term.

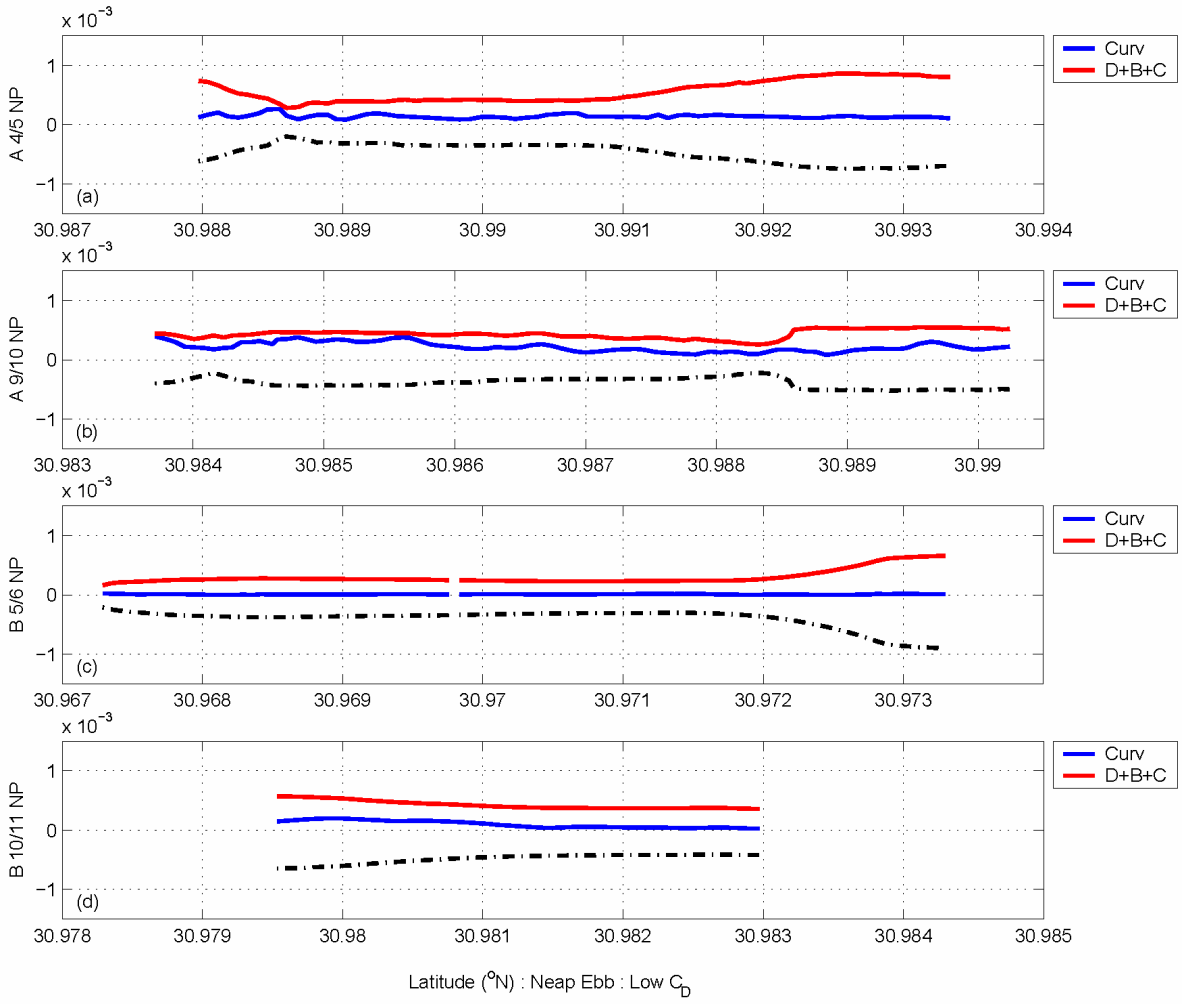

Figure 7.30: Satilla River lateral momentum balance terms (blue curvature, red the sum of density, bottom stress, and Coriolis) illustrating the 'best fit' C_D choice for maximum flood at spring tide for sections (a) Domain A 4/5, (b) Domain A 9/10, (c) Domain B 5/6, and (d) Domain B 10/11. The black dashed line in each subpanel represents the lateral cross-section bathymetry. The bottom stress term was calculated using the low drag coefficient, $C_D = 3.1 \times 10^{-3}$.

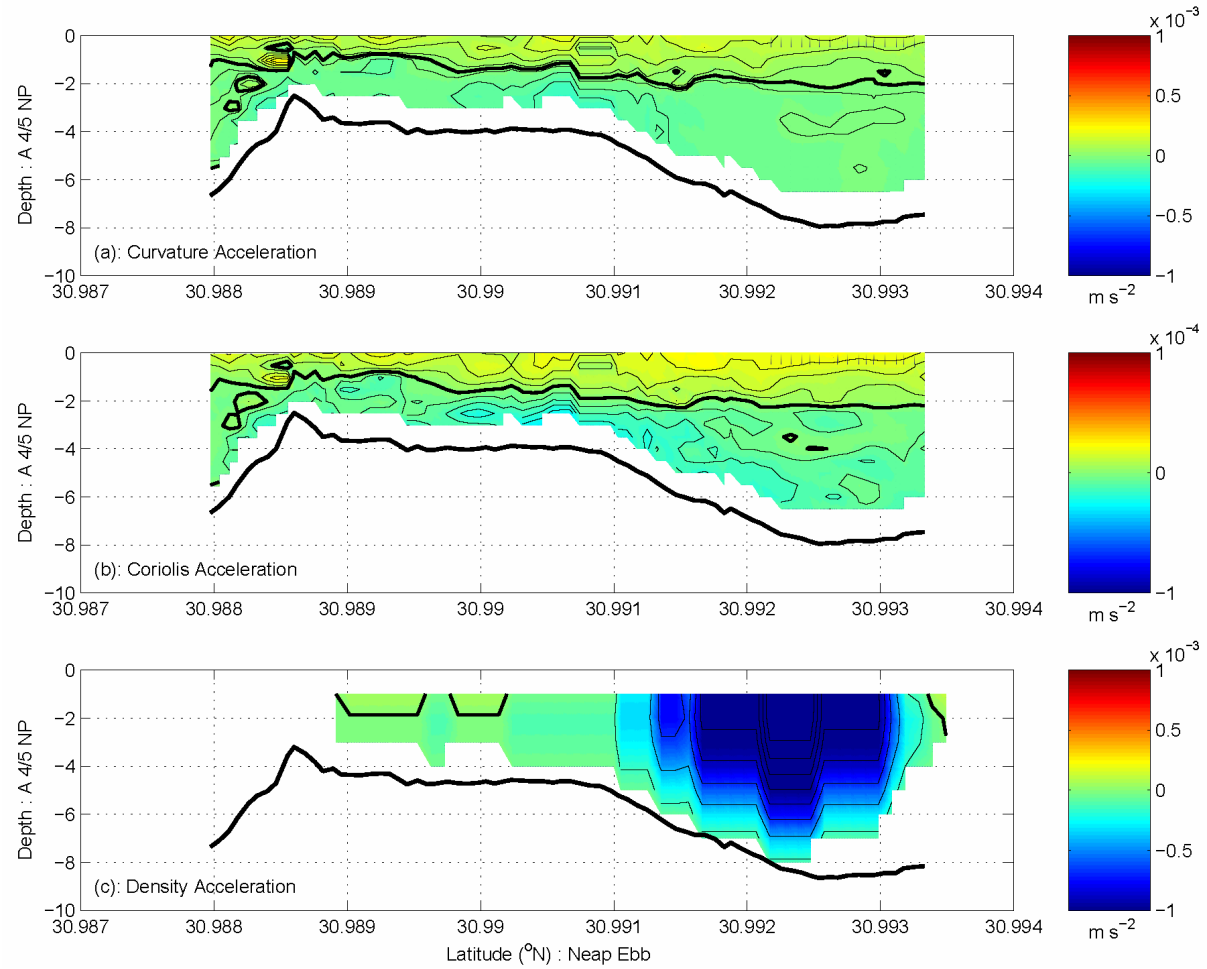

Figure 7.31: The (a) curvature acceleration, the (b) Coriolis acceleration, and the (c) density acceleration terms for the LMBM at section Domain A 4/5 for maximum ebb at neap tide. The solid black line in the subpanels indicates the zero crossing.

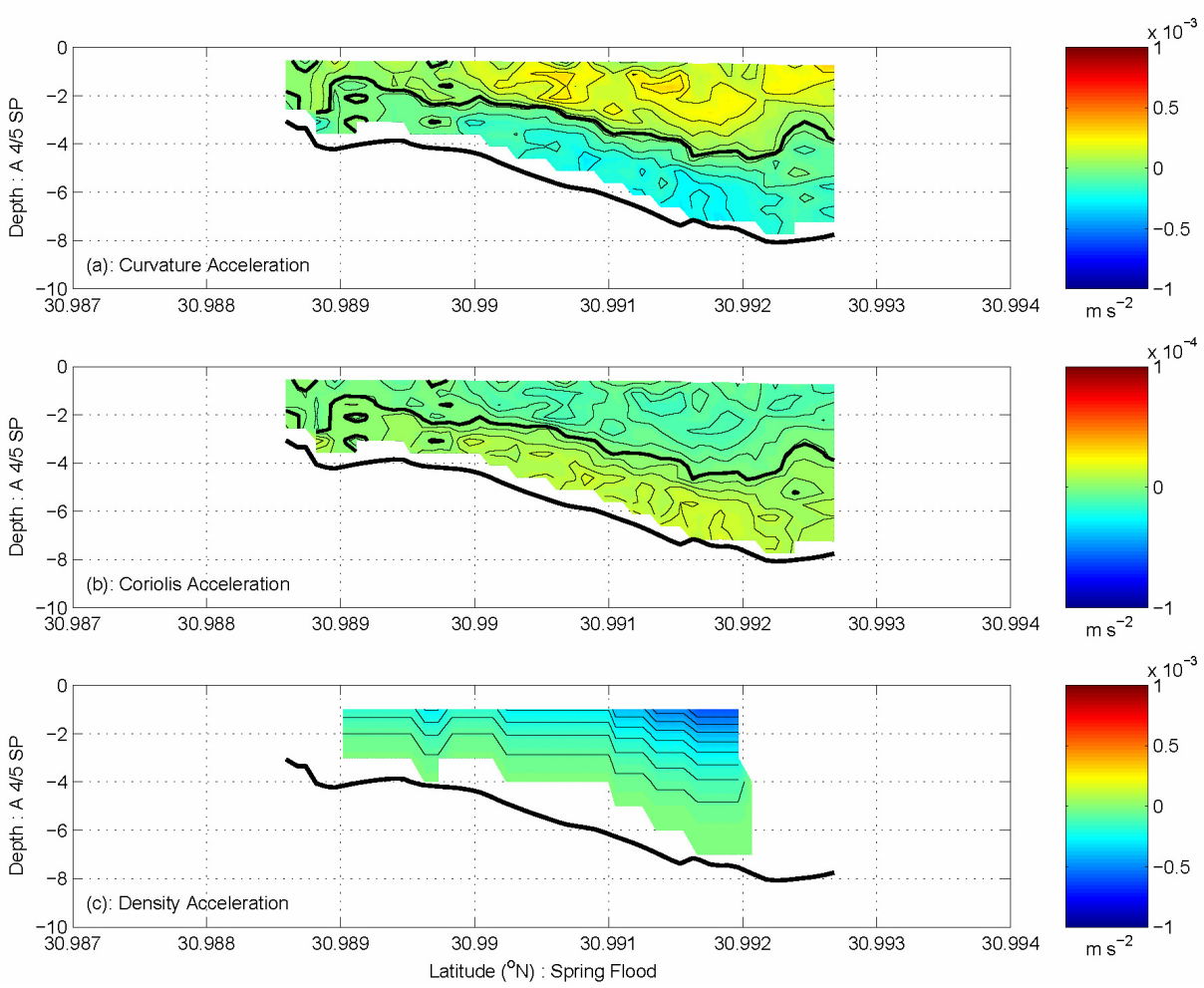

Figure 7.32: The (a) curvature acceleration, the (b) Coriolis acceleration, and the (c) density acceleration terms for the LMBM at section Domain A 4/5 for maximum flood at spring tide. The solid black line in the subpanels indicates the zero crossing.

Lastly, the current LMBM was developed assuming steady-state conditions and neglecting advective accelerations. While suitable for this application, these assumptions in the formulation of the LMBM may not be appropriate in all cases. Recent research (Geyer 1993; Chant and Wilson 1997; Seim and Gregg 1997; and Lacy and Monismith 2001) suggests that the assumption of steady-state conditions is more applicable than neglecting advective accelerations. Chant and Wilson (1997) found that it was necessary to include advective accelerations to close the lateral momentum balance and to account for changes in the flow field around a headland near the George Washington Bridge in the Hudson River. Likewise, Lacy and Monismith (2001) found that the addition of lateral advection was necessary to close the momentum balance when the channel configuration was complex producing large lateral gradients or in areas where the bathymetry changes rapidly, such as an area with broad shoals like Grizzly Bay.

The effect of the advective accelerations in the Satilla can be seen in the velocity profiles shown in Figures 7.12 and 7.13 and by noting that the core of axial momentum is found shifted to the inside of the *thalweg*, a feature generated by these non-linear interactions. Therefore, though regionally and geomorphologically different from the above study sites, advective accelerations *should not* be neglected in the future formulation of a lateral momentum balance for the Satilla River. Despite these limitations, the LMBM does well to describe changes in the lateral momentum balance of the Satilla River during both maximum ebb and maximum flood for spring tide and during maximum flood for neap tide in a variety of channel reaches driven by secondary flows in a simple straightforward manner.

7.4 Conclusions

This chapter explores the changes in the strength, signal, and balance of mechanisms that drive secondary circulation in four different lateral cross-sections, two in a bend to the north, and two in an adjacent bend to the south, during maximum ebb and maximum flood for both spring and neap tides, and the ability to describe these changes with a simple lateral momentum balance model. As in Chapters 5 and 6, acoustic current meter data is used to directly observe and quantify the *spatial* changes in the strength and direction of secondary flows driven by channel curvature, Coriolis acceleration, friction, and the differential advection of density. Secondary circulation was found best described as an evolving helix down the axis of the estuary and was found to have a non-negligible impact on the fluxes of mass and momentum in the downstream direction.

The balance of mechanisms responsible for the strength and location of secondary flows in the Satilla River varies with changes in channel geometry, neap-to-spring variations in salinity and velocity, ebb and flood tidal phase, and lateral cross-channel position. A simple steady-state lateral momentum balance model between the Coriolis acceleration, centrifugal acceleration, the lateral baroclinic gradient, and bottom stress is sufficient to explain the observed changes in secondary flow during maximum ebb and maximum flood conditions for spring and neap tides in the Satilla in a variety of differently curved lateral channel cross-sections. Sensitivity analyses on the lateral momentum balance model determined that the best choice values for the local radius of curvature and channel width are those associated with the *thalweg* and that the best choice value for the drag coefficient, C_D, depends the phase of the tide (maximum ebb or maximum flood), the phase of the fortnightly tidal cycle (spring or neap), and on the local

ambient stratification conditions (increasing form drag). It was found that the choice of C_D for maximum ebb at neap tides was slightly higher than the choice of C_D for maximum ebb and maximum flood at spring tides and for maximum flood at neap tides. The increase in C_D necessary to close the lateral momentum balance model in the Satilla between maximum ebb and maximum flood is likely due to a combination of changes in vertical stratification and the influence of form drag distorting the flow field. The lateral momentum balance model results shows that there is a shift in the overall primary momentum balance between maximum ebb at neap tide and maximum flood at neap tide and maximum ebb and flood at spring tide. For maximum ebb and flood at spring tide and maximum flood at neap tide, the primary momentum balance is between centrifugal acceleration, the lateral baroclinic density gradient, and bottom stress. While for maximum ebb at neap tide, depending on the strength of the local stratification and effective form drag, the primary momentum balance is between centrifugal acceleration and the lateral baroclinic density gradient. The strength of the lateral baroclinic density gradient, enhanced by tidal straining, masks the effect of bottom stress.

The primary balance of forces that drive secondary circulation in a channel cross-section varies with lateral position. In the *thalweg*, the primary dynamic balance varies from a three-way balance between the centrifugal acceleration, the lateral baroclinic density gradient, and bottom stress when the local ambient stratification is weak to a two-way balance between centrifugal acceleration and the lateral baroclinic density gradient when the local ambient stratification is strong. In the shallows and on the flank of the shoal, the primary dynamic balance is between the centrifugal acceleration, the lateral baroclinic density gradient, and bottom stress, which is reduced to a two-way balance

between curvature and bottom stress when water depths are shallow and stratification is weak. Bottom stress drives secondary circulation in the very shallow intertidal areas of the Satilla River where bathymetry changes rapidly, acting independently of tidal phase (ebb or flood).

This chapter demonstrates that the balance of mechanisms that drive a secondary circulation shift in a lateral cross section and vary depending on the phase of the tide and the fortnightly tidal cycle. It is important to be able to estimate the relative magnitude of mechanisms that drive secondary flow in order to clarify their role in local and estuarine-wide mixing. Knowledge of this role will better able us to predict important parameters such as the length of the salt intrusion and to determine the dispersion and distribution of various waterborne properties (e.g., larvae, sediment, and pollutants) in the estuarine environment.

8. FINAL SUMMARY AND CONCLUSIONS

Estuaries have always been important in the development and growth of human societies. These unique transitional environments between riverine systems and the coastal ocean are among the most biologically productive areas in the world, and they provide a major freshwater source for continued economic growth and development in many coastal communities. This is especially true in today's society where over 23% of the world's population lives within 100 miles of a coastline, and in a nation whose urban centers are ever expanding coastward.

Transport and mixing of momentum and salt in an estuary varies in time and space due to river discharge, changes in tidal amplitude and phase, wind stress, and lateral mixing processes. Lateral mixing commonly refers to poorly resolved, rarely quantified interaction(s) between processes like secondary circulation, river discharge, wind stress, and tidal forces. Modern instrumentation and better computational techniques have generated a resurgent interest in better comprehending such interactions. The intent of this dissertation was to detail the impact of secondary circulation on the lateral momentum balance in a sinuous coastal plain estuary. This endeavor was made to improve our general understanding of secondary circulation, to identify its primary driving forces, and to better parameterize key physical processes necessary for further study in current numerical models.

Secondary circulation is broad and often confusing term used to describe several mechanisms whose result is to vertically overturn the water column along the transverse axis of a channel. Most commonly, secondary circulation is generated by one or more of

the following mechanisms: channel curvature, unusual bottom topography or channel geometry, domain size, and/or the differential advection of density. Secondary circulation may be composed of one or more cells that can act to reduce or enhance local velocity and density gradients. In the field, a physical manifestation of secondary flow is often observed as one or more foam lines down the longitudinal axis of an estuary.

Field data for this dissertation was collected in the naturally sinuous Satilla River in southeast Georgia during the spring of 1997 and during the spring and fall of 1999. A shallow coastal plain estuary, the Satilla is a typical partially-mixed estuary characterized by 1 - 2.5 meter range semidiurnal tides. It has a strong neap-to-spring axial current inequality ranging from 0.5 m s^{-1} to 1.5 m s^{-1}; and likewise, has strong neap-to-spring vertical salinity variations in the *thalweg* from 7 PSU to 2 PSU. The density structure of the Satilla River is most sensitive to variations in salinity.

Chapter 5 demonstrates that the strength of the mechanisms that drive secondary flow in a stratified channel bend can be modulated on the fortnightly cycle in response to changes in the axial current speed, the lateral baroclinic gradient, neap-to-spring variations in salinity, and freshwater discharge. Acoustic current meter data can be used to directly observe and quantify the strength and the direction of curvature-induced secondary circulation. Secondary circulation in the first major bend of the Satilla River is consistent with flow due to channel curvature except possibly at neap tides when the shear of the along-channel flow is too small to overcome the cross-channel baroclinic pressure gradient force.

Seim and Gregg (1997) provide a simple method for estimating the critical along-channel flow velocity necessary below which secondary flow due to channel curvature

can be halted, by quantifying the contribution of the axial current to the strength of the centrifugal acceleration. The Seim and Gregg (1997) curvature-induced overturning model was used to demonstrate that conditions necessary to limit or halt curvature-induced secondary flow, in the first bend of the Satilla River, can be met near neap tide for up to two days but do not occur at spring tide. The implications of these model results suggest that the density structure characteristics at neap tide could be maintained around a channel bend, potentially longer than a tidal cycle, until either the mixing properties (e.g., river discharge, bottom topography, flow separation) change or another bend is encountered, leading to an unexpected local increase in salt and/or momentum. Secondary circulation can act as a 'trapping' mechanism (i.e., it can effectively limit vertical mixing to the upper half of the water column) during neap tide when the vertical salinity difference is sufficient ($\geq$ 1 PSU) and axial current is weak ($\leq$ 0.65 m s^{-1}).

The character of the secondary circulation pattern in the first and second major bends of the Satilla River alternates between a single circulation cell at spring tide to a stacked two-cell configuration at neap tide. The single cell configuration at spring tide is due to curvature-induced secondary flow. Likewise, the uppermost cell of the two-cell configuration at neap tide is due to curvature-induced secondary flow while the lowermost cell is generated by a relaxation of the pycnocline between ebb and flood tides. The lateral seiching in response to internal adjustments of the density field between ebb and flood tides is a local feature and is likely to be detected only in nearby downstream bends within close proximity (1500 – 4000 m). The strength and duration of the lowermost cell in the two-cell configuration decreases in response to a decrease in the vertical salinity gradient or to a decrease in freshwater discharge. As freshwater input

decreases, the axial salinity gradient decreases, this in turn, reduces the lateral and vertical salinity gradients, which can enhance mixing by secondary circulation.

Chapter 6 explores the changes in the strength, signal, and balance of mechanisms that drive secondary circulation in four different channel reaches, from highly curved to nearly straight, the changes in the strength of secondary flow in relation to changes in freshwater discharge, and the ability to describe these changes with a simple lateral momentum balance model. As in Chapter 5, acoustic current meter data is used to directly observe and quantify the strength, direction, and duration of secondary flows driven by channel curvature, Coriolis acceleration, friction, and the differential advection of density. Likewise, secondary circulation driven by channel curvature dominates at three of the four mooring locations, located in channel bends, while secondary circulation driven by the differential advection dominates at the fourth location, a nearly straight reach of the Satilla River.

Changes in freshwater discharge were found to modify the strength and the character of secondary flows in the Satilla. Though the 1997 and 1999 experiments described in this dissertation did not cover the full dynamic range of river discharge conditions, it is possible to estimate the contribution of changes in freshwater input to the strength of secondary flows. During low discharge conditions, the strength of secondary flow is relatively unaffected, the result of either a weak vertical salinity gradient or a shift in its location upriver. Conditions necessary to limit or halt secondary flow driven by centrifugal acceleration are less frequent and secondary flow acts unimpeded as a lateral mixing agent. In contrast, during high discharge conditions, the strength of secondary flow driven by channel curvature was found to be reduced by the addition of sufficient

freshwater discharge, especially during ebb tides due to tidal straining, which enhances vertical stratification on ebb and reduces vertical stratification on flood. Tidal straining is most effective at enhancing vertical stratification under high discharge conditions and/or when the average axial velocity is high, as during spring tides. Conditions necessary to limit or halt secondary flow are more common during times of high discharge and there is a noticeable decrease in the effectiveness of secondary circulation as a lateral mixing agent. Consequently, secondary flow driven by centrifugal acceleration, in addition to being sensitive to changes in river discharge, is modified by tidal straining during the ebb phase of the tidal cycle.

As demonstrated in Chapter 5, the Seim and Gregg (1997) model is effective at explaining the observed fortnightly changes in secondary flow driven by centrifugal acceleration, the dominant mechanism for driving lateral flows in the Satilla River. However, while this model explains the general differences observed in curvature-driven secondary flow on the fortnightly time scale, additional processes that govern secondary flow (i.e., density and friction) must be considered when applying it to either weakly curved channels or straight reaches. As a result, analytical scale estimate formulas, adjusted to observed secondary flows, are used as first order estimates to determine the relative importance of curvature, Coriolis, friction, or density-driven secondary flows, and to assess the dominant terms in a simple lateral momentum balance at a number of locations, under a variety of conditions.

As explored in Chapters 6 and 7, it was determined that secondary circulation alters the distribution and the transfer of longitudinal momentum in the downstream direction and that the balance of mechanisms responsible for the strength and location of

secondary flows in the Satilla River varies with channel geometry, discharge conditions, fortnightly tidal cycle, ebb and flood tidal phase, and lateral cross-channel position. A steady-state momentum balance between the Coriolis acceleration, centrifugal acceleration, the lateral baroclinic gradient, and bottom stress is sufficient to explain the observed changes in secondary circulation on the tidal and fortnightly time scales in the Satilla River under widely different discharge conditions and in several differently curved channel reaches. The primary momentum balance at spring tide is between centrifugal acceleration and bottom stress. At neap tide, depending on local stratification and form drag, the primary momentum balance shifts from a two-way balance between centrifugal acceleration and the lateral baroclinic gradient at low drag states to a three-way balance between centrifugal acceleration, the lateral baroclinic gradient, and bottom stress at high drag states. The primary balance of forces that drive secondary circulation in a channel cross-section varies with lateral position. In the *thalweg*, the primary dynamic balance is between the centrifugal acceleration and the lateral baroclinic pressure gradient. In the shallows and on the shoal flanks, the primary dynamic balance is between the centrifugal acceleration, the lateral baroclinic pressure gradient, and bottom stress. Bottom stress drives secondary circulation in the very shallow intertidal areas of the Satilla River where bathymetry changes rapidly, acting independently of tidal phase (ebb or flood).

It is important to be able to understand what processes generate and limit the strength of secondary circulation in estuaries in order to predict the length of the salt intrusion, the locus of momentum transfer, and to determine the dispersion and distribution of various properties (e.g., larvae, sediment, and pollutants) in the estuarine environment.

9. RECOMMENDATIONS AND FUTURE RESEARCH

Though much has been learned about secondary circulation, its cross-channel characteristics, its modulation on the tidal and fortnightly cycles, and its role in modifying the lateral momentum balance, more can be done to better understand its impact on the estuarine environment. This section is designed to give recommendations and suggestions for future research regarding this subject. Many of these ideas and suggested studies evolved from questions that arose during this dissertation research.

Interesting future projects can be done using the data sets as described in this dissertation. One such study would be to investigate the temporal evolution of secondary circulation at spring and at neap tides and to understand its relationship with the dominant M_2 and M_4 tidal currents of the Satilla River, Georgia. This effort would require a temporal interpolation of the lateral spatial data as well as a simple tidal prediction model to capture the dominant tidal features and their influence on secondary flow.

Another interesting study would be to understand the influence of severe weather events (tropical storms and hurricanes) on the signature of secondary flow. This project could use long term mooring data from both SAT 1 and SAT 2 experiments to determine the response of the secondary flow to severe weather events, specifically Hurricanes Floyd and Irene that occurred during the SAT 2 experiment.

The lateral momentum balance model used for the Satilla River could be applied and tested in other estuarine environments. This experiment could help determine a new method by which to scale estuarine behavior. Simple estimates of axial current speed, *thalweg* depth, bank-to-bank or bank-to-shoal measurements, local radius of curvature,

and salinity structure can be obtained from the current literature and a good regional bathymetric map. It would be interesting to determine if the estuaries group the same as they might on a classical Hansen-Rattray diagram.

A simple numerical model could be constructed using the lateral momentum balance model as a basis. This would permit a diagnostic look at the terms in our lateral momentum balance model that we were unable to resolve or estimate due to data constraints. A benefit of such a modeling effort would be to provide additional sensitivity analyses under widely varying environmental, temporal, and spatial conditions. As an example, this type of modeling effort could allow for the calculation of a variable drag coefficient both in time and space.

While proxy methods can provide insightful information about salinity and sediment structure to our existing data sets, some additional field observations could greatly improve our current understanding of the Satilla River. Future recommendations for field data include a need for better salinity measurements both in the lateral and vertical directions, boundary layer velocity data, and sediment measurements including form and distribution. This dissertation has demonstrated that while much can be understood with coarse measurements of the lateral salinity structure and near bottom current velocities close to the boundary layer, little is known about how these features interact within the bottom boundary layer, the effect of changes in discharge, and how the salinity and velocity structure may be influenced by changes in sediment type and form.

It is fortunate to have such diverse data sets from the Satilla River, Georgia. It is anticipated that many rich and detailed revelations about secondary circulation and estuarine dynamics can be explored and elucidated within this framework.

APPENDIX A: EQUATIONS

SEIM AND GREGG OVERTURNING MODEL

$$-\frac{\left(u_s^2-\overline{u_s^2}\right)}{R}=-\frac{g}{\rho_o}\int_z^\eta \frac{\partial\rho}{\partial n}dz+\frac{g}{\rho_o}\frac{\partial\overline{\rho}}{\partial n}h \quad \textbf{(A1.1)}$$

The Seim and Gregg (1997) overturning model (Equation A1.1) written in curvilinear coordinates (or natural coordinates) is derived from the lateral momentum balance. The Seim and Gregg (1997) model is based on an inviscid cross-channel momentum balance between centrifugal acceleration and the lateral baroclinic pressure gradient. In Equation A1.1, the first term (starting on the left hand side) is centrifugal acceleration, derived from the difference between the depth-dependent and depth-average streamwise velocity, the second term is the depth-dependent lateral baroclinic pressure gradient, and the third term is the depth-average expression of the lateral baroclinic pressure gradient. In order to scale and evaluate the second term in Equation A1.1, Seim and Gregg (1997) assume that the cross-channel density gradient has no dependence on depth.

Using alpha,

$$\alpha=\left(u_s^2-\overline{u_s^2}\right)\Big/\overline{u_s^2} \quad \textbf{(A1.2)},$$

as a measure of vertical shear and scaling the right hand side of Equation A1.1 as $\frac{g}{\rho_o}\frac{\Delta\overline{\rho}}{B}h$ where g is gravity, ρ_o is an ambient reference density, $\Delta\overline{\rho}$ is the depth-average density difference, B is the effective channel width, and h is the water depth yields the expression:

$$-\frac{\left(u_s^2 - \overline{u_s^2}\right)}{R} = \frac{g}{\rho_o}\frac{\Delta\overline{\rho}}{B}h \quad \textbf{(A1.3)}.$$

Rewritten, Equation A1.3 may be more easily expressed as the minimum depth-average speed necessary to overturn the water column in terms of the vertical density difference.

$$\overline{u_s^2} \geq \frac{1}{\alpha}\frac{R}{B}\frac{gh}{\rho_o}\Delta\overline{\rho} \equiv \frac{1}{\alpha}\frac{R}{B}g'h \quad \textbf{(A1.4)}$$

where R is the radius of curvature, g′ is reduced gravity, and the remaining terms are as given above. Alternatively, Equation A1.4 can be expressed in terms of an internal Froude number where

$$\alpha Fr_i^2 \frac{B}{R} \geq 1 \quad \textbf{(A1.5)}$$

and where

$$Fr_i^2 = \frac{\overline{u_s^2}}{g'h} \quad \textbf{(A1.6)}$$

is a necessary condition for the centrifugal acceleration to overcome the buoyancy force and turbulently mix the density field.

$$\frac{\partial u_n}{\partial t} + u_s \frac{\partial u_n}{\partial s} + f u_s - \frac{u_s^2}{R} + g\frac{\partial \eta}{\partial n} = -\frac{g}{\rho_o}\int_z^\eta \frac{\partial \rho}{\partial n} dz + \frac{\partial}{\partial z}\left(A_z \frac{\partial u_n}{\partial z} \right) \quad \textbf{(A2.1)}$$

(A) (B) (C) (D) (E) (F) (G)

The terms in Equation A2.1 are as follows: (A) is the local time rate of change of transverse velocity, (B) is the advective acceleration of transverse velocity by the axial velocity, (C) is the Coriolis acceleration where f is the Coriolis parameter, (D) is the centrifugal acceleration where R is the local radius of curvature, (E) is the barotropic pressure gradient (surface water slope), (F) is the lateral baroclinic pressure gradient (due to vertical stratification), and (G) is vertical stress divergence where A_z is the vertical eddy viscosity. The subscript s is used to indicate motion in the axial (or streamwise) direction and the subscript n is used to indicate motion in the lateral (or normal) direction.

Using a Reynolds stress parameterization to represent vertical shear stress and substituting

$$\frac{\tau_n}{\rho_o} = \left[A_z \frac{\partial u_n}{\partial z} \right]_{z=-h} \quad \textbf{(A2.2)}$$

into Equation A2.1 and representing τ_n in Equation A2.2 by the expression:

$$\tau_n = \rho_o C_D |u_n| u_n = \frac{1}{16} \rho_o C_D |u_s| u_s \quad \textbf{(A2.3)}$$

Equation A2.1 can also be expressed in the following form:

$$\frac{\partial u_n}{\partial t} + u_s \frac{\partial u_n}{\partial s} + f u_s - \frac{u_s^2}{R} + g\frac{\partial \eta}{\partial n} = -\frac{g}{\rho_o}\int_z^\eta \frac{\partial \rho}{\partial n} dz + \frac{\partial}{\partial z}\left(\frac{\tau_n}{\rho_o} \right) \quad \textbf{(A2.4)}$$

Depth-averaging (as indicated by the overbar) Equation A2.4 yields the expression:

$$\frac{\partial \overline{u}_n}{\partial t} + \overline{u_s \frac{\partial u_n}{\partial s}} + f\overline{u}_s - \frac{\overline{u_s^2}}{R} + g\frac{\partial \eta}{\partial n} = -\frac{g}{\rho_o}\frac{\partial \overline{\rho}}{\partial n}h - \frac{\tau_{n,b}}{\rho_o h} \quad \textbf{(A2.5)}$$

Steady-state conditions are assumed to hold true if there is a short baroclinic adjustment time,

$$T_{bc} = \frac{B}{\sqrt{g'h}} \quad \textbf{(A2.6)}$$

relative to semidiurnal tidal forcing, where B is the effective channel width (the lesser of bank to bank or bank to shoal), *g'* is reduced gravity, and h is the depth of the *thalweg* (Chant and Wilson 1997; Lacy and Monismith 2001). Likewise, advective acceleration can be neglected if the frictional time scale,

$$T_f = \frac{L_s}{\overline{u}_s} \quad \textbf{(A2.7)}$$

is short relative to the advective time scale,

$$T_{adv} = \frac{L_s}{\overline{u}_s \Delta u_n} \quad \textbf{(A2.8)}.$$

In Equations A2.7 and A2.8, L_s is the length scale of the axial flow field, $\overline{u}_s$ is the depth-average streamwise velocity, and Δu_n is the change in the normal (lateral) velocity over the distance L_s (Geyer 1993).

Subtracting Equation A2.5 from Equation A2.4 and assuming steady-state conditions (focusing on maximum ebb and maximum flood conditions where acceleration is at a minimum) and neglecting advective acceleration results in Equation A2.9, a lateral momentum balance model applicable to data collected in the Satilla River, Georgia. This model is evaluated at seasonal moorings and pre-determined lateral cross-sections in the

Satilla River estuary. A benefit to this approach is that the barotropic water slope (and the most difficult parameter to estimate or measure) has been eliminated from the final expression.

$$f\left(u_s-\overline{u}_s\right)-\frac{\left(u_s^2-\overline{u_s^2}\right)}{R}=-\frac{g}{\rho_o}\int_z^\eta\frac{\partial\rho}{\partial n}dz+\frac{g}{\rho_o}\frac{\partial\overline{\rho}}{\partial n}h+\frac{\partial}{\partial z}\left(\frac{\tau_n}{\rho_o}\right)+\frac{\tau_{n,b}}{\rho_o h} \quad \textbf{(A2.9)}$$

The terms on the left hand side of Equation A2.9 represent secondary circulation driven by Coriolis and centrifugal acceleration, respectively, and terms on the right hand side of Equation A2.9 represent the depth-dependent and depth-average baroclinic pressure gradient, shear stress divergence, and bottom stress, respectively.

$$f\left(u_s-\overline{u}_s\right)-\frac{\left(u_s^2-\overline{u_s^2}\right)}{R}=-\frac{g}{\rho_o}\int_z^\eta\frac{\partial\rho}{\partial n}dz+\frac{g}{\rho_o}\frac{\partial\overline{\rho}}{\partial n}h+\frac{\partial}{\partial z}\left(\frac{\tau_n}{\rho_o}\right)+\frac{\tau_{n,b}}{\rho_o h} \quad \textbf{(A3.1)}$$

(A) (B) (C) (D) (E) (F)

This lateral momentum balance model is based on the cross-channel momentum balance between the centrifugal acceleration, planetary rotation, the lateral baroclinic pressure gradient, and the Reynolds stress in the y-z direction (vertical shear stress). The terms in Equation A3.1 are as follows: (A) is secondary circulation driven by the difference between the depth-dependent and depth-average Coriolis acceleration where f is the Coriolis parameter, (B) is secondary circulation driven by the difference between the depth-dependent and depth-average centrifugal acceleration where R is the local radius of curvature, (C) is the depth-dependent lateral baroclinic pressure gradient, (D) is the depth-average lateral baroclinic pressure gradient, (E) is vertical shear stress divergence where τ_n is the Reynolds stress parameterization of vertical shear stress, and (F) is bottom shear stress. The subscript s is used to indicate motion in the axial (or streamwise) direction and the subscript n is used to indicate motion in the lateral (or normal) direction. In Equation A3.1, bottom shear stress is expressed as

$$\tau_{n,b}=\rho_o C_D\left|u_{n,1mab}\right|u_{n,1mab}=\frac{1}{16}\rho_o C_D\left|u_{s,1mab}\right|u_{s,1mab} \quad \textbf{(A3.2)}$$

to account for the contributions of the axial and lateral velocity to the observed values of shear stress.

Geyer (1993b) examined a balance between centrifugal acceleration and vertical shear stress while Seim and Gregg (1997) examined a balance between centrifugal acceleration and the baroclinic pressure gradient. In a similar study, Dronkers (1996) investigated a balance between centrifugal acceleration, the lateral baroclinic gradient, and vertical shear stress. Our model evaluation is done in direct comparison with recent estuarine studies and will examine centrifugal acceleration balanced by the lateral baroclinic pressure gradient, vertical shear stress, and Coriolis acceleration. Planetary rotation was preserved in this model to account for other estuaries where such effects are not negligible.

Equation A3.1 is used to evaluate the lateral momentum balance at a series of seasonal moorings during spring and neap tides and in a series of pre-determined channel cross-sections during spring and neap under maximum ebb and maximum flood conditions. The focus on Equation A3.1 will be on terms A, B, D, and F which can be directly calculated with the Satilla River data sets. Bottom stress is calculated using Equation A2.3 for cross-channel shear at one meter above the bottom (1 mab) at each mooring or cross-section location. The depth-average lateral baroclinic gradient and bottom shear stress are assumed to represent the importance of the depth-dependent lateral baroclinic gradient and vertical shear stress, respectively.

APPENDIX B: DEFINITIONS

Advection

Transport due to the mean flow. This transport is directed primarily in the horizontal direction, though it occurs on a smaller scale in the vertical, and can be thought of as a current moving fluid parcels.

Along-channel

The principle axial or longitudinal axis of a channel. The along-channel component of the current flows in the axial direction. The dominant scale of motion in an estuary is in the along-channel direction.

Anastomosing

Derived from medical terminology, and used to describe stream braiding, anastomosing means the process of dividing and re-joining. In current hydrological literature, anastomosing is synonymous with (stream) braiding.

Anticyclonic

Flow in a clockwise direction. Flow is anticyclonic in a concave bend on ebb and convex bend on flood.

Axial

Motion along the longitudinal axis of a channel. Axial is often interchanged with along-channel.

Baroclinic

The state of stratification in a fluid in which surfaces of constant pressure (isobaric) intersect with surfaces of constant density (isosteric). The number, per unit area, of isobaric-isosteric solenoids intersecting a given surface is a measure of baroclinicity. A simple indicator of the baroclinic state is the rate of change of density at a point with depth. Estuarine systems, unless well mixed, are baroclinic in nature.

Baroclinic flow

Flow induced by horizontal pressure forces resulting from vertical density differences.

Barotropic

This is the state of zero baroclinicity. A fluid can be considered barotropic when the rate of change of density at a point with depth does not change. The barotropic state is a simplifying assumption in fluid dynamics. Estuaries that are well mixed can often be assumed barotropic.

Barotropic flow

Flow induced by horizontal pressure forces resulting from a slope in the water surface.

Barotropic Froude number, Fr

The ratio of tidal amplitude to the water depth. In this interpretation, the barotropic Froude number is the ratio of the axial current speed relative to the speed of a shallow water wave on a density interface

Blackwater

A typical characteristic of rivers whose headwaters originate in the sandy coastal plains. Coastal plain rivers are little affected by clay materials from piedmont regions. The predominant dark tea colored water ('blackwater') is from tannic acids derived from humic materials found in the extensive flood plain swamps bordering these rivers.

Bulk Richardson Number, Ri_b

This equivalent to the gradient Richardson number is used operationally to determine the Richardson number for a layer (usually in the atmosphere).

Burger Number, S´

A modified ratio of the Rossby to Froude numbers. The Burger number indicates the relative importance of stratification to rotation effects. The rotation effects include both local channel curvature and Coriolis.

Centrifugal force

The negative of the centripetal acceleration. A sideways forced acting on a fluid particle because of its movement in a curve.

Circulation parameter

The ratio of the surface residual current to the depth or cross sectional mean current.

Coefficient of longitudinal dispersion

A coefficient in an equation relating the cross-sectionally averaged flux of salt to the longitudinal gradient of salinity.

Concave

In this dissertation, a concave bend is a bend to the north. On flood, flow in a concave bend is cyclonic and on ebb, the flow is anticyclonic.

Convection

Convection is vertical overturning induced by static instability. Examples of convection are buoyant thermals and growing cumulonimbus clouds.

Convex

In this dissertation, a convex bend is a bend to the south. On ebb, flow in a convex bend is cyclonic and on flood, the flow is anticyclonic.

Coriolis acceleration

An acceleration of a parcel moving in a (moving) relative coordinate system. The total acceleration of the parcel, as measured in an inertial coordinate system, may be expressed as the sum of the acceleration within the relative system, the acceleration of the relative system itself, and the Coriolis acceleration. If Newton's laws are to be applied in the relative system, the Coriolis acceleration and the acceleration of the relative system (through the advection terms) must be treated as forces.

Coriolis force

An apparent force in a non-inertial coordinate system. This 'deflecting' force, arising from the earth's rotation, is required to be included in the equations of motion if Newton's laws are to be applied to this relative system. It acts normal to the velocity, proportional to the speed, deflecting to the right in the Northern Hemisphere and to the left in the Southern Hemisphere. Most simply, it is the apparent sideways force on an object or particle moving with respect to the earth.

Coriolis parameter, f

Twice the component of the earth's angular velocity about the local vertical, $f = 2\Omega \sin\phi$, where Ω is the angular speed of the earth and ϕ is the latitude. Since the earth is in rigid rotation, the Coriolis parameter, acting as a force per unit mass, is equal to the component of the earth's vorticity about the local vertical.

Cross-channel

The principle transverse or lateral axis of a channel. The cross-channel component of the current flows in the transverse direction. Motion in the cross channel direction in an estuary is secondary to motion in the axial direction.

Current ellipse

A progressive vector diagram for a complete tidal cycle of a harmonic component of a tidal current or of the full tidal current. This current diagram plots out the elliptical pattern of the local tidal current.

Curvilinear coordinates

Any linear coordinates that are not Cartesian coordinates. If u, v, w are three functions of the Cartesian coordinates x, y, z, and if at least one of these function s is not a linear combination of x, y, z, then u, v, w are curvilinear coordinates of the point whose Cartesian coordinates are x, y, z provided the Jacobian $\partial(u,v,w)/\partial(x,y,z)$ is not equal to zero. Any surface along which one of the three curvilinear coordinates is constant is called a coordinate surface; there are three families of such surfaces. Any line along which two of the three curvilinear coordinates are

constant is called a coordinate line; there are three sets of such lines. Three distinct coordinate lines may be drawn through each point of space. The three straight lines are called the local axes. If the local axes are everywhere mutually perpendicular, the curvilinear coordinates are said to be orthogonal or rectangular (i.e., they form a basis). Examples of frequently used curvilinear coordinates are polar coordinates, cylindrical coordinates, and spherical coordinates. The natural coordinate system is an orthogonal curvilinear coordinate system used often to simplify equations in fluid dynamics.

Cyclonic

Flow in a counterclockwise direction. Flow is cyclonic in a concave bend on flood and convex bend on ebb.

Datum

A point, line, or surface (here Mean-Lower-Low-Water or MLLW) used as a reference in surveying or mapping.

Densimetric Froude Number, Fr_d

A Froude number for the upper layer in a two-layer system. The use of reduced gravity accounts for the density difference between the upper and lower layers. It indicates the relative strength of axial current shear to the strength of vertical stratification. It can also be interpreted as the ratio of the axial current speed relative to the speed of a shallow water wave on a density interface.

Diffusive fraction

The fraction of the salt balance that is carried by processes relating to the tidal oscillatory currents.

Ebb channel

A feature common to estuaries in the southeastern United States, the ebb channel is a major channel as compared with the shallower minor flood channel. Ebb channels are often characterized by clean, sand-sized material with varying amounts of shell debris. The ebb channel is considerably deeper than the marginal flood channels and is regulated by the size of the tidal prism at the inlet. The ebb channel is often regarded as the *thalweg* (Sexton and Hayes 1996).

Ebb current

Non-technically, it is often referred to as the ebb tide or ebb. It is the movement of a tidal current away from the coast or down an estuary or tidal waterway and is the opposite of a flood current.

Ebb dominant

A tidal oscillation in velocity in which ebb currents are greater than and have a shorter duration than flood currents. This type of estuary is often characterized as hyposynchronous, where friction exceeds the effects of convergence and the tidal range decreases toward the head.

Eddy diffusivity (eddy diffusion coefficient)

A coefficient relating the turbulent diffusion of a variable to its gradient.

Eddy viscosity

A coefficient relating the turbulent shear stress to the velocity gradient.

Eddy kinematic viscosity, K

This viscosity is represented by K_m, K_v, K_z, or A_z, based on molecular analogy, and is equivalent to the molecular kinematic viscosity for eddy motions. Typical values for the vertical eddy kinematic viscosity in the Planetary Boundary Layer ranges from 0.1 to 2000 m^2s^{-1}. Likewise, the typical values for K_m in the salt wedge estuary range from $3x10^{-5}$ to $1x10^{-1}$ m^2s^{-1}. It is important to note that this is a property of the flow, not of the fluid.

Ekman depth, D_E

The depth of influence of the Ekman boundary layer. The force balance in the Ekman boundary layer is between the Coriolis force, the pressure gradient force, and vertical shear stress.

Ekman number, Ek

The Ekman number is the ratio of viscous forces (friction) to the Coriolis force in a rotating fluid. It can be used to determine the relative ratio between frictional effects and planetary rotation in an estuary. An Ekman number can be expressed as either a horizontal Ekman number or vertical Ekman number as in this case.

Entrainment

A mixing process in which a fluid is transported one way across a density interface. This is different from turbulent exchange, which is a two-way exchange of equal volumes across a density interface. Mathematically, entrainment is expressed as a velocity and the rate of change of the depth of the entraining fluid.

Estuary

A semi-enclosed coastal body of water having open communication with the sea at one end, and within which, the waters are influenced by river discharge, winds, and the tides. Waters in an estuary range from fresh to slightly brackish (1 PSU ~ 1 part per thousand (‰) salinity) near the 'head' to highly saline (ocean salinity ~ 35 PSU) near the 'mouth.' Classically defined by Stommel, there are four types of estuaries based on their vertical salinity concentration: the well-mixed estuary, the partially stratified estuary, the highly stratified estuary, and the salt wedge estuary. Some authors refer to the partially and highly stratified estuary collectively as the partially mixed estuary.

Estuarine Richardson Number, Ri_e

Equivalent to the gradient Richardson number but specific to an estuarine system. The estuarine Richardson number includes the buoyant effects of the freshwater discharge (Q_f), the channel width (B), and the shear effects from the tides (U_t).

Estuarine Froude Number, Fr_e

A form of the Froude number but specific to an estuarine system. The estuarine Froude number includes the buoyant effects of the freshwater discharge (Q_f), the channel width (B), and the depth at the estuary mouth (h).

Flood channel

A feature common to estuaries in the southeastern United States, the flood channel is a minor channel as compared with the dominant deeper ebb channel. Flood channels often have fairly high mud concentrations and are usually positioned next to barrier islands and may be closed off by landward-migrating swash bars. Flood channels are generally on either side of the main ebb channel. (Sexton and Hayes 1996).

Flood current

Non-technically, it is often referred to as the flood tide or flood. It is the movement of a tidal current toward the coast or up an estuary or tidal waterway and is the opposite of a ebb current.

Flood dominant

A tidal oscillation in velocity in which flood currents are greater than and have a shorter duration than ebb currents. This type of estuary is often characterized as hypersynchronous, where convergence exceeds the effects of friction and the tidal range increases toward the head.

Flux Richardson Number, Ri_f

The flux Richardson number is the ratio of the buoyancy forces to shear forces in the Turbulent Kinetic Energy equation. Because this definition of the Richardson number depends on the turbulent fluxes directly, Ri_f cannot be evaluated if there is no turbulence. A direct result is that the flux Richardson number can only tell if a fluid will become more 'laminar' due to stability effects.

Form drag

Form drag is the drag due to pressure forces in a flow field. Pressure forces can be generated by internal or external changes in the flow field due to changes in bathymetry, to flow around local obstacles, and/or the divergence of the flow due to stratification effects. Total drag is the summation of skin friction and form drag.

Fortnight

Two week. Fortnight is derived from a Middle English alteration of '*fourtene night*' to '*fourtenight*' (Oxford English Dictionary).

Free density interface

A density interface that is not directly affected by nearby physical boundaries. This does not preclude, however, that such an interface may be indirectly affected by close proximity to physical boundaries.

Froude Number, Fr

A dimensionless number comparing the speed of the flow to the velocity of propagation of a surface long wave (shallow water wave). A Froude number is a condition of state, that is, a Froude number implies that the fluid is already subject to turbulent conditions.

Gradient Richardson Number, Ri

The gradient Richardson number is the most commonly used form of the Richardson number, and is what is implied when simply the 'Richardson number' is discussed in the literature. It is different from the flux Richardson number in that it uses the flux-gradient approximation to estimate the turbulent fluxes in the flux Richardson number form. The use of this form can indicate when a fluid (under stabilizing or destabilizing effects) will become laminar or turbulent.

Highly Stratified Estuary

This type of estuary is typical of fjords. A highly stratified estuary has an upper saline layer that varies from nearly zero at its 'head' to oceanic at its 'mouth' while the salinity in its lower layer remains nearly constant (and usually highly saline) throughout the length of the estuary. The feature of the nearly constant saline lower layer is most noticeably due to sills or vertical channel constrictions often found near the 'mouth' which acts as a trap for the denser bottom waters. Vertical mixing is both limited and unidirectional, with salt water being mixed upward from the lower anoxic bottom waters into the lighter less saline water due to internal waves driven by shear instability between the layers.

High Water

The highest water level reached during a tidal cycle. It is commonly called high tide.

High Water Slack

High water slack occurs just prior to the current reversal between flood and ebb and is a time when the acceleration in the tidal current is at a minimum.

Hypersynchronos Estuary

An estuary where convergence exceeds friction and the tidal range increases towards the head. These types of estuaries are often 'flood dominant.'

Hyposynchronos Estuary

An estuary where friction exceeds the effects of convergence and the tidal range decreases towards the head. These types of estuaries are often 'ebb dominant.'

Incompressible Fluid

A fluid in which the density of the fluid does not change appreciably as a fluid parcel is moved from one location to another. For practical purposes, air and water are usually considered incompressible, with the exception that in the atmosphere, the density is allowed to vary in the vertical direction. This is accounted for in the Boussinesq approximation of the equations of motion.

Intense mixing periods

Times when intense mixing takes place due to critical internal Froude number conditions.

Internal Froude Number

A Froude number formed from layer thicknesses and densities.

Isohaline

A line of constant salinity.

Lateral Mixing

The mixing that occurs in a channel that is transverse to the primary direction of flow. This is sometimes referred to as cross-channel mixing, secondary circulation, secondary flow, transverse mixing, or transverse flow.

Low Water

The lowest water level reached during a tidal cycle. It is commonly called low tide.

Low Water Slack

Low water slack occurs just prior to the current reversal between ebb and flood and is a time when the acceleration in the tidal current is at a minimum.

Macrotidal Estuary

An estuary with a tidal range between 4 and 6 meters. These estuaries are often flood dominant.

Magnetic Declination

Magnetic declination, magnetic variation, or magnetic compass correction is the angle formed between true north and the projection of the magnetic field vector on the horizontal plane. By convention, declination is measured positive for east longitudes and negative for west longitudes. (National Geophysical Data Center)

Max Ebb Current

The time period of the tidal cycle during which ebb currents are maximized. In the Satilla River, Georgia, this generally occurs about one hour after slack water.

Max Flood Current

The time period of the tidal cycle during which flood currents are maximized. In the Satilla River, Georgia, this generally occurs about two hours after slack water.

Mean High Water (MHW)

The average level of all high waters at a place over a 19-year period.

Mean Higher High Water (MHHW)

The average level of the higher high water of the day at a place over a 19-year period.

Mean Low Water (MLW)

The average level of low water at a place over a 19-year period. An approximation to this level (called the low water datum) was commonly used as the chart datum for bathymetric surveys prior to 1983.

Mean Lower Low Water (MLLW)

The average level of the lower low water of the day at a place over a 19-year period. An approximation to this level (the lower low water datum or MLLW) is used a chart datum for the Atlantic and Pacific Coasts of the United States. The North American datum for hydrographic surveys which references Mean Lower Low Water is referred to as the North American Datum of 1983 (NAD 83). The North American Datum of 1983 is considered equivalent for charting purposes to the World Geodetic System 1984 (WGS 84).

Mean Sea Level (MSL)

The average height of the sea surface, based upon hourly observations of the tide height on the open coast or in adjacent waters which have free access to the sea. These observations are to have been made over a 'considerable' period of time. In the United States, mean sea level is defined as the average height of the surface of the sea for all stages of the tide over a 19-year period. Selected values of mean seal level serve as the sea level datum for all elevation surveys in the United States (Huschke 1989).

Mesotidal Estuary

An estuary with a tidal range between 2 and 4 meters. These estuaries are often a mix between flood and ebb dominant. An estuary, which is synchronous, in which convergence and friction are equal and the tidal range is constant along the estuary.

Microtidal Estuary

An estuary with a tidal range less than 2 meters. These estuaries are often ebb dominant.

Molecular dynamic viscosity, μ

This viscosity is represented by μ and represents the viscosity associated with molecular motions. A typical value for the molecular dynamic viscosity in the planetary boundary layer is 1.5×10^{-5} m^2 s^{-1} and in the salt wedge estuary is 1.2×10^{-3} kg $m^{-1}s^{-1}$.

Molecular kinematic viscosity

This viscosity is represented by ν which is the ratio of the molecular dynamic viscosity over the density (μ/ρ) and represents the viscosity associated with molecular motions. Typical values for molecular kinematic viscosity in the planetary boundary layer is 1.5×10^{-5} m^2s^{-1} and is about 1.2×10^{-6} m^2s^{-1} in the salt wedge estuary. This value changes with temperature and salinity, but is most affected by temperature changes. A convenient way to recall is to think of how slow molasses flows in January! (provided you are in a cold climate)

Natural Coordinates (Curvilinear coordinates)

An orthogonal, or mutually perpendicular, system of curvilinear coordinates for the description of fluid motion, consisting of an axis ***s*** tangent to the instantaneous velocity vector and an axis ***n*** normal to this velocity vector to the left in the horizontal plane, to which a vertically directed axis z may be added for the description of three-dimensional flow. Such a coordinate system often permits a concise formulation of dynamical problems, especially in the Langrangian system of hydrodynamics. Original reference: Holmboe, J., Forsythe, G.E., and Gustin, W., 1945: *Dynamic Meteorology*, p. 173.

Neap Range

The average semidiurnal tidal range occurring at the time of neap tide.

Neap Tide

A tide of decreased amplitude, occurring semimonthly one or two days after quadrature. The first and third quarters (the crescent and gibbous phases) of the moon are positions of quadrature.

North American Datum of 1983 (NAD 83)

The North American datum for hydrographic surveys which references Mean Lower Low Water. The North American Datum of 1983 is considered equivalent for charting purposes to the World Geodetic System 1984 (WGS 84).

Overmixed

The limit set on the occurrence of two-way flow by the critical densimetric Froude number (Dyer 1997).

Overstraining

The diminution of stratification by tidal straining and the restoration of homogeneous conditions (Dyer 1997).

Ozmidov length scale, L_o

This length scale represents the largest vertical excursion an eddy can have under stratified conditions. Based on the ratio between the buoyancy force and dissipation, it includes the effects of stratification on the largest energy containing eddies to the dissipation of the smallest energy dissipating eddies. Frequently mentioned in the literature, its use as a dynamic length scale appears to be often overlooked.

Partially mixed estuary

A larger class of estuaries which combines the partially stratified and highly stratified estuarine types into one category.

Partially stratified estuary

A shallow estuary which is characterized by a weak two layer system, in which the upper layer is slightly less saline than the lower one, with a mixing layer at their interface. There is a net flow of water seaward in the upper fluid layer and a net flow landward in the lower layer. This circulation pattern of inflow at the bottom and outflow at the top is often referred to as the 'estuarine' or 'gravitational' circulation, and gives rise to the longitudinal salinity variation in both layers.

Potential temperature, θ

Potential temperature is the temperature that an air parcel would have if it were taken from its initial position down to standard pressure (1000 mb) through an adiabatic process. In contrast to temperature, this conservative property, increases with height under statically stable conditions.

Quadratic friction law

A law relating the bed shear stress to the square of the flow velocity. Used as a first order improvement in two-dimensional models.

Quadrature

In astronomy, the arrangement of the earth, sun, and another planet or the moon, in which the angle subtended at the earth between the sun and the third body, in the plane of the elliptic, is 90º (Huschke 1989). The first and third quarters of the moon are positions of quadrature.

Radius of Curvature, R

In this dissertation, the radius of a circle imposed on a river bend or on the *thalweg* of a river bend. It is a measure of the rate of change of curvature in a system. A radius of curvature equal to infinity implies a straight reach.

Reduced gravity, g'

The apparent gravitational force exerted in a fluid including the effects of density. It is often noted in the literature as $g' = g\Delta\rho/\rho_o$ where g is the acceleration due to gravity, $\Delta\rho$ is the difference in density between specified layers, and ρ_o is a background reference density.

Reversing current

A tidal current which flows alternately in approximately opposite directions, with periods of slack water at each reversal. Such currents occur chiefly in restricted channels; open sea areas generally have rotary currents.

Reynolds flux

The turbulent flux of a scalar property such as salt.

Reynolds number, Re

This number describes the ratio of the inertial forces over the frictional forces in the equations of motion. It was originally formulated by Osborne J. Reynolds in 1938 to describe the transition from laminar flow (dominated by molecular processes) to turbulent flow (dominated by chaotic mixing processes). When Re is less than 2000, the flow is typically considered laminar, and when Re is greater than 4000, the flow is typically considered turbulent. The flow is considered transitional when $2000 < Re < 4000$.

Reynolds stress

The turbulent flux of momentum, the frictional force due to turbulence.

Richardson number, Ri

The Richardson number in general is the ratio between the stability of a fluid, limiting turbulent motions, and shearing stresses, producing turbulent motions. There are several forms and specific definitions for each type of Richardson number. Most common forms of the Richardson number include the flux, R_f, the gradient, Ri, the bulk, Ri_b, and the estuarine, Ri_e. Though not specifically stated, the gradient Richardson number is often implied when there is no direct reference to form of the Richardson number. A Richardson number is a condition of potential, that is, a Richardson number implies that the fluid is subject to turbulent mixing.

Rossby Number, R_o

The Rossby number is the ratio of centripetal acceleration to the Coriolis force in a rotating fluid. It can be used to determine the relative ratio between planetary rotation and curvature effects in an estuary.

Rossby Radius of Deformation, $R_{o,def}$

The Rossby radius of deformation gives the minimum horizontal length scale on which rotation effects are significant.

Rotary currents

A rotary current is a tidal current that changes direction progressively through 360 degrees during a tidal cycle.

Salt continuity

An equation that states that salt is neither created nor destroyed. The 'salt balance' is another statement of salt continuity.

Salt marsh

A brackish region surrounding a salt wedge, partially mixed, or well-mixed estuary. Salt marshes have well-vegetated saline intertidal flats and may front the open ocean. Salt marshes are defined to consist only of a veneer of sediments that are deposited inter-tidally (Davis 1985). Salt marshes in southeast Georgia are frequently typified by *Spartina alterniflora* and *Juncus roemerianus* marsh grasses.

Salt Wedge Estuary (SWE)

The salt wedge estuary is one of the four types of estuaries as classified by Stommel. This estuary is characterized by a coherent salt wedge that progresses upstream with the incoming flood tide under the less dense river discharge flowing seaward above. This type of estuary is predominant where river discharge is great and wind and tidal actions are weak. Examples of this type of estuary are the Fraser River in British Columbia and the lower Mississippi River where it enters the Gulf of Mexico.

Scour lag

A phase lag between the current velocity and the suspended sediment concentration due to the time taken for eroded sediment to disperse throughout the water column.

Secondary Circulation

A secondary circulation, also known as a transverse circulation or secondary flow, is a field of fluid motion which can be considered superimposed on a primary field of motion through the action of friction, usually in the vicinity of solid boundaries (Huschke 1989). Secondary circulation is a broad and often confusing term used to describe several mechanisms whose result is to vertically overturn the water column along the secondary (transverse) axis of the channel. A secondary circulation maybe composed of one to many cells that could potentially act to reduce or enhance local lateral gradients. The physical manifestation of secondary flows is often observed in the field as foam lines down the longitudinal axis of an estuary.

Secondary flow

An alternative expression for secondary circulation. The flow is directed at right angles to the primary axis of the channel.

Settling lag

A phase lag between the current velocity and the suspended sediment concentration due to the settling of particles through the water towards the bed.

Shear

Rate of change of a property in the vertical direction, often associated with wind shear.

Significant weather

Significant weather observations are any recorded weather event, temperature, pressure, humidity, or precipitation that is deemed important or 'unusual' to warrant attention. Significant weather events are recorded to reproduce, along with normal climatological conditions, a reasonably accurate weather history.

Sill

A sill is a vertical constriction to a channel.

Similarity Approach

An approach that is used to understand physical problems with which we are unable to accurately describe the physics. This approach frequently uses the formulation of dimensionless groups of fundamental properties. Ideas about turbulence are formulated using this approach by analogy to molecular motions.

Skin Friction

Local wall shear stress is often referred to as skin friction. Total drag is the summation of skin friction and form drag.

Slack Water

The condition when a tidal current has zero speed. Slack water in general is found only in reversing currents, since rotary currents usually change through 360 degrees in direction with no condition of zero speed.

Spring Range

The average semidiurnal tidal range occurring at the time of spring tide.

Spring Tide

Tide near the time of syzygy, when the ranges between high water and low water are greatest. The new and full moon are positions ofsyzygy.

Stand

The condition at high water or low water when there is no change in the height of the tide.

Static stability

A fluid is statically stable when less dense fluid is layered over more dense fluid. For example, warm air over cold air is statically stable as is moist air over dry air. When a fluid is statically unstable, convective mixing takes place to equalize the gradients. In the PBL, static stability requires that density decreases with altitude and likewise in the SWE, static stability requires that density increases with depth.

Stratification Number

A measure of stratification that is given by the amount of energy lost by the tidal wave within the estuary relative to that used in mixing the water column.

Stratification parameter

The ratio of the surface to bottom salinity difference to the depth of cross-sectional mean salinity.

Synchronous Estuary

An estuary where convergence and friction are equal and the tidal range is constant along the estuary.

Syzygy

The points in the moon's orbit about the earth at which the moon is new or full. That is, syzygy occurs when the earth, sun, and moon are in alignment.

Thalweg

The line of maximum depth in a channel cross-section (Dutch). The position of the *thalweg* is variable and is commonly found at the outside of channel bends. Opposite the *thalweg* is usually a bar or mud accumulation point (Leopold, Wolman, and Miller 1995). If an estuary were entirely drained of water, the *thalweg* would be the non-ephemeral river bed.

Thermal wind

The vertical variation of a geostrophic wind or current with height in hydrostatic equilibrium.

Thermocline

Similar to an inversion in the atmosphere, it is a zone of rapid temperature change with depth in the ocean, separating the upper turbulent mixed layer from the colder non-turbulent bottom waters.

Threshold lag

A phase lag between the current velocity and the suspended sediment concentration due to the threshold of the sediment movement.

Tidal excursion

The net axial distance over which a water parcel travels during one phase of the tidal cycle (ebb or flood) in relation to the dominant tidal constituent (often M_2).

Tidal intrusion front

A convergence near the mouth on an estuary or fjord where the in-flowing saline water plunges beneath the impounded fresher water.

Tidal prism

The volume of water within the estuary between high and low tides.

Tidal pumping

The tidally averaged transport of salt due to phase differences in the velocity, the salinity, and the water depth.

Tidal straining

The differential movement of two layers of water due to tidal friction at the base of the lower layer slowing it down relative to the upper layer. Also known as Strain Induced Periodic Stratification (SIPS), this condition can lead to enhanced vertical density gradients.

Transverse

Motion along the lateral axis of a channel. Transverse is often interchanged with cross-channel.

Transverse circulation

An alternative expression for secondary circulation or secondary flow. The flow is directed at right angles to the primary axis of the channel.

Trapping efficiency

The total sediment accumulated in an estuary divided by the fluvial input.

Triple junction

The location where two rivers, a river and a creek, or two creeks meet and join. A triple junction is often a location where turbulent flow conditions are almost always present.

Turbulent exchange

Turbulent mixing in which equal volumes of fluid are exchanged across a density interface. This is different from entrainment that is a one way transport of fluid across a density interface. Turbulent exchange mathematically is expressed in terms of an eddy flux.

Vertical gravitational circulation

The density induced flow in which a saline layer tends to flow underneath a less saline layer which tends to flow in the opposite direction, with mixing between them.

von Karman-Prandtl equation

An equation formalizing the logarithmic velocity profile near the bed.

Well-mixed estuary

A shallow estuary whose waters are homogeneously mixed from top to bottom along any point in the estuary. Salinity increases in a fairly linear fashion with distance along the estuary from its head to its mouth and salt is diffused upstream by longitudinal dispersion. Net flow of water is seaward at all depths.

World Geodetic System 1984 (WGS 84)

The North American datum for hydrographic surveys which references Mean Lower Low Water. The World Geodetic System 1984 is considered equivalent for charting purposes to the North American Datum of 1983 (NAD 83).

REFERENCES

Alexander, C. A., S. A. Elston, and C. Venherm, 2003: Drought and flood condition salinity surveys of the Ashepoo, Combahee, and South Edisto Rivers, ACE Basin National Estuarine Research Reserve, South Carolina. Marine Research Division of the South Carolina Department of Natural Resources, Charleston, South Carolina.

Apel, J. R., 1990: *Principles of Ocean Physics*., Vol. 38. International Geophysical Series. San Diego, CA: Academic Press, Inc.

Bathurst, J. C., C. R. Thorne, and R. D. Hey, 1977: Direct measurements of secondary currents in river bends. *Nature* **269**, 504-506.

Blanton, J. O., M. Alber, and J. Sheldon, 2001: Salinity response of the Satilla River estuary to seasonal changes in freshwater discharge. *Proceedings of the 2001 Georgia Water Resources Conference*. K. J. Hatcher (Ed.), Athens, GA: Institute of Ecology, The University of Georgia.

Blanton, J. O., C. Alexander, M. Alber, and G. C. Kineke, 1999: The mobilization and deposition of mud deposits in a coastal plain estuary. *Limnologica* **29**, 293-300.

Blanton, J. O. and F. A. Andrade, 2001: Distortion of tidal currents and the lateral transfer of salt in a shallow coastal plain estuary. *Estuaries* **24**: 467-480.

Blanton, J. O., G. Lin, and S. A. Elston, 2002: Tidal current asymmetry in shallow estuaries and tidal creeks. *Continental Shelf Research* **22**, 1731-1743.

Blanton, J. O., H. E. Seim, C. Alexander, J. A. Amft, and G. C. Kineke, 2003: Transport of salt and suspended sediments in a curving channel of a coastal plain estuary: Satilla River, GA. *Estuarine, Coastal, and Shelf Science* **57**, 993-1006.

Bousmar, D. and Y. Zech, 2002: Discussion of "Two-dimensional solution for straight and meandering overbank flows" by D. Alan Ervine, K. Babaeyan-Koopaei, and Robert H. J. Sellin. *Journal of Hydraulic Engineering* **128**, 550-551.

Bowden, K. F., 1963: The mixing processes in a tidal estuary. *International Journal of Air and Water Pollution* **7**, 343-356.

Boxall, J. B. and I. Guymer, 2003: Analysis and prediction of transverse mixing coefficients in natural channels. *Journal of Hydraulic Engineering* 1**29**:2, 129-139, doi:10.1061/(ASCE)0733-9429(2003)129:2(129).

Boxall, J. B., I. Guymer, and A. Marion, 2003: Transverse mixing in sinuous natural open channel flows. *Journal of Hydraulic Research* **41**:2, 153-165.

Brennan, M. L., d. H. Schoellhamer, J. R. Burau, and S. G. Monismith, 2002: Tidal asymmetry and variability of bed shear stress and sediment bed flux at a site in San Francisco Bay, USA. *Proceedings of INTERCOH-2000: Coastal and Estuarine Fine Sediment Processes*, J. C. Winterwerp and C. Kranenburg (Eds.), Elsevier.

Britter, R. E. and J. E. Simpson, 1978: Experiments on the dynamics of a gravity current head. *Journal of Fluid Mechanics* **88**, 223-240.

Callander, R. A., 1978: River meandering. *Annual Review of Fluid Mechanics* **10**, 129-158.

Chant, R. J., 2002: Secondary circulation in a region of flow curvature: Relationship with tidal forcing and river discharge. *Journal of Geophysical Research* **107:**C9, 3,131-3,141, doi:10.1029/2001JC001082.

Chant, R. J., and R. E. Wilson, 1997: Secondary circulation in a highly stratified estuary. *Journal of Geophysical Research* **102**, 23,307-23,315.

Clarke, J., and A. Gibson, 1987: Regulatory identification of hydrocarbon contaminants in dredged material. *Environmental Effects of Dredging: Technical Notes.*, U.S. Army Engineering Waters Experiment Station: Waterways Experiment Station.

Coleman, G. N., J. Kim, and P.R. Spalart, 2000: A numerical study of strained three-dimensional wall-bounded turbulence. *Journal of Fluid Mechanics* **416**, 75-116.

Csanady, G. T., 2001: *Air Sea Interaction: Laws and Mechanisms*. Cambridge, United Kingdom: Cambridge University Press.

Dame, R., M. Alber, D. Allen, M. Mallin, C. Montague, A. Lewitus, A. Chalmers, R. Gardner, C. Gilman, B. Kjerfve, J. Pickney, and N. Smith, 2000: Estuaries of the South Atlantic Coast of North America: Their geographical signatures. *Estuaries,* **23:**6, 793-6,819.

Davis, R. A. (Ed), 1985: *Coastal Sedimentary Environments*. Second Revised, Expanded Edition. New York, NY: Springer-Verlag.

Deines, K. L., 1999: Backscatter estimation using Broad Band Acoustic Doppler Current Profilers. *Proceedings IEEE 6th Working Conference on Current Measurement*, San Diego, CA: International Society of Electrical and Electronic Engineers.

Dewig, R., 9 June 1999. 'New' water getting bad reviews. *Savannah Morning News*.

Dietrich, W. E. and P. J. Whiting, 1989: Boundary shear stress and sediment transport in river meanders of sand and gravel. *River Meandering, Water Resources Monograph 12*. S. Ikeda and G. Parker (Eds.), Washington, D. C.: American Geophysical Union, 1-50.

Dronkers, J., 1996: The influence of buoyancy on transverse circulation and on estuarine dynamics. *Buoyancy Effects on Coastal and Estuarine Dynamics*. D. G. Aubrey, and C. T. Friedrichs (Eds.), Washington, D.C.: American Geophysical Union Press, **53**, 341-356.

Dunne, T. and L. B. Leopold, 1978: *Water in Environmental Planning*. New York, NY: W.F. Freeman and Company.

Dutton, J.A., 1986: *The Ceaseless Wind: An Introduction to the Theory of Atmospheric Motion*. New York, NY: Dover Publications, Inc.

Dyer, K. R., 1977. Lateral circulation effects in estuaries. *Estuaries, Geophysics, and the Environment.* Washington, D.C.: National Academy of Sciences, 22-29.

Dyer, K. R., 1997: Estuaries: A *Physical Introduction, Second Edition*. Chichester, United Kingdom: John Wiley & Sons, Ltd.

Elston, S. A., J. O. Blanton, and H. E. Seim, 2000: Secondary circulation in curved and straight estuarine reaches. *10th International Biennial Conference on Physics of Estuaries and Coastal Seas Proceedings*. SRAMSOE Report No. 366, Gloucester Point, VA: Virginia Institute of Marine Science, 172-175.

Elston, S. A., J. O. Blanton, H. E. Seim, J. Amft, and M. Sharman, 1999: An investigation in secondary circulation in a shallow well-mixed Georgia estuary. *Abstract Proceedings from the 15th Biennial International Estuarine Research Federation Conference 1999*, New Orleans, LA: Estuarine Research Federation, 35.

Emery, W. J. and R. E. Thompson, 1998: *Data Analysis Methods in Physical Oceanography.* Gray Publishing, Turbridge Well, Kent, Great Britain, Pergamon.

Ervine, D. A., K. Babaeyan-Koopaei, and R. H. J. Sellin, 2000: Two-dimensional solution for straight and meandering overbank flows. *Journal of Hydraulic Engineering* **126**:9, 653-669.

Ervine, D. A., K. Babaeyan-Koopaei, and R. H. J. Sellin, 2002: Closure to "Two-dimensional solution for straight and meandering overbank flows" by D. Alan Ervine, K. Babaeyan-Koopaei, and Robert H. J. Sellin. *Journal of Hydraulic Engineering* **128**, 551-552.

Fagherazzi, S., E. J. Gabet, and D. J. Furbish, 2004: The effect of bidirectional flow on tidal channel planforms. *Earth Surface Processes and Landforms* **29**, 295-309.

Falcón, M., 1984: Secondary flow in curved open channels. *Annual Review of Fluid Mechanics* **16**, 179-193.

Farrington, B., 17 May 2003. State to close water deal. *Savannah Morning News*.

Ferziger, J. H., J. R. Koseff, and S. G. Monismith, 2002: Numerical simulation of geophysical turbulence. *Computers and Fluids* **31**, 557-568.

Fischer, H. B., E. J. List, R. C. Y. Koh, J. Imberger, and N. H. Brooks, 1979: *Mixing in Inland and Coastal Waters*. San Diego, CA: Academic Press, Inc.

Frey, R. W. and P. B. Basan, 1985: Coastal salt marshes. *Coastal Sedimentary Environments*. Davis, R. A. (Ed), New York, NY: Springer-Verlag, 225-301.

Friedrichs, C. T. and L. D. Wright, 1997: Sensitivity to bottom stress and bottom roughness estimates to density stratification, Ekernförde Bay, southern Baltic Sea. *Journal of Geophysical Research* **102**:C3, 5,721-5,732.

Fugate, D. C. and R. J. Chant, 2005: Near-bottom shear stresses in a small, highly stratified estuary. *Journal of Geophysical Research* **110**, C03022, 1-13, doi:10.1029/2004JC002563.

Garrett, C., 2002: Frictional processes in estuaries. *The Second Meeting on Physical Oceanography of Sea Straits,* Villefranche, 15th-19th April 2002.

Garvine, R. W., R. K. McCarthy, and K.-C. Wong, 1992: The axial salinity distribution in the Delaware estuary and its weak response to river discharge. *Estuarine, Coastal, and Shelf Science* **35**, 157-165.

Geyer, W. R., 1993a: The importance of suppression of turbulence by stratification on the estuarine turbidity maximum. *Estuaries* **16**:1, 113-125.

Geyer, W. R., 1993b: Three-dimensional tidal flow around headlands. *Journal of Geophysical Research* **98**:C1, 955-966.

Geyer, W. R. and R. P. Signell, 1992: A reassessment of the role of tidal dispersion in estuaries and bays. *Estuaries* **15**:2, 97-108.

Geyer, W. R., J. H. Trowbridge, and M. M Bowen, 2000: The dynamics of a partially mixed estuary. *Journal of Physical Oceanography* **30**, 2,035-2,048.

Gill, A. E., 1982: *Atmosphere-Ocean Dynamics*., International Geophysics Series - Volume 30. United Kingdom: Academic Press, Inc.

Hansen, D. W. and M. Rattray, 1965: Gravitational circulation in straits and estuaries. *Journal of Marine Research* **23**, 104-122.

Hey, R. D., 1984: Plan geometry of river meanders. *River Meandering: Proceedings of the Conference Rivers 1983*. C. M. Elliot (Ed.), New York, NY: American Society of Civil Engineers, 30-43.

Holton, J. R., 1992: *An Introduction to Dynamic Meteorology, Third Edition*. San Diego, CA: Academic Press, Inc.

Howard, J. D. and R. W. Frey, 1975: Estuaries of the Georgia Coast, U.S.A.: Sedimentology and Biology. I. Introduction. *Senckenbergiana Maritima* **7**, 1-31.

Huschke, R. E. (Ed.), 1989: *Glossary of Meteorology, Fifth Edition*. Boston, MA: American Meteorological Society.

Huzzey, L. M., 1982: The dynamics of a bathymetrically arrested estuarine front. *Estuarine, Coastal, and Shelf Science* **15**, 537-552.

Huzzey, L. M., 1988: The lateral density distribution in a partially mixed estuary. *Estuarine, Coastal, and Shelf Science* **9**, 351-358.

Huzzey, L. M. and J. M. Brubaker, 1988: The formation of longitudinal fronts in a coastal plain estuary. *Journal of Geophysical Research* **93**:C2, 1,329-1,334.

Julien, P. Y., 2002: *River Mechanics.* Cambridge, United Kingdom: Cambridge University Press.

Kalkwijk, J. P. T. and R. Booij, 1986: Adaptation of secondary flow in nearly-horizontal flow. *Journal of Hydraulic Research* **24**:1, 19-37.

Kantha, L. H. and A. Rosati, 1990: The effect of curvature on turbulence in stratified fluids. *Journal of Geophysical Research* **95**:C11, 20,313-20,330.

Kasai, A., A. E. Hill, T. Fujiwara, and J. H. Simpson, 2000: Effect of the Earth's rotation on the circulation in regions of freshwater influence. *Journal of Geophysical Research* **105**:C7, 16,961-16,969.

Kay, D. J., D. A. Jay, and J. D. Musiak, 1996: Salt transport calculations from Acoustic Doppler Current Profiler (ADCP) and Conductivity-Temperature-Depth (CTD) Data: A Methodological Study. *Buoyancy Effects on Coastal and Estuarine Dynamics.* D. G. Aubrey, and C. T. Friedrichs (Eds.), Washington, D.C.: American Geophysical Union Press, **53**, 195-212.

Kjerfve, B., 1986: Circulation and salt flux in a well-mixed estuary. *Physics of Shallow Estuaries and Bays.* J. van de Kreeke (Ed.), Berlin, Germany: Springer-Verlag, Lecture Notes on Coastal and Estuarine Studies **16**, 22-29.

Kjerfve, B. and J. A. Proehl, 1979: Velocity variability in a cross-section of a well-mixed estuary. *Journal of Marine Research* **37**, 409-418.

Kjerfve, B. and H. E. Seim, 1984: Construction of net isopleth plots in cross-sections of tidal estuaries. *Journal of Marine Research* **42**, 503-508.

Klymak, J. M., 1998: ADCP data processing guide version 0.1. Applied Physics Laboratory at the University of Washington – Seattle, Seattle, Washington.

Klymak, J. M. and M. C. Gregg, 2003: The role of upstream waves and a downstream density pool in the growth of lee waves: Stratified flow over the Knight Inlet Sill. *Journal of Physical Oceanography* **33**, 1,446-1,461.

Knighton, D., 1998: *Fluvial Forms and Processes: A New Perspective*. New York, NY: John Wiley & Sons.

Krueger, G., 21 November 1999. Disease killing area blue crab. *Savannah Morning News*.

Kundu, P. K. and I. M. Cohen, 2004: *Fluid Mechanics, Third Edition*. San Diego, CA: Elsevier Academic Press, Inc.

Lacy, J. R., 2000: Circulation and transport in a semi-enclosed estuarine subembayment. Ph.D. Dissertation, 226 pp., Stanford University, California, United States.

Lacy, J. R. and S. G. Monismith, 2001: Secondary currents in a curved, stratified, estuarine channel. *Journal of Geophysical Research* **106:**C12, 31,283-31,302.

Lacy, J. R, M. T. Stacey, J. R. Burau, and S. G. Monismith, 2003: Interaction of lateral baroclinic forcing and turbulence in an estuary. *Journal of Geophysical Research* **108:**C3, 3,089-3,122, doi:10.1029/2002JC001392.

Landers, M., 25 June 2003. Environment challenged. *Savannah Morning News*.

Landers, M., 15 February 2004. Current damages. *Savannah Morning News*.

Landers, M., 7 March 2004. Project restores the river's natural curves. *Savannah Morning News*.

Lane, S. N., K. F. Bradbrook, K. S. Richards, P. M. Biron, and A. G. Roy, 2000: Secondary circulation cells in river channel confluences: measurement artifacts or coherent flow structures? *Hydrological Processes* **14**, 2047-2071.

Leopold, L. B., M. G. Wolman, and J. P. Miller, 1995. *Fluvial Processes in Geomorphology.* New York, NY: Dover Publications, Inc.

Lerczak, J. A. and W. R. Geyer, 2004: Modeling the lateral circulation in straight, stratified estuaries. *Journal of Physical Oceanography* **34**, 410-428.

Li, C., A. Valle-Levinson, L. P. Atkinson, K. C. Wong, and K. M. M. Lwiza, 2004: Estimation of drag coefficient in James River estuary using tidal velocity data from a vessel-towed ADCP. *Journal of Geophysical Research* **109**, C03034, 1-11, doi:10.1029/2003JC001991.

MacCready, P., 1999: Estuarine adjustment to changes in river flow and tidal mixing. *Journal of Physical Oceanography* **29**, 708-726.

MacCready, P., 2004: Toward a unified theory of tidally-averaged estuarine salinity structure. *Estuaries* **27**:4, 561-570.

MacCready, P., G. Pawlak, K. A. Edwards, and R. McCabe, 2003: Form drag on ocean flows. Submitted to the Proceedings of the 13th 'Aha Huliko'a Hawaiian Winter Workshop on "Near Boundary Processes and their Parameterization", 1-18.

Maddux, T. B., S. R. McLean, and J. M. Nelson, 2003: Turbulent flow over three-dimensional dunes: 2. Fluid and bed stresses. *Journal of Geophysical Research* **108:**F1, 6010, 1-17, doi:10.1029/2003JF000018.

Mertz, G. and Y. Gratton, 1995: The generation of transverse flows by internal friction in the St. Lawrence Estuary. *Continental Shelf Research* **15:**7, 789-801.

Moran, M. A., Sheldon, Jr., W. M., and Sheldon, J. E., 1999: Biodegradation of dissolved organic carbon in five estuaries of the Southeastern United States. *Estuaries* **22:**1, 55-64.

Moum, J. N. and J. D. Nash, 2000: Topographically induced drag and mixing at a small bank on the continental shelf. *Journal of Physical Oceanography* **30**, 2,049-2,054.

Moum, J. N. A. Perlin, J. M. Klymak, M. D. Levine, T. Boyd, and P. M. Kosro, 2004: Convectively driven mixing in the bottom boundary layer. *Journal of Physical Oceanography* **34**, 2,189-2,202.

Mulholland, P. J. and C. R. Olsen, 1992: Marine origin of Savannah River estuary sediments: Evidence from radioactive and stable isotope tracers. *Estuarine, Coastal, and Shelf Science* **34**, 95-107.

Murray, S. P., and A. Siripong, 1978: Role of lateral gradients and longitudinal dispersion in the salt balance of a shallow, well-mixed estuary. *Estuarine Transport Processes.* B. Kjerfve (Ed.), Columbia, SC: University of South Carolina Press, 113-124.

Nash, J. D. and J. N. Moum, 2001: Internal hydraulic flows on the continental shelf: High drag states over a small bank. *Journal of Geophysical Research* **106:**C3, 4,593-4,611.

National Climate Data Center, March through May 1997. Local unedited climate data for Kings Bay, Georgia (KNBQ). Downloaded online ASCII data files from http://www.ncdc.noaa.gov/cgi-bin/nndc/buyOL-002.cgi

National Geophysical Data Center, NOAA Satellites and Information, National Environmental Satellite, Data, and Information Service, Geomagnetic Data Home Page. Geomagnetic Declination Online Calculator, GD Online Calculator Ver. 4, http://www.ngdc.noaa.gov/cgi-bin/seg/gmag/fldsnth2.pl

Nelson, J. M. and J. D. Smith, 1989: Flow in meandering channels with natural topography. *River Meandering, Water Resources Monograph 12*. S. Ikeda and G. Parker (Eds.), Washington, D. C.: American Geophysical Union, 69-102.

Nicholls, R. J. and C. Smalls, 2002: Improved estimates of coastal population and exposure to hazards released. *EOS*, **83**:28, 301-305.

Nichols, M. M. and R. B. Biggs, 1985: Estuaries. *Coastal Sedimentary Environments*. Davis, R. A. (Ed), New York, NY: Springer-Verlag, 77-186.

Nunes, R. A. and J. H. Simpson, 1985: Axial convergence in a well-mixed estuary. *Estuarine, Coastal, and Shelf Science* **20**, 637-649.

Ott, M. W., 2000: Mixing and secondary circulation in Juan de Fuca Strait. Ph.D. Dissertation, 162 pp., University of Victoria, Canada.

Ott, M. W., R. Dewey, and C. Garrett, 2002: Reynolds stresses and secondary circulation in a stratified rotating shear flow. *Journal of Physical Oceanography* **32**, 3,249-3,268.

Ott, M. W. and C. Garrett, 1998: Frictional estuarine flow in Juan de Fuca Strait, with implications for secondary circulation. *Journal of Geophysical Research,* **103**:C8, 15,657-15,666.

Peters, H., 1997: Observations of stratified turbulent mixing in an estuary: Neap-to-spring variations during high river flow. *Estuarine, Coastal, and Shelf Science* **45**, 69-88.

Peters, H., 2003: Broadly distributed and locally enhanced turbulent mixing in a tidal estuary. *Journal of Physical Oceanography* **33**, 1,967-1,977.

Pollard, R. and J. Read, 1989: A method for calibrating ship-mounted Acoustic Doppler Profilers and the limitations of Gyro Compasses. *Journal of Atmospheric and Oceanic Technology,* **6**:6, 859-865.

Pond, P. and P. Pickard, 1989: *Introductory Dynamical Oceanography, Third Edition*. Oxford, United Kingdom: Pergamon Press.

Prandle, D., 1985: On salinity regimes and the vertical structure of residual flow in narrow tidal estuaries. *Estuarine, Coastal, and Shelf Science* **20**, 615-635.

Pritchard, D. W., 1952: Salinity distribution and circulation in the Chesapeake Bay estuarine system. *Journal of Marine Research* **13**, 133-144.

Pritchard, D. W., 1956: The dynamic structure of a coastal plain estuary. *Journal of Marine Research* **15**, 33-42.

RD Instruments, 1997: *Broad Band Acoustic Doppler Current Profiler Technical Manual.* San Diego, CA, RD Instruments.

Reeves, J., 30 September 2004. Alabama, Florida seek to block new water allotments for Georgia. *Savannah Morning News.*

Rhoads, B. L. and S. T. Kenworthy, 1995: Flow structure in an asymmetrical stream confluence. *Geomorphology* **11**, 273-293.

Ridd, P. V., T. Stieglitz, and P. Larcombe, 1998: Density-driven secondary circulation in a tropical mangrove estuary. *Estuarine, Coastal, and Shelf Science* **47**, 621-632.

Ritter, D. F., R. C. Kochel, and J. R. Miller, 2002: *Process Geomorphology, Fourth Edition*. Boston, MA: McGraw Hill.

Schramkowski, G. P. and H. E. de Swart, 2002: Morphodynamic equilibrium in straight tidal channels: Combined effects of Coriolis force and external overtides. *Journal of Geophysical Research* **107**:C12, 3,227-3,243, doi:10.1029/2000JC000693.

Scully, M. E. and C. T. Friedrichs, 2003: The influence of asymmetries in overlying stratification on near bed turbulence and sediment suspension in a partially-mixed estuary. *Ocean Dynamics* **53**, 208-219, doi:10.1007/s10236-003-0034-y.

Seim, H. E., 1999: ADCP data processing guide version 0.1 modifications. Skidaway Institute of Oceanography, Savannah, Georgia.

Seim, H. E., J. O. Blanton, and T. F. Gross, 2002: Direct stress measurements in a shallow, sinuous estuary. *Continental Shelf Research* **22**, 1,565-1,578.

Seim, H. E. and M. C. Gregg, 1997: The importance of aspiration and channel curvature in producing strong vertical mixing over a sill. *Journal of Geophysical Research* **102**:C2, 3,451-3,472.

Sexton, W. J. and M. O. Hayes, 1996: Holocene deposits of reservoir-quality sand along the central South Carolina coastline. *American Association of Petroleum Geologists Bulletin* **80**:6, 831-855.

Sharman, M., 1999: Preliminary analysis of vessel-mounted ADCP data. Senior Thesis, 83 pp., Department of Environmental Engineering, The University of Western Australia.

Simpson, J. H., J. Brown, J. Matthews, and G. Allen, 1990. Tidal straining, density currents, and stirring in the control of estuarine stratification. *Estuaries* **13:**2, 125-132.

Simpson, J. H., E. Williams, L. H. Brasseur, and J. M. Brubaker, 2005. The impact of tidal straining on the cycle of turbulence in a partially stratified estuary. *Continental Shelf Research* **25**, 51-64.

Smith, J. D. and S. R. McLean, 1984. A model for flow in meandering streams. *Water Resources Research* **20**:9, 1,301-1,315.

Soulsby, R. L., 1990: Tidal current boundary layers. *The Sea, Volume 9: Ocean Engineering Science.* B. Le Méhauté and D. M. Hanes (Eds.), New York, New York: John Wiley & Sons, Inc., 523-566.

Stacey, M. T., S. G. Monismith, and J. R. Burau, 1999: Observations of turbulence in a partially stratified estuary. *Journal of Physical Oceanography* **29**, 1,950-1,970.

Stacey, M. T. and D. K. Ralston, 2005: The scaling and structure of the estuarine bottom boundary layer. *Journal of Physical Oceanography* **35**, 55-71.

Sternberg, R. W., G. Kineke, and R. Johnson, 1991: An instrument system for profiling suspended sediment, fluid, and flow conditions in shallow marine environments. *Continental Shelf Research* **11**, 109-122.

Sutherland, B. R., M. R. Flynn, and K. Dohan, 2004: Internal wave excitation from a collapsing mixed region. *Deep-Sea Research II* **51**, 2,889-2,904.

Swift, M. R., D. W. Fredriksson, and B. Celikkol, 1996: Structure of an axial convergence zone from Acoustic Doppler Current Profiler measurements. *Estuarine, Coastal, and Shelf Science* **43**, 109-122.

Thompson, F., 1917: The Mistress of Vision. *The Oxford Book of Mystical Verse*. D. H. S. Nicholson and A. H. E. Lee (Eds.), Oxford, United Kingdom: Clarendon Press, 240.

Thorne, C. R., and R. D. Hey, 1979: Direct measurements of secondary currents at a river inflection point. *Nature* **280**, 226-228.

Thorne, C. R., and S. Rais, 1984: Secondary current measurements in a meandering river. *River Meandering: Proceedings of the Conference Rivers 1983*. C. M. Elliot (Ed.), New York, NY: American Society of Civil Engineers, 675-686.

Tritton, D. J., 1988: *Physical Fluid Dynamics, Second Edition*. New York, NY: Oxford University Press.

Trowbridge, J. H., W. R. Geyer, M. M. Bowen, and A. J. Williams III, 1999: Near-bottom turbulence measurements in a partially mixed estuary: turbulent energy balance, velocity structure, and along-channel momentum balance. *Journal of Physical Oceanography* **29**, 3,056-3,072.

Turrell, W. R., J. Brown, and J. H. Simpson, 1996: Salt intrusion and secondary flow in a shallow, well-mixed estuary. *Estuarine, Coastal, and Shelf Science* **42**, 153-169.

Turrell, W. R., and J. H. Simpson, 1988: The measurement and modelling of axial convergence in shallow well-mixed estuaries. *Physical Processes in Estuaries.* J. Dronkers and W. van Leusen (Eds.), New York, New York: Springer-Verlag, 130-145.

Uehara, T., 1984: Field study on unsteady salinity intrusion into a small estuary. *Journal of Hydroscience and Hydraulic Engineering* **2**:1, 99-111.

UNESCO, 1985: The international system of units (SI) in oceanography. *UNESCO Technical Papers No. 45*, Paris, France: IAPSO Publication Science No 32.

United States Geological Survey, 2004: Published daily mean stream flow data for Station 02228000, Satilla River at Atkinson, Georgia. *National Water Information System*, located at http://waterdata.usgs.gov/nwis.

Valle-Levinson, A. and L. P. Atkinson, 1999: Spatial gradients in the flow over an estuarine channel. *Estuaries* **22**:2A, 179-193.

Valle-Levinson, A., W. C. Boicourt, and M. R. Roman, 2003: On the linkages among density, flow, and bathymetry gradients at the entrance to the Chesapeake Bay. *Estuaries* **26**:6, 1,437-1,449.

Valle-Levinson, A., C. Li, K.-C. Wong, K. M. M. Lwiza, 2000a: Convergence of lateral flow along a coastal plain estuary. *Journal of Geophysical Research* **105**, 17,045-17,061.

Valle-Levinson, A., K.-C. Wong, K. M. M. Lwiza, 2000b: Fortnightly variability in the transverse dynamics of a coastal plain estuary. *Journal of Geophysical Research* **105**, 3,413-3,424.

Walker, S. A., G. A. Hamill, and H. T. Johnston, 1999: Development and erosion of a mixing layer in a stratified flow. *Mixing and Dispersion in Stably Stratified Flows.* P. A. Davies (Ed.), Oxford, United Kingdom: Clarendon Press, 229-249.

Webster, D. R., D. B. DeGraff, and J. K. Eaton, 1996: Turbulence characteristics of a boundary layer over a two-dimensional bump. *Journal of Fluid Mechanics* **320**, 53-69.

Whiting, P. J. and W. E. Dietrich, 1991: Convective accelerations and boundary shear stress over a channel bar. *Water Resources Research* **27**:5, 783-796.

Williams, A., J. Tochko, R. Keohler, W. Grant, T. Gross, and C. Dunn, 1987: Measurements of turbulence in the oceanic bottom boundary layer with an acoustic current meter array. *Journal of Atmospheric and Oceanic Technology* **4**, 312-327.

Williams, D., 14 October 1999. Florida water officials pitch aquifer storage. *Savannah Morning News*.

Winterwerp, J. C., 2001: Stratification effects by cohesive and noncohesive sediment. *Journal of Geophysical Research* **106**:C10, 22,559-22,574.

Wong, K.-C., 1994: On the nature of transverse variability in a coastal plain estuary. *Journal of Geophysical Research* **99**, 14,209-14,222.

World Resources Institute, 1994: *World Resources 1994-95: A Guide to the Global Environment*. Oxford, U.K.: Oxford University Press.

VITA

Susan Anne Elston is the youngest daughter of Dr. Asaph Clayton Vandewater Elston and Mrs. Mary Elizabeth McIntyre Elston. She was born in Denver, Colorado and was reared in La Crosse, Wisconsin, along the banks of the Mighty Mississippi River. Childhood experiences along the river and at a nearby pond further developed her innate love of water and weather. A lifelong career studying meteorology and oceanography thus blossomed from such humble beginnings.

She earned a Bachelor of Science from the University of Wisconsin – Madison in Atmospheric Sciences and in Mathematics in 1992. She earned a Master of Science from the University of Wisconsin – Madison with a minor in Mathematics in 1995. Returning to her love of water, she decided to take the plunge and get a doctorate in Physical Oceanography from the Georgia Institute of Technology in 2005.

She currently lives in historically maritime Savannah, Georgia, with her husband and their collection of furry animals.